UNIVERSITÀ DEGLI STUDI DI PALERMO

Dottorato di Ricerca in Scienze Fisiche
Dipartimento di Fisica e Chimica-Emilio Segré
Settore Scientifico Disciplinare - FIS/05 - Astronomia e Astrofisica

Accretion disc tomography in Low-Mass X-Ray Binaries: A multi-wavelength approach

IL DOTTORE
ALESSIO ANITRA

IL COORDINATORE
PROF. MARCO CANNAS

IL TUTOR
PROF. TIZIANA DI SALVO

CO TUTOR
PROF. ROSARIO IARIA

CICLO XXXVI
ANNO CONSEGUIMENTO TITOLO 2024

Contents

List of Figures

List of Tables

Abstract

X-ray binaries systems where a compact object accretes matter from a companion star, offer exceptional opportunities to explore astrophysical phenomena, including the General Relativity and Magneto-Hydrodynamics, which cannot "yet" be reproduced in laboratories. Particularly, the study of accretion discs in low-mass X-ray binary systems not only offers pivotal clues to the physics of accretion and the processes releasing a huge amount of electromagnetic radiation in X-rays and gamma-rays, but also can unravel the geometry of these systems. The core of this thesis encompasses a multi-wavelength temporal and spectral analysis of LMXBs, stretching from optical to X-ray wavelengths.

My first work presented in Chapter 5 delves into the spectral analysis of the low-mass X-ray pulsar 4U 1822-371. This study reveals for the first-time significant evidence of a reflection component in the x-ray spectrum of a high inclination source and provides updated orbital ephemerides. The analysis con-tributes to understanding the system's geometry proposing a unique configuration for the source.

With my second project (Chapter 6) I broadened the scope of my analysis to the optical range, analysing the double-peaked Hβ line profile in the optical spectrum of Swift J1357.2-0933, a transient LMXB hosting one of the galaxy most massive stellar-mass black hole candidates. This investigation not only estimated the black hole's systemic and radial velocity but also uncovered compelling evidence of a narrow core within the Hβ emission profile.

Building on these findings, my final project (Chapter 7) introduces an innovative method that applies X-ray spectral models to optical data. I applied a non-relativistic version of the DISKLINE model to describe the optical Hα and Hβ line profiles. Applying this method to two sample sources, Swift J1357.2-0933 and MAXI J1305-704, yielded estimates for the inner and outer radii of the disc's emitting region. Remarkably, the method also determined the disc's inclination angle with a precision surpassing existing literature values.

Overall, this comprehensive approach advances our understanding of LMXB geometries. It constrains critical parameters such as the inclination angle, size of the accretion disc, and the varying temperature and ionization states across different disc regions. These insights are not only pivotal for unraveling the nature of the accretion process but also for creating a 'topographic map' of the disc, shedding light on the entire structure of the disc and the physics governing it.

1 Introduction

In the age of the ancients, humans have garnered extensive knowledge about the cosmos simply by observing the night sky. The history of astronomy, likely the oldest of the natural sciences, is lost in the dawn of time, as ancient as the origin of humankind itself. This was the flame that inspired humanity, guiding them in their quest to understand the most enigmatic phenomena of the universe. Among these, neutron stars and black holes hold a prominent place, representing the final stages in the stellar evolution of massive stars. Investigating these objects offers us a favored approach to grasping the intricacies of General Relativity and Quantum Mechanics. The advent of X-ray astronomy in the early 1960s unveiled that X-ray binary systems are among the most powerful X-ray emitters in our Galaxy, featuring black holes or neutron stars drawing in material from a companion star. In the process of accretion, gravitational energy from the mass received from the companion star is primarily transformed into X-rays.

Typically, X-ray spectra of X-ray Binaries (hereafter XRBs) disclose a blackbody-like component at soft X-ray energies, specifically below 10 keV, emitted from an accretion disc that forms around the compact object. In these systems, the accreted material does not plummet straight onto the black hole or neutron star due to its inherent specific angular momentum, leading it to travel in circular orbits. As this angular momentum diminishes, the matter moves into increasingly smaller orbits around the compact object, spiraling inward to create what is known as an accretion disc. However, these discs are not the sole elements featured in X-ray spectra from such sources. Often, a spectral component resembling a power law, extending into hard X-ray regions (sometimes exceeding 100 keV), is also observed. This aspect is identified as the spectral signature of an accretion-disk corona, which is a comparatively hotter, less dense, and optically thinner section of the accretion flow.

The interaction of the high energy radiation with the disc results in a key feature of LMXB spectra, known as the reflection spectrum. It is distinguished by a thick forest of fluorescence lines, with the Iron Kα line between 6.4 - 6.97 keV according to the ionization state of the matter in the disc, being particularly prominent. Believed to emitted from the disc innermost regions, the presence of this component and the analysis of the emission line profiles serve as crucial tools for acquiring physical insights about the source and exploring the physics of the accretion flow in the region of strong gravitational influence near the compact object.

However, focusing solely on X-rays when examining an accretion disc is an incomplete

approach. As the plasma temperature increases closer to the compact object, the radiation emitted by the disc covers a broad range of energies, spanning from X-rays in the inner regions to optical wavelengths in the outermost part. The optical spectra of these systems are also rich in multiple emission lines, resulting from atomic transitions of lighter elements like Hydrogen and Helium. The distinctive double-peak profile induced by the Doppler effect in these lines is crucial for deciphering the geometry and dynamics of the system, providing information on the radial velocity of the companion star, the compact object, and possibly on their masses.

My thesis delves into a comprehensive multi-wavelength temporal and spectral analysis of low mass x-ray binaries, extending from optical to X-ray wavelengths. It amalgamates methodologies employed for examining standard spectral components in X-ray spectra with those used in optical studies, yielding insights into the synergy between these two aspects. In particular, my research aims to dissect the geometry of X-ray binaries with a low mass companion, with a focus on the accretion disc. I aim to define key parameters such as the inclination angle of the system, the size of the disc and the variation of temperature and ionization states in different regions of the accretion disc. This effort seeks to create a "topographic map" of the disk, shedding light on its entire structure and underlying physics.

The structure of my thesis is organized in the following way. Chapters 2 and 3 lay the groundwork for my research, delving into the nature of compact objects and X-ray binary systems. These chapters discuss their formation, the critical role of accretion in these systems, and the physical processes that result in the various components of the emitted spectrum. Chapter 4 then shifts focus to the multi-wavelength instruments utilized throughout the thesis. Chapter 5 marks the beginning of my research, offering a detailed spectral analysis of the pulsating neutron star in the low mass X-ray binary 4U 1822-371. This analysis reveals substantial evidence of a reflection component and suggests a novel configuration for the source. In Chapter 6, the scope of the analysis broadens to include the optical spectrum, specifically investigating the double-peaked Hβ line profile of Swift J1357.2-0933. This transient low-mass X-ray binary is notable for hosting one of the most massive stellar-mass black hole in our galaxy. The Chapter presents findings on the systemic and radial velocities and highlights the discovery of a distinct feature within the Hβ emission profile. Chapter 7 builds on these earlier discoveries, introducing a groundbreaking approach that applies X-ray spectral models to optical data. Utilizing a non-relativistic version of the diskline model, this method is applied to the optical Hβ and Hα profiles of the sources Swift J1357.2-0933 and MAXI J1305-704. This innovative approach yields estimates for the inner and outer radii of the accretion disc and system inclination angle. In the Conclusion, I will present the key findings of this thesis, outline the unresolved questions, and discuss how my ongoing work could play a role in addressing these outstanding issues.

2 X-ray Binary systems

The Earth's atmosphere acts as a barrier to X-rays, preventing them from reaching the surface. This unique property of X-rays played a crucial role in shaping the field of X-ray astronomy and necessitated the development of specialized space-based observatories. In the early 1960s, the first X-ray detections were made using basic detectors placed on suborbital rockets, revealing the first indications of potential X-ray sources.

In 1962, data collected by an Aerobee rocket led to the first evidence of soft X-rays from sources outside the solar system (Giacconi et al. 1962). The source behind this emission, later named Scorpius X-1, was the first extra-solar X-ray source revealed in history, and its discovery marked a significant milestone in the field of X-ray astronomy. The discovery of *Scorpius X-1* highlighted the potential of X-ray astronomy as a powerful tool for the study of astrophysical phenomena, and a few years later, on December 12, 1970, *Unrhu*, the first satellite entirely dedicated to X-ray observations of the sky, was launched into orbit, starting the era of X-ray astronomy.

Subsequent observations and analyses unveiled that Scorpius X-1 is a binary star system composed of two stars. One takes the form of a main sequence regular star, comparable in mass to our Sun, while the second is a compact object, thought to be either a neutron star or a black hole. Before delving into the intricate scenario of binary systems, it is useful to shed some light on their primary stars, the **compact object**.

2.1.0 Dead stars

Stars are burning balls of gas, held up by the struggle between two opposing forces: the gravity pressure, which tries to crush the star inward, making it smaller and denser, and the pressure generated by nuclear reactions happening in the core of the star. There, hydrogen nuclei (proton) constantly collide and fuse into helium through nuclear fusion. This process releases an enormous amount of energy that pushes outward, countering the relentless compression of gravity.

As a star evolves nuclear processing continues until the available nuclear fuel in the star is exhausted. The more massive the star, the faster it evolves and the quicker it will be on its way to

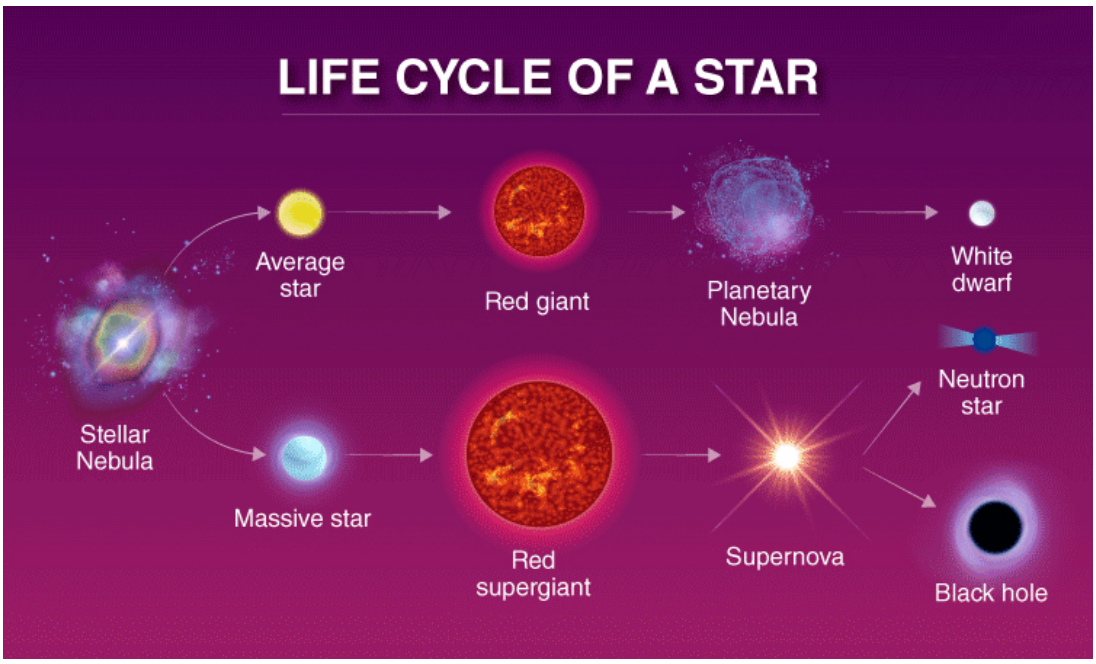

Figure 2.1: Sketch of the evolutionary paths of a solar-mass star and a massive one (https://byjus.com/physics/life-cycle-of-stars/).

synthesizing heavier and heavier elements. In the most massive stars, the thermonuclear fusion will stop with the synthesis of iron. The production of heavier elements would no longer be energetically convenient since iron has the highest binding energy per nucleon of any element possible. At the end of stellar evolution, the core will exhaust its nuclear fuel and, as the nuclear reactions stop, gravity will take over. The core collapses until something else steps in to resist gravity and create a new stable equilibrium, thus forming a new object much smaller and denser than the progenitor star, a **compact object**. Since there are no longer any nuclear reactions in the core, what will oppose gravitational contraction? In stars comparable to or slightly more massive than our Sun, as the core shrinks, the outer layers of the star expand, transforming the star into a red giant. The core, now incredibly hot and dense, gets so compressed that electrons get packed closer and closer together until the classic gas formula is no longer able to describe the behaviour of the gas. This is fully composed of electrons and protons, which are both examples of fermions, implying that when these particles are confined within progressively smaller volumes, the combination of the *Pauli exclusion principle* and the *Heisenberg uncertainty principle* (expressed as $\Delta p \Delta x \approx \hbar$) guarantees that as the separation between the particles reduces (Δx), their momenta (Δp) necessarily increase. This quantum mechanical crowding of fermions creates an outward pressure related to degenerate gas, known as **degeneracy pressure**. It is the resistance the fermions offer to further compression and it is the only force pushing back against the relentless gravitational force trying to collapse the core. The balance between degeneracy pressure and gravity establishes a stable conformation, preventing further collapse. This results in the formation of an extremely dense $\left(\rho \sim 10^{18}\ \mathrm{g\ cm^{-3}}\right)$ object, roughly the size of Earth, primarily consisting of electrons and protons, and exhibiting a surface temperature that can reach up to 10000 K. This object is known as a **White Dwarf** (WD). See Fig. 2.1 for a summary sketch of stellar evolution. As nuclear fusion ceases to occur, the WD, if isolated, will slowly cool down

over the course of billions of years.

2.2.0 Degeneracy pressure

What has been said above is true as long as the mass of the star is comparable to or slightly higher than that of the Sun. Indeed, the nature of the compact object depends on the mass of the core of the original star (M_c). If $M_c < 1.44\,M_\odot$, the core collapses until the fermionic gas becomes degenerate and the degeneracy pressure succeeds in balancing the gravitation shrinking, stabilizing the object in a WD. The above mass value is called the **Chandrasekhar limit** and can be easily derived from basic physical considerations. The equilibrium condition of a WD can be expressed by placing the gravitation pressure equal to the degenerate pressure.

Degeneracy pressure can be described as the pressure exerted by a fermionic gas confined within the star, as it collides with the interior boundaries of the star. The rate at which collisions occur per unit area and time along the x-direction can be expressed as $N = nv_x$, where 'n' denotes the particle density. During each collision, a momentum equivalent to $2p_x$ is transferred, with contributions along the y-axis cancelling each other out. Given the momentum along the x-direction $p_x = mv_x$, we can derive the degenerate pressure as $P_D = 2p_x n/m$. Here, m is the mass of the fermions in the gas. Given that electrons are significantly less massive than protons and neutrons, the contribution of other particles becomes negligible. Therefore, the pressure stemming from degenerate electrons alone is sufficient to counteract the gravitational forces. Considering that each electron occupies a volume Δx^3, the Pauli exclusion principle guarantees that a single state can only be filled by a single electron. Consequently, the electron density can be expressed as $n = 1/\Delta x^3$. Applying the Heisenberg uncertainty principle ($\Delta p \approx \hbar/\Delta x$) we find that the degenerate pressure adopts the form (Longair 2011):

$$P_D = \frac{2\hbar n_e^{5/3}}{m_e}. \tag{2.1}$$

Equating this expression to the gravitational pressure $P_g = GM^2/(4\pi R^4)$ gives a dependence between the radius (R) and the inverse cube root of the mass, $M^{(-1/3)}$. Consequently, as the mass of the white dwarf increases, its radius (R) decreases, leading to a corresponding increase in degenerate pressure. If the electrons attain relativistic velocities, then $v_x = c$, and the pressure adopts a different form as expressed by:

$$P_D = 2\hbar c n_e^{4/3}. \tag{2.2}$$

It becomes evident that the relativistic degenerate pressure exhibits a slower trend compared to its non-relativistic counterpart. If we hypothetically increase the mass of the WD, its size would decrease until the electron velocities reach relativistic speeds. This alteration in the pressure trend disrupts the equilibrium, thereby triggering gravitational collapse. Taking this change in trend as the tipping point for the WD collapse, when we equate the gravitational pressure and the relativistic degenerate pressure, we arrive at the critical mass value for a WD, denoted as

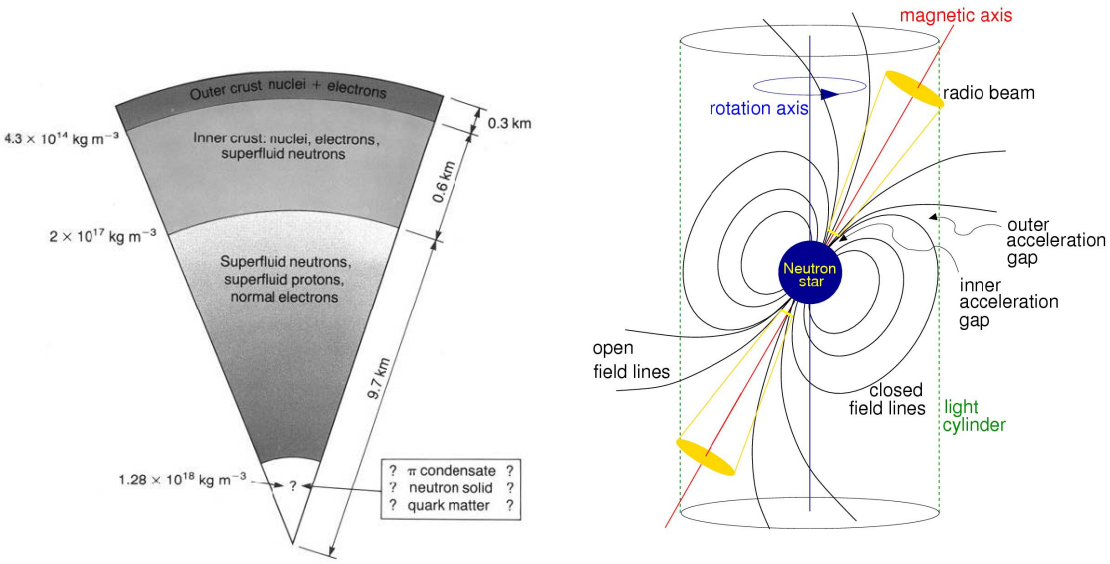

Figure 2.2: **Left panel**: A representative model showing the different inner layers of a neutron star (Longair 2011). **Right panel**: Magnetic dipole model of a Pulsar.

$M_c = 1.44 M_\odot$, the above mentioned Chandrasekhar limit (Longair 2011). What happens now? What stands in the way of collapse at this point?

2.3.0 Neutron Stars

Shortly after Chadwick discovered the neutron in 1932 (Chadwick 1932), scientific exploration delved into the possibility of a stable celestial body composed entirely of these particles. In 1934, astronomers Walter Baade and Fritz Zwicky introduced the concept of Neutron Stars, underlining their extraordinary density and linking their genesis to supernova explosion (Baade & Zwicky 1934). In 1939, Robert Oppenheimer and George Volkoff pioneered the development of the first theoretical model for the composition of Neutron Stars, proposing the presence of neutron matter at exceedingly high densities ($\rho = 5 \times 10^{15}\,\mathrm{g\,cm^{-3}}$) and inferring a limit mass value of $0.7 M_\odot$ with a radius of R = 9.6 km (Oppenheimer & Volkoff 1939). However, the concept of neutron stars fell into oblivion for more than three decades due to the prevailing belief that their small size made them too faint to be observable at astronomical distances with optical telescopes. The scientific community overlooked these objects until 1963, when the identification of the first non-solar X-ray source by Giacconi et al. (1962), spurred dozens of theorists to turn their attention toward investigating the physics behind these compact stars. During the same period, on November 28, 1967, Jocelyn Bell, a graduate student at the University of Cambridge, and her supervisor Anthony Hewish detected a radio pulsating signal exhibiting a periodicity of 1.3373 seconds (Hewish et al. 1968). Initially humorously dubbed "Little Green Man 1" (LGM-1) due to its initial association with extraterrestrial origin, it was subsequently identified as the first radio Pulsar (PSR B1919+21). This discovery earned Anthony Hewish the Nobel Prize in Physics (Jocelyn Bell was sidelined, even though her significant contribution to the discovery had already been acknowledged).

But what leads to the origin of these objects? As mentioned in the previous section as density rises, the electron gas experiences an increase in velocity, subsequently boosting its energy. At a critical point, when the total energy of an electron surpasses the difference in energy between a neutron and a proton ($\Delta E = 1.29 MeV$), the inverse β decay process ($p + e^- \longrightarrow n + \nu_e$) comes into play. This process, known as **neutronisation**, leads to the conversion of protons and electrons into neutrons, and as a WD primarily consists of nuclei of carbon, oxygen, and iron, these nuclei tend to accumulate an excess of neutrons until they experience fragmentation, leading to the release of a neutron gas into the degenerate relativistic electron gas. This phenomenon is referred to as **neutron drip** and begins at a density of approximately $\rho \sim 4 \times 10^{14}\,\mathrm{kg\,m^{-3}}$ (Longair 2011). This process will lead to the innermost layers converting nearly all matter into neutrons. Since neutrons are 2,000 times heavier than electrons, their velocity will cease to be relativistic, resulting in degenerate pressure with a steeper trend ($P_D \propto n^{5/3}$), effectively counterbalancing the gravitational forces. As a result, we will obtain a stable object primarily composed of neutrons, commonly referred to as a **Neutron Star** (NS).

However, neutrons naturally undergo decay into protons and electrons with an average lifetime of 14.8 minutes. So, why do NSs remain stable? As an NS consists of a neutron-electron degenerate gas, when a neutron decays, the released electron must occupy the first available energy state. If the Fermi energy exceeds the kinetic energy of the emitted electron, the process would be energetically unfavourable. The critical density at which this occurs is $\rho = 1.2 \times 10^{10}\ \mathrm{kg\ m^{-3}}$ (Longair 2011).

NSs rank among the most densely packed objects in the universe. Their extraordinary density has presented the scientific community with a mystery surrounding the nature of the material composing them. Inside NSs, matter attains densities far surpassing those found in atomic nuclei, rendering it impossible for experimental testing in laboratories. Consequently, the scientific community has developed several theoretical models aimed at establishing the equation of state for ultra-dense matter a fundamental pursuit in modern physics and astrophysics. The left panel of Fig. 2.2 shows an example of the internal structure of a traditional NS. The various layers in the model are as follows:

- The **outer layer** is mainly composed of atomic polymers of ^{56}Fe, which behave as a one-dimensional solid with high conductivity and zero resistivity, and with a density lower than $10^9\,\mathrm{kg\,m^{-3}}$.
- The **outer crust**, with densities ranging from 10^9 to $4.3 \times 10^{14}\,\mathrm{kg\,m^{-3}}$, is a solid region composed of heavy nuclei within a relativistic degenerate electron gas.
- In the **inner crust**, where the density is higher (ranging from 4.3×10^{14} to $2 \times 10^{17}\,\mathrm{kg\,m^{-3}}$), the matter consists of a mixture of neutron-rich nuclei and a gas of free degenerate neutrons and relativistic electrons. As we delve deeper, the density rises, causing nuclei to begin to dissolve, giving way to a neutron liquid.
- In the **central core** region, beyond a critical density of $3 \times 10^{18}\,\mathrm{kg\,m^{-3}}$, neutrons undergo geometric overlap, potentially transitioning into non-nucleonic states. Consequently, the

core might consist of solid-phase neutrons, quarks, or other exotic forms of matter.

While the state of the matter in the outer and inner crusts is well-documented (see Baym et al. 1971), the composition and structure of the innermost sections are subjects of intense debate. Theoretically, the inner core of the NS can be described by the Equation of State of dense matter (EoS), delineating the intricate relationship between pressure and energy density. Within this context, a myriad of exotic models has been postulated, predicting phenomena such as hyper ionization of matter, the emergence of hyperons, pion and kaon condensation, and the presence of quark matter composed of u, d, s quarks.

All of these EoS can be divided into two main categories: *stiff* and *soft*. A stiff equation portrays matter as highly resistant to compression, resulting in a rapid pressure increase with density. **This leads to a NS that is less compressible, typically resulting in a larger radius for a given mass and possibly a higher maximum mass**. Conversely, a soft equation characterizes easily compressible matter, manifesting as a gradual pressure increase with density. In this case, NSs generally display higher compactness and have correspondingly lower maximum masses (Lattimer & Prakash 2016). The difference between stiff and soft equations of state is important in understanding the structure and properties of NSs, as it affects their mass-radius relationship. It is clear, therefore, that astrophysical observations play a crucial role in defining the EoS within the cores of NSs. Currently, obtaining constraints on mass and radius stands as one of the most effective methods to confirm or disprove a substantial array of proposed EoS (Degenaar & Suleimanov 2018).

2.4.0 Pulsar

The first NS observed by Jocelyn Bell in 1968 turned out to be a **Radio Pulsar**. A Pulsar is a highly magnetized, rotating NS, emitting beams of electromagnetic radiation from its magnetic poles. NSs are among the most magnetized objects in the universe. When a star with a radius of 10^6 km collapses into a body with a radius of 10 km, the magnetic flux must be conserved. This conservation implies that, as the flux is proportional to BR^2, reducing the radius by a factor of 10^5 necessitates the magnetic field to increase by a factor of 10^{10}. This means that an initial magnetic field of just 100 G becomes 10^{12} G. This mechanism can give rise to the existence of objects known as **Magnetars**, characterized by extremely intense magnetic fields on the order of 10^{14-15} G (Rea 2013). However, magnetic flux is not the only quantity that must remain unchanged after the collapse; the conservation of angular momentum ensures that young NS possess not only an exceptionally high magnetic field but also a rapid spin. Now, it is clear that if the magnetic field is tilted with respect to the rotational axis of an angle α, and it rotates at the spin frequency of the NS Ω, it acts as a rotating magnetic dipole, emitting radiation in accordance with the Larmor formula (Jackson 1975):

$$\mathrm{P} \propto \Omega^4 \mathrm{B} \mathrm{R}^3 \sin\alpha. \tag{2.3}$$

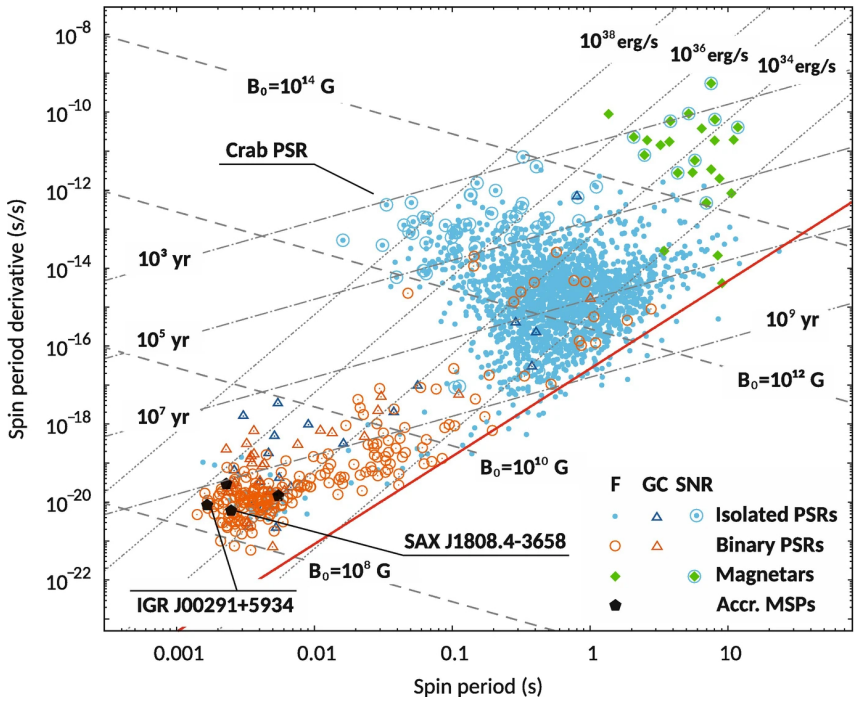

Figure 2.3: $P - \dot{P}$ diagram of rotation-powered Pulsars, where it is possible to see different sub-classes of them. Lines of the constant magnetic field, spin-down age, and spin-down power are plotted with dashed, dotted and dot-dashed lines, respectively while the red solid line is the Pulsar death line (Di Salvo & Sanna 2022).

However, because this emission typically manifests at extremely low radio frequencies (P < 1 kHz), which are lower than the plasma frequency of the interstellar medium or the ionized nebula enveloping these objects, its propagation is hampered, making it challenging to observe. The magnetic dipole radiation actively extracts rotational energy from the NS, leading to an increase in its spin period over time. Specifically, the braking of the star goes as $\dot{\Omega} \propto -\Omega^n$, where the n is the *braking index*. However, this is not the sole emission mechanism for these isolated NSs.

Given that the surface of an NS acts as a perfect rotating conductor, surface charges accumulate at the poles due to the *Hall effect*. These charges are then guided along the intense magnetic field lines. As a result, charged particles undergo acceleration and migrate towards the poles. There, they release accumulated energy as $\gamma-$rays, often through processes like Inverse Compton scattering of surrounding thermal photons (see, e.g., Bussard et al. 1986; Sturner & Dermer 1994). Subsequently, these gamma-ray photons are prone to pair production, populating the Pulsar polar caps with electrons and positrons. This cascade effect generates more $\gamma-$rays, contributing to the emission process. At this point, the most plausible scenario is that the relativistic particles produced, moving along the curved and open field lines (see Fig. 2.2), emit synchrotron radiation predominantly in the gamma or X-ray bands (Radhakrishnan & Cooke 1969). Both the latter and the radio rotational powered emission are indeed continuous emissions. However, the majority of the beamed emission originates possibly from the polar caps and, as the magnetic axis is misaligned with the rotational axis, this configuration makes the beam of light can only be observed when it intersects the observer line of sight, creating the illusion of pulsed emission due to the so-called **lighthouse effect**. Consequently, the periodicity of the pulses corresponds to

the spin period of the NS.

Since the detection of the first radio Pulsar PSR B1919+21, many different classes have been discovered. The diverse population of Pulsars exhibits a range of features that can be well-understood in the P-$\dot{P}$ diagram (see Fig. 2.3). Within the central region, Pulsars associated with supernova remnants are placed, characterized by an age on the order of 10^5 years, boasting an intense magnetic field. Another noteworthy classification is with the *Rotating Radio Transients (RRATs)*, marked by sporadic and infrequent bursts of radio emission (e.g. RRAT J1819-1458, see Hu et al. 2011). Shifting attention to the upper-left quadrant, where magnetic field strengths escalate to approximately 10^{14} G, the domain of *Magnetars* unfolds. The lower-left angle is populated by rapidly rotating Pulsars with spin periods less than 10 milliseconds and a weak magnetic field ($B \sim 10^{8-10}$ G) called **Millisecond Pulsars**. The weak magnetic field and the fact that most of them are in binary systems with (nearly) zero eccentricity have led to the hypothesis that these systems may indeed be nothing more than 'recycled Pulsars' that have undergone spin-up processes, eventually attaining millisecond periods. This concept is commonly referred to as the **recycling scenario** (Alpar et al. 1982; Backer et al. 1982). According to this model, young, newly-formed Pulsars, while radiating away a fraction of their rotational energy, experience a braking effect that gradually increases their spin period, causing them to move to the right in the diagram along a line of constant magnetic field strength. As spin frequency and magnetic field deacrese, likely due to the ohmic dissipation of the magnetosphere (see Ostriker & Gunn 1969), Pulsars eventually enter a state where the weakened rotational energy and magnetic field are insufficient to power the rotational emission resulting in the cessation of Pulsar activity. In the diagram, this occurs when crossing the so-called *death line* and entering the region known as the *Pulsar graveyard*. If the Pulsar is part of a binary system, when the mass transfer starts, it can become active as an **X-ray Pulsar** and undergo spin-up by accumulating mass and angular momentum from matter transferred from its companion star until it achieves a spin period on the order of milliseconds. When the accretion phase concludes, the vast amount of rotational energy acquired allows radio emission to resume despite its low magnetic field (B $\sim 10^8$ G), and the object is reborn as a Millisecond Pulsar. We will delve deeper into the accretion mechanisms in binary systems in the upcoming chapters.

2.5.0 Black holes

In a 1783 letter to the Royal Society, the mathematician and natural philosopher John Michell, explored the idea of "*dark stars*", celestial bodies with gravity so strong that nothing, not even light, could escape their gravitational pull. However, this concept did not gain widespread attention at the time. A few centuries later, on November 4, 1915, Albert Einstein unveiled his general theory of relativity, offering a new understanding of gravity as the curvature of spacetime caused by mass and energy. However, Einstein field equations proved intricate and demanding to solve, particularly in the context of strong gravitational fields (Einstein 1915). A few months later, in January 1916, the German physicist Karl Schwarzschild, serving on

the Eastern Front during World War I, discovered an exact solution to the field equations for a non-rotating spherical distribution of mass. This solution unveiled a critical radius, identified as the **Schwarzschild radius** ($R_s \sim 2GM/c^2$), where escaping the gravitational pull becames impossible (Schwarzschild 1916). This radius signalled the presence of a so-called **event horizon**, a boundary beyond which nothing can return.

We already explored the gravitational collapse of an object surpassing the Chandrasekhar mass limit, resulting in the formation of an NS sustained by neutron degeneracy pressure. Another critical threshold, known as the *Tolman-Oppenheimer-Volkoff (TOV) limit*, exists, typically ranging from 2 to 3 $M_\odot$ for NS. Once surpassing the TOV limit, even the resilience of neutron degeneracy pressure proves inadequate to halt gravitational collapse, causing the star to undergo further compression and ultimately leaving behind nothing but a space-time singularity and farther out at its Schwarzschild radius, a boundary beyond which nothing, not even light, can return, what we call an event horizon. This is what is commonly referred to as a **Black Hole** (BH). The term "black holes" was coined by physicist John Archibald Wheeler during one of his lectures in 1967. He chose the adjective "black" to underline their role as perfect absorbers, and coupled it with "hole" to vividly convey the concept of a cosmic abyss where once matter descends, there is no return.

A black hole can be comprehensively defined by a minimal set of parameters. Specifically, throughout its formation process, nearly all characteristics of the original star are lost, retaining only three key attributes: mass (M), angular momentum (J), and electric charge (Q). As stated by Wheeler *black holes have no hair*, they lack any additional distinguishing features or extraneous details. The classification of black holes is delineated into three principal categories: *supermassive*, *intermediate*, and *stellar-mass black holes*. As previously mentioned, *stellar-mass black holes*, varying from 3 to 20-30 solar masses, arise as the aftermath of massive stars succumbing to gravitational collapse. mass black holes, with a mass ranging from 10^2 to 10^4 solar masses, remain a subject of intense debate, supported by observed candidates and limited confirmed detections. The confirmation of their existence is exemplified by the detection of the brightest ultraluminous X-ray source (ULXs) HLX1 in the nearby galaxy ESO 243-49 (Lasota et al. 2011). Lastly, supermassive black holes, with masses ranging from 10^6 to 10^9 solar masses, reside in the nuclei of galaxies.

Since BHs do not emit any type of radiation, it is impossible to detect them directly through our instruments. What reveals their presence is, in fact, their interaction with radiation and matter surrounding them (Salpeter 1964). The first supermassive BH has been detected in active galactic nuclei and through the elliptical motion of stars accelerated around a central dark region. Detecting Intermediate-mass BHs presents a challenge due to their relatively weaker gravitational influence compared to supermassive ones. However, they can potentially be identified through gravitational wave emissions, especially when two smaller BHs merge. This scenario occurred when a signal called GW190521, was observed by *LIGO* and *Virgo* interferometers on May 21, 2019. This signal was identified as the product of a merger between two BHs with masses approximately 85 and 66 solar masses, leading to the formation of an intermediate-mass BH of 142 solar masses (Abbott et al. 2020). Stellar-mass black holes are identified in X-ray binaries

through the detection of X-ray emissions originating from matter in the accretion disc (Remillard & McClintock 2006). A pivotal moment in the identification of stellar BH occurred in 1971 when Cygnus X-1 became the first celestial object officially recognized as a BH (Bolton 1972; Webster et al. 1972). Currently, the astronomical landscape includes approximately 20 X-ray binaries identified as black-hole binaries, harbouring a compact object too massive to be a neutron star binary.

In the forthcoming sections, I will delve into the detailed processes of accretion of mass that make these systems among the brightest objects in the X-ray sky.

2.6.0 Low and High Mass X-ray Binary systems

More than a decade after its initial discovery, Scorpius X-1 was recognized as the first X-ray binary by Giacconi in 1974 (Giacconi 1974). This revelation marked the identification of a unique binary star system, hosting a compact object, specifically, a NS as the primary star, actively involved in the process of accreating matter from its companion star, known as the secondary star. Through ongoing scientific exploration, it has become evident that similar binary systems are widespread and stand out as some of the brightest sources of X-rays in our galaxy.

X-ray binary systems (XRBs) can originate through different mechanisms. One pathway involves the gravitational binding of two stars, where one of them undergoe a supernova explosion, transforming into a compact object. Alternatively, a system may form through the capture of another star within a Globular Cluster. In the former scenario, the stars were initially in the main sequence, and the more massive one concluded its evolution by exploding into a supernova, ultimately becoming a Neutron Star. In instances where less than half of the system's mass is lost during this supernova event, the binary system perseveres. However, if more than half of the system's mass is shed, the companion star experiences a forceful kick, potent enough to unbind the system (see Verbunt 1993).

The first classification of these binary systems hinges on the nature of the compact object, resulting in the differentiation between **Cataclysmic Variables** (CVs) and **X-ray Binaries** (XRBs). CVs involve white dwarfs as primary stars and are marked by erratic and dramatic fluctuations in brightness (Warner 1995). Conversely, systems hosting either a BH or a NS fall under the classification of XRBs. A significant distinction lies in the realm of X-ray luminosity, where CVs exhibit lower luminosity within the range of $10^{29} - 10^{33}$ erg s^{-1} (Warner 1995). In contrast, NS and BH XRBs show overlapping luminosity ranges, spanning from 10^{30} to 10^{39}erg s^{-1}. This differentiation not only delineates the two main categories but also underscores the diverse energy outputs and processes at play in these systems.

XRBs are systematically classified based on the mass of their companion stars, dividing into two distinct categories: **low-mass X-ray binaries** (LMXBs) and **high-mass X-ray binaries** (HMXBs) (for a review see Fornasini et al. 2023). LMXBs are typically associated with low-mass older Population II companion stars, approximately $10^9 - 10^{10}$ years old and generally with a mass lower than 1 $M_\odot$. The companion star in an LMXB can be a late-type main-sequence star,

an A-type star, a white dwarf, or an F-G-type subgiant. In contrast, HMXBs are linked to youthful and high-mass companion stars, often of spectral type O or B, which generate intense stellar winds. If the compact object is an NS with a high magnetic field (typically around 10^{12} G), the material undergoes accretion onto the magnetic poles, giving rise to observable X-ray pulsations (Alonso-Hernández et al. 2022). In LMXBs, NSs exhibit a lower magnetic field, ranging from 10^8 to 10^9 G, and may showcase type I X-ray bursts, characterized by thermonuclear flashes on the NS's surface. Additionally, LMXBs can exhibit coherent pulsations due to accreting material in the polar caps, as observed in **Accreting Millisecond X-ray Pulsars** (Di Salvo & Sanna 2022). LMXBs can be observed in old Galactic regions such as Globular Clusters, while HMXBs predominantly populate the Galactic Disk. Notably, LMXBs tend to be more compact, characterized by shorter orbital periods, compared to HMXBs. HMXBs can further be divided into subgroups like Be/X-ray binaries and SG/X-ray binaries, based on the type of companion star.

2.7.0 Accretion and Luminosity

A defining feature of all X-ray binary systems is their remarkable X-ray brightness. Their exceptional brightness arises from a fundamental process known as mass accretion, which takes place between the companion star and the compact object. Mass accretion is a phenomenon in which material from the companion star gradually accumulates onto the compact object, under the influence of gravity. Its remarkable efficiency in converting gravitational potential energy into radiation, especially in the form of X-rays, is responsible of the brightness of these systems.

As material falls onto a compact object, its kinetic energy rises while its gravitational potential energy becomes increasingly negative. Near the compact object, especially in the context of a BH or a NS, velocities achieve highly relativistic values (Mukhopadhyay & Dutta 2012). Upon reaching the surface of the object, the material experiences swift deceleration, resulting in the transformation of kinetic energy into heat. Assuming we have a test mass m, and the compact object has mass M and radius R, the energy accreted and released in the form of radiation equals the variation in gravitational energy of the mass moving from infinity to the surface of the object:

$$\Delta E_g = \frac{GMm}{R}. \tag{2.4}$$

Here, G is the gravitational constant. To have an idea of the energy involved, consider an NS with a typical radius of 10 km and a mass of $1.4\,M_\odot$. The energy released by just a gram of matter is approximately 10^{20} erg, which is 100 times greater than the energy released by the thermonuclear fusion of a gram of hydrogen into helium in the core of our Sun (Frank et al. 2002). By differentiating ΔE_g with respect to time, we obtain what is referred to as the **accretion luminosity**:

$$L_{\rm acc} = \frac{GM\dot{m}}{R}. \tag{2.5}$$

From the equation above, it is evident that in accretion solely due to the force of gravity, the

emitted luminosity is linearly connected to the **mass accretion rate** $\dot{m}$, i.e. the rate of the mass "stripped" from the companion star. The efficiency of accretion as an energy release mechanism is strongly dependent on the compactness of the accreting object. The larger the ratio M/R, the greater the efficiency. Therefore, it is useful introducing the factor $\eta = \mathrm{GM/Rc^2}$ and expressing the accretion luminosity as $L_{\mathrm{acc}} = \eta \dot{m} c^2$. In the case of a standard NS, the efficiency factor is approximately 0.15. However, if we consider a WD, which has a radius of about 10^9 cm, this factor is significantly smaller. Now, what about a BH?

Common sense, driven by its immense gravitational potential energy, might lead us to think a BH as a perfect converter of gravitational energy into radiation. Indeed, if the matter accreting onto a BH could be brought into the hole infinitely slowly until $R = GM/c^2$, all the rest mass energy could, in principle, be extracted, resulting in $\eta = 1$[1]. Nevertheless, the absence of a well-defined physical surface in a BH makes troublesome the definition of its efficiency. Considering its event horizon ($R_s = 2GM/c^2$) as a surface would yield an efficiency of 0.5, much higher than that of an NS. However, it is crucial to note that a BH itself cannot emit any radiation[2] and the observable radiation is emitted from the matter rotating around it (which has lost half of its gravitational potential energy into radiation). In light of these considerations, the true radius should be the radius of the innermost stable circular orbit (R_{ISCO}). Beyond this distance, matter is compelled to fall radially into the BH due to its immense gravitational pull. For a non-rotating BH, this radius is three times the R_s (Frank et al. 2002), causing the efficiency of a BH to diminish to 0.1, which is lower than that of an NS.

Looking back at the accretion luminosity, assuming all emitted photons adhere to a blackbody distribution, we can apply the Stefan-Boltzmann law: $L/4\pi R^2 = \sigma T^4$, where σ is the Stefan-Boltzmann constant, to calculate the associated temperature. With a typical luminosity for an X-ray binary $\left(L = 10^{37}\mathrm{ergs}^{-1}\right)$, Wien law allows us to determine the peak wavelength of the emitted radiation (λ_{max}), resulting in $\lambda_{\mathrm{max}} = 1.45 \times 10^{-7}$ cm, falling squarely within the X-ray spectrum. This implies that the zenith of emitted radiation tied to mass accretion falls occurs in the X-ray range, highlighting that "X-ray binaries" goes beyond being a mere catchy name.

2.8.0 Accretion processes

The distinctive features previously outlined between LMXBs and HMXBs, particularly those pertaining to the nature of companion stars, play a fundamental role in understanding the physics and mechanisms governing mass transfer in these systems. In the case of HMXBs, the accretion process is predominantly driven by the stellar wind originating from the high-mass companion star, typically an O or B-type star and captured by the compact object gravitational field. In contrast, in LMXBs the accretion process unfolds through **Roche Lobe overflow**. This entails the low-mass companion star transferring mass to the compact object when it exceeds its Roche lobe. Since the focal point of this thesis revolves around LMXBs, we will delve into the intricate

[1] To delve deeper into the physics of BHs, explore the dedicated section in the (Frank et al. 2002).
[2] This is not strictly true if we consider Hawking radiation (Hawking 1975).

details of this latter process, setting aside the discussion related to HMXBs (to delve dipper into mass transfer processes in HMXBs see Frank et al. 2002).

2.8.1 Roche lobe overflow

The gravitational interaction between two celestial bodies in a binary system poses a complex challenge for resolution. In 1879, the French astronomer and physicist Édouard Roche addressed this challenge in his work titled "*Sur l'équilibre des satellites et sur leur figure*", introducing the concept of gravitational equipotential surfaces, now widely recognized as **Roche lobes**.

Roche approach revolves around focusing on the orbit of a test particle within the gravitational potential generated by two massive bodies orbiting each other, influenced by their mutual gravitational attractions. Assuming both objects can be treated as point masses and they follow circular Kepler orbits[3], any gas flow between them is governed by the Euler equation. When expressed in a frame of reference rotating with the binary system, this equation takes the following form:

$$\frac{\partial \mathbf{v}}{\partial t} + (\mathbf{v} \cdot \nabla)\mathbf{v} = -\nabla\Phi_{\mathrm{R}} - 2\omega \wedge \mathbf{v} - \frac{1}{\rho}\nabla P, \tag{2.6}$$

where ω is the angular velocity of the binary, P is the pressure and $(-2\omega \wedge \mathbf{v})$ is the Coriolis force. The term Φ_R in the equation represents the aforementioned **Roche potential**, and its divergence accounts for centrifugal and gravitational effects. It can be written as (Frank et al. 2002):

$$\Phi_{\mathrm{R}}(\mathbf{r}) = -\frac{GM_1}{|\mathbf{r} - \mathbf{r}_1|} - \frac{GM_2}{|\mathbf{r} - \mathbf{r}_2|} - \frac{1}{2}(\omega \wedge \mathbf{r})^2 \tag{2.7}$$

where r_1 and r_2 denote the position vectors of the centres of the two stars. In Fig. 2.4 a 3D representation of the Roche potential for a binary system is plotted. Given M_1 and M_2 the masses of the primary and secondary star, the configuration of the potentials is determined by the mass ratio $q = M_1/M_2$, with the overall scale determined by the binary separation a, which can be expressed through Kepler's third law: $a^3 = P^2 M/4\pi^2$, with $\mathrm{M} = \mathrm{M}_1 + \mathrm{M}_2$.

To fully grasp the importance of Roche's work, we can consider introducing a small test mass into this system. If this mass is located significantly distant from either of the two stars ($r >> a$), then the object would simply experience the gravitational potential of a large star with a combined mass of $M_1 + M_2$. As the mass nears one of the two objects, the gravitational field of that particular object becomes increasingly dominant. Consequently, if the mass is located close to one of them, it will solely perceive the potential of the nearby object. The scenario becomes intriguing when the mass is located between the two extremes. In such a case, it becomes possible to identify an eight-shaped equipotential surface encompassing both objects. The two lobes constituting this surface, each encircling its respective body, are termed **Roche lobes**. These lobes are connected by an unstable equilibrium point known as the **inner Lagrangian point** L_1.

To visualize the concept of L_1, imagine a ball settled at the summit of a hill. Similar to the ball, a mass at L_1 is in an unstable equilibrium state and, with a little push, can roll down the hill

[3]Tidal effects often circularize initially eccentric orbits relatively quickly, making this a reliable approximation (Frank et al. 2002).

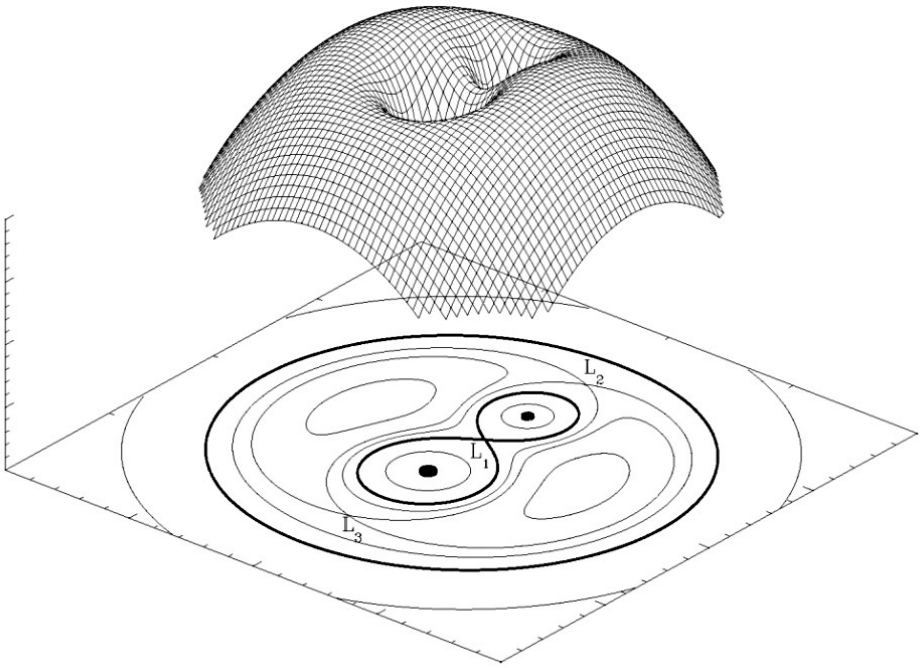

Figure 2.4: 3D representation of the Roche potential in *a* binary system. Three of the five Lagrange points, L_1, L_2, L_3, are highlighted (https:www.heaven.waarnemen.com).

toward either of the two stars. If both stars are smaller than their respective Roche lobes, there is no reason for matter to be gravitationally pulled off either star by the other, resulting in no material transfer, and the system is described as *detached*.

Over time, it is reasonable that the secondary will progressively fill its Roche lobe. In LMXB systems, this primarily occurs due to the system losing angular momentum through mechanisms like *magnetic braking* and *gravitational wave emission*, leading to a reduction in orbital separation and a shrinking of the companion's Roche lobe until it touches the star. Alternatively, the companion can evolve off the main sequence, turning into a giant or a subgiant. This phenomenon is more prevalent in high-mass stars ($M > 0.8\,M_\odot$), which evolve at significantly shorter timescales, while the evolution timescale for a low-mass star is comparable to the age of the universe (see Kippenhahn & Weigert 1990). At this moment, the system transitions into a *semi-detached* state. Drawing on the analogy of the ball atop the hill, the outer layers of the companion star approach L_1 so closely that any perturbation[4] would suffice to propel its material to "roll down" into the Roche lobe of the compact object. Here, the gravitational pull of the star captures it, triggering the transfer of mass from one object to another through **Roche lobe overflow**. If, for some reason, both stars simultaneously fill their Roche lobes, we encounter a peculiar system terms as *contact binary* (e.g. see Jayasinghe et al. 2020).

It is evident from the Equation 2.7 that the precise definition of equipotential surfaces and, consequently, the actual dimensions of the Roche lobes pose non-trivial challenges that necessitate computational mathematical methods. However, approximate analytical formulas can be derived. As the lobes lack a spherical shape, determining an average radius to characterize them becomes

[4]These perturbations persist, originating from factors such as the star's internal pressures (Frank et al. 2002)

crucial, and a suitable measure involves the radius of a sphere with the same volume as the lobe. For an LMXB system with a small mass ratio ($0.1 \lesssim q \lesssim 0.8$), Paczynskii's formula proves useful (Paczyński 1971):

$$\frac{R_2}{a} = 0.462 \left(\frac{M2}{M_1 + M_2} \right)^{1/3}. \tag{2.8}$$

Here, R_2 describes the radius of the Roche lobe of the companion star, and a denotes the orbital separation[5]. Another often practical approximation for mass ratios $0.03 \lesssim q \lesssim 1$ accurate to 5%, is: $R_1/R_2 = (M_1/M_2)^{0.45}$. In this thesis, a comprehensive expression applicable to all q values with 1% accuracy, as provided by Eggleton (1983a), will be employed:

$$\frac{R_2}{a} = \frac{0.49 q^{2/3}}{0.6 q^{2/3} + \ln(1 + q^{1/3})}. \tag{2.9}$$

The process of mass transfer induces changes in both the mass ratio and the separation a along with the orbital period, as this exchange involves not only matter but also angular momentum. The determination of the Roche geometry by a and q, as evident from equation 2.9, implies that the Roche lobe of the mass-losing star undergoes either contraction or expansion during the process. It is natural to question whether such a variation of the Roche lobe could affect the mass transfer process.

The outcome largely depends on the angular momentum of the system J, defined as $J = (M_1 a_1^2 + M_2 a_2^2)\omega$, where a_1 and a_2 denote the relative distances of the stars from the centre of mass. In the mass transfer process, the conservation of the angular momentum of the system is not guaranteed. If all the mass lost by the companion contributes to accreting onto the compact object, we have a **fully conservative** transfer, resulting in the conservation of angular momentum ($\dot{J} = 0$). Conversely, if a part of the mass is lost, as in the presence of outflows of matter (see di Salvo et al. 2008), the transfer becomes **non-conservative**. To understand how the temporal evolution of a, J, and M_2 occurs in the system, it is useful to apply the logarithmic derivative to the angular momentum J:

$$\frac{\dot{a}}{a} = \frac{2\dot{J}}{J} + \frac{2\left(-\dot{M}_2\right)}{M_2}(1 - q). \tag{2.10}$$

In the case of $\dot{J} = 0$ then the contraction or expansion of a depends on q. Since the secondary loses mass $\dot{M}_2 < 0$, if $q < 1$ (i.e., the case of LMXB systems), a will increase over time. Conversely, if $q > 1$, the system will shrink. From a physical standpoint, this occurs because matter moves toward the compact object near the centre of mass, compelling the secondary star to orbit at a greater distance to conserve angular momentum. Considering the variation of R_2, differentiating Eq.2.8 and combining with Eq. 2.10 yields:

$$\frac{\dot{R}_{2,\,\mathrm{L}}}{R_{2,\,\mathrm{L}}} = \frac{2\dot{J}}{J} + \frac{2\left(-\dot{M}_2\right)}{M_2}\left(\frac{5}{6} - q\right). \tag{2.11}$$

Again, if $\dot{J} = 0$, the change in R_2 is contingent on the mass ratio. If $q > 5/6$, the Roche lobe

[5]The radius of the primary object lobe R_1 can be determined by replacing q with q^{-1}.

radius will shrink onto the companion, and any angular momentum loss accelerates this process leading to the destruction of the secondary star. For $q < 5/6$, the Roche lobe radius increases, detaching from the secondary star and signifying the end of Roche lobe overflow. At this point, mass transfer persists either when the secondary star enlarges by going off the main sequence and evolving into a giant or when the binary loses angular momentum.

The first case is unlikely for LMXBs, while the momentum loss can occur through two main processes: **gravitational radiation emission** or **magnetic braking**. Magnetic braking reduces the rotational energy and angular momentum of the secondary star due to the interaction between the star magnetic field and its stellar wind (Eggleton 1976). The angular momentum loss rate due to this phenomenon scales with a^2 (Verbunt & Zwaan 1981). Concerning gravitational wave emission, this is only feasible through the presence of a gravitational quadrupole, and the emission rate is proportional to a^{-4}(Kraft et al. 1962; Landau & Lifshitz 1975). A hasty conclusion might be drawn that, since the dependence of the momentum lost via magnetic braking is steeper, it would be the dominant process. However, this does not hold in LMXB systems where the low-mass companion star has mass below 0.3 $M_\odot$ that, being mostly convective and lacking a radiative structure, is expected to lose its large-scale, dipolar magnetic field (Nelson & Rappaport 2003), preventing magnetic braking. However, in this case the system has a small orbital separation making the angular momentum emission via gravitational waves relevant.

2.9.0 Accretion disc

When the flow of matter from the companion exceeds the L_1 point, it possesses a high specific angular momentum, which inhibits a direct radial accretion onto the compact object. In a good approximation, the trajectory of the stream of matter can be linked to the orbit of a test particle with an angular momentum released from L_1, that is essentially an elliptical orbit within the binary plane, gradually precessing due to the presence of the companion. As the continuous stream endeavours to adhere to this orbit, it repeatedly intersects itself, inducing dissipative phenomena like collisions between gas streams at varying velocities or viscous dissipation. On the other hand, the gas retains the angular momentum it had upon leaving L_1, so it will tend towards the orbit of lowest energy for that angular momentum, i.e. a circular orbit. This *circularization radius* R_{circ}, typically ranges 2-3 times smaller than the Roche lobe of the primary (Frank et al. 2002). Consequently, the incoming flow of transferred matter accumulates into a ring, orbiting at R_{circ}. Within this ring, various dissipative processes, including gas collisions, internal stresses, and shocks, dynamically convert gravitational potential energy into internal energy, eventually manifesting as heat. Naturally, a fraction of this energy is radiated, resulting in loss of energy. The sole mechanism for the gas to deal with this energy drain is by sinking deeper into the gravitational sink of the primary, orbiting more closely and consequently shedding angular momentum. This process causes the gas to spiral inward towards the primary object, forming concentric circular orbits that give rise to what is commonly referred to as an **accretion disc**. As material moves inward, the angular momentum released in this process is transferred

from the inner rings to the outer regions of the disc. The outermost ring, orbiting at R_{circ}, is consequently compelled to expand in both smaller and larger radii. This implies that the outer edge of the disc will extend beyond R_{circ}, as long as the tidal forces from the companion prevent the disc from expanding further. This **Tidal radius** relies on several binary parameters, but its value can be shown to be close to $\mathrm{R_T} = 0.9\,\mathrm{R_1}$ (Frank et al. 2002).

The accretion disc can be conveniently divided into concentric rings and due to viscous dissipation, the kinetic energy of the gas transforms into electromagnetic radiation[6]. Since the circular orbits are Keplerian the Virial theorem can be applied, resulting in the kinetic energy constituting half of the potential energy. The energy released through this process is thus expressed as $\Delta E = \Delta E_{acc}/2$. This, in turn, leads to a **disc Luminosity** equal to $L_{\mathrm{disk}} = GM\dot{m}/2R = L_{\mathrm{acc}}/2$. Consequently, half of the available energy is radiated, while the material within the disc undergoes a gradual inward spiral.

2.10.0 Eddington limit

Once the matter reaches the innermost orbit of the disc, its angular momentum diminishes to the extent that it becomes compelled to undergo radial accretion onto the compact object. Upon impact with the surface, its potential energy is released in the form of electromagnetic radiation which subsequently interacts with the inflowing matter from the star, exerting pressure on it. This naturally leads to the question: Can the radiation pressure stemming from accretion impede the very accretion process itself? The answer to this question was addressed in the early 20th century by the already-known astrophysicist Sir Arthur Eddington. The foundational assumptions guiding his analysis were as follows:

- Matter is assumed to consist of fully ionized hydrogen, creating a balanced mixture of protons and electrons.
- Interactions between matter and radiation are limited to Thomson scattering.
- Mass accretion is presumed to be both stationary and isotropic.

The first assumption ensures that radiation predominantly influences free electrons through Thomson scattering, given the negligible Thomson cross-section for protons owing to their substantial mass (Longair 2011). Since Thomson scattering boasts the lowest cross-section among the typical interaction processes between matter and radiation, the second approximation guarantees that the Eddington limit serves as an upper limit.

In this scenario, the stability of accretion is tied to the delicate interplay between the forces of gravity and radiation pressure. Gravity, being primarily effective on protons owing to their mass being 2000 times greater than that of electrons, exerts an attractive force, drawing matter towards the compact object. Conversely, radiation pressure primarily influences electrons, driven

[6]The discussion about viscosity is left to the next chapter

by their high Thomson cross-section[7], exerting a force that propels matter away. Nevertheless, the impacts of these two forces are interlinked, as electrons and protons are tethered together by Coulomb forces.

The gravitational force can be expressed as $GM(m_p + m_e)/r^2 \sim GMm_p/r^2$, acting radially from the centre of the star. If we denote the luminosity of the source as L, the radiative force in spherical symmetry is the pressure $L/4\pi cr^2$ multiplied by the effective area of each interacting particle, namely the Thomson cross-section σ_T. The resulting force on each electron-proton pair is then:

$$\left(GMm_{\rm p} - \frac{L\sigma_{\rm T}}{4\pi c}\right)\frac{1}{r^2}. \tag{2.12}$$

When the forces of radiation pressure and gravity achieve a perfect equilibrium, the system attains the **Eddington limit**:

$$L_{Edd} = \frac{4\pi GMm_p c}{\sigma_T} \sim 1.3 \times 10^{38}(M/M_\odot)\, erg\, s^{-1} \tag{2.13}$$

For a NS with a typical mass of 1.4 $M_\odot$, the Eddington luminosity is $\sim 2 \times 10^{38}$ erg s^{-1}. However, it is crucial to bear in mind the assumptions made during the derivation of Eq. 2.13. We presumed an isotropic and spherically symmetric accretion flow, and while this greatly simplifies our calculations, in the systems we are investigating accretion predominantly occurs through an accretion disc. This implies that matter does not accrete spherically but instead has a preferred direction along the disc plane. Other significant assumptions included that the accreting material was predominantly composed of fully ionized hydrogen, a presumption partly justified by the fact that the object in accretion generates most of its luminosity in the form of X-rays (Frank et al. 2002).

It is essential to highlight that the Eddington limit is a theoretical boundary that can be exceeded in real systems. Various sources have demonstrated luminosities well beyond their Eddington limit, such as *Holmberg II X-1*, characterized by an X-ray luminosity that can reach up to 10^{40} erg s^{-1} (Barra et al. 2023), or the binary system *NGC 1313 X-1*, with a luminosity of 1.1×10^{40} erg s^{-1} (Bachetti et al. 2013; Gúrpide et al. 2022). These sources belong to a subclass of binary systems, already introduced, named **ULXs**, characterized by their super-Eddington luminosities ranging from 10^{39} to 10^{42} erg s^{-1} (Kaaret et al. 2017). Initially, their behaviour was explained by postulating the presence of Intermediate Mass BH in these systems, accreting at their Eddington limit. However, in 2014, pulsations were detected for the first time coming from a sector in the galaxy M82, with a flux corresponding to an X-ray luminosity of 4.93×10^{39}erg s^{-1}, suggesting the presence of a highly magnetized NS. This association implies a luminosity approximately 30 times that of the Eddington limit for a 1.4 $M_\odot$ object. Subsequently, additional coherent pulsations have been identified in several ULXs (Israel et al. 2017; Sathyaprakash et al. 2019), underscoring the necessity for new models to clarify how systems hosting a NS can achieve such huge luminosities. However, not all ULXs are found to be pulsars leaving the

[7]Thomson cross-section is defined as $\sigma_{\rm T} = \frac{8\pi}{3}\left(\frac{e^2}{mc^2}\right)^2$

possibility of BH nature in some other sources (Liu et al. 2013).

2.11.0 X-ray Pulsars

In Sections 2.4 and we saw how XBRs can exhibit coherent pulsations in the X-ray band. The occurrence of these pulsations depends on the magnetic field strength of the compact object, typically an NS. With a magnetic field strong enough (usually 10^{10}G, Di Salvo & Sanna 2022) it is possible for the inner part of the accretion disc to be disrupted by the magnetic field lines. In this scenario, the material from the disc is channelled along magnetic field lines and funnelled onto the polar caps of the NS. Since the resulting emission from this impact produces mostly x-ray radiation observed as pulsated because of the lighthouse effect (discussed in Section 2.4), such systems are known as **X-ray Pulsars**. The period of these pulsations corresponds to the spin period of the compact object and is typically observed in the range of $\sim 10^{-3}$ s to 10 s or more.

Physically, this process is driven by the competition between the pressure applied by the magnetic field to the accreting plasma and the pressure exerted by the latter, referred to as *ram pressure*. Consider a dipolar magnetic field, with a magnetic moment $\mu \sim B_s R_s^3$, this may disrupt an almost spherical flow at a distance r from the star. The magnetic pressure can be expressed as $\mathrm{P} = 4\pi\mu^2/8\pi\mu_0 \mathrm{r}^6$ (Frank et al. 2002), while the ram pressure $\rho \mathrm{v}^2$, considering v as the free-fall velocity of matter v_{ff}, can be expressed as: $P_{ram} = (2GM)^{1/2}\dot{M}/4\pi r^{5/2}$, where $\dot{M}$ is the accretion rate of the source. When the two pressures reach an equilibrium, due to the steeper dependence on r of the magnetic term, we can find a radius beyond which the magnetic pressure takes over. This radius is called the **Alfvén radius** and can be written as follows:

$$R_M = 5.1 \times 10^8 \dot{M}_{16}^{-2/7} m_1^{-1/7} \mu_{30}^{4/7} \text{ cm}. \tag{2.14}$$

Here, μ_{30} represents the magnetic moment μ in units of $10^{30}\,\mathrm{G\,cm^3}$. For small magnetic fields, the Alfven radius is smaller than the typical radius of an NS, precluding the emergence of the magnetosphere from the star. However, with a typical accretion rate at 10% of the Eddington limit, a magnetic field on the order of 10^8 G (Di Salvo & Sanna 2020) is enough to yield a radius greater than that of a standard NS. It is noteworthy that the assumption of spherically symmetric accretion becomes invalid when accounting for accretion discs. In practice, the ram pressure of matter concentrates in the disk plane, facilitating further penetration into the NS magnetosphere. This reduces the magnetospheric radius R_m with respect to the Alfvén radius by a factor ϕ, typically ranging between 0.2 and 0.5 (Shakura & Sunyaev 1973a). For typical values in an NS LMXB, ϕ is mainly dependent on luminosity and approximates 0.2 - 0.3 (Burderi et al. 1998).

The interaction between the accretion flow and the NS magnetosphere allows for an exchange of angular momentum between the disc and the compact object. To provide a quantitative description of the exchanged momentum, we define the **corotation radius** R_{co} as the radius at which the angular velocity of the matter in the disk (Ω) matches the spin of the NS (Ω_0) i.e., $R_{\mathrm{co}} = (GM)^{1/3}/\Omega_0^{2/3}$. Depending on the values of R_{co} three possible scenario can be foreseen:

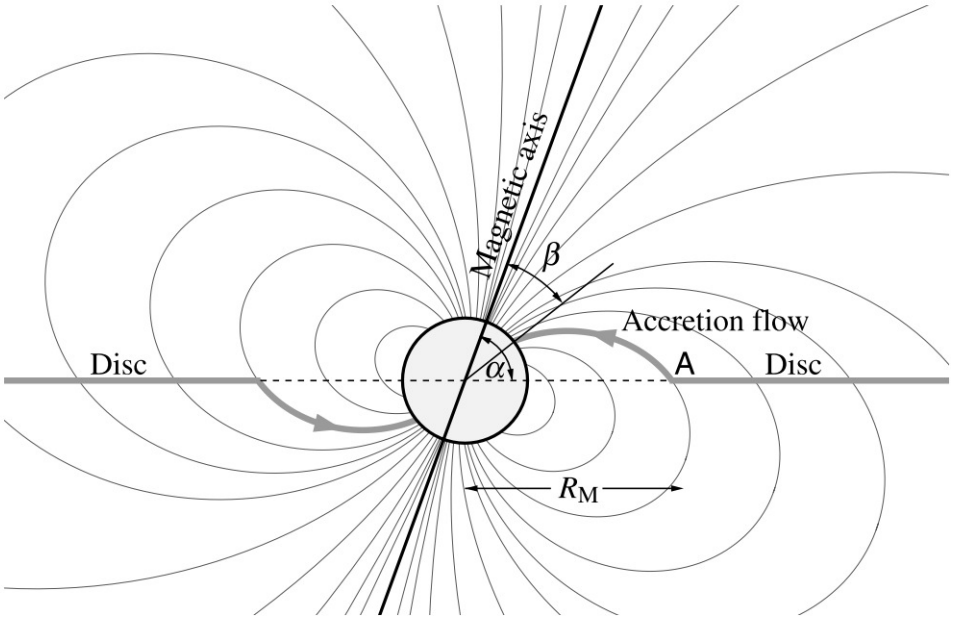

Figure 2.5: Accretion onto a highly magnetized compact object via magnetic field lines from a truncated disc (Frank et al. 2002).

- If $R_m < R_{co}$, the matter channelled along the field lines rotates at a higher velocity than the NS, applying a torque that spins up the star. This behaviour is expected in LMXBs hosting an old NS, where the magnetic field has been weakened over time allowing the accreted material to approach closer to the NS (Ghosh & Lamb 1979a).
- If $R_m > R_{co}$, the matter in the disc has a lower angular velocity, causing the accretion flow to impart a torque that decelerates the NS resulting in a spin-down (see Fig. 2.5). When the rotation speed of the NS significantly exceeds that of the material in the accretion disc, the magnetic field lines can exert a torque on the disc strong enough to create a centrifugal barrier witch propels the matter out of the disc (**propeller effect**).
- If $R_m = R_{co}$ the system achieves a stable configuration when there is no transfer of angular momentum.

The net momentum N acting on the NS can be expressed as follows (Di Salvo & Sanna 2022):

$$N = \left(\dot{m}\sqrt{GMR_m} + \frac{\mu^2}{qR_m^3}\right) n(\omega) - \frac{\dot{E_{dip}}}{2\pi\nu_s} \tag{2.15}$$

Here, $\dot{E_{dip}}$ is the energy lost due to dipole radiation (see section 2.4), and $n(\omega)$ is a parameter dependent on $(R_m/R_{co})^{3/2}$, taking the values ± 1 for spin-up or spin-down regimes, respectively. This determines whether the net momentum is positive (spin-up) or negative (spin-down). The spin-up regime is exactly what makes the binary pulsars, that have crossed the death line in the $P\dot{P}$ diagram, become observable as radio millisecond pulsars. The recycling scenario theory, as introduced in the previous sections, is therefore capable of explaining the existence of extremely fast and very old radio pulsars. However, the confirmation that NS LMXBs could be accelerated to such short rotation periods came only with the discovery of SAX J1808.4-3658 (Wijnands

& van der Klis 1998), a pulsating X-ray source with a period of 401 Hz, the first discovered **Accreting Millisecond Pulsar**. In the next chapter, we will shift our focus towards a more detailed analysis of the radiative processes that play a role in LMXB systems, breaking down the spectrum of these systems into their main components.

3

X-ray spectral components in LMXBs

LMXB systems exhibit spectra that are the results of a deep forest of distinct components, each reflective of various physical processes occurring within these systems.

At lower X-ray energies, typically in the soft X-ray range (in the range 0.5-2 keV), we observe a thermal **blackbody-like component**. This emission is generally associated with the accretion disc or, in systems where the compact object is a NS, with the surface of the star. At higher X-ray energies (up to tens of kev), the spectral landscape shifts towards a dominant hard component, described by a power-law distribution with a high-energy cutoff. This component is believed to result from Compton scattering processes. In this scenario, low-energy photons from the accretion disc or the NS surface gain energy upon interacting with a hot electron cloud, often referred to as the **Corona** (Poutanen & Coppi 1998). Another significant element of LMXB spectra is the **reflection component**. This occurs when high-energy photons, having undergone Comptonization in the corona, interact with and are reflected off the cooler gas of the accretion disc. This interaction leads to spectral features such as fluorescent lines and a hump at higher energies, providing insights into the disc composition and the corona geometry. In addition, in some LMXB spectra has been detected a **power-law hard tail** component dominates the spectrum at the highest energies (Di Salvo et al. 2006). Fig. 3.1 depicts a typical spectrum of a LMXB system, with its various components distinctly highlighted.

To properly comprehend the geometry of the system and the accretion processes taking place, it is essential to investigate the origin of these spectral components and the factors affecting their spectral profiles. Understanding these elements provides essential insights into the complex interactions of physical processes within these systems.

3.1.0 The Shakura-Sunyaev accretion disc

The physics behind the accretion disc is governed by the interplay between gravity, angular momentum, and viscosity. Gravity pulls material towards the central object, while viscosity, acts as the mechanism for angular momentum transfer, allowing material to move inward and to be accreted onto the central object. The solutions to the equations that describe the accretion flow within the accretion disc have given rise to a variety of models depending on radiative

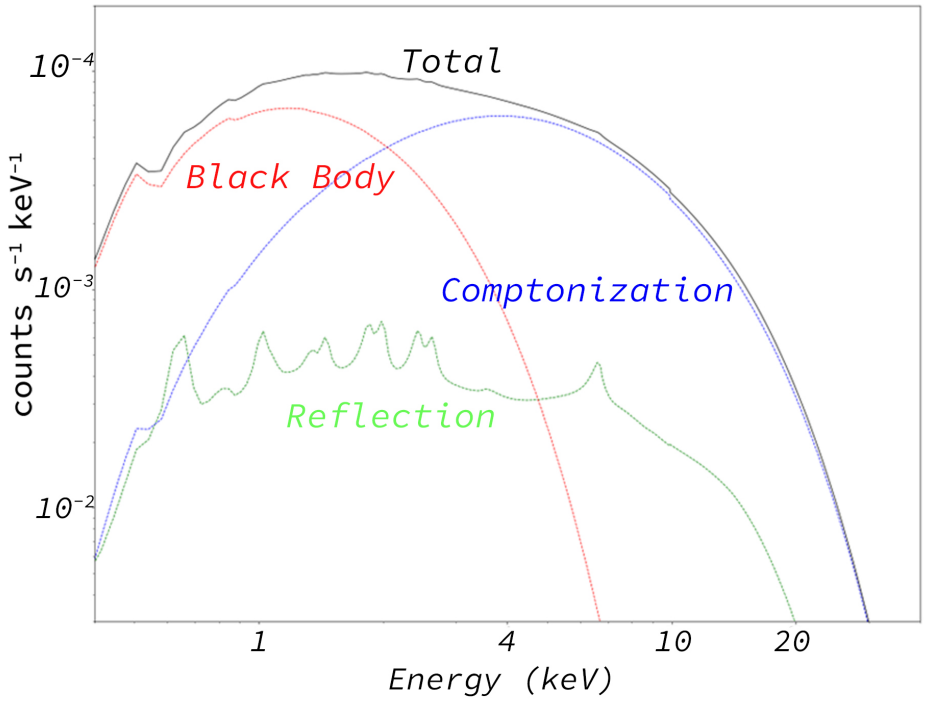

Figure 3.1: The three main components of a LMXB spectrum.

efficiency, dominant pressure and gas opacity. In exploring the nature of accretion discs, a fundamental approach is to consider a *standard disc model*, first proposed by astrophysicists Shakura and Sunyaev in 1973 (Shakura & Sunyaev 1973a), and it involves an **optically thick** and **geometrically thin disc**.

The geometrically thin assumption is well justified by the flow of matter being concentrated close to the equatorial plane and this simplifies the dynamics to primarily two dimensions (radial and azimuthal). The Shakura-Sunyaev disc is also radiatively efficient, dominated by the pressure of the gas and where the heating produced by viscosity is radiated locally. Moreover, The flow being optically thick, it is cooled efficiently and its temperature is close to that of a blackbody.

The importance of this model mainly lies in how it handles viscosity. Particles in neighbouring rings of the disc display chaotic thermal motions, causing them to interact with each other and generate viscous friction. To more precisely determine the type and influence of these viscous forces, one can calculate the Reynolds number, usually defined as $R = \rho v L/\mu$, where ρ is the fluid density, v is the mean velocity of the fluid, L is a characteristic linear dimension and μ is the dynamic viscosity of the fluid. If the Reynolds number is less than 1, viscous forces assume a central role, while beyond a critical Reynolds number ($R > 10^3$), the flow becomes turbulent. As reported by Longair (2011) in the context of an accretion disc around a NS, R is approximately 10^{12}, indicating that molecular viscosity does not primarily govern the structure of the accretion disc. Instead, turbulent viscosity does. Herein lies the crux of our troubles with viscosity. Turbulence constitutes one of the most complex domains within physics, and we have yet to comprehend the underlying physical mechanisms of it.

In the conventional Shakura & Sunyaev (1973a) disc model, viscosity is simply expressed as

$\eta = \alpha\, c_s H$, with c_s the speed of sound in the disc, and H the scale height of the disc. Hence, the magnitude of viscosity is parameterized by the dimensionless parameter α. With this approach, commonly referred to as the "$\alpha - prescription$", all our ignorance regarding the mechanics of viscosity has been hidden within α, rather than expressed in η (Frank et al. 2002). We will see later how α enters the equations describing the local structure of the disc with only small exponents, thus enabling the development of a fully coherent theory of discs, even when disregarding the magnitude or the true nature of viscosity.

We must acknowledge that the radial structure of a thin disc changes on timescales approximately equivalent to the viscous timescale, usually of order of days to weeks (Frank et al. 2002). In many systems, the mass transfer rate changes over longer timescales. In such scenarios, the local mass-transfer rate remains constant over time within each ring of the disc, allowing us to treat it as a **steady disc**. A significant consequence of this is that we can express the viscous energy rate, $D(R)$, within a steady disc per unit area, as described by Frank et al. (2002):

$$D(R) = \frac{3GM\dot{M}}{8\pi R^3}\left[1 - \left(\frac{R_*}{R}\right)^{1/2}\right], \tag{3.1}$$

where R_* is the radius of the compact object. As a result, the energy flux through the surfaces of a steady thin disc is unaffected by viscosity. This is noteworthy, as D(R) is a parameter of great observational significance, and while its connection to viscosity is uncertain, its dependencies on other factors, like $\dot{M}$ and R, are well known.

Now that we have made the necessary assumptions, it is time to go further and delve into the equations that govern the complex structure of an alpha-steady-standard disc. In the Shakura-Sunyaev model, the disc is typically divided into three distinct regions, each defined by unique dominant physical processes and governed by specific equations. These regions are:

- **The Inner Region**: Located closest to the compact object. Here, radiation pressure predominates over gas pressure. The temperatures and densities are exceedingly high, and the primary interaction between matter and radiation is electron scattering on free electrons.

- **The Middle Region**: In this zone, gas pressure is the dominant force, although electron scattering continues to be the main source of opacity. This region is generally characterized by conventional gas dynamics and radiative processes.

- **The Outer Region**: This is the coolest segment of the disc. Gas pressure maintains its dominance, but the opacity is now largely due to free-free (bremsstrahlung) and bound-free transitions.

The equations describe the disc across these regions are a combination of the hydrostatic equilibrium equation, which balances the vertical gravitational force against the pressure gradient, the state equation, which correlates the pressure, density, and temperature of the plasma within the disc, the energy transport equation and the equation for viscous dissipation, as

previously introduced. This thesis will not delve into the derivation of each equation, for a more in-depth exploration one should refer to Shakura & Sunyaev (1973a). Instead, our focus will be on presenting the set of solutions pertinent to the disc outermost region (where $P_r \ll P_g$ and $\sigma_{\text{ff}} \gg \sigma_{\text{T}}$) :

$$u_0 = 6.1 \cdot 10^5 \cdot \alpha^{-4/5} \cdot \dot{m}^{7/10} \cdot m^{1/5} \cdot r^{-3/4} \cdot (1 - r^{-1/2})^{7/10} \tag{3.2}$$

$$T = 8.6 \cdot 10^7 \cdot \alpha^{-1/5} \cdot \dot{m}^{3/10} \cdot m^{-1/5} \cdot r^{-3/4} \cdot (1 - r^{-1/2})^{3/10} \tag{3.3}$$

$$z_0 = 6.1 \cdot 10^3 \cdot \alpha^{-1/10} \cdot \dot{m}^{3/20} \cdot m^{9/10} \cdot r^{9/8} \cdot (1 - r^{-1/2})^{3/20} \tag{3.4}$$

$$n = 3 \cdot 10^{25} \cdot \alpha^{-7/10} \cdot \dot{m}^{11/20} \cdot m^{-7/10} \cdot r^{-15/8} \cdot (1 - r^{-1/2})^{11/20} \tag{3.5}$$

$$\tau = \sigma_{\text{ff}} \cdot u_0 = 3.4 \cdot 10^2 \cdot \alpha^{-4/5} \cdot \dot{m}^{1/5} \cdot m^{1/5} \cdot (1 - r^{-1/2})^{1/5} \tag{3.6}$$

$$v_r = 5.8 \cdot 10^5 \cdot \alpha^{4/5} \cdot \dot{m}^{3/10} \cdot m^{-1/5} \cdot r^{-1/4} \cdot (1 - r^{-1/2})^{-7/10} \tag{3.7}$$

$$H \lesssim 2.1 \cdot 10^9 \cdot \alpha^{1/20} \cdot \dot{m}^{17/40} \cdot m^{-9/20} \cdot r^{-21/16} \cdot (1 - r^{-1/2})^{17/40} \tag{3.8}$$

Where we introduced the following non-dimensional parameter:

$$m = \frac{M}{M_\odot}, \quad \dot{m} = \frac{\dot{M}}{3 \cdot 10^{-8} \frac{M_\odot}{\text{yr}}} \times \left(\frac{M_\odot}{M}\right), \; r = \frac{R}{3R_g} = \frac{1}{6}\frac{Rc^2}{GM} = \frac{M_\odot}{M}\frac{R}{9\ \text{km}}. \tag{3.9}$$

Here we have the expression in terms of the radial distance r of the following parameters: the surface density of the matter u_0, the central temperature of the disc T, the half-thickness z_0, which defines the disc vertical scale, the density n, the optical depth τ, the radial velocity v_r, and the disc scale height H. From the equations, it is clear that the α-parameter, whose exact value remains undetermined, has a relatively minor impact on the disc characteristic parameters, since its appearance in these equations with a relatively low exponent. Moreover, based on equation 3.2, the ratio of disc height to radius (H/R) indicates that the disc is indeed thin. Additionally, the expression for optical depth τ confirms that the disc maintains a high level of optical thickness across a wide range of plausible accretion rates.

3.1.1 Disc spectrum

Due to the high optical thickness, photons undergo several scatterings before escaping from the disc, leading to a dynamic exchange of energy between the disc material and the radiation until the thermal balance is achieved. Consequently, each ring of the disc emits as a **black body**, characterized by a temperature $T(r)$. By setting the black body radiation, whose flux is expressed by the Stefan-Boltzmann law $\phi_{bb} = \sigma T^4$, equal to the viscous energy rate $D(R)$ as described in the equation 3.1, we obtain (Frank et al. 2002):

$$\sigma T^4 = \frac{3G\dot{m}M}{8\pi r^3}. \tag{3.10}$$

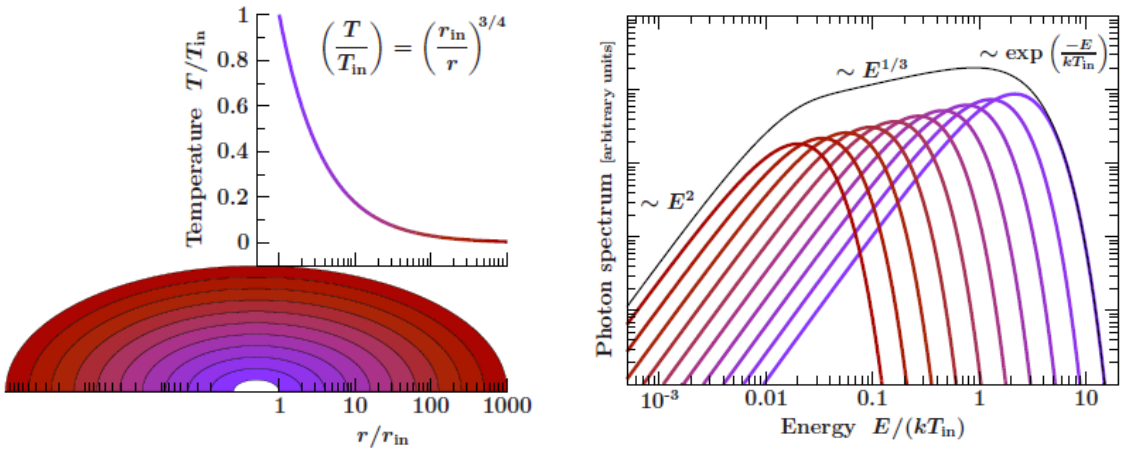

Figure 3.2: **Left panel**: Temperature profile $T \propto r^{-3/4}$, displayed on a logarithmic scale, divided into 10 rings. **Right panel**: Black body spectrum resulting from the superposition of contributions from the 10 rings, where the colour corresponds to that indicated on the left (Hanke 2011).

M denotes the mass of the central object, r represents the radial distance from the centre, and $\dot{m}$ indicates the mass transfer rate through the disc. This implies that individual rings of the disc emit a black body with peak temperatures at the temperature of their respective radial distances from the centre, where the temperature increases, following a trend of $T \propto r^{-3/4}$, as r decreases approaching the compact object (as plotted in Fig. 3.2). Setting aside the atmosphere of the disc, its total intensity is proportional to the black body intensity at a specific temperature T, integrated across the full radial range of the disc:

$$I = \int 2\pi r B(T,\nu) dr \quad \text{with} \quad B(T,\nu) = \frac{2h\nu^3}{c^2} \frac{1}{e^{h\nu/kT} - 1}. \tag{3.11}$$

Here, $B(T,\nu)$ is the widely known *Planck function*. This analysis illustrates that the spectrum of a typical disc is shaped like $I(\nu) \propto \nu^{1/3}$. In the lower energy spectrum, where $h\nu << kT$, the function resembles the *Rayleigh-Jeans limit*, expressed as $B = \frac{2\nu^2 kT}{c^2} \propto E^2 T$. Beyond the energy peak, where $h\nu >> kT$, the *Wien approximation* comes into play, causing the function to decrease exponentially as $B \propto e^{-h\nu/kT}$.

The spectrum energy dependency shifts across different ranges: it rises as E^2 at low energies, increases moderately as $E^{1/3}$ near the peak, and beyond the peak, it exponentially decreases as $e^{-h\nu/kT}$ (see Fig. 3.2). An observer would perceive a spectrum that is a convolution of all the black body emissions from each radius of the disc. Typically, this emission is modelled as a black body peaking at (less than) 1 keV, corresponding to a temperature around 10^7 K, or as a multi-colour black body.

Due to limitations in the Shakura-Sunyaev model in describing spectral features of certain astronomical sources (particularly those with low accretion rates), alternative theoretical models have been proposed over time. Among these, the **Advection Dominated Accretion Flow** (ADAF), initially introduced by Ichimaru (1977), has gained prominence. In scenarios where the radiation is not efficient in cooling the accretion flow, the resultant viscous dissipation is

predominantly retained as thermal energy within the gas of the accretion flow. This energy is then radially *advected* alongside the matter flux towards the central compact object. A small fraction of this energy undergoes radiative release (Narayan et al. 1996), leading to a substantially reduced radiative efficiency in contrast to the standard disc model. The ADAF model finds particular applicability in black hole accretion contexts, where a segment of the accretion-induced energy is channeled into the black hole. Conversely, in NS systems, the energy is ultimately emitted at the stellar surface, facilitating a more efficient radiative process.

Distinct regimes of advection-dominated accretion flows are discernible, primarily contingent on the rate of accretion and the associated optical depth. In a "*slim accretion disk*," high accretion rates correspond with an increased optical depth, leading to the entrapment of radiation within the gas (Abramowicz et al. 1988). In an alternative regime, characterized by low accretion rates, the accretion flow is optically thin and as a consequence the radiative cooling is not efficient (Narayan & Yi 1994; Abramowicz et al. 1988).

3.2.0 Comptonization

When a population of cold photons encounters a region of free electrons, their interaction leads to changes in the photon spectrum, primarily due to Compton scattering. This occurs because, when the average energy of the electrons is higher than that of the photons, the photons gain energy and are scattered to higher energies. Conversely, if the electrons are less energetic than the photons, the photons lose energy and are scattered to lower energies. The spectrum is considered '**Comptonized**' when it is predominantly influenced by Compton scattering processes. This requires the plasma to be sufficiently thin, ensuring that other processes, such as bremsstrahlung, can be neglected.

In cases where the electrons are non-relativistic ($kT_e << m_e c^2$) and the photons have an energy $h\nu << m_e c^2$, the loss of energy of the photon per collision due to direct Compton is[1]:

$$\frac{\Delta\varepsilon}{\varepsilon} = -\frac{h\nu}{m_e c^2}(1 - \cos\alpha) \tag{3.12}$$

From the electrons reference frame, the photons undergo Thomson scattering. Since the probability distribution for the scattering angle is symmetric (Longair 2011), the average over the scattering angle α eliminates the contribution from $\cos\alpha$, resulting in:

$$\left\langle \frac{\Delta\varepsilon}{\varepsilon} \right\rangle = -\frac{h\nu}{m_e c^2}. \tag{3.13}$$

For a thermal or quasi-thermal electron distribution at temperature T_e[2] that transfer energy to the

[1]The non-relativistic regime ensures that Thomson cross-section σ_T can be used

[2]'quasi-thermal' indicates a distribution that is not perfectly Maxwellian but where the electrons still have a thermally distributed range of velocities

photons through inverse Compton scattering we have (Longair 2011):

$$\left\langle \frac{\Delta\varepsilon}{\varepsilon} \right\rangle = \frac{4kT_{\mathrm{e}}}{m_{\mathrm{e}}c^2}. \tag{3.14}$$

As a result, the average energy lost or gained by the photons can be expressed as:

$$\left\langle \frac{\Delta E}{E} \right\rangle = \frac{4kT_{\mathrm{e}} - h\nu}{m_{\mathrm{e}}c^2}. \tag{3.15}$$

If $h\nu = 4kT_e$, no energy transfer occurs, while if $h\nu > 4kT_e$ electrons gain energy, and conversely if $h\nu < 4kT_e$ photons gain energy. In scenarios where electrons have higher temperatures than photons, each scatter results in a photon energy increase of $4kT_e/m_ec^2$, and the number of scatters is significantly influenced by the optical depth τ of the medium.

For $\tau >> 1$, photons undergo a random walk out of the source, travelling a distance $l = N^{1/2}\lambda$, where N is the number of scatterings and λ is the mean free path of the photons ($\lambda = (n_e\sigma_T)^{-1}$ with n_e being the electron density). Consequently, the number of scatterings is given by $N = \tau^2$. Conversely, when $\tau < 1$ most photons leave the source directly, and the number of scatterings approximates to τ. The parameter that indicates the significance of Inverse Compton scattering in this process is the *y-parameter*. It is defined as the product of the average energy change per scattering and the average number of scatterings. Hence, the y-parameter can be expressed as : $y = \max(\tau, \tau^2)kT_e/m_ec^2$.

If $y \geq 1$, the Comptonization process is significant, indicating that the Comptonized spectrum contains more energy than the original spectrum of seed photons. As a result, both the total photon energy and the spectrum undergo substantial modifications. Conversely, for $y \ll 1$, the total energy change is minimal. The question now is: how is the spectrum altered? Let us consider a familiar "real-world" example, a LMXB system. In binary systems, radiation emitted from the NS surface or the surrounding accretion disc generally exhibits a blackbody spectral shape. Within these systems, there frequently exists a hot electron cloud with temperatures exceeding 10^8 K, named **Corona**, which plays a crucial role in the production and scattering of radiation. When the photons interact with the electrons, given that their energy is significantly higher than the energy of the photons, the photons will undergo inverse Compton scattering. This scenario aligns well with the case where $4kT > h\nu$.

How the corona modifies the incident blackbody spectrum depends on the optical depth of the cloud. In the case of an optically thick Corona, the photon population undergoes enough scatterings to reach thermal equilibrium, and their energy distribution will turn into a *Bose-Einstein distribution*. In this scenario, known as **saturated Comptonization**, the new spectrum, while structurally similar to a blackbody spectrum, lacks the necessary photon count to form a true blackbody distribution at the elevated energy levels (the energy peak of the spectrum is 3 times the electrons' energy, see Fig. 3.3). Conversely, when the corona is optically thin, the photons do not achieve thermalization, and distinct photon populations encounter varying numbers of scatterings. Consequently, for each different scattering order, i.e. the number of scatterings the photons have experienced, we observe a different fraction of photons, each associated with

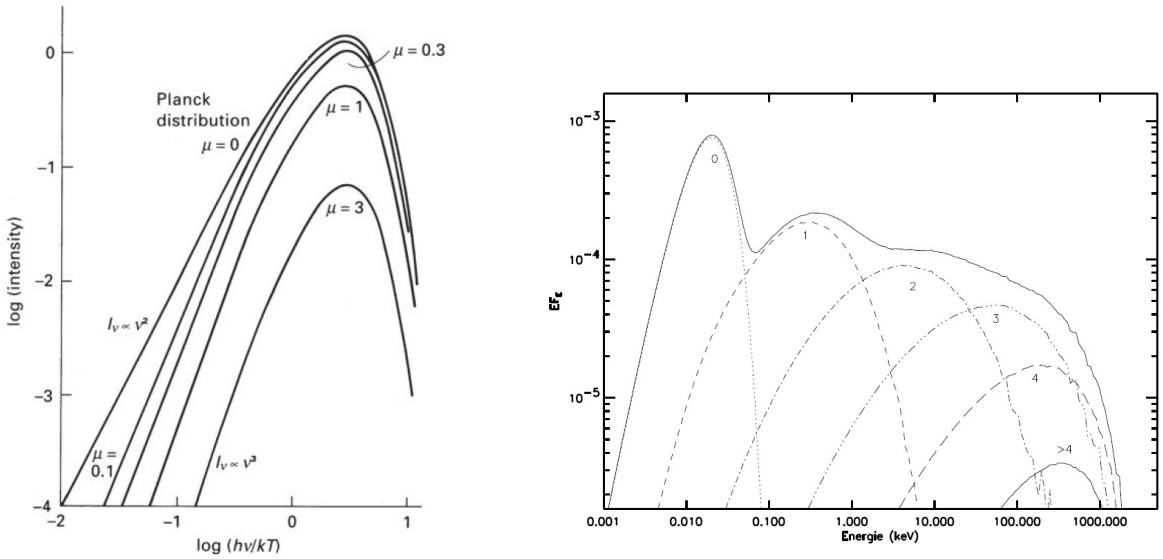

Figure 3.3: **Left panel**: The spectral intensity profiles of Bose-Einstein distributions are illustrated for varying magnitudes of the dimensionless chemical potential, denoted by μ (Longair 2011). **Right panel**: Comptonization spectrum from a seed blackbody spectrum at a temperature of $kT = 5eV$, into a homogeneous plasma sphere with a temperature of $kT_e = 300\,keV$ and an optical depth $\tau = 0.1$ (Malzac 2005).

a spectrum that peaks at energy shifted from the initial energy, depending on the number of scatterings. The resultant spectrum is a convolution of all these individual spectra, which, as illustrated in Fig. 3.3, extends progressively up to a cutoff energy, corresponding to the electron thermal energy. Such spectra, which do not achieve saturation, are classified as **unsaturated Comptonization**.

3.2.1 Shapes of Corona

Where does the Corona come from? Various theoretical models have been proposed to explain its existence. Shakura & Sunyaev (1973a) postulated that Coronal formation could be attributed to the evaporation of thermally elevated matter from the accretion disc surface. Complementing this perspective, (Narayan & Yi 1995) posited that in case of ADAFs, the Coronal structure may arise from the hot, ionized gases inherent to the ADAF system. This is because the inefficient cooling of the ADAF would mean that the gas remains hot and ionized, leading to optimal condition for the formation of a Corona.

Generally, it is believed that given the high degree of ionization of inner disk material, electron detachment from atomic structures is markedly facilitated. Moreover, the accretion disc rotating plasma generates magnetic fields. These are prone to distortion and entanglement due to the disc differential rotational dynamics. Tangled magnetic field lines snap and realign, releasing a significant amount of energy. The phenomenon of magnetic reconnection, wherein these entangled magnetic field lines undergo realignment and release substantial energy, is crucial in the energization of disc material. This process enables the disc material to acquire sufficient kinetic energy to leave the disc plane (Galeev 1979), thereby engendering a less dense, thermally

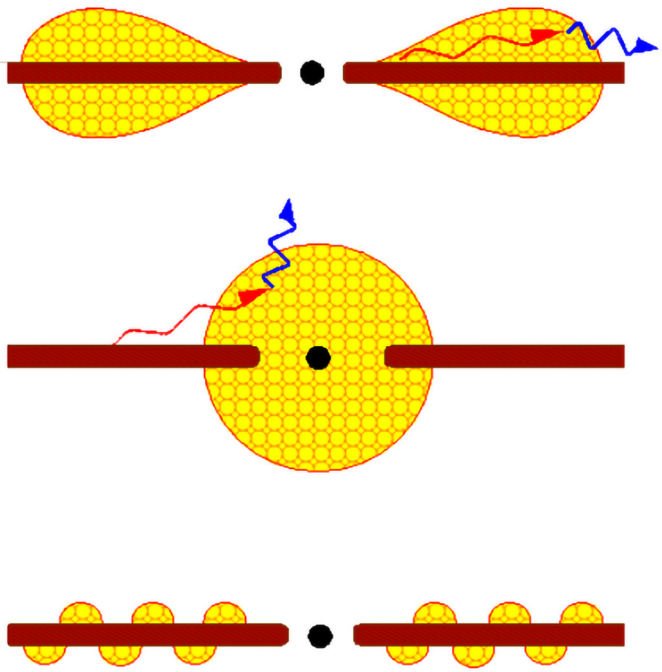

Figure 3.4: The figure shows three possible models of corona: the top panel represents the accretion disk corona, the middle one the spherical, compact corona and the last panel shows the patchy model (Egron et al. 2013).

enhanced region above and below the disc, forming the Corona. This configuration, often referred to as the **accretion disc Corona** (ADC), encapsulates a less dense, heated zone enveloping the disk. However, several Corona models have been theorized. Notably, these include the **spherical model**, delineating the Corona as a spherically enveloping cloud encompassing solely the compact object and the disc inner regions. In contrast, the irregular corona model, the so called **patchy** or "**pill box**" Corona, posits the emergence of active regions localized at delimited disc points, similar to the solar circuit, influenced by the dynamics of magnetic re-connection. These models are shown in Fig. 3.4. The precise origin of the hard photons in various states is somewhat ambiguous and might be associated with alterations in the geometry or other physical properties of the corona. We will revisit ADC sources in Chapter 5, where I present my analysis of the spectrum of X1822-371, the prototype of ADC sources.

3.3.0 Reflection spectrum

We now delve into the analysis of the a crucial spectral component of X-ray spectra of LMXBs: the **reflection component**. We have already discussed the blackbody emission originating from the accretion disc and the NS surface, as well as the Comptonization spectrum produced by the Corona. Notably, the latter is expected to interact, at least partially, with the disc. Given the disc is optically thick, photons reprocessed in the corona become entrapped within the disc, where they interact with its cooler matter. This interaction results in a reprocessing of these photons,

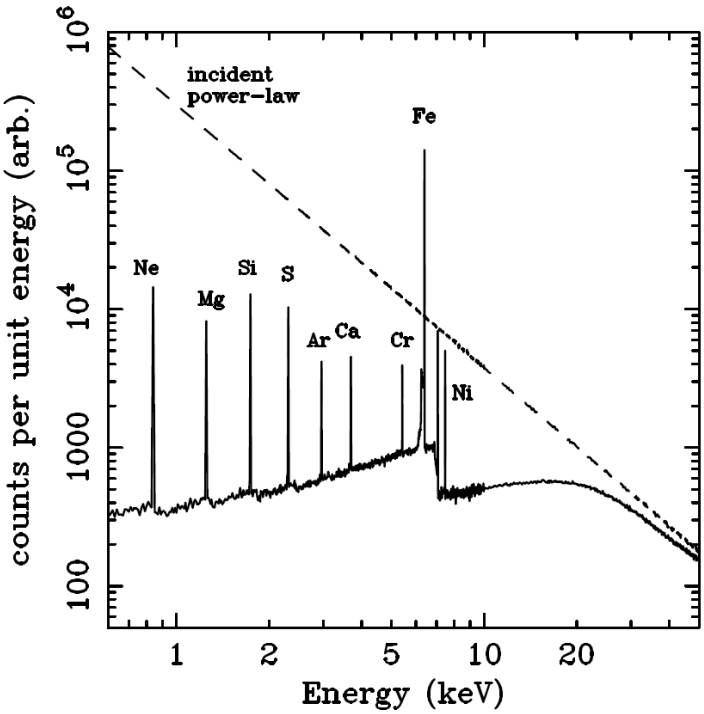

Figure 3.5: A simulated reflection spectrum created using a power-law reflected off a cold plasma. It is possible to see a forest of emission lines, including the most significant one at 6.4 keV, associated with the neutral Fe Kα line. Additionally, key reflection characteristics, such as the Compton reflection hump, are observable in this spectrum. (Reynolds 1996)

and when they finally emerge, they display a completely renewed spectrum, aptly termed the reflection spectrum.

The soft X-rays are absorbed by the cold plasma, leading to the creation of a thick forest of absorption edges and fluorescence lines. A particularly prominent feature among them is the **Iron Kα line**, ranging between 6.4 - 7 keV, varying with the disc ionisation state. In the hard X-ray spectrum, typically with E > 15 keV (Egron 2013), photons lose energy through Compton scattering until they escape from the disc. This process produces a broad spectral hump around 30 keV, also known as the **Compton reflection hump**. A typical reflection spectrum from a neutral disc is illustrated in Fig. 3.5.

As will be discussed, the presence of this spectral component, especially the emission lines, offers an important opportunity to gather essential insights about the observed source. The emission is thought to emanate from the innermost regions of the accretion disc, making it a direct tool for probing the physics in the area of intense gravitational influence near the compact object. The subsequent discussion will focus on the Iron line, how the inclination with respect to our line of sight, the ionization state or other physical properties of the disc matter affect its profile (Egron 2013; Fabian et al. 2000; Reynolds 2003).

When radiation hits the surface of an accretion disc, the photons interact with the matter primarily in two ways: Compton scattering off free electrons or **photo-absorption** by neutral atoms or ions. For photo-absorption to occur, the photon must exceed the ionisation energy associated with the different electronic levels. The highest cross-section for this process is

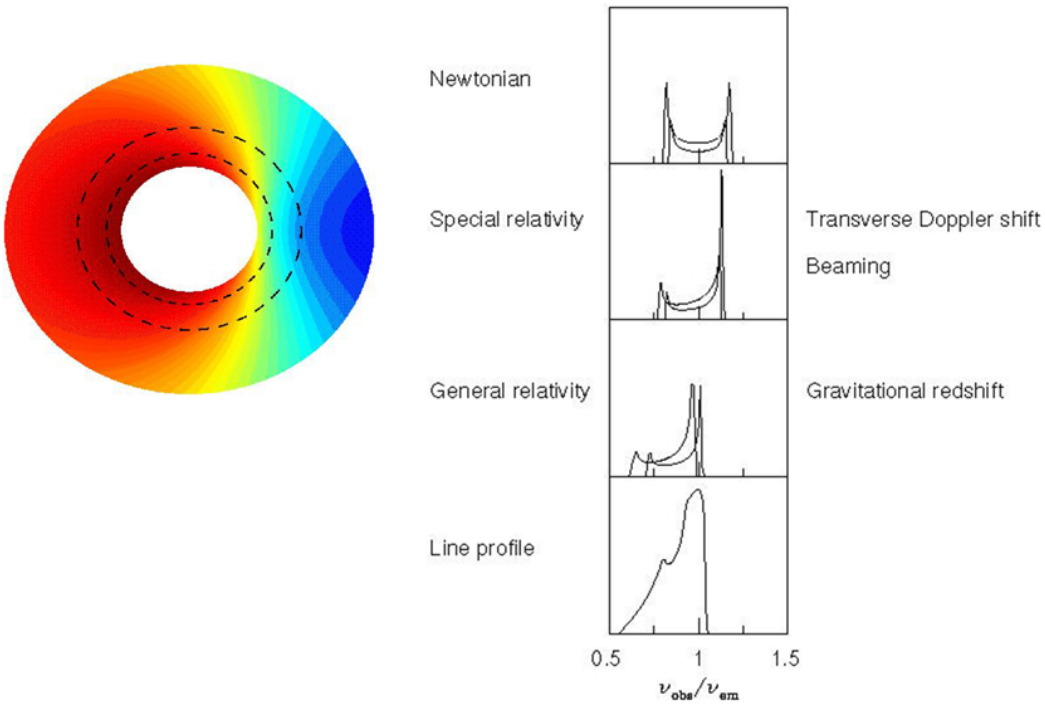

Figure 3.6: **Left panel**: sketch of the accretion disc from above. The blue part represents the approaching matter while the red part represents the receding. **Rigth panel**: Effects on the iron emission line profile due to Newtonian Doppler shift, relativistic beaming, and gravitational redshift, from top to bottom respectively (Fabian et al. 2000).

associated with the ejection of electrons from the innermost atomic shells, particularly the K-shell (Longair 2011). When an electron is ejected due to photo-absorption, creating a vacancy in the K-shell, an electron from the L-shell will typically move down to fill this vacancy. This transition can happen in a radiative way, through *Fluorescence*, and manifests as a Kα line in the spectrum. Alternatively, following the non-radiative way, the excess energy can be used to eject another electron from the atom, giving the *Auger Effect* (Bambynek et al. 1972). Since the likelihood of fluorescence increases with the atomic number, the combination between the high atomic number (Kaastra & Mewe 1993) and the high cosmic abundance makes the Kα line associated with iron the most prominent feature. When the plasma exhibits a higher degree of ionization, emission lines corresponding to Fe XXV (helium-like) at 6.67 - 6.70 keV, and Fe XXVI (hydrogen-like) at 6.95 - 6.97 keV, become evident.

When thinking of an emission line, the first picture that typically comes to mind is a Gaussian or Lorentzian profile, characterized by its sharp and narrow shape. However, the spectral lines observed in reflection spectra, generally those emitted from an accretion disc, show a much more interesting profile. Consider a ring in the accretion disc at a specific radius, the matter in this ring orbits at the corresponding Keplerian velocity. From the perspective of an observer at a distance, part of this matter seems to approach them, while at the same time, on the opposite side of the disc, it is moving away. This simultaneous motion causes a dual shift to the emission line, making it appear both blue and red-shifted, creating a symmetrical double-horned profile. Moreover, due to emissions arising from different rings of the disc, the line profile is further

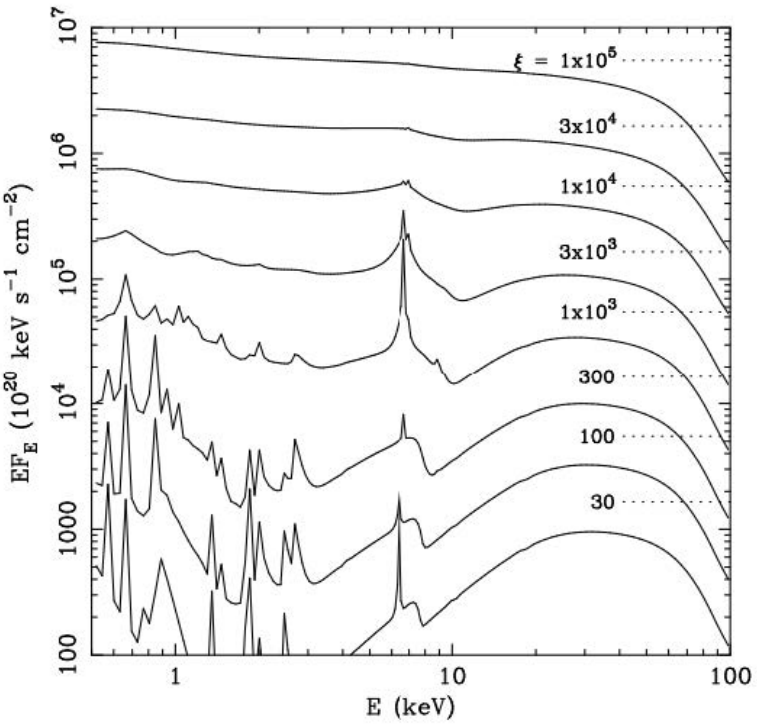

Figure 3.7: Example of reflection spectra from ionized matter at different values of the ionization parameter ξ in unit of ergs cm s^{-1} (Fabian et al. 2000).

broadened by the range of velocities across the disc[3] (Horne & Marsh 1986). Specifically, the Fe Kα line is produced in the inner regions of the accretion disc, where matter moves at relativistic speeds. This high velocity results in relativistic beaming, which enhances the blue peak of the line and diminishes the red one. In addition, the line is subject to gravitational redshift caused by the strong gravitational field near the compact object, shifting the line to lower energies. As a consequence, the emission line is observed as both broadened and asymmetric, as illustrated in Fig. 3.6.

Discussing the ionization state of a disc delves into a more intricate subject. To comprehensively understand how it varies across the disc, one must consider modelling the radiative transfer and resolving the thermal and ionization equilibrium of each fluid element, including the impact of irradiation from various parts of the disc itself. Nonetheless, by adopting certain assumptions, such as considering the disc structure to be stationary, time-independent, and of uniform density, and assuming thermal and ionization equilibrium, we can deduce the resultant reflection spectrum (for an exhaustive review of this topic, refer to Fabian et al. 2000).

The ionization state is quantified by the ionization parameter ξ, which represents the ratio between the rate of photo-ionization and the rate of recombination:

$$\xi(r) = \frac{4\pi F_x(r)}{n(r)}. \tag{3.16}$$

[3]Given the Doppler broadening $\Delta\lambda \simeq \lambda_0(v/c)$, it is possible to estimate the radius of the disc from which the line is emitted, considering v as the Keplerian velocity $v = \sqrt{GM/r}$.

Where $F_x(r)$ is the bolometric X-ray luminosity per unit area at a given radius r, and $n(r)$, is the local electron number density. The value of ξ is fundamental in distinguishing four distinct regimes of reflection.

In the **Neutral Reflection Regime**, where the ionisation parameter $\xi < 100\,\mathrm{erg\,cm\,s^{-1}}$, X-ray reflections are reminiscent of those from a cool gas laden with neutral metals. The detected iron line is a "cold" iron line at 6.4 keV, and the contribution from the Compton back-scattered continuum is negligible. Furthermore, there is a faint iron K-shell edge at 7.1 keV.

In the **Intermediate Ionization** range (where ξ is between 100 and 500 $\mathrm{erg\,cm\,s^{-1}}$), iron is partially ionized into Fe XVII to Fe XXIII. These iron ions can absorb specific X-ray photons and release energy through the Auger effect, thereby weakening the iron line.

In the **High Ionisation Regime**, spanning values of ξ from 500 up to 5000 $\mathrm{erg\,cm\,s^{-1}}$, ions are excessively ionised to engage in the Auger effect, allowing thus the detection of $K\alpha$ iron emissions from Fe XXV and Fe XXVI at 6.67 keV and 6.97 keV, respectively. Moreover, the Compton back-scattered continuum robustly influences the emission observed at 6 keV, giving rise to a pronounced iron absorption edge.

In the **Fully Ionised Regime**, where ξ exceeds 5000 $\mathrm{erg\,cm\,s^{-1}}$, the disc exhibits such a high degree of ionisation that it ceases to produce atomic features; hence, no iron emission lines or edges are present. In Fig. 3.7 is possible to see how the spectrum changes varying the ionization parameter.

Furthermore, the profile of the line and the entire reflection spectrum are shaped by additional system parameters, such as the disc inner and outer radii, its emissivity profile, the iron abundance, and the inclination angle with respect to our line of sight. The importance of analysing this spectral component is crucial since the models used to describe it provide essential information about the structure of the system. For instance, determining the inner radius of the disc is crucial. It aids in constraining the spin of the black hole, understanding the geometry of the accretion flow, and, in the context of LMXBs with a NS as the primary object, it helps to set an upper limit on the radius of the NS. This is especially relevant for the study on the Equation of State of ultra-dense matter (Egron 2013; Degenaar et al. 2015; Di Salvo et al. 2015; Ludlam et al. 2017). A detailed discussion of these models is deferred to the next chapter, where we will delve fully into the spectral analysis of these sources.

3.4.0 Spectral and Timing proprieties

When XRBs, hosting NS and BH systems, are observed at different epochs they can display a rich variety of spectral states due to the different assembly mechanisms of their spectral components. This was first noticed in Cyg X-1, a BH binary exhibiting two main states: **high/soft state** and **low/hard state**. In a high/soft state, a source exhibits a high flux in soft X-rays and a lower one in hard X-rays. This state is characterized by a dominant thermal component, usually around 1 keV, associated with a black body from the accretion disc that reaches the central object. At higher energies levels, a non-thermal component emerges, represented by a soft power law

with an index $\Gamma \sim 2.1 - 3$ extending at least to hundreds of keV (Gierliński et al. 1999). The component, termed the *hard tail*, has been detected in various systems (Paizis et al. 2006; Fiocchi et al. 2006; Del Santo et al. 2013), and is typically explained as the result of inverse Compton scattering of soft photons from the disc by electrons in a hot relativistic non-thermal Corona. Moreover, this emission irradiates the disc generating a strong reflection component (Done et al. 2007).

Spectra in the **hard state** are generally described by power-law models with index Γ approximately ranging from 1.5 to 2.0, and they extend to energies exceeding 10 keV. These spectral configurations are explained through thermal Comptonization models, with electron temperatures lies in the range of 70-120 keV for BH XRBs (Done et al. 2007) while the temperatures are usually lower for NS systems (Di Salvo et al. 2019; Gierliński & Done 2003). The origin of the seed photons is an area of ongoing research debate, especially in NS LMXBs. They may originate from synchrotron radiation within the corona or the thermal emission of the accretion disc. The *Eastern model*, as proposed by Mitsuda et al. (1989), posits a smaller corona encircling the NS, acting as the source of seed photons. On the other hand, the *Western model* by White et al. (1988) suggests a more extended corona over the disc, serving as the seed photon source. Additionally, the accretion rate in the hard state may be lower compared to the soft state. This is evidenced by the weak thermal component in the low-energy spectrum, which aligns with a cooler accretion disc than that observed in the soft state, with temperatures around 0.5 keV (Di Salvo et al. 2001). This implies that the disc is truncated at a farther distance from the compact object, with the inner region likely comprising a hot, optically thin plasma (Esin et al. 1997). Moreover, the disk is less ionized and the reflection features are weaker than in the soft state. The hard state is also connected to the jet detection and for this reason, is perfect for multi-wavelength analysis (Corbel et al. 2003).

Investigating each state is crucial for an enhanced comprehension of accretion processes, especially focusing on the spectral and temporal variations that define each state. In particular, monitoring the activity of a source can be effectively done using the hardness intensity diagram (HID) for BHs, and the color-color diagram (CCD) for NSs. While HID is predominantly utilised for BHs to illustrate the characteristic q-shaped track during spectral evolution, it is equally applicable in analysing the spectral behavior of NSs (see Muñoz-Darias et al. 2014).

The CDD shows the ratio of count rates in two high-energy bands (hard color) plotted against the one taken in two low-energy bands (soft color). Depending on the track followed in the diagrams we can divide LMXBs into **Atoll** or **Z-sources** (Hasinger & van der Klis 1989). The Atoll sources present two different spectral states: the "*banana*" and "*island*" states, called this way for their shape (see Fig. 3.8). In the Z-sources instead, three branches are distinguishable: the *horizontal branch* (HB), the *Normal branch* (NB), and the *flaring branch* (FB).

Atoll and Z-sources differ mainly in luminosity and, perhaps, magnetic field: Z-sources are brighter (with luminosities close to the Eddington limit (Ford et al. 2000)) and with a higher magnetic field ($B \geq 10^9$ G Gierliński & Done 2002), but both timing and spectral properties depend only on the position in the CCD diagram. The evolution of a Z source occurs in a timescale of a few days, while a source moves along the atoll track in a timescale of weeks

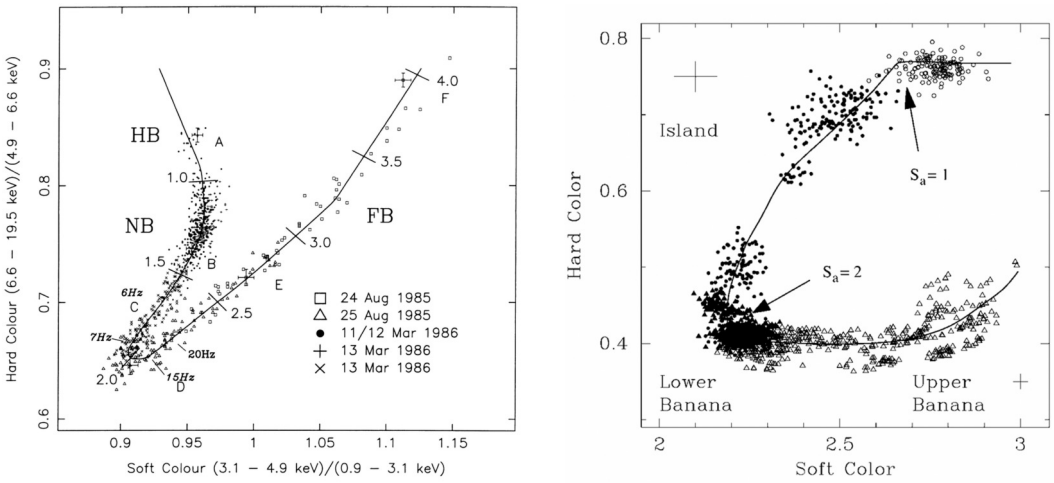

Figure 3.8: **Left panel**: colour-colour diagram of Sco X-1 showing the complete Z track (Dieters & van der Klis 2000). **Right panel**: Color-color diagram of 4U 1608-52. The soft color ratio is calculated between the count rates in the 3.5-6.4 keV and 2.0-3.5 keV bands, while the hard color ratio in the 9.7-16.0 keV and 6.4-9.7 keV bands (Méndez et al. 1999)

.

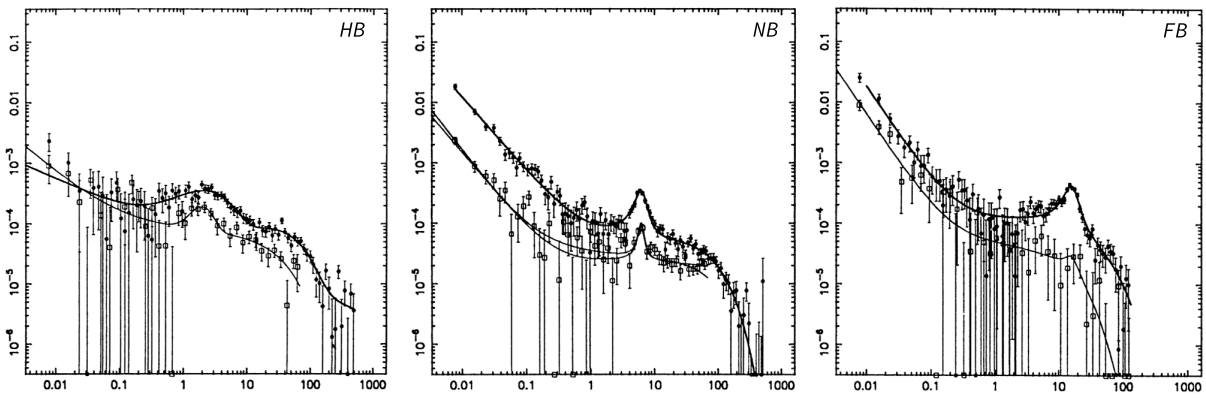

Figure 3.9: Representative power spectra from the three main branches of the Z track for the LMXB Sco X-1, as reported in Dieters & van der Klis (2000). In the picture, it is possible to see how the frequency of the QPOs shown varies along the Z-track.

and in both cases, the evolution is thought to be driven by the variability in the mass accretion rate (Vrtilek et al. 1991; Patruno & Watts 2020). The study of both periodic and aperiodic variabilities is typically referred to as timing analysis (Gilfanov 2010) and relies on the analysis of the power density spectra (PSD). Here, the 'power', i.e. the amplitude of variability, is broken down by Fourier frequency. This fragmentation allows for the identification of any periodic elements within the signal, along with the primary noise phenomena (van der Klis 1989). Each spectral state has distinct timing characteristics. For example, the hard state of BH LMXBs is often characterized by a "flat top" signal in the PSD, indicating band-limited noise with breaks occurring at both low and high frequencies (Psaltis et al. 1999). Some atoll sources exhibit PSDs that are remarkably similar, especially at lower luminosities, whereas, at higher luminosities, this flat-topped noise can sometimes fade away (Belloni et al. 2002). In contrast, the PSDs of Z-sources feature a low-amplitude X-ray modulation called quasi-periodic oscillations (QPOs), whose frequency varies along different branches (van der Klis 1989). Specifically, there are

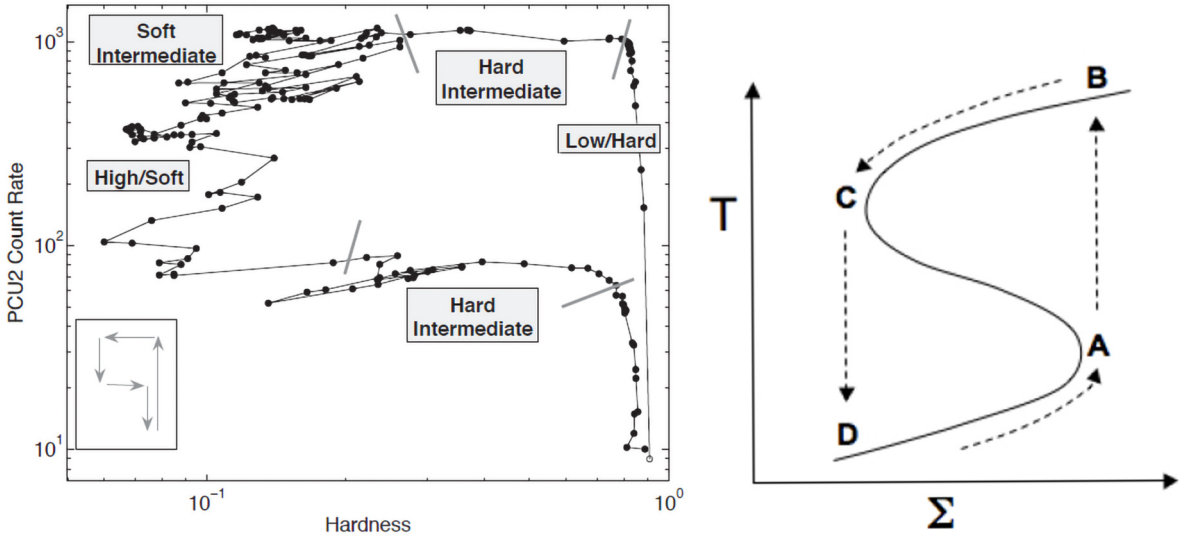

Figure 3.10: **Left panel**: Hardness-Intensity diagram of GX 339-4 outburst in 2002/2003 observed by RXTE/PCA. The arrows on the bottom-left indicates the motion of the source along the track (Belloni 2005). **Right panel**: Plot of temperature versus the surface density showing the S-curve for the disc instability model (Hartmann 1998, adapted by).

three different types of QPOs, one associated with the horizontal branch (HBO), one associated with the normal and flaring branches (see Fig. 3.9), and, in some sources shows a twin peaks kHz frequency QPO (kHzQPO) (van der Klis 1989). The high-frequency peak is close to the expected Keplerian frequency of the matter around the compact object and all the models that try to explain the kHz QPO associate the latter with the motion of the plasma in the disk around the NS. For this reason, that feature can be used to estimate the inner radius of the disc and, possibly, the mass of the NS.

3.5.0 Transient sources

The vast majority of LMXBs that host a Black Hole exhibit transient activity. These systems oscillate between long periods of low X-ray emission (**quiescence**), with luminosity around $L_X \sim 10^{30-34}$ erg s^{-1} (Armas Padilla et al. 2014b), during which the accretion is likely inactive. They also experience occasional episodes of intense X-ray luminosity (**outbursts**) that can reach up to the Eddington limit. Such systems are referred to as **transients system**. The transient behavior is linked to the accretion disc structure and how certain parameters vary with the accretion rate. The origin of such behaviour is explained by the theory of the so-called **Disc Instability Model** (DIM), mainly introduced for dwarf novae and some LMXBs (see Lasota et al. 2011, for a detailed review). It suggests that the accretion disc around a compact object undergoes thermal and viscous changes driven by accumulation of matter from the companion star, leading to a buildup of a cold, dense disc in a quiescent state. When a critical density is reached, a portion of the disc experiences a local rise in temperature, enhancing ionization and opacity within the disc, and leading to a sudden increase in viscosity. This viscosity spike causes a rapid inflow of matter towards the central compact object, resulting in an outburst. After the

material in the disc is accreted during an outburst, the system returns to a quiescent state, awaiting the accumulation of enough matter to trigger the next outburst.

To understand the outburst cycles, one effective method is to plot the disc surface density against its effective temperature, forming what is known as an **S-curve**, delineated by three distinct branches. The lower branch represents the disc cool, stable state during quiescence, while the upper branch represents the hot, ionized state during outbursts. The middle, unstable segment of the S-curve marks the transition between these two states (see Fig 3.10). Changes in the disc temperature and density drive its movement along this curve, causing shifts between stable and unstable states and leading to the characteristic outbursts observed in these systems. Therefore, the S-curve is an essential tool for predicting and elucidating the timing and features of these outbursts.

The transition from quiescence to outburst and back in BH LMXBs is denoted by a specific spectral path of the source, reflected in its HID. Like in NS LMXBs, the HID is a well-known diagram used to map the different phases of BHs. The diagram plots the total count rate against hardness, defined by the ratio of counts in two energy bands. A BH path in this diagram typically exhibits a "q" shape, through which the source primarily varies across four spectral states. The beginning and end of an outburst are marked by the source entering the lower right side of the "q". This state called *the Low/Hard State (HS)*, is characterized by a power-law index of 1.6 - 1.7, spectra and PDS are often accompanied by low-frequency QPOs (Casella et al. 2004) and jets (Fender et al. 2004). As luminosity increases, the disc emission becomes more visible at lower energies while maintaining a hard spectrum. The source then enters the *Hard Intermediate State (HIS)*, corresponding to the top horizontal side of the "q" (see Fig. 3.10). In the *Soft Intermediate State (SIS)*, the spectrum softens further, and finally, in the *High/Soft State*, the spectrum is dominated by a very soft thermal disc component. Following this state, the system retraces these stages in reverse order but at a lower luminosity, eventually returning to quiescence. This typical loop of LMXBs from a hard state to a soft state and then back at varying levels of luminosity, is known as **hysteresis** (Zdziarski et al. 2004; Miyamoto et al. 1995).

4 Data Analysis

The research presented in this thesis includes astronomical data spanning a broad spectrum of wavelengths, encompassing both optical and X-ray domains. Specifically, the work in Chapter 5 employs a combined spectral and timing analysis of data from the XMM-Newton and Nuclear Spectroscopic Telescope Array (NuSTAR). Chapter 6 shifts focus to optical analysis, leveraging data from the Gran Telescopio Canarias (GTC), while Chapter 7 presents an analysis utilizing three optical telescopes: GTC, the Very Large Telescope (VLT), and the Magellan Clay Telescope. To enhance understanding of the analyses in the subsequent chapters, I will outline the key features of these instruments in the upcoming sections.

4.1.0 X-ray Astronomy

X-ray astrophysics, emerging in the 1960s, presents distinctive challenges as it requires observations beyond Earth atmosphere, due to it is opaque to X-rays. X-rays range from 0.1 to 100 keV in energy, with lower-energy X-rays termed 'soft' and higher-energy ones as 'hard'. The field of X-ray astronomy depends on photon-counting detectors to analyze the position, energy, and timing of incoming photons, providing insights into the nature of sources and the mechanisms of X-ray. In high-energy astrophysics, the focus is on the particle aspect of photons. X-ray sources, emitting low-intensity flux, allow the detection of individual photons. Contemporary detectors like proportional counters, scintillation detectors, and Charge-Coupled Devices (CCDs) record the charge excited from the incoming photons. An ideal detector would offer high spatial, temporal, and energy resolutions with a broad collecting area, such perfection remains unachieved, though progress is ongoing.

Post-World War II developments in this field began with the study of the Sun's corona X-ray emission via rocket flights. The first significant breakthrough in X-ray history was the discovery of Scorpius X-1 in 1962, which earned Giacconi a Nobel Prize and paved the way for the identification of more X-ray sources, including binary systems and supernova emissions. After this, NASA launch of the *Uhuru* satellite in 1970 was a landmark, mapping over 300 X-ray sources and paving the way for more sophisticated satellites like *ANS*, *Ariel-V*, and *HEAO-1*, which furthered the understanding of X-ray binaries and other astronomical phenomena.

The introduction of the *Einstein* Observatory in 1978 was revolutionary, providing the first X-ray images of various celestial objects and automating data reduction for public access. The 1980s witnessed considerable progress with the launch of satellites like *Hakucho*, *Tenma*, *EXOSAT*, and *Ginga*, leading to discoveries such as quasi-periodic oscillations in X-ray binaries and in-depth studies of iron lines in AGNs and the Galactic center. The 1990s continued this trend with the *ROSAT* satellite, a collaborative effort that cataloged over 150,000 astronomical objects. Russia's *Granat* mission in 1989, precursor to the *INTEGRAL* mission, produced detailed imaging of the Galactic center. In 1993, the *ASCA* satellite, born from a collaboration between ISAS and NASA, broke new ground with the introduction of X-ray sensitive CCDs, enhancing both imaging and spectroscopy in the field.

NASA *RXTE* satellite, launched in 1995, was pivotal in studying the variability of bright X-ray sources and contributed significantly to our understanding of spin periods in X-ray binaries and the detection of quasi-periodic oscillations. Its monitoring role was succeeded by the Japanese *MAXI* detector on the ISS after the mission concluded in 2012. In 1996, the *BeppoSAX* satellite, a joint Italian-Dutch mission, was launched, enabling the observation of X-ray sources across a wide energy spectrum. This capability allowed for diverse studies in X-ray astronomy, covering galactic sources, AGNs, galaxy clusters, and more.

Currently, we are in a "Golden Age" of X-ray astronomy, with an array of missions like *Chandra*, *XMM-Newton*, *Swift*, *INTEGRAL*, *MAXI*, *NuSTAR*, *Nicer*, and the recently launched *XRISM*. These satellites boast advanced capabilities such as high angular resolution, extensive effective areas, and a wide energy range, allowing for comprehensive studies of a variety of X-ray sources, from the most luminous to those shrouded in mystery.

4.1.1 XMM-Newton

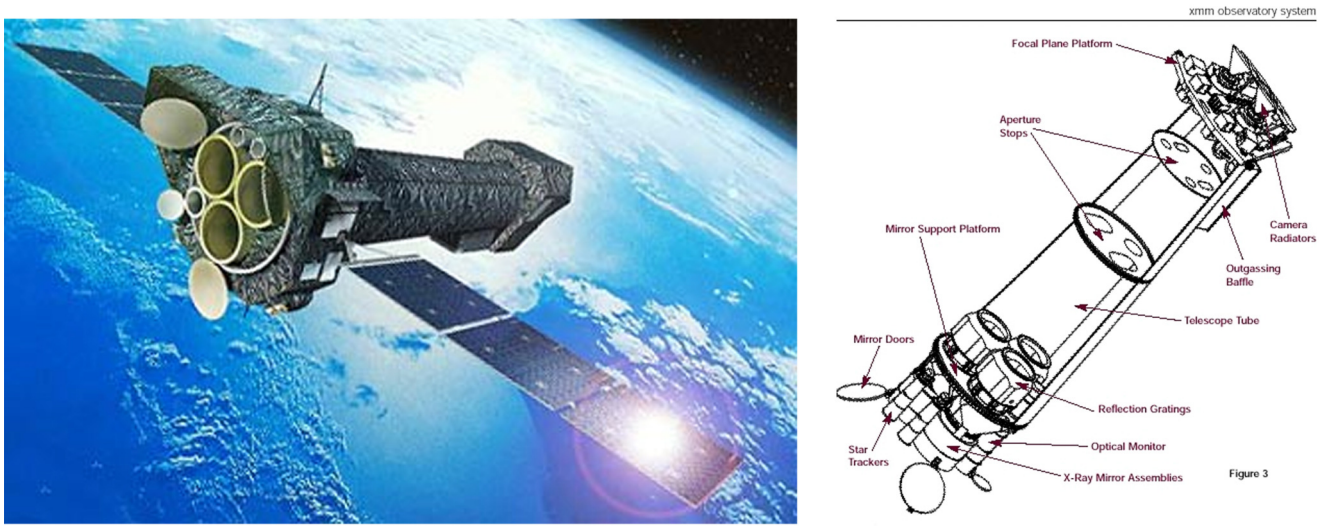

Figure 4.1: **Left panel**: sketch of the XMM-Newton observatory in orbit around the Earth. Image from the ESA website (D. Ducros). **Right panel**: Schematic sketch of the main components of the XMM spacecraft.

Table 4.1: The basic characteristics of XMM-Newton scientific instrumentation

Instrument	EPIC MOS	EPIC pn	RGS	OM
Bandpass	0.15-12 keV	0.15-12 keV	0.35-2.5 keV	180-600 nm
Orbital target vis.	5-135 ks	5-135 ks	5-135 ks	5-145 ks
Sensitivity (erg s^{-1} cm^{-2})	10^{-14}	10^{-14}	8^{-10}	20.7 mag
Field of view (FOV)	30’	30’	5’	17’
PSF (FWHM/HEW)	5”/14”	6”/15”	N/A	1.4”-2.0”
Pixel size	40 μm (1.1”)	150 μm (4.1”)	81 μm (910 Å)	0.476513”
Timing resolution	1.75 ms	0.03 ms	0.6 s	0.5 s
Spectral resolution	70 eV	80 eV	0.04/0.025 Å	180

The X-Ray Multi Mirror Mission (XMM-Newton) is the largest scientific satellite ever launched, weighing 4 tonnes and measuring 10 meters in length. Deployed by the European Space Agency (ESA) on December 10, 1999, its structure includes (see Fig. 4.1):

- **Focal Plane Platform** (FPP): Carries three imaging cameras (an EPIC PN and two EPIC MOS) and two Reflection Grating Spectrometers (RGS), all operable simultaneously.
- **Telescope Tube**: A 6.80-meter-long carbon fiber tube.
- **Mirror Support Platform** (MSP): Holds three mirror assemblies, the Optical Monitor (OM), and two star-trackers.
- **Service Module** (SVM): Contains the spacecraft subsystems.

The satellite optics are designed for maximum effective area across a wide energy range, focusing on around 7 keV (the Iron line region). Each of its three X-ray telescopes is a Wolter-I type, featuring 58 gold-coated nested mirrors (each a combination of a paraboloid and a hyperboloid) to achieve effective reflectivity at high energies.

The telescopes performance is assessed based on **image quality**, **effective area**, and **stray light rejection efficiency**. The effective area determines a detector ability to capture radiation at various photon energies. As it shown in Fig. 4.2, EPIC-pn camera has a larger effective area compared to the two EPIC-MOS cameras, due to different light paths in the three Wolter-type X-ray telescopes. The image quality, consistent across the 0.1-6 keV range and only slightly energy-dependent above 6 keV, is gauged by the point-spread function (PSF). XMM-Newton excels in its effective area, especially at low energies (2 keV) while maintaining efficiency at higher energies (7 keV) (see Fig. 4.2). The mirrors are most effective in the 0.1 to 10 keV range, with a peak around 1.5 keV. The EPIC pn camera, in the focus of one X-ray telescope, has a higher effective area compared to the two MOS cameras, which have grates refracting some light away. Stray light rejection efficiency is crucial to minimize instrumental noise from non-source light. X-ray baffles, consisting of two plates with concentric annular apertures, are used to mitigate this issue.

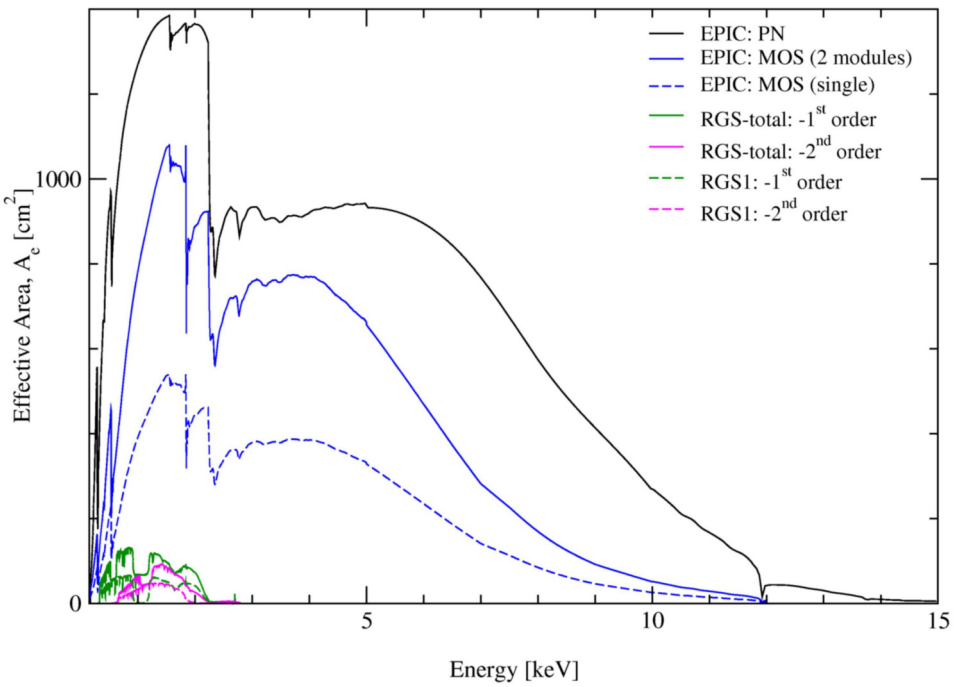

Figure 4.2: Effective area of the XMM-Newton X-ray telescopes, EPIC-pn, EPIC-MOS, and RGS

Key features of XMM-Newton include: simultaneous operation of all science instruments, high sensitivity, boasting the largest effective area of a focusing telescope (1550 cm^2 at 1.5 keV), good angular resolution (FWHM around 600), moderate to high spectral resolution (70-80 eV for EPIC cameras, higher for RGS), simultaneous optical/UV observations via the co-aligned OM telescope and in the end a long continuous target visibility, thanks to its highly elliptical orbit allowing up to 40 hours of continuous target observation (For a detailed list of instrumental characteristics, see table 4.1).

European Photon Imaging Camera - EPIC

The European Photon Imaging Camera (EPIC) on the XMM-Newton spacecraft is comprised of two types of cameras: two EPIC Metal Oxide Semiconductor (**MOS**) CCD arrays (Turner et al. 2001) and one pn-CCD, referred to as **EPIC-pn** (Strüder et al. 2001). These cameras are adept at conducting sensitive imaging observations over a 30' field of view and an energy spectrum ranging from 0.2 to 12 keV. Their design achieves an angular resolution of 6" at full width at half maximum (FWHM) and a half energy width (HEW) of 15", where half the total energy of the observed phenomenon is concentrated. The EPIC MOS and pn cameras are distinct in their functionality. The pn camera is notable for its rapid readout process, made possible by individual readout nodes for each pixel column. In contrast, the MOS cameras offer superior quantum efficiency due to their front-illuminated chips, whereas the pn CCDs are back-illuminated (see Fig. 4.3). The physical structure of these cameras also differs; the pn camera consists of a single silicon wafer with 12 integrated CCD chips, while each MOS camera is assembled from 7 front-illuminated chips, arranged at a 90-degree angle to each other. Mounted on X-ray telescopes

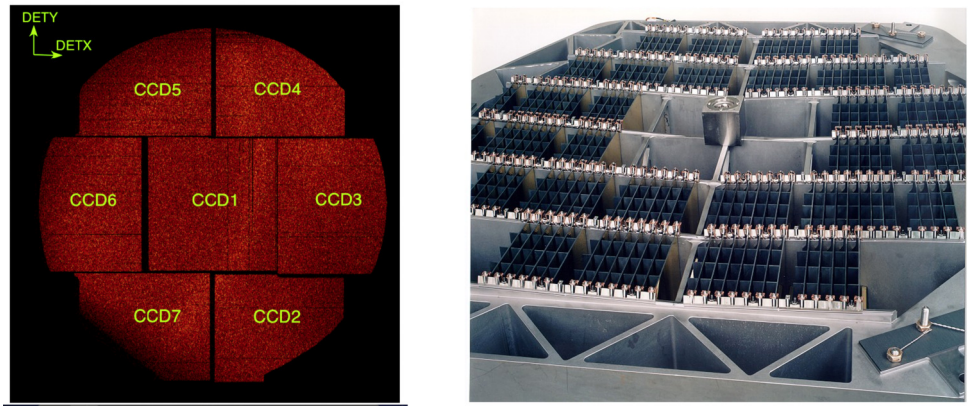

Figure 4.3: **Left panel**: layout of EPIC MOS cameras on the XMM-Newton spacecraft with the 7 CCDs, with each CCD covering an area of 10.9 by 10.9 arcminutes. The seemingly empty spaces between the MOS chips are actually non-functional areas at the edges of the detectors, as described in the XMM-Newton Users' Handbook. **Right panel**: Detailed view of one of the RGAs.

alongside the RGS spectrometers, the MOS cameras capture only 44% of the reflected light.

EPIC cameras function in three primary modes: *imaging*, *timing*, and the *burst mode*, the latter being exclusive to the EPIC-pn. Imaging mode encompasses full-frame, small window, and large window options, each providing varying coverage and readout approaches. The timing mode maintains spatial resolution along only one axis, facilitating faster readout and reducing **pile-up**. Pile-up happens when an X-ray source is extremely bright causes multiple photons to hit the same pixel during one read-out cycle, leading the detector to misinterpret them as a single event having the sum of photon energies, rather than separate photons. As a result, it leads to an inaccurate count of the photons and mistakes in measuring their energy. The burst mode of the EPIC-pn, in particular, is designed for observing extremely bright sources. It offers an exceptionally high temporal resolution and effectively eliminates pile-up issues, albeit at the expense of a reduced duty cycle. This mode is crucial for precise observations of highly luminous sources.

Reflection Grating Spectrometers (RGS)

The EPIC MOS cameras on XMM-Newton are accompanied by two Reflection Grating Spectrometers (**RGS**) positioned behind them. These spectrometers capture half of the incoming X-ray light using an array of reflection gratings. These gratings diffract X-rays towards nine back-illuminated CCD detectors, which operate in single-photon counting mode to determine the position and energy of each photon.

Each RGS setup consists of two identical chains containing two Reflection Grating Array units (RGA), two Focal Plane Camera units (RFC), two Analogue Electronic units (RAE), and four Digital Electronic units (RDE). The RGA in each chain houses 182 diffraction gratings, each measuring 10 x 20 cm (see Fig. 4.3). These gratings are made of Silicon carbide (SiC) substrates with a 2000-Angstrom gold coating. They are uniquely oriented to ensure a consistent grazing angle for incident rays across all gratings.

The RGS instruments offer a resolving power between 150-800 in the 0.33 to 2.5 keV range, with the maximum effective area at 0.83 keV. This range is particularly beneficial for analyzing emission and absorption features in X-ray spectra in detail.

Optical Monitor (OM)

XMM-Newton is equipped with an aligned 30 cm Ritchey-Chretien telescope for optical/UV observations, known as the Optical Monitor (OM), which has a 3.8-meter focal length (see Fig. 4.1). It features three optical and UV filters, with two grisms one covering optical and the other the UV, enabling high-resolution time-based photometry with exceptional sensitivity. This is largely due to the absence of atmospheric disturbances like extinction and background noise. However, the OM usage is limited around bright optical sources due to its highly sensitive detector. This monitor is particularly useful for analyzing the optical and UV flux of X-ray sources, which are often variable, in conjunction with the X-ray telescope.

4.1.2 NuSTAR

The Nuclear Spectroscopic Telescope Array (**NuSTAR**) is a pioneering X-ray mission offering high-sensitivity imaging in energies above 10 keV, a feat enabled by advanced hard X-ray optics and solid-state detector technologies. It features two co-aligned hard X-ray telescopes, operating in the 3 to 79 keV range, with radiation focused by Wolter-I conical mirrors onto solid-state detectors, connected by a 10-meter deployable mast. NuSTAR key characteristics include an energy resolutiom of 400 eV at 10 keV and 900 eV at 68 keV, a field of view that varies with energy, exceptional temporal resolution for analyzing fast X-ray pulsars, and a significantly reduced background above 10 keV due to an effective anti-coincidence shield. The NuSTAR instrument features two aligned hard X-ray telescopes, each with optics mounted on a composite bench that ensures thermal stability. This bench is part of an aluminum structure attached to the spacecraft, and the optics are connected by a mast made of carbon fibers and aluminum (see Fig. 4.5). This design minimizes thermal distortions, although residual deflections due to solar heating can still affect the telescope focus, causing vignetting[1]. To correct this, NuSTAR employs a sophisticated metrology system, comprising two IR lasers and a star tracker, which continuously monitors and adjusts the alignment of the optics and the focal plane.

The optics include 133 multilayer-coated shells, shaped to a Wolter-I geometry, with each shell constructed from thin glass layers. The optics are coated with materials like Platinum and Tungsten to enhance reflectivity at specific energy thresholds and to reduce vignetting. NuSTAR design allows for a broad field of view and substantial collecting area at higher energies.

Each telescope focal plane module (FPM) features a CdZnTe pixel detector surrounded by a CsI anti-coincidence shield to reduce background noise. The FPMA and FPMB modules, while similar, have slight variations in their effective area. The detectors design, consisting of a 32x32 pixel array, ensures a wide field of view and enables independent pixel readouts. This mechanism

[1]Vignetting causes image edges to appear darker, especially in *NuSTAR*, where the optical system geometric alignment leads to less efficient focusing of X-rays at higher angles, reducing intensity at the field of view edges.

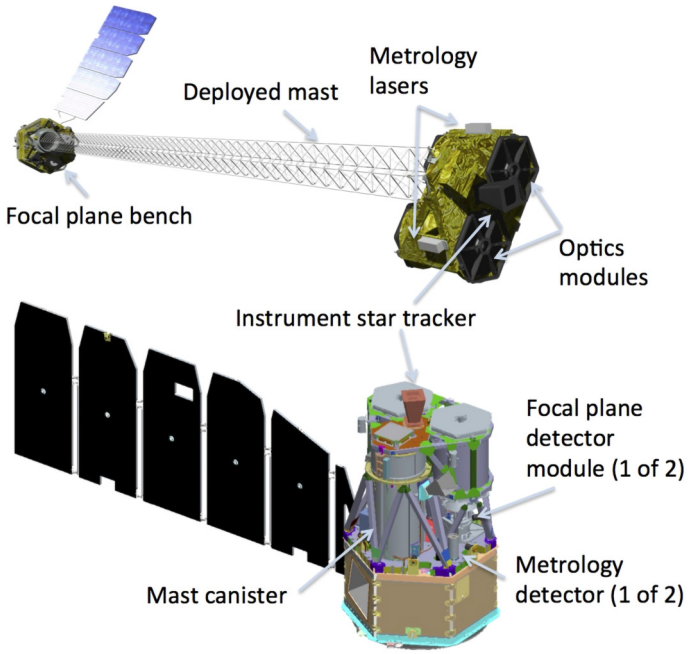

Figure 4.4: Illustration of NuSTAR spacecraft displaying key components (from https://heasarc.gsfc.nasa.gov/docs/nustar/nustar_about.html).

effectively prevents pile-up issues, allowing NuSTAR to handle high event rates without data loss or distortion.

Its angular resolution of 18" FWHM and a half power diameter of 58' make it an invaluable instrument for detailed X-ray spectral studies, particularly useful for analyzing complex reflection spectra emitted by X-ray binaries. This wide energy range, combined with its resolution capabilities, positions NuSTAR as a powerful tool in the field of high-energy astrophysics. In Table 4.2 main NuSTAR characteristics are resumed.

4.1.3 The Neils Gehrels Swift Observatory

The Neil Gehrels Swift Observatory, formerly known as the **Swift Gamma-Ray Burst Mission**, is a multi-wavelength space observatory dedicated to the study of gamma-ray bursts (GRBs). It was launched into orbit on November 20, 2004, and was renamed in 2018 in honor of the late Neil Gehrels, its lead scientist.

The primary mission of the Swift Observatory is to rapidly detect, locate, and observe GRBs, one of the most energetic events in the universe, which are believed to be associated with the collapse of massive stars or the merger of NSs. Besides of GRBs it can also adeptly investigates all kind of transient high-energy phenomena. Result of a partnership led by UK, USA and Italy, the telescope is located in a circular orbit close to Earth and maintains an average elevation of approximately 600 kilometers. The observatory is composed of three main instruments:

Table 4.2: The basic characteristics of NuSTAR

Parameter	Value
Energy range	3-78.4 keV
Angular resolution (HPD)	58”
Angular resolution (FWHM)	18”
FoV (50% resp.)	10’ at 10 keV
	6’at 68 keV
Sensitivity (6-10 keV)	2×10^{-15} erg cm^{-2} s^{-1}
Sensitivity (10-30 keV)	1×10^{-14} erg cm^{-2} s^{-1}
Background in HPD (10-30 keV)	1.1×10^{-3} counts/s
Background in HPD (30-60 keV)	8.4×10^{-4} counts/s
Energy resolution (FWHM)	400 eV at 10 keV
	900 eV at 68 keV
Temporal resolution	2 μs
Target of opportunity response	<24 hr

the **Burst Alert Telescope (BAT)**, the **X-Ray Telescope (XRT)** and the **Ultraviolet/Optical Telescope (UVOT)**.

- **BAT** is a highly sensitive, large FOV, coded-aperture telescope designed to rapidly detect and locate GRBs in real-time. The telescope boasts an large field of view, covering 80% of the sky, crucial as GRBs are inherently unpredictable and can emerge in any part of the sky.

  Unlike mirror-based telescopes BAT utilizes a coded aperture mask for capturing space images. This method involves a plate with varied-shaped apertures positioned above the detector array. As radiation strikes this specialized mask, it produces a shadow on the detectors, forming a shadowgram. This shadowgram is then meticulously converted into a precise sky image, enabling the accurate determination of the source location.

  Upon identifying a GRB, the BAT rapidly computes its coordinates with a remarkable precision of 1 to 4 arcminutes. In its construction, the BAT includes also an array of detectors crafted from semiconductor materials, typically lead and silicon. These detectors are sensitive to soft X-rays and gamma rays in the energy range 15-190 keV.

- **XRT** is an advanced imaging spectrometer, operating in the 0.2-10 keV energy range (Burrows et al. 2000). It is specifically engineered for conducting in-depth observations of GRB afterglows detected from BAT and it uses a grazing incidence Wolter 1 telescope. Key features of the XRT include high-resolution imaging and spectroscopy capabilities. It boasts an effective area of 110 cm^2 and a field of view spanning 23.6 x 23.6 arcminutes. The telescope is equipped with a CCD detector, encompassing an image area of 600 x 602 pixels, which achieves a Full Width at Half Maximum energy resolution, ranging from 190 eV at 10 keV to as low as 50 eV at 0.1 keV.

  The XRT operates in three distinct modes to accommodate various observational needs: Imaging (IM) Mode, Photon Counting (PC) Mode and Windowed Timing (WT) Mode. In

Figure 4.5: Illustration of Swift spacecraft design.

IM mode it generates an integrated image, measuring the total energy deposited in each pixel. While it does not facilitate spectroscopy, it is essential for accurately positioning light sources. Utilizing sub-array windows, the PC mode provides full spectral and spatial information, achieving a temporal resolution of 2.5 seconds. The WT mode offers the highest temporal resolution at 1.8 ms, and it is ideal for timing studies of light sources.

- The **UVOT** makes Swift a complete multi-wavelength facility. The UVOT is a 30 cm modified Ritchey-Chretien UV/optical telescope cO-aligned with the XRT, enabling simultaneous observation of ultraviolet (170-260 nm) and optical (260-650 nm) radiation within a 17' x 17' field of view. Unlike typical optical telescopes, it uses photon counting detectors for detailed timing and spatial data, similar to X-ray instruments.

  UVOT offers also diverse operational modes: image mode for traditional imaging, event mode for individual photon analysis, and time-tag mode for precise temporal studies. This versatility permits adaptation to various scientific objectives. It also benefits from a fast readout time, minimizing the delay between GRB detection by BAT and subsequent UV/optical observations. Further expanding its capabilities, UVOT incorporates a suite of filters and grisms, allowing both broadband and narrow-band imaging alongside low-resolution spectroscopy.

4.2.0 Optical instruments

Optical astronomy, unlike its counterpart in X-ray astronomy, is a time-honored field, deeply woven into the tapestry of human history since the earliest days of civilization. Its story starts with the ancient Babylonians, Egyptians, Greeks, and Chinese, who gazed up at the sky, charting the stars and planets. They built the foundations of astronomy, using the celestial bodies for navigation, timekeeping, and, often, spiritual guidance. During the Middle Ages, Islamic scholars in the Middle East and North Africa kept the astronomical flame alive. They refined tools like the astrolabe, crucial for measuring the positions of stars, and made significant contributions to celestial mapping.

This story takes a dramatic turn in 1608 in the Netherlands, where **Hans Lippershey**, while experimenting with lenses, discovered that viewing objects through a combination of a convex

and a concave lens made them appear closer. Lippershey applied for a patent for his device, which he described as a tool for "*seeing faraway things as if they were nearby*." The patent was ultimately denied, partly because the simplicity of the design made it easy to replicate. His telescope was a refracting type, using lenses to bend light and magnify images, with a small magnification factor, about 3x, but it was revolutionary for its time. News of Lippershey invention spread quickly across Europe. In 1609, the Italian scientist **Galileo Galilei**, upon hearing of this new invention, constructed his own version without having seen the original design. Galileo improved upon the original design, increasing the magnification, and turned it towards the sky, revealing the craters of the Moon, the moons of Jupiter, and the phases of Venus. This was a pivotal moment, changing our understanding of the universe forever.

As the 17th century unfolded, the field of optical astronomy was revolutionized by the mind of **Johannes Kepler** and **Isaac Newton**. Newton, in particular, made a landmark contribution in 1668 with the invention of the first reflecting telescope, addressing the limitations inherent in refracting telescope designs. The 18th and 19th centuries saw William Herschel discoveries Uranus and the rise of the Great Refractors, large lens telescopes like the Yerkes Observatory's 40-inch telescope, the biggest of its type. The 20th century marked the era of "large telescopes." Mount Wilson's Hooker Telescope, a 100-inch behe-moth, came to life in 1917. Here, Edwin Hubble revealed the nature of galaxies and the expanding universe. Not to be outdone, the Palomar Observatory's 200-inch Hale telescope, seeing first light in 1948, pushed the boundaries, exploring distant galaxies and quasars. On December 7, 1968, the first optical space telescope the Orbiting Astronomical Observatory 2 (OAO-2), was launched by NASA marking a milestone in the history of astronomy. Later, on April 24, 1990, the Hubble tele-scope began to peer into the far corners of the universe, offering breathtaking images and forever entering the public imagination.

Meanwhile On Earth, the twin Keck telescopes in Hawaii, each with a 10-meter mirror composed of segment-ed hexagons, opened new windows on the cosmos in the 1990s. They represent the pinnacle of ground-based observatory design. The turn of the millennium saw the inauguration of the VLT in Chile, with four 8.2-metre telescopes working in concert, illustrating the power of optical interferometry. Soon in 2027, the next chapter will feature the Extremely Large Telescope (ELT) in Chile, destined to become the largest optical telescope in the world.

4.2.1 Gran Canaria Telescope

The Gran Telescopio Canarias (GTC), located at the Roque de los Muchachos Observatory in La Palma, Canary Islands, is one of the world largest optical telescopes (see Fig. 4.6). It features an altazimuth mount and a Ritchey-Chrétien optical layout with Nasmyth, Cassegrain, and Folded Cassegrain foci. It operates across a wavelength range from 365nm to 2.5 μm. The telescope is composed of a segmented primary mirror with a diameter of 10.4 meters, made up of 36 hexagonal Zerodur segments, each coated with aluminum and weighing 470 kg and Covering a total area of 75.7 square meters and designed to mimic a 10.4 m diameter circular mirror. The secondary mirror is a lightweight convex hyperbolic of beryllium of about 1.2 m with

Figure 4.6: From left to right: an image of the Gran Telescopio Canarias, followed by the Magellan Telescope, and concluding with the Very Large Telescope facility.

an aluminum coating, and the tertiary mirror is a flat, elliptical mirror. The telescope is equipped with advanced adaptive optics for image correction, and various instruments for spectroscopy and imaging. It operates in both visible and infrared wavelengths, ensuring high-quality imaging. The telescope achieves pointing accuracy of 1 to 2 arcsec and can perform blind offsetting effectively. Small distance offsets maintain an accuracy of about 0.2 arcsec, while larger offsets can increase errors to 0.5 arcsec.

The GTC is equipped with several state-of-the-art instruments designed for a range of astronomical observations. These include:

- **OSIRIS**: An imaging system and spectrograph for low-resolution observations in visible wavelengths.
- **CanariCam**: Used for mid-infrared imaging, spectroscopy, and polarimetry (decomissioned in 2021).
- **EMIR**: A near-infrared multi-object spectrograph.
- **MEGARA**: Provides high spectral resolution capabilities in the visible range.
- **HORS**: A high-resolution optical spectrograph.

Each GTC instrument offers unique capabilities, from detailed spectroscopic studies to wide-field imaging, enabling comprehensive research in fields such as exoplanet discovery, galaxy evolution and stellar physics. In the next subsection I will provide a short description of OSIRIS instrument, since it is the main instrument used in the analysis presented in chapter 6.

OSIRIS

OSIRIS (Optical System for Imaging and low-intermediate-Resolution Integrated Spectroscopy) operates in a wavelength range of 365 to 1000 nm and offers broad imaging, spectroscopy, and tunable filters. Its wide field of view and narrow-band tunable filters imaging are exceptional for detailed celestial studies. It includes multi-object spectroscopy, allowing simultaneous examination of multiple sources. Equipped with a cooling system to reduce detector

Table 4.3: Resolutions and spectral ranges of OSIRIS and Magellan telescope.

ID	λ_c (Å)	λ range (Å)	D (Å/pix)	Resolution	Peak Efficiency	Type
R300B	4405	3600 - 7200	4.96	360	70%	Grism
R300R	6635	4800 - 10000	7.74	348	70%	Grism
R500B	4745	3600 - 7200	3.54	537	68%	Grism
R500R	7165	4800 - 10000	4.88	587	67%	Grism
R1000B	5455	3630 - 7500	2.12	1018	65%	Grism
R1000R	7430	5100 - 10000	2.62	1122	65%	Grism
R2000B	4755	3950 - 5700	0.86	2165	87%	VPH
R2500U	3975	3440 - 4610	0.62	2555	70%	VPH
R2500V	5185	4500 - 6000	0.80	2515	80%	VPH
R2500R	6560	5575 - 7685	1.04	2475	80%	VPH
R2500I	8650	7330 - 10000	1.36	2503	80%	VPH
Magellan Telescope						
VPH-ALL	7100	4250-10000	1.890	860	30%	VPH
VPH-Blue	5000	3800-6200	0.682	1900	31%	VPH
VPH-Red	8000	6000-10000	1.175	1810	35%	VPH

noise, it ensures high-quality data. Accurate calibration and proper setup are crucial for leveraging its advanced capabilities.

The OSIRIS instrument employs a detector with two Marconi CCD 44-82 chips, each with 2048 x 4096 pixels. These pixels are physically 15 µm in size, equating to a 0.127" sky scale, although 0.254" binned pixels are typically used. The CCD control system supports various readout modes and gain settings, with standard observing modes for Imaging and Spectroscopy ensuring linearity up to 16 bits. The acquisition mode, used for test images, has higher noise and limited linearity. For main observing modes, specific reference positions on the CCD are used to place targets, avoiding detector blemishes. The positions are provided by the Principal Investigator in the Phase-2 stage that defines the observing strategy. Different modes like Broad Band Imaging, Long Slit Spectroscopy, Tunable Filter Imaging, and Multi-Object Spectroscopy have their own standard pointing positions, chosen to optimize field of view, minimize cosmetic effects, and ensure proper alignment and centering of the target.

OSIRIS offers longslit spectroscopic observations with a variety of slit of 7.4' in the spatial direction and with widths ranging from 0.4" to 10" and a wide variety of grisms and volume-phased holographic gratings (VPHs) covering low to intermediate resolutions, from R=300 up to R=2500[2]. The resolutions and spectral ranges vary, with dispersions measured for binned pixels in standard operation mode. Table 4.3 summarises the resolutions and spectral ranges available.

[2] R is the energy resolution defined as $\Delta\lambda/\lambda$, where $\Delta\lambda$ represents the smallest difference in wavelengths that can be distinctly detected at a wavelength λ.

4.2.2 Magellan Clay telescope

The Magellan Telescopes, including the Magellan Clay Telescope, are a pair of 6.5-meter optical telescopes located at the Las Campanas Observatory in Chile (see Fig. 4.6). Named after the astronomer Walter Baade and the philanthropist Landon T. Clay, these telescopes are operated by a consortium of institutions such as the Carnegie Institution for Science, University of Arizona, Harvard University, the University of Michigan, and the Massachusetts Institute of Technology. The first light for the Clay telescope was on September 7, 2002.

One of the key features of the Magellan Clay Telescope is its adaptive optics system. This system employs flexible secondary mirrors that can change shape to compensate for distortions caused by the Earth's atmosphere, allowing the telescope to produce extremely clear and sharp images. The high elevation of Las Campanas Observatory (over 2,500 meters) and the dry conditions of the Atacama Desert contribute to more than 300 clear nights per year, making it an ideal location for astronomical observations.

The telescope is equipped with a variety of instruments including the **Magellan Inamori Kyocera Echelle** (MIKE) spectrograph, **Low-Dispersion Survey Spectrograph-3** (LDSS-3), **Megacam imager, MagAO** adaptive optics system, and the **Michigan/Magellan Fiber System** (M2FS). These instruments allow for a wide range of astronomical studies, from the Solar System to distant galaxies. For example, the Magellan Planet Search program uses the MIKE instrument on the Clay telescope to search for exoplanets.

The Clay telescope also boasts the MagAO Adaptive Optics System, introduced in 2013. MagAO includes an adaptive secondary mirror that enables it to take some of the sharpest visible-light images ever achieved by a ground-based telescope. This system can resolve objects as small as 0.02 arcseconds across, which is quite remarkable for earthbound telescopic observations. As we did in the previous section, here we will only delve into the LDSS-3 instrument, as it was used in our analysis.

Low-Dispersion Survey Spectrograph-3 (LDSS-3)

The LDSS-3 is a high-efficiency spectrograph and optical imager located at the Nasmyth West port of the Magellan Clay telescope. It stands out for its ability to perform sky subtraction, enabling it to observe very faint celestial objects effectively. The instrument design features a wide field of view and multi-object observational capability, making it ideal for statistical astronomical studies. In operation, LDSS-3 focuses the telescope onto a multi-aperture mask in an 8-position wheel. Light passes through the apertures into a collimator that converts it into parallel beams, then through a filter and/or grism, and is finally focused by the camera onto an external detector at an f/2.5 focal ratio. The instrument includes removable Hartmann masks for focusing, can accommodate three grisms for varying spectral resolutions, and holds up to seven filters at once.

LDSS-3 operates in three primary modes: *imaging mode* with SDSS griz filters and additional bandpass filters, *long-slit* and multi-object spectroscopy, and a *nod and shuffle* mode for improved

sky subtraction. The grisms offer variable wavelength coverage, and various long-slit masks are available in different configurations to accommodate different observational needs. These include 4' long slits of different widths (0.75", 1.00", 1.25", 1.5") as well as masks with several 16" long slits of various widths (2.15", 1.4", 0.85", 0.5", 0.65", 1.10", 1.75"). The instrument detailed features, including its diverse range of capabilities, are outlined in Table 4.3.

4.2.3 Very Large Telescope

The **Very Large Telescope** (VLT), operated by the European Southern Observatory (ESO), stands as one of the most advanced astronomical observatories globally. Situated at the Paranal Observatory in the Atacama Desert of Chile, it benefits from some of the clearest and darkest skies on Earth, ideal for astronomical observations.

The VLT is composed of four Unit Telescopes (UTs) – **Antu**, **Kueyen**, **Melipal**, and **Yepun** – each featuring a primary mirror 8.2 meters in diameter (four telescopes are shown in Fig 4.6). These telescopes are complemented by a set of smaller, movable Auxiliary Telescopes (ATs), each 1.8 meters in diameter, integral to the VLT Interferometer (VLTI). This configuration allows the telescopes to operate either independently or in concert, achieving the angular resolution of a telescope up to 200 meters in diameter when used in interferometry mode. Each of the VLT's four telescopes, named in the Mapuche language, has its unique set of instruments and capabilities:

- **UT1 Antu** (The Sun): Commissioned on May 25, 1998, Antu is notable for hosting the *FORS2* among other instruments, a versatile optical instrument functioning in the 330-1100 nm range, capable of both imaging and spectroscopy. It offers a variety of filters, two magnifications, and features for polarimetry and long-slit spectroscopy.

- **UT2 Kueyen** (The Moon): Operational since March 1, 1999, Kueyen's arsenal includes *X-shooter*, which covers a broad spectrum from ultraviolet to near-infrared, and *UVES* (Ultraviolet and Visual Echelle Spectrograph) for high-resolution studies in visible and near-ultraviolet wavelengths.

- **UT3 Melipal** (The Southern Cross): Operating since April 1 1999, across a wide range of wavelengths, Melipal is equipped with SPHERE for direct imaging and study of exoplanets and *VISIR* for mid-infrared imaging and spectroscopy, useful in diverse areas like star formation and galactic centers.

- **UT4 Yepun** (Venus): Achieving first light on September 4, 2000, Yepun houses *HAWK-I*, a high-resolution near-infrared camera, and MUSE, a 3D spectrograph that allows comprehensive observations of astronomical objects.

The VLT employs adaptive optics technologies, such as the Multi-conjugate *Adaptive optics Demonstrator* (MAD) and the *Nasmyth Adaptive Optics System* (NAOS), to correct for atmospheric blurring. This system uses flexible mirrors and real-time computer control to sharpen images significantly, enhancing the telescopes observational capabilities.

4.3.0 Spectral analysis

In this thesis, considerable spectral analysis has been conducted using the X-ray spectral fitting program XSPEC (Arnaud 1996), developed by Keith Arnaud. It is thus important to discuss the functionality and application of this software in the context of our research.

XSPEC operates by initially importing the source spectrum, background data, detector response matrix, and effective area files. These are typically prepared using the specific telescope cookbook. Data can be regrouped as needed, grouping channels or counts per bin, or employing an optimal binning dependent on the energy. The key point to note is that the spectrum we obtain is not the actual spectrum but rather the total photon counts detected in each channel. This observed spectrum is connected to the actual spectrum S(E), through a relationship involving the exposure time T, the instrumental response matrix RMF(PI,E), and the telescope and detector effective area ARF(E):

$$C(PI) = T \int RMF(PI, E) \cdot ARF(E) \cdot S(E)\, dE. \tag{4.1}$$

What XSPEC does is to use a **forward-folding approach**. This method involves assuming a physical model for S(E), convolving it with the instrument response files, and then comparing the result with the observed counts. A fit statistic is calculated to determine how well the model matches the actual data.

Our aim is to align theoretical models with observed data and seek a statistically acceptable fit. This involves adjusting the initial parameters to minimize the discrepancy between the model predictions and the observed data, often using chi-square minimization or other maximum likelihood techniques. Our goal is to grasp the source physical behavior and refine the spectral model to closely match reality while maintaining physically meaningful parameter values.

To assess the model accuracy, we employ statistical tests like **chi-square** (χ^2), defined as the sum of the squared differences between the observed $C_{\rm data}$ and model-predicted $C_{\rm model}$ counts per energy bin, normalized by the (Gaussian) error in each bin:

$$\chi^2 = \sum \left(\frac{C_{\rm data} - C_{\rm model}}{\sigma} \right)^2 \tag{4.2}$$

A good fit is indicated by a reduced chi-square (χ^2/d.o.f.), where d.o.f. represents the **degrees of freedom**, is approximately 1. If this value significantly exceeds 1, the model might be inadequate. Conversely, a value lower than 1 might suggest data overestimation errors or an over-parameterised model relative to the data quality. This is evaluated by computing the probability to obtain a chi-square as large as or larger than the observed value under the assumption that the model is correct. This p-value is a crucial statistical tool: a high p-value, indicates that the observed and expected distributions are consistent; if it is small, they are probably in disagreement. In particular, if p-value is less than 5%, indicates a statistically significant deviation, leading us to reject the hypothesized distribution at the 5% significance level. If it is less than 1%, the

disagreement is called highly significant, and we reject the assumed distribution at the 1% level.

An X-ray spectrum is typically characterized by various components, and distinct models are employed to fit each of these components. In general, the spectrum is constructed from a combination of **additive** and **multiplicative** models. An additive model is used to describe a component of the spectrum that contributes additional flux to the total observed spectrum. An expample is a blackbody model, a power-law or a Gaussian line model. A multiplicative model modifies the shape of the spectrum by applying a factor that changes the flux at each energy bin, rather than adding new components to the spectrum. These models are typically used to account for processes that affect the entire spectrum, such as an absorption edge.

Another category of spectral models are **convolutive** models. The are used to modify the spectrum in a way that depends on the spectral shape itself. Unlike additive models that add spectral components or multiplicative models that scale the spectrum, convolutive models apply a transformation that is a function of the spectrum. Convolutive models are often used to represent physical processes that scatter photons into or out of the line of sight, changing the energies of the photons in the process. They effectively "convolve" the original spectrum with a kernel or function that represents the physical scattering or redistribution process. Examples are the reflection model RFXCONV, the relativistic smearing model RDBLUR or the partial covering model PARTCOV.

In the upcoming Chapters, we delve into the works presented in this thesis.

5

Spectral analysis of the low-mass X-ray Pulsar 4U 1822-371: a reflection component in a high inclination system

Summary

The X-ray source 4U 1822-371 is an eclipsing low mass X-ray binary and X-ray pulsar, hosting a neutron star which shows periodic pulsations in the X-ray band with a period of 0.59 s. The inclination angle of the system is so high (80-85 degrees) that it should be hard to observe both the direct thermal emission of the central object and the reflection component of the spectrum, because hidden by the outer edge of the accretion disc. Despite the number of studies carried out on this source, many aspects like the geometry of the system, its luminosity and its spectral features are still debated. The analysis aims to investigate on the presence of a reflection component, never observed before in a high inclination ADC source such as 4U 1822-371. I found significant evidences of the presence of a reflection component in the spectrum, besides two narrow (Gaussian) lines at 6.4 and 7.1 keV associated with neutral (or mildly ionised) iron, Fe Kα and Kβ transitions, respectively. The continuum spectrum is well fitted by a saturated Comptonisation model with an electron temperature of 4.9 keV and a thermal, blackbody-like component, possibly emitted by the accretion disc, at lower temperature. I identify emission lines from O VIII, Ne IX, Mg XI and Si XIV. I also added two new eclipse times related to a *NuSTAR* and *Swift* observations to the most recent ephemeris reported in the literature, thus updating the ephemeris. I proposed a new scenario of the geometry of the system: 4U 1822-371 is accreting at the Eddington limit with an intrinsic luminosity of $\sim 10^{38}$ erg s^{-1}, while the observed luminosity is two orders of magnitude lower because of the high inclination angle of the system.

The work presented in this chapter was published under the title "**Spectral analysis of the low-mass X-ray Pulsar 4U 1822-371: a reflection component in a high inclination system**" in Astronomy & Astrophysics,Volume 654, A160, 2021 (https://doi.org/10.1051/0004-6361/202140557).

5.1.0 The puzzling ADC source

As discussed in section 2.11, highly magnetized NSs in LXMBs possess the capability to channel matter from the inner regions of the disc towards their poles, leading to pulsations observable in the X-ray spectrum. The source analysed in this chapter is an exemplary case of such a phenomenon - an X-ray pulsar. Specifically, 4U 1822-371 is an eclipsing LMXB system discovered in (Griffiths et al. 1978) with an orbital period of 5.57h, hosting a neutron star NS which shows periodic pulsations in the X-ray band (Iaria et al. 2013a) with a period of 0.59 s .

As estimated by Mason & Cordova (1982) using infrared observations, the inclination angle with respect to our line of sight lies in the range 76 - 84 degrees. Such a high inclination angle implies that the direct emission from the innermost region should be shaded by the swelling in the external region of the accretion disc, caused by the inflowing matter transferred by the secondary star and impacting the outer disc. This source, in fact, is considered the prototype of the accretion disc Corona sources, i.e. as said in Chapter 3, a particular system geometry where most of the observed radiation emitted by the accretion flow is scattered by a sandwich Corona around the disc (Shakura & Sunyaev 1973b). Another interesting feature of 4U 1822-371 is its activity as X-ray pulsator. Analysing RXTE data, Jonker & van der Klis (2001) discovered coherent X-ray pulsations at $\sim$ 0.59 s and inferred a pulse period derivative of (-2.85 $\pm$ 0.04) $\times$ 10^{-12} s s^{-1}, indicating a spin-up of the neutron star. Taking into account the observed luminosity of 10^{36} erg s^{-1}, estimated by Mason & Cordova (1982) for a distance of the source of 2.5 kpc, they also calculated the strength of the NS magnetic field; using the relation of Ghosh & Lamb (1979b), linking the luminosity and the spin-up rate, they found an extremely high value of 8 $\times$ 10^{16} G for the magnetic field, suggesting a possible underestimation of the luminosity.

Burderi et al. (2010) studied the orbital evolution of the system, refining the orbital ephemeris of the source and concluding that the orbital period increases at a rate of $\dot{P}_{orb} = 1.50(7) \times 10^{-10}$ s s^{-1} (see also Parmar et al. 2000). Such a high orbital period derivative cannot be explained by a conservative mass transfer at the accretion rate inferred from the observed source luminosity. According to these authors, a highly non conservative mass transfer is required, at a rate up to seven times the Eddington limit for a NS with a mass of 1.4 $M_\odot$ (see e.g. Burderi et al. 2010; Bayless et al. 2010; Iaria et al. 2011; Mazzola et al. 2019), indicating that a large part of the matter pulled off by the companion star is ejected from the system. The luminosity produced by this accretion process is about 10^{38} erg s^{-1}, in contrast to the luminosity reported by Mason & Cordova (1982), but the magnetic field strength inferred with this luminosity implies a more reasonable value of 8 $\times$ 10^{10} G (see also Jonker & van der Klis 2001).

The best model of the X-ray spectrum is still debated; the main observed spectral component is a Comptonisation spectrum, which is the result of the inverse Compton scattering of soft thermal photons, emitted by the compact object surface or by the accretion disc, off the hot electrons that form the innermost part of the Corona around the NS. Hellier & Mason (1989) fitted an EXOSAT spectrum of 4U 1822-371 using a power law and a blackbody component (peaked at 1.8-2.0 keV) in addition to an iron line, measuring an apparent radius for the region of

the blackbody emission of about 0.25 km, i.e. much smaller than the neutron star radius.

More recently, Iaria et al. (2013a) performed an orbital phase-dependent spectral analysis of *Chandra* and *XMM-Newton* observations of 4U 1822-371, fitting the spectrum with a blackbody, at the temperature of 0.061 keV, and a Comptonised component characterized by an electron temperature of 3.01 keV and emitted by an optically thick (inner) corona having an optical depth of τ = 19.1. Both these components are partially absorbed by local neutral matter and interstellar medium. Several emission lines are observed at low energies, probably emitted by plasma in the bulge at the outermost region of the disc, in addition to two narrow fluorescence iron lines associated with the Fe XXV and Fe XXVI, produced in the innermost regions. The authors proposed that the partial covering component observed in the source spectra may be ascribed to local neutral matter present around the system that cannot accrete onto the NS since it is emitting at the Eddington limit. They also ascribed the observed low luminosity of 10^{36} erg s^{-1} to the high inclination of the source; the presence of an extended, optically thin corona (τ = 0.01) that scatters a small fraction of the inner emission along the line of sight may explain why such a low luminosity is derived for this source.

In this work I investigate the geometry of the system through a spectral analysis of X-ray data collected from not-simultaneous *XMM-Newton* and *NuSTAR* observations, taking advantage from the large effective area in a broad energy range and moderately good energy resolution at the iron-line energy. I find that the iron line may indeed be a blending of lines from iron in different ionisation states. Also, the large width of one of these line components and the presence of a Compton hump at high energies suggest the presence of reflection, which could represent the first evidence of a reflection component for a high inclination system such as 4U 1822-371.

5.2.0 Observations and data extraction

4U 1822-371 was observed by the *XMM-Newton* observatory in 2017 March 3rd between 01:10:54 UTC and 19:12:27 UTC (ObsId. 0784820101) for a duration of 69 ks. During this observation, the EPIC-pn and MOS2 cameras were operated in timing mode with a medium filter, while the MOS1 camera was set in small window mode with a thick filter. The timing mode is useful to avoid photon pile-up, avoiding loss in photon counts as well as a hardening of the spectrum. I verified MOS 1 was affected by pile-up, since the camera was operated in imaging mode during the observation, and I found an incompatibility between data collected by the Epic-pn and the MOS 2, below 3 keV due to detector instrumental features. For these reasons, and since Epic-pn has a greater effective area than the MOS cameras in the same energy range, for our analysis I preferred to use the Epic-pn data. To get a better coverage of the spectrum at the lower energies I also used data collected by the two RGS cameras, which provide a high-energy resolution in the range between 0.35 keV and 2.5 keV.

I reduced the *XMM-Newton* data using the Science Analysis Software (SAS) v17.0.0. I first extracted the images from the event files to select the region from which events are collected: as regard the EPIC-pn data I selected the columns in the interval $26 < RAWX < 47$ for the source

and $3 < RAWX < 5$ for the background, respectively. For the RGS background I selected a region in the CCD9, where generally the background is dominating, because it is located close to the optical axis and records fewer source photons. I accumulated the EPIC-pn 0.3-10 keV light curve, with a bin time of 100 seconds, considering $PATTERN <= 4$, to extract only single and double good events, and $FLAG = 0$, to avoid events from the pixels at the edges of the CCD.

In the light curve of the source I found three partial eclipses, separated by a period of about 20 ks; in order to exclude from the average spectrum, the time intervals during which the luminosity is reduced, I created a set of Good Time Intervals (GTI) to exclude the eclipses from the following spectral analysis. I eventually extracted source and background spectra and combined the RGS1 and RGS2 spectra, 1st and 2nd order.

The *NuSTAR* observation was performed between 2018 April 25th 14:26:09 and April 27th, 07:10:26 (ObsID 30301009002) for a total exposure time of 29 ks. I used the NUPIPELINE and NUPRODUCTS scripts within HEASOFT to obtain the average spectra: for both the source and background of FPMA and FPMB, I selected a circular region with a radius of 30 arcsec. As done for EPIC-pn data, I produced light curves and created the GTI files, after which I extracted the source and background (out-of-eclipse) average spectra, the ancillary files and the response matrices for each of the two *NuSTAR* telescopes. I rebinned these spectra in order to have a minimum of 30 counts per bin. The *NuSTAR* spectra provide a better coverage of the spectrum at high energies: this feature makes *NuSTAR* a perfect complement for our work, because, together with the low energy coverage provided by *XMM-Newton*, it allows analysing in detail all the main features (discrete features as well as the continuum) that characterise a reflection spectrum emitted by X-ray Binaries.

5.3.0 Timing analysis

The *NuSTAR* ObsID 30301009002 represents the most recent observation of 4U 1822-371 and, as explained in the previous section, the extracted light curve shows an eclipse that has never been used to perform an analysis aimed at studying the orbital parameters of the system. Eclipses occur when the companion star moves in front of the accretion disc, blocking the line of sight from the observer. They happen once in each orbital cycle, thus helping constraining the orbital period. In systems with high but non-eclipsing inclinations, usually i<75 degrees, X-ray light curves often show dips. These are typically caused by the central X-ray source being obscured by neutral or slightly ionised material in the outer accretion disc (White & Mason 1985). For this reason I performed a timing analysis in order to investigate if it is possible to extend the most recent orbital ephemeris of the system, reported by Mazzola et al. (2019), and improve the accuracy of the orbital parameters. I applied the barycentric correction to the event file, extracted as discuss in section 5.2, using the Ftool BARYCORR. I folded the light curve extracted over the entire energy range from the two *NuSTAR* cameras, FPMA and FPMB, using as reference time T_{fold} = 50353.08728 MJD and a trial orbital period of P_{fold} = 0.232109571 days (Mazzola et al. 2019). The eclipse arrival time was evaluated by using the method described by Burderi et al.

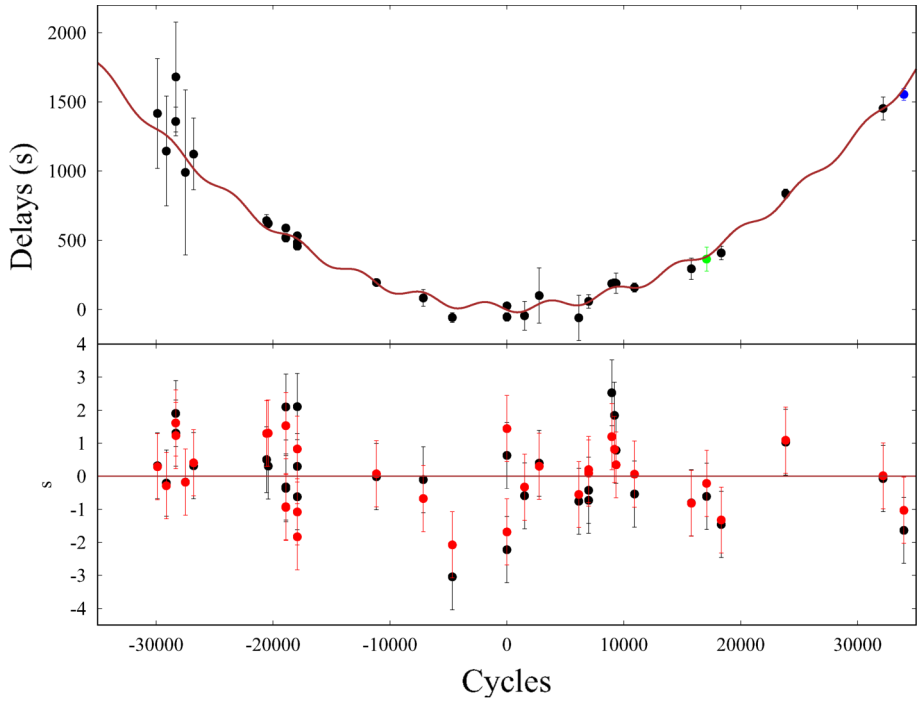

Figure 5.1: **Top panel:** Delays of the eclipse arrival times as a function of the orbital cycle for the LQS model. **Bottom panel:** Residuals in units of σ, obtained with the cubic (black) and LQS (red) model, respectively.

Table 5.1: In the top table, the eclipse arrival times are listed, and in the bottom table, the best-fit values for the parameters derived with the different models described in the text (quadratic, cubic, and LQS) are shown.

Eclipse time	Cycles	Delays (s)	Satellite
54317.0587(10)	17078	364(87)	Swift
58234.1536(5)	33954	1554(43)	NuSTAR

Parameter	Quadratic	Cubic	LQS
a (s)	12 ± 12	-3 ± 12	13 ± 11
b (10^{-4} s)	-11 ± 5	19 ± 12	-5 ± 6
c (10^{-6} s)	1.42 ± 0.04	1.51 ± 0.05	1.41 ± 0.04
d (10^{-12} s)	-	-6 ± 2	-
A (s)	-	-	34 ± 11
N_{Mod} (10^{-3})	-	-	5.4 ± 0.1
N0 (10^{-3})	-	-	-3.1 ± 0.3
P_{Mod} (years)	-	-	3.43 ± 0.07
T_0 (TJD)	50353.08741(14)	50353.08725(14)	50353.08744(13)
P_0 (days)	0.232109559(6)	0.232109593(14)	0.232109565(7)
$\dot{P}$ (10^{-10} s s^{-1})	1.42(3)	1.51(5)	1.41(4)
$\ddot{P}$ (10^{-19}s s^{-2})	-	-0.94(35)	-
χ^2(dof)	47.43(31)	38.21(30)	34.30(28)

(2010), finding a value of T_{ecl} = 58234.1536(5) MJD/TDB.

I extended the ephemeris of the source with a further eclipse arrival time extracted from a *Swift* observation performed between 2007-08-03 01:20:01 and 2007-08-05 21:07:22 (ObsID 00036691002 and 00036691003). Using the same method adopted for the *NuSTAR* observation I find an arrival time of T_{ecl} = 54317.0587(10) MJD/TDB.

The inferred delays of the eclipse arrival times with respect to the adopted ephemeris and the corresponding number of orbital cycles, are reported in Table 5.1. I fitted the delays as a function of the cycles using three different models. I first modelled the data with the quadratic function $y = a + bN + cN^2$, where the parameters a and b represent the correction to the value of the eclipse time (ΔT_{ecl}) and the orbital period ($\Delta P/P_0$), respectively, while the term c describes the variation of the orbital period and allow us to determine its derivative ($P_0/2\dot{P}$). I obtained a χ^2 $(d.o.f.)$ = 47.43(31) and a $\dot{P}$ = 1.42(3) $\times 10^{-10}$ s/s, the results are reported in Table 5.1.

To improve the fit I added to the previous model a cubic term ($y = a + bN + cN^2 + dN^3$), where the new coefficient describes the orbital period second derivative ($P_0^2\ddot{P}_{orb}/6$). The model improves the fit achieving a χ^2 (d.o.f.) = 38.21(30), and allows to infer a $\dot{P}$ = 1.51(5) $\times$ 10^{-10} s/s and $\ddot{P}$ = -0.94(35) $\times$ 10^{-19} s/s^2 in line with previous results (Mazzola et al. 2019). I tested the improvement of the fit with an F-test, comparing the quadratic and cubic models, obtaining a probability of chance improvement of about 0.01, indicating that the addition of the cubic term is significant at 99% confidence level. Adopting the cubic ephemeris, I updated the orbital ephemeris of the source as:

$$T_{ecl} = 50353.08725(14)MJD/TDB + 0.232109593(14)N$$
$$+1.752(29) \times 10^{-11}N^2 - 8.44(52) \times 10^{-22}N^3 \ .$$

Mazzola et al. (2019) inferred the possible presence of a sinusoidal modulation of the delays; to investigate it I used a model composed by a quadratic and sinusoidal function, $LQS = a + bN + cN^2 + Asin[2\pi(N - N_0)/N_{mod}]$, where A is the semi amplitude of the modulation. The best fit parameters are reported in the third column of table 5.1, while in Figure 5.1 the residuals of the cubic and LQS model are compared. I obtained a χ^2 $(d.o.f.)$ = 34.30(28) and an F-test probability of chance improvement of about 0.03 with respect to the quadratic model, meaning that the sinusoidal modulation improves the fit at the 97% confidence level. The origin of this modulation is still debated and may be associated with the gravitational quadrupole coupling (GQC) mechanism via tidal interaction or with the presence of a third body in the system (Mazzola et al. 2019). Future observations may allow us to further extend the ephemeris, confirming or disproving this modulation, and possibly explaining its origin.

5.4.0 Spectral Analysis

I initially fitted the data from the two not-simultaneous observations separately in order to understand in detail their spectral features and whether the two dataset were compatible with each other. I have decided to consider the energy range 4 - 45 keV for the *NuSTAR* spectrum

and 0.6 - 10 keV for the *XMM-Newton* one. I dropped the *NuSTAR* data above 45 keV and below 4 keV, because at higher energies the background spectrum overcomes the source and at lower energies the spectrum is contaminated by a flux excess in FPMA camera (Madsen et al. 2020). For *XMM-Newton* I considered the RGS data only between 0.6 - 2 keV, because above this threshold the instrument is not well calibrated and below some systematic features are expected, i.e. at the Oxygen edge, in addition, I ignored EPIC-pn data under 2 keV, due to some systematic features at 1.8 keV (caused by an instrumental Si edge).

5.4.1 Comparison with previous spectral decomposition

I initially used the model proposed by Iaria et al. (2013a), which presents the most recent spectral analysis of 4U 1822-371 in the literature to date, with the aim to test if a model without a reflection component can adequately describe our spectra. The model comprises of a Comptonised component (CompTT in XSPEC) partially absorbed by neutral local matter and absorbed by the interstellar medium. In this case, I assumed the same abundance (Asplund et al. 2009) and the same cross-section (Verner et al. 1996) chosen by the authors of the aforementioned paper, with the aim to compare our results to those available in the literature. For both datasets, I have taken into account possible inter-calibration issues, by including a constant multiplicative component, fixed to 1 for Epic-pn and for the *NuSTAR* FPMA camera, and kept free to vary for the other instruments (note that the *RGS* parameters are linked to the *pn* ones while the *FPMB* parameters are linked to the *FPMA* ones). The contribution of the interstellar photoelectric absorption is modelled by the PHABS component, while to take into account the partial photo-electric absorption due to local matter I used the model *phabs∗[c∗cabs∗phabs∗(CompTT)+(1-c)∗CompTT]*. The first term within brackets represents the partially absorbed Comptonisation spectrum, where C is a constant limited between 0 and 1, that expresses the partial covering fraction. The second PHABS component is the photo-absorption due to local matter, while CABS, which takes into account the effect of Thomson scattering, is linked to the second PHABS, under the assumption that the local matter is the main responsible of this effect.

To get a constraint on photoelectric absorption, I firstly fit EPIC-pn and RGS data together, taking advantage of the good spectral coverage of the RGS at low energies, where the effect of photoelectric absorption is more relevant. I used the same strategy to constrain the partial photo-absorption by the local matter in the system. Since 4U 1822-371 has always shown a steady behaviour with little spectral variations (Iaria et al. 2024, 2013b), I do not expect a great difference between the parameters of the model of the two observations, although they were taken one year apart. After a first attempt, I noticed the presence of several emission features in both the *XMM-Newton* and *NuSTAR* spectra, so that to improve the fit I added three Gaussian lines at energies of 6.49 keV, 6.67 keV and 7.1 keV, attributable to Fe I Kα, Fe XXV and Fe I Kβ emission, respectively. In the *NuSTAR* spectrum, the Kα emission lines are less distinguishable and the energy of the one at 7.1 keV was fixed during the fit due to a tendency to overlap with the other Gaussian profiles. I also improved the model by adding four emission lines at lower energies to fit localized features in the *XMM-Newton* band, at 0.65 keV, 0.916, keV 1.346 keV

and 2.002 keV, , respectively. The centroids of the Gaussian components are in lines with the ones reported by (Iaria et al. 2013a), and I associate them to transitions of O VII, Ne IX, Mg XI, and Si XIV ions, respectively.

The best-fit values obtained for the model parameters are shown and compared to the one reported by Iaria et al. (2013a) in table 5.2. Only some of the values found for the *XMM-Newton* spectra are consistent within the errors to the ones previously reported, like the electron temperature of the plasma kT_e, while particular the equivalent hydrogen column density of the interstellar photoelectric absorption and the soft seed-photons temperature kT_0 show deviations from previous results. From the fit of the *NuSTAR* data, most of the parameters slightly deviate from the ones found in the aforementioned paper; besides the parameters related to the components PHABS and CABS (linked to the previous fit), the temperature of the electron cloud and seed photons reaches significantly higher values than what is found by Iaria et al. (2013a) and for the *XMM-Newton* spectrum. The best fit normalization value of the Gaussian at 7.1 keV, which is 18% of the one found for the Fe I emission line, as well as its centroid energy, are in agreement with the association of this line with the Fe I K_β transition. From Fig. 5.2 it is evident that the *NuSTAR* spectrum shows peculiar residuals in the iron emission region and from 10 to 40 keV. It is possible that the mismatch between the model and the data stands to indicate that the spectrum needs a reflection continuum component, since the latter residuals can be attributable to the Compton reflection hump, that is a typical signature of a reflection component.

5.4.2 Testing for the presence of a reflection component

To test the possible presence of a reflection component, I tried two different models: in MODEL 1, I used the self-consistent model RFXCONV, while in MODEL 2 the reflection is described by the combination of DISKLINE and PEXRIV models. I initially modified the previous model by replacing COMPTT with another Comptonisation model (NTHCOMP), substituting the PHABS model with TBABS, i.e the Tuebingen-Boulder ISM absorption model, setting the most updated ISM abundance and cross-section (see Wilms et al. 2000; Verner et al. 1996). I decided to analyse simultaneously the *XMM-Newton* and *NuSTAR* spectra, because the *Epic-pn* and *NuSTAR* data overlap in the Iron emission-line region, guaranteeing a better statistics. Moreover merging the low energies range of *XMM-Newton* and the higher one of *NuSTAR*, I can analyse all the reflection spectral features (since the Compton hump is visible only in the *NuSTAR* spectrum because the *Epic-pn* one is limited to 10 keV). Nevertheless, I left the continuum parameters free to vary among the two spectra, constraining only the inner disc radius, the ionisation parameter, and the inclination angle to be the same. This is because, leaving free the ionisation parameter, the best fit gives compatible values for the two spectra. Also, I do not expect changes in the inner disc radius since the accretion rate in this source is quite stable over the years. I improved the fit by removing the partial covering component and introducing a soft blackbody (BBODY in Xspec) with temperature $kT_{bb} = 0.2$ keV; I also added the reflection model, which is used to replace the broad Gaussian line at 6.7 keV, and kept the two Gaussian emission lines related to Fe I K_α and K_β, respectively. As done before, the inter-calibration constant was set to 1 for

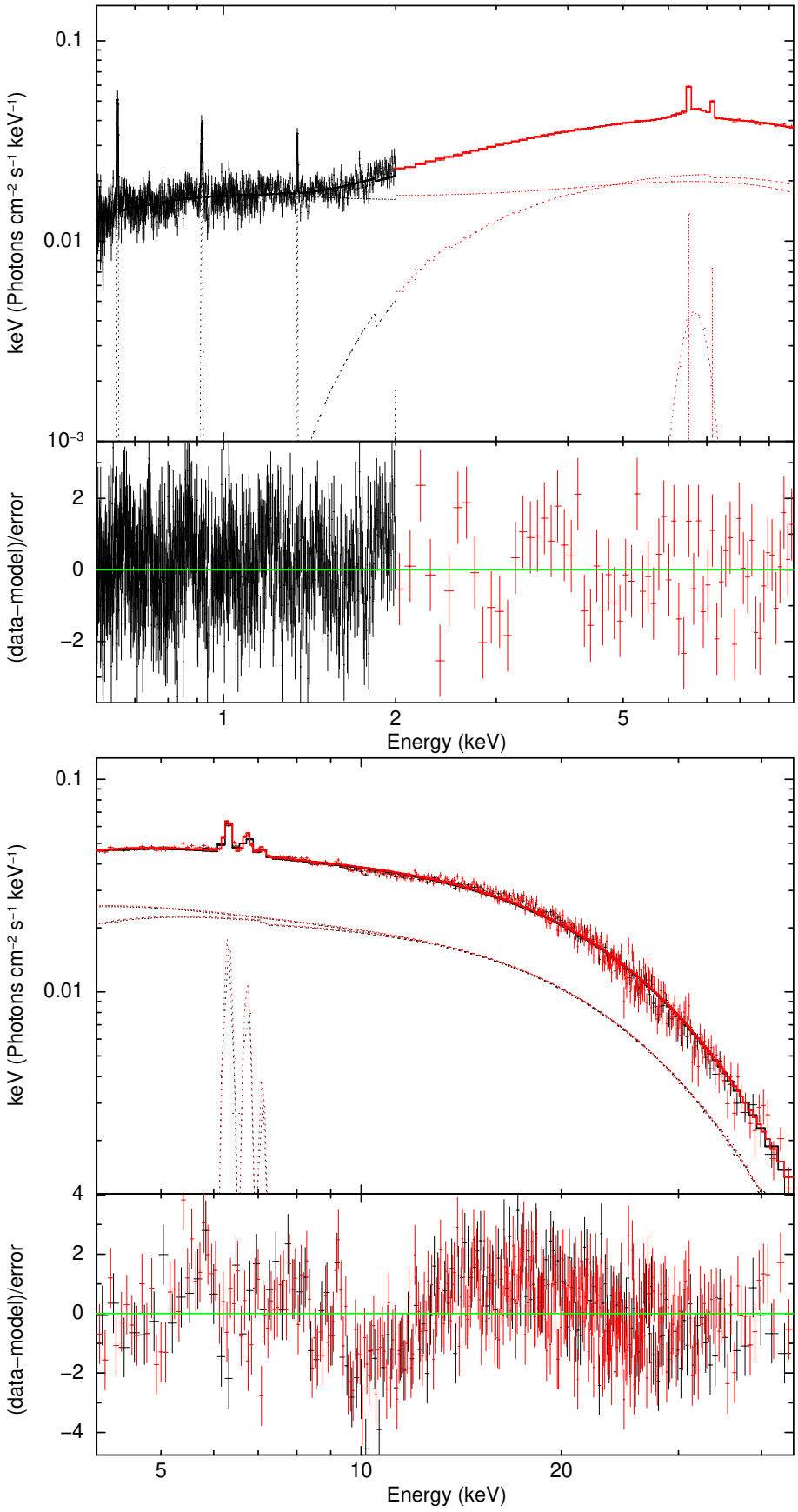

Figure 5.2: Spectra and residuals in units of sigma with respect to the Model: CONSTANT*PHABS [C*CABS*PHABS*(COMPTT)+(1-C)COMPTT + 7 GAUSSIAN LINES] for the *XMM-Newton* spectrum (top panel) and *NuSTAR* spectrum (bottom panel), respectively. Data were rebinned for visual purposes only.

Table 5.2: Comparison of best-fit values for the parameters of the model described in the text, with those found by Iaria et al. (2013a).

Parameter	XMM*	NuSTAR*	I-2013
$N_{H_{phabs}}$ (10^{22} cm^{-2})	$0.010^{+0.003}_{-0.003}$	0.01†	$0.163^{+0.008}_{-0.006}$
$N_{H_{pcf}}$ (10^{22} cm^{-2})	$4.02^{+0.05}_{-0.08}$	4.02†	4.97 ± 0.12
c	$0.538^{+0.002}_{-0.003}$	0.54†	0.607 ± 0.009
kT_0 (keV)	$0.199^{+0.002}_{-0.003}$	0.85 ± 0.02	0.061 ± 0.003
kT_e (keV)	$3.089^{+0.008}_{-0.013}$	5.05 ± 0.03	3.05 ± 0.04
τ	$22.92^{+0.04}_{-0.06}$	12.9± 0.1	21.0 ± 0.4
N_{Cp} (10^{-2})	$5.00^{+0.007}_{-0.008}$	2.91 ± 0.04	7.7 ± 0.2
E_{Line} (keV)	6.48 ± 0.01	6.31 ± 0.03	6.402 ± 0.004
σ (keV)	< 0.006	0.075†	0.075 ± 8
N (10^{-4})	$2.6^{+0.2}_{-0.1}$	5.9 ± 0.5	3.24 ± 0.13
E_{Line}(keV)	6.65 ± 0.03	6.74 ± 0.05	6.703 ± 0.013
σ (keV)	$0.37^{+0.02}_{-0.03}$	0.0755†	0.025†
N (10^{-4})	$5.9^{+0.3}_{-0.4}$	3.3 ± 0.5	0.70 ± 0.08
E_{Line} (keV)	$7.10^{+0.02}_{-0.01}$	7.1	6.991 ± 0.009
σ (keV)	< 0.05	0.075†	$0.056^{+0.008}_{-0.016}$
N (10^{-4})	1.3 ± 0.2	$1.1^{+0.4}_{-0.6}$	$1.38^{+0.11}_{-0.06}$
E_{Line}	$0.6535^{+0.0003}_{-0.0002}$	-	$0.651794^{+0.000336}_{-0.000004}$
σ (keV)	$0.0009^{+0.0004}_{-0.0003}$	-	< 0.0007
N(10^{-4})	1.6 ± 0.2	-	3.6 ± 0.4
E_{Line}	0.916 ± 0.001	-	0.914 ±0.001
σ (keV)	$0.002^{+0.0008}_{-0.0011}$	-	0.004 ± 0.001
N(10^{-4})	$1.4^{+0.3}_{-0.2}$	-	3.8 ± 0.3
E_{Line}	$1.346^{+0.003}_{-0.002}$	-	1.343†
σ (keV)	< 0.004	-	0.003†
N(10^{-4})	0.7 ± 0.2	-	0.6 ±0.2
E_{Line}	2.002†	-	$1.984^{+0.01}_{-0.006}$
σ (keV)	0.004†	-	0.004†
N(10^{-4})	< 0.4	-	1.5 ±0.15
$\chi^2_{red}(dof)$	1.16(1544)	1.31(1379)	1.06(2400)

† We decide to keep frozen these parameters to the values found for the XMM-newton spectrum.

* Model: CONSTANT*PHABS(C*CABS*PHABS*(COMPTT) + (1-C)COMPTT+3GAUSSIAN).

the Epic-pn and FPMA data sets, as the normalization relative to the *NuSTAR* spectra (as many other spectral parameters) are free and not fixed to those of *XMM-Newton*. The RGS spectral parameters were linked to the pn ones, except for the inter-calibration constant that was left free to vary, and similarly for the FPMB spectrum with respect to the FPMA one.

The first reflection model that I used includes the convolution model RFXCONV (developed by Kolehmainen et al. 2011), used to reproduce only the reflection component, and applied to the continuum Comptonisation model NTHCOMP, whose parameters are linked to those of the continuum NTHCOMP already included in the model. The reflection component is smeared by the convolution model RELCONV (Dauser et al. 2010) to take into account Doppler and relativistic effects. The RELCONV model assumes a broken power law for the disc emissivity law, with two different indexes below and above a given radius R_{br}. I forced the two indexes to assume the same value because our spectra are not sensitive enough to reveal a difference in the emissivity index.

The second model includes the DISKLINE model, that describes only the smeared iron emission line profile, combined to the PEXRIV model, used to represent only the reflection component, that is an exponentially cutoff power-law spectrum reflected from ionised material (Zdziarski et al. 1996). The parameters of PEXRIV, that characterise the continuum spectrum, have been appropriately linked to those of NTHCOMP component: I set the electron temperature to 2.7 times that of the NTHCOMP (as it is appropriate for a saturated Comptonisation, see also Egron et al. 2013) and I linked the photon index of the power-law in PEXRIV with the one of the comptonisation component. In order to smear the spectrum for relativistic effects, I multiplied the reflection component by the convolution model RDBLUR (developed by Fabian et al. (1989)). To fit the residuals evident in the spectra at low energies (see Fig. 5.2), I added several Gaussian components aside from the two related to the iron K-shell emission, that are interpreted as the emission lines associated to the atomic transitions shown in Table 5.3. I also added an absorption edge at 9.44 keV which can be traced back to the Fe XXVI K-edge that is necessary to fit the *NuSTAR* residuals. Since this feature is not required to fit the *XMM-Newton* spectrum, it may be a systematic feature and therefore I freeze its absorption depth to zero for the RGS and Epic-pn spectra.

I also tried to model the spectrum with other reflection models: the self-consistent model RELXILLCP (Dauser et al. 2016), and with a variant of MODEL 2, where the component PEXRIV is replaced by PEXRAV. Indeed RELXILLCP should predict a soft excess in the data that might also account for the BBODY component; moreover, the PEXRIV component may not adequately describe the ionised reflection physics and for this reason I tried to replace it with PEXRAV, that assumes neutral matter in the disc. However the RELXILLCP component proved unable to model adequately the spectrum of this source (the χ^2/dof is 2193.0/1558 and 1636.3/1376 for the *XMM-Netwon* and *NuSTAR* data, respectively). The inadequacy of RELXILLCP in describing our data might be related to the temperature of the seed photons, that is fixed at 0.06 keV in the model, being significantly different with respect to the temperature of 0.6-0.8 keV that I find for this system. I added a low-energy exponential roll-over to the model, using the EXPABS component, to solve this problem, but without the EXPABS or BBODY component the *XMM-Newton* spectrum shows significant residuals at low energies. The associated chi-square over d.o.f. is 3830.3/2935 and

3472.6/2932, for the model without and with the BBODY component, respectively, the best-fit parameters are reported in Table 5.4. The model including PEXRAV achieved a good fit to the data, with a lower chi-square with respect to what I obtain with PEXRIV (χ^2/dof = 3291.1/2929), with consistent best fit values of the parameters, when the inner disc radius is fixed to 75 R_g. But if this parameter is left free to vary the fit is unstable and the best fit values are physically inconsistent. I, therefore, conclude that these models do not provide a better fit to the data in our case. The results obtained by these fits and a more detailed discussion of the model are showed and discussed in the Appendix 5.7.

The shape of the relativistic iron line profile is mainly influenced by different parameters that characterize the mentioned reflection models: the inner disc radius R_{in}, the system inclination with respect to our line of sight, the ionisation parameter ξ, and the reflection fraction defined as the fraction of the radiation reflected by the disc in terms of the solid angle $\Omega/2\pi$ that the disc subtends as seen from the corona (Kolehmainen et al. 2011). In our first fit, I noticed that the model that includes the RFXCONV component was unable to constrain the value of the disc inner radius and the system inclination. Therefore, considering that the value of the system inclination has been debated several times in the literature, I decided to keep it frozen at the value found by Jonker et al. (2003) of 82 degrees, while I kept fixed the disc inner radius at the magnetospheric radius expected for this source, i.e. 75 R_g. I estimated this value as a fraction ϕ of the Alfvén radius R_A, defined by the relation given by Frank et al. (2002):

$$R_m = \phi R_A = \phi \times 2.9 \cdot 10^8 L_{37}^{-2/7} M_1^{1/7} R_6^{-2/7} \mu_{30}^{4/7} \text{ cm} \tag{5.1}$$

where M_1 is the mass of the neutron star in units of 1.4 $M_\odot$, R_6 is its radius in units of 10^6 cm, L_{37} is the luminosity in units of 10^{37} erg s^{-1} and μ_{30} is the magnetic dipole moment in units of 10^{30} G cm^3. The parameter ϕ, set to ~ 0.4, takes into account the case of accretion of matter via a geometrically thin disc, which reduces the size of the magnetosphere in the equatorial plane. Considering that Jonker & van der Klis (2001) have estimated a magnetic field of 8×10^{10} G assuming a luminosity at the Eddington limit of 1.8×10^{38} erg s^{-1}, I obtained an inner radius of 149 km, i.e. about 75 R_g (see also Iaria et al. 2015).

The best fit values related to the models are reported in Table 5.4: the obtained parameters are consistent with the expected ones and the residuals (shown in Fig. 5.4) suggest a good fit of the data. I tested the improvement of the fit using the statistical test F-TEST, comparing our model, which includes the self-consistent reflection component, with a model containing the same components except for the reflection, that is instead fitted with another broad gaussian at 6.7 keV used to model the Fe XXV fluorescence line. I obtain a probability of chance improvement of $\sim 9 \times 10^{-34}$, meaning that the inclusion of the RFXCONV significantly improves the quality of the fit with respect to a simple Gaussian component.

I also fitted the data to a model that uses a combination of PEXRIV and DISKLINE to fit the reflection component instead of RFXCONV. Although this model is not self-consistent, in the sense that the iron line is not self-consistently calculated from the reflection spectrum, I find that this provides a better fit with respect to RFXCONV, as shown by the results reported in Table 5.4;

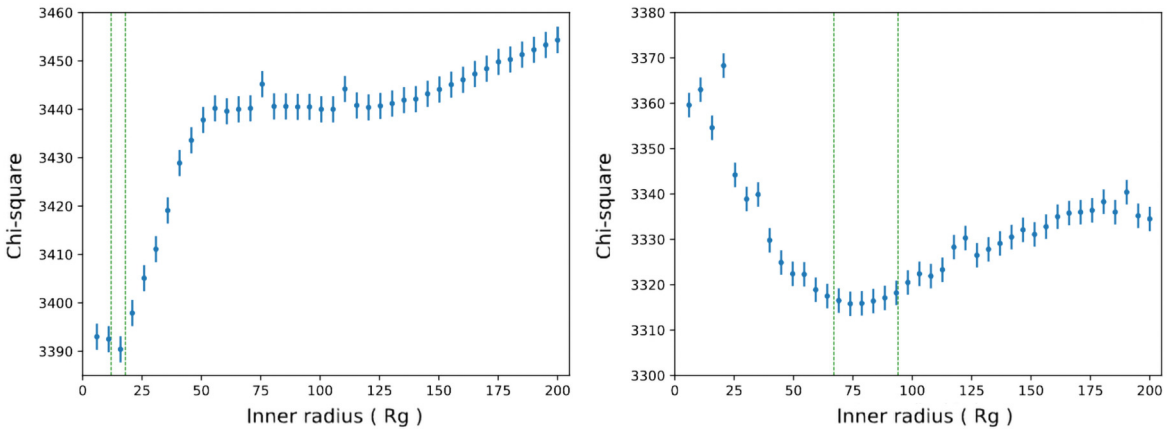

Figure 5.3: Variation of the chi-square as a function of different values of the inner radius of the disc from 6 to 200 R_g, using Model 3 (left panel) and Model 2 (right panel), respectively. The highlighted boxes in the figures evidence the best fit value of the inner disc radius for the two models ($R_{in} = 15 \pm 3$ R_g and $R_{in} = 75^{+19}_{-7}$ R_g, respectively), while the error bars associated to each chi-square value represent $\Delta\chi^2 = 2.7$ corresponding to the 90% confidence level for a single parameter.

it clearly improves the χ^2 value and allows to obtain a constraint both for the system inclination and for the inner disc radius, perfectly in line with what I expect for the system. I tested the improvement of the fit using the statistical test F-test, comparing the two relativistic models and I obtained a probability of chance improvement of $\sim 5.4 \times 10^{-22}$, meaning that Model 2 ensures a significantly better fit to the data.

Keeping the inclination parameter fixed, I tried to let free to vary the inner radius between 6 and 200 R_g, in the RfxConv model, and I noticed that the χ^2 value improves significantly, ranging from 3430 with 2921 dof (degrees of freedom) to 3378 with 2920 (dof), reaching a best fit value of 15 ± 3 R_g (see Table 5.4). To test the chi-square improvement, I used the Xspec command *steppar* to perform a fit while stepping the value of the parameter through the range between 6 and 200 R_g, with a number of steps of 39, using the Model 3 and Model 2. The results related to rfxconv model show that the chi-square reaches a minimum at the best-fit value and increases rapidly as the radius increases, achieving higher, but flat values between 50 and 125 R_g, and then increasing again for higher values of the radius (Fig. 5.3). This result suggests a geometry of the system where the inner region of the accretion disc is close to the neutron star surface, although the presence of coherent pulsating emission and the estimated value of the magnetospheric radius make unlikely such a small value for the inner radius of the accretion disc. However, such a high improvement in the fit-quality cannot be neglected; for this reason, I will discuss this result in the following section. It is also noteworthy that this result is in contrast with what I find using the pexriv+diskline to model the reflection spectrum, since in that case an absolute minimum of the chi-square is found for an inner disc radius in the range of $R_{in} = 75^{+19}_{-7}$ R_g (left panel of Fig. 5.3).

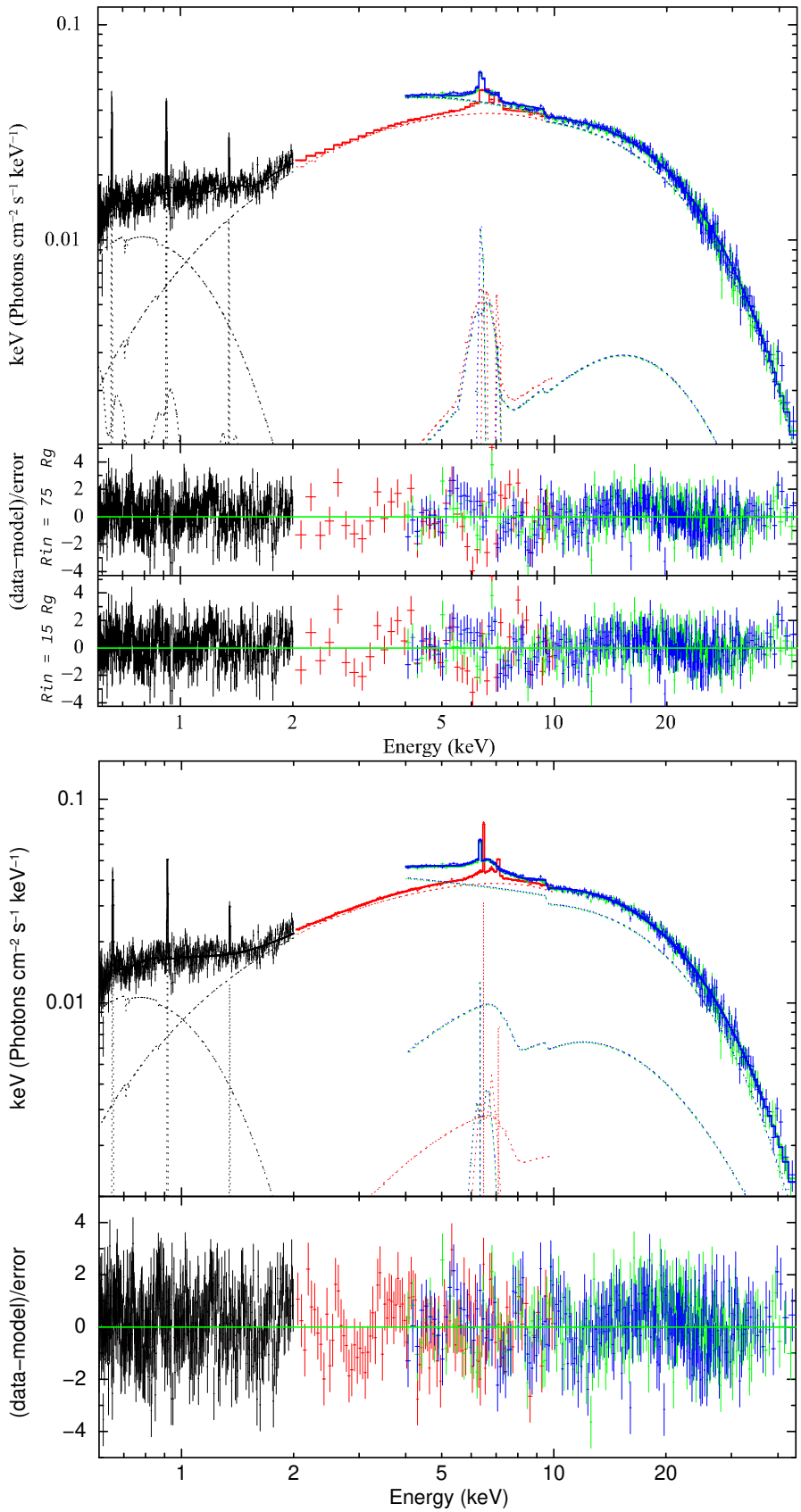

Figure 5.4: The top and bottom figures show the spectra and residuals in units of sigma with respect to models described in the text. The top figure shows the fit to the model CONSTANT* EDGE* TBABS*(6GAUSSIAN+ BBODY + RELCONV* RFXCONV* NTHCOMP + NTHCOMP) together with the residuals in units of sigma obtained fixing the parameter R_{in} to 75 R_g, and those obtained when R_{in} assumes its best-fit value of 15 R_g, respectively. The bottom figure shows the fit to MODEL 2: CONSTANT* EDGE* TBABS*(6GAUSSIAN+ BBODY + DISKLINE + RDBLUR* PEXRIV + NTHCOMP) together with the residuals in units of sigma with respect to the model.

Table 5.3: Emission lines at soft X-ray energies.

Id.	Expected (keV)	E (keV)	σ (eV)	N (10^{-4}) (ph cm^{-2} s^{-1})
O VIII	0.6536	$0.6537^{+0.0001}_{-0.0004}$	0.9± 0.3	2.9 ± 0.3
Ne IX (i)	0.9162	0.9149 ±0.0007	1.6 ± 0.9	1.9 ± 0.3
Mg XI (i)	1.3433	$1.347^{+0.002}_{-0.003}$	<5	0.8 ± 0.2
Si XIV	2.005	2.06 ± 0.06	18^{+5}_{-3}	2.0 ±0.4

5.5.0 Results and discussion

I analysed not simultaneous *XMM-Newton* and *NuSTAR* observations of 4U 1822-371, studying the average broad-band spectra and focusing on the possible presence of reflection features. As seen in the previous section, the addition of the reflection models improved the fit, reducing the residuals related to the iron fluorescence line and Compton reflection hump. The quality of our analysis was then ascertained using an F-test statistics, which returned a very low probability of chance improvement and confirmed the need of a reflection component, despite the high inclination of the system (note that the emission of the accretion disc decreases as the cosine of the inclination angle). In the following I first summarize the best-fit results, discussing the case in which the accretion disc extends close to the neutron star, and then I propose a possible scenario that can explain the observed features. The continuum emission is well fitted by the BBODY and NTHCOMP components. The first marks the presence of a blackbody emission at 0.196 keV that may be produced by the disc or the neutron star surface. The saturated Comptonisation spectrum is produced in an optically thick corona with $\tau \sim 19 - 20$ with an electron temperature for MODEL 1 and MODEL 2, respectively, of $3.31^{+0.07}_{-0.06}$ keV and 3.26 ± 0.03 keV for EPIC/pn plus RGS spectrum and 5.02±0.03 keV and 4.87 ± 0.02 keV for the *NuSTAR* spectra. The mismatch between the temperatures of the Comptonisation component may depend on the different epoch in which the two observations were performed. Although the two spectra show small, but significant, differences, I do not expect a significant variation in the reflection continuum spectrum, since the latter contributes to a small fraction of the total spectrum.

To understand the geometry of the system, I first must address which is the region producing the continuum emission. I calculated the blackbody radius for both models, that is the radius of the (spherical) region where the blackbody radiation is emitted, then I inferred the size of the (spherical) region producing the seed photons experiencing inverse Compton scattering off the hot electrons of the Corona. Matching the expression that defines the normalization parameter in the BBODY component with the Stefan-Boltzmann law, that links the radiation flux to the fourth power of the temperature, I have that:

$$K = \frac{4\pi R_{bb}^2 \sigma T^4}{10^{39}\mathrm{erg}} \left(\frac{10\mathrm{kpc}}{D}\right)^2 , \tag{5.2}$$

where σ is the Stefan-Boltzmann constant that takes the value $\sigma = 5.6704 \times 10^{-5}$ erg/(cm^{2}s

Table 5.4: Best-fit values for the parameters of the models described in the text.

Component	Parameter	Model 1†	Model 2⋆	Model 3∇	Model 4‡	Model 4A⊙	Model 4B□	Model 5•
EDGE	E(keV)	9.44 ± 0.08	$9.58^{+0.08}_{-0.07}$	9.50 ± 0.08	9.54 ± 0.06	$9.56^{+0.09}_{-0.08}$	9.50 ± 0.07	$9.57^{+0.09}_{-0.08}$
	τ	0.075 ± 0.008	0.091 ± 0.06	$0.065^{0.006}_{-0.007}$	0.010 ± 0.009	0.08 ± 0.01	0.9 ± 0.01	0.08 ± 0.01
TBABS	nH (10^{22})	$0.15^{+0.02}_{-0.01}$	0.12^{*}	$0.168^{+0.004}_{-0.005}$	0.112 ± 0.006	0.11 ± 0.01	0.13 ± 0.02	0.12^{*}
BBODY	kT(keV)	$0.194^{+0.005}_{-0.006}$	0.196 ± 0.003	0.194 ± 0.002	-	$0.203^{+0.008}_{-0.006}$	$0.208^{+0.007}_{-0.01}$	0.19 ± 0.003
	N (10^{-4})	$3.3^{+0.3}_{-0.2}$	3.14 ± 0.04	$3.46^{+0.03}_{-0.19}$	-	3.2 ± 0.2	$3.0^{+0.3}_{-0.2}$	3.20 ± 0.06
EXPABS	E_{Cut}(keV)	-	-	-	-	$2.08^{+0.08}_{-0.15}$	-	-
XMM	Γ	$1.334^{+0.016}_{-0.004}$	1.300 ± 0.001	$1.394^{+0.002}_{-0.001}$	-	-	$1.248^{+0.009}_{-0.008}$	$1.297^{+0.003}_{-0.002}$
NTHCOMP	kT_e(keV)	$3.31^{+0.07}_{-0.06}$	3.26 ± 0.03	3.79 ± 0.05	-	-	2.98 ± 0.04	3.17 ± 0.03
	kT_{bb}(keV)	0.84 ± 0.01	0.757 ± 0.002	0.914 ± 0.002	-	-	0.65 ± 0.04	$0.751^{+0.005}_{-0.01}$
	N (10^{-3})	9.6 ± 0.2	$10.2^{+0.1}_{-0.2}$	$9.64^{+0.02}_{-0.15}$	-	-	$10.9^{+0.4}_{-0.3}$	10.3 ± 0.1
NUSTAR	Γ	1.538 ± 0.005	$1.4841^{+0.0007}_{-0.0009}$	1.55 ± 0.001	-	-	$1.38^{+0.02}_{-0.04}$	1.560 ± 0.005
NTHCOMP	kT_e(keV)	5.02 ± 0.03	4.87 ± 0.02	5.00 ± 0.02	-	-	$4.25^{+0.07}_{-0.12}$	4.97 ± 0.02
	kT_{bb}(keV)	$0.86^{+0.02}_{-0.03}$	$0.557^{+0.001}_{-0.002}$	$0.846^{+0.002}_{-0.001}$	-	-	1.1 ± 0.1	$0.825^{+0.005}_{-0.042}$
	N (10^{-3})	1.64 ± 0.06	$2.57^{+0.08}_{-0.07}$	$1.671^{+0.005}_{-0.025}$	-	-	7.1 ± 0.4	$1.5984^{+0.0011}_{-0.0004}$
RELCONV	Index	$2.6^{+0.3}_{-0.2}$	-	2.16 ± 0.06				
	Rbr	250^{*}	-	250^{*}	-	-	-	-
	Incl (deg)	82^{*}	-	82^{*}	-	-	-	-
	R_{in}	$75^{\dagger}$	-	15 ± 3	-	-	-	-
	$R_{out}(10^3)$	1.0^{*}	-	1.0^{*}	-	-	-	-
RFXCONV	rel_{refl}	$-0.61^{+0.04}_{-0.05}$	-	>-0.9	-	-	-	-
	log_{xi}	$2.00^{+0.07}_{-0.21}$	-	$1.72^{+0.03}_{-0.09}$	-	-	-	-
RELXILLCP	Index	-	-	-	$0.9^{+0.3}_{-0.4}$	1.38 ± 0.5	$1.09^{+0.3}_{-0.4}$	-
XMM	Incl(deg)	-	-	-	82.5^{*}	82.5^{*}	82.5^{*}	-
	Γ	-	-	-	< 1.2	1.418 ± 0.004	-	-
	log_{xi}	-	-	-	1.05 ± 0.03	1.08 ± 0.08	$1.06^{+0.06}_{-0.04}$	-
	kTe(keV)	-	-	-	$2.76^{+0.02}_{-0.01}$	3.4 ± 0.1	-	-
	$refl_{frac}$	-	-	-	$1.6^{+0.1}_{-0.2}$	2.8 ± 0.3	-	-
	N(10^{-3})	-	-	-	$1.090^{+0.009}_{-0.005}$	1.87 ± 0.08	$1.0^{+0.3}_{-0.4}$	-
EXPABS	E_{Cut}(keV)	-	-	-	-	3.0 ± 0.1	-	-
RELXILLCP	Γ	-	-	-	< 2.6	$1.5^{+0.01}_{-0.03}$	-	-
NUSTAR	log_{xi}	-	-	-	$2.08^{+0.07}_{-0.06}$	$2.70^{+0.04}_{-0.03}$	2.37 ± 0.06	-
	kTe(keV)	-	-	-	$4.15^{+0.04}_{-0.07}$	4.17 ± 0.07	-	-
	$refl_{frac}$	-	-	-	3.2 ± 0.3	$3.5^{+0.3}_{-0.2}$	-1^{*}	-
	N(10^{-3})	-	-	-	$1.65^{+0.02}_{-0.04}$	$2.43^{+0.04}_{-0.07}$	5.1 ± 0.5	-
DISKLINE	E_{XMM} (keV)	-	6.58 ± 0.03	-	-	-	-	6.61 ± 0.04
	E_{NuSTAR} (keV)	-	6.41 ± 0.05	-	-	-	-	-3.0 ± 0.8
	Index	-	-2.3 ± 0.3	-	-	-	-	$-2.3^{+0.3}_{-0.4}$
	R_{in}	-	75^{+11}_{-9}	-	-	-	-	75^{*}
	Incl (deg)	-	$85.7^{+0.1}_{0.4}$	-	-	-	-	< 62
	N_{XMM} (10^{-4})	-	$5.1^{+0.4}_{-0.2}$	-	-	-	-	5.0 ± 0.5
	N_{NuSTAR} (10^{-4})	-	$5.0^{+0.7}_{-0.6}$	-	-	-	-	5.2 ± 0.7
PEXRIV	rel_{refl}	-	-1^{*}	-	-	-	-	-
	xi	-	9 ± 2	-	-	-	-	-
	N_{XMM}	-	$0.125^{+0.008}_{-0.004}$	-	-	-	-	-
	N_{NuSTAR}	-	< 0.51	-	-	-	-	-
PEXRAV	rel_{refl}	-	-	-	-	-	-	-1^{*}
	N_{xmm}	-	-	-	-	-	-	$0.0547^{+0.0078}_{-0.0088}$
	N_{nustar}	-	-	-	-	-	-	0.24 ± 0.02
XMM	E (keV)	6.51 ± 0.01	$6.505^{+0.005}_{-0.02}$	6.51 ± 0.01	6.513 ± 0.007	6.512 ± 0.007	6.509 ± 0.007	6.500 ± 0.005
GAUSSIAN	σ (eV)	<77*	1.8E-14*	44*	0.075^{*}	0.075^{*}	0.075^{*}	$1.8 \times 10^{-17*}$
	N (10^{-4})	3.4 ± 0.3	3.16 ± 0.2	3.4 ± 0.2	4.6 ± 0.2	4.6 ± 0.2	5.1 ± 0.2	$3.0^{+0.2}_{-0.3}$
	E (keV)	$7.08^{+0.02}_{-0.01}$	7.10 ± 0.01	$7.06^{+0.02}_{-0.01}$	7.04 ± 0.02	7.04 ± 0.2	7.02 ± 0.02	$7.12^{+0.01}_{-0.02}$
	σ (eV)	49^{+1}_{-3}	1.8E-14*	44^{1}_{-2}	0.075^{*}	0.075^{*}	0.075^{*}	1.8^{*}
	norm (10^{-4})	2.4 ± 0.2	1.4 ± 0.2	2.0 ± 0.2	2.5 ± 0.2	2.8 ± 0.2	2.73 ± 0.02	1.6 ± 0.3
NUSTAR	E (keV)	6.38 ± 0.02	6.35 ± 0.05	6.38 ± 0.02	6.33 ± 0.02	6.32 ± 0.03	6.35 ± 0.02	$6.37^{+0.02}_{-0.04}$
GAUSSIAN	σ (eV)	75^{*}	1.8E-14*	75^{*}	0.075^{*}	0.075^{*}	0.075^{*}	1.8^{*}
	N (10^{-4})	4.2 ± 0.4	2.4 ± 0.4	4.1 ± 0.4	5.3 ± 0.4	4.04 ± 0.04	4.46 ± 0.04	$2.5^{+0.5}_{-0.6}$
	E (keV)	7.08^{*}	7.11^{*}	7.06^{*}	6.81 ± 0.04	7.04^{*}	7.02^{*}	7.12^{*}
	σ (eV)	75^{*}	1.8E-14*	75^{*}	0.075^{*}	0.075^{*}	0.075^{*}	1.8^{*}
	N (10^{-4})	0.9 ± 0.3	< 0.1	0.5 ± 0.3	2.5 ± 0.4	0.6 ± 0.3	$1.4^{+0.3}_{-0.4}$	< 0.3
	χ^2/dof	3430.23/2921	3303.95/2916	3377.9/2920	2193.0/1558 (XMM) 1636.3/1376 (NuSTAR)	3830.3/2935	3472.6/2932	3512.5/2932

* Kept frozen during the fit.

† MODEL 1 : CONSTANT*EDGE*TBABS*(6GAUSSIAN+ BBODY + RELCONV*RFXCONV*NTHCOMP + NTHCOMP).

⋆ MODEL 2 : CONSTANT* EDGE* TBABS*(6GAUSSIAN+ BBODY + DISKLINE + RDBLUR*PEXRIV + NTHCOMP).

∇ MODEL 3 has the same components of Model 1, but in this case the inner radius R_{in} is free to vary.

‡ MODEL 4: CONSTANT*EDGE* TBABS*(6GAUSSIAN + RELXILLCP)

⊙ MODEL 4A has the same components of the MODEL 4 with the addition of BBODY and EXPABS.

□ MODEL 4B is a variant of MODEL 4A with the omission of the component EXPABS and the RELXILLCP component used to model the reflection component only and the illuminating continuum described by NTHCOMP.

• MODEL 5: CONSTANT*EDGE* TBABS*(6GAUSSIAN+ BBODY + DISKLINE + RDBLUR* PEXRAV + NTHCOMP).

K^4), K is the blackbody normalization, which depends on the blackbody observed flux, and D is the distance to the source that was assumed to be $6.1^{+1.6}_{-2.7}$ kpc, most recent estimate reported in Arnason et al. (2021). Taking into account these parameters I find a blackbody radius of 23 ± 7 km and 22 ± 7 km, for Model 1 and Model 2, respectively. Both radii have to be corrected by a hardening factor of ∼ 1.4, because of distortions of the blackbody spectrum mostly due to Thomson scattering (see e.g. Foster et al. 1986), getting a blackbody radius of 32 ± 10 km and 31 ± 10 km, respectively.

To find the seed-photon emission radius I have to analyse the best-fit values obtained for the Comptonisation spectrum and *de-comptonise* it, to trace the continuum emission before it interacts with the Corona. From the two models I extrapolated the value of the flux, F_x = (1.65 - 0.92) × 10^{-9} erg s^{-1} cm^{-2}, and calculated the bolometric luminosity ($L_x \sim 6 \times 10^{36}$ $ergs^{-1}$). I can derive the optical depth of the Corona using the relation of Zdziarski et al. (1996):

$$\Gamma + \frac{1}{2} = \left[\frac{9}{4} + \frac{1}{\left(kT/m_e c^2\right)\tau(1+\tau/3)}\right]^{1/2} . \tag{5.3}$$

Using the best-fit values of the parameters, I got values of the optical depth of τ =19 ± 1 and 20.4 ± 0.2, for the two models respectively. Hence I can state that the comptonisation spectrum is emitted by an optically thick Corona surrounding the region of the system where the seed photons are emitted, as I expect from the fact that I found a saturated comptonisation spectrum, with a shape quite similar to a blackbody, with low values of the photon index and electron temperature.

In order to obtain the flux associated with the de-comptonised spectrum f_{seed}, I divided the bolometric flux of the comptonisation component by the factor (1+y), where y is the Compton y-parameter calculated under the assumption of the optically thick case (y = 9(1) - 10.6(2)), and in the end I derived the seed-photon radius R_{sp} from the following equation:

$$R_{sp} = 3 \times 10^4 \; f_{seed}^{1/2} \; T_{bb}^{-2}(\mathrm{keV}) \; D \;\; \mathrm{km} \, , \tag{5.4}$$

obtaining a value of 2 ± 1 km and 3 ± 1 km for Model 1 and 2, respectively.

The value found for the seed-photon radius suggests an emission from a smaller region than the NS surface, such as the magnetic polar caps of the neutron star. The latter hypothesis may be justified by the presence of coherent pulsations at 0.59 s detected by Jonker & van der Klis (2001). However, it is difficult to think these two thermal emissions could be originated from the compact object, because of the large difference between the temperature of the two components (the seed-photons temperature is about 0.9 keV, while the blackbody one is 0.2 keV) and because I would expect some (thermal, blackbody-like) contribution from the accretion disc (see below).

Regarding the reflection component, the value I found for the emissivity-law index is in agreement with what I expect: I obtained a value of $2.6^{+0.3}_{-0.1}$ and 2.3± 0.3 for Model 1 and Model 2, respectively. I expect an emissivity index of about 2-3 depending on whether the reflection spectrum is dominated by the illuminating flux coming from the central source (in this case the flux illuminating the disc decreases with distance as r^{-2}) or by the intrinsic disc emission (whose intensity decreases with distance approximately as r^{-3}). I found a value of the ionisation

parameter ξ (defined as $\xi = 4\pi F_x/n_e$ Fabian et al. (2000), where F_x is the X-ray flux and n_e electron number density, respectively) of 9 ± 2 and a $\log\xi$ of $2.00^{+0.07}_{-0.21}$, for the two models, respectively, that is in line with the energies of the emission lines observed in the spectrum; such ionisation parameter implies a relatively low ionisation state of matter in the disc, with the iron line dominated by the Fe I-XX Kα transition (Fabian et al. 2000).

As mentioned in the previous section, I found two different minima of the chi-square for Model 1, which differ for the values of the inner accretion disc radius. In the first case, the radius is truncated at the magnetospheric radius predicted for this pulsar, i.e. 75 R_g, while for the second one I obtained a configuration where the disc extends closer to the neutron star (with an inner radius of 15 R_g) corresponding to a significantly lower χ^2 value. Note that when I use Model 2 to fit the spectrum I find a clear minimum of the chi-square for a value for the inner disc radius of about $\sim$ 75 R_g, compatible with the estimated position of the magnetospheric radius of the source. In correspondence I find different values of the reflection fraction: when the radius is kept frozen at 75 R_g, this parameter assumes the stable value of $0.61^{+0.04}_{-0.05}$, while when I let free the inner radius, the reflection fraction tends to the value of 0.9, suggesting that when the accretion disc gets closer to the central object, the portion of the radiation reflected by the disc has to increase. The reflection fraction of Model 2 is instead fixed at -1 because I cannot determine at the same time the reflection fraction and the normalization of the pexriv component, given that its normalization cannot be fixed to that of the Comptonisation spectrum since these parameters are defined in different ways and cannot be easily compared. Thus I decided to let free the pexriv normalization and fixed the reflection fraction at its maximum expected value. However, in order to give an estimation of the reflection fraction in this case, I have evaluated the flux of the reflection component (rdblur*pexriv+diskline) and the flux of the Comptonisation continuum both in the energy range 0.1 − 100 keV, in order to calculate their ratio, finding that the reflection component corresponds to $\sim$ 7% of the Comptonisation component.

In the following I discuss the results described above considering a scenario in which the intrinsic luminosity of the central source is at the Eddington limit and most of this emission is blocked by the outer rim of the accretion disc; in this case, what I see is just the fraction of the intrinsic emission of the central source that is scattered along our line of sight by an extended, optically thin, corona.

5.5.1 The presence of two Coronae

The results discussed above are obtained considering the observed source luminosity of $\sim 6 \times 10^{36}$ erg s^{-1}. However, this luminosity may not be the intrinsic source luminosity. Three independent arguments are present in literature suggesting that the observed luminosity does not reflect the intrinsic luminosity emitted by the source: i) Burderi et al. (2010), studying the orbital period evolution of the system, found a constraint on the orbital period derivative of $\dot{P}$ = 1.50(7)$\times$ 10^{-10} s s^{-1}, i.e. three orders of magnitude larger than that calculated for a system assuming a conservative mass transfer. This constraint led the authors (see also Bayless et al. 2010; Iaria et al. 2011; Mazzola et al. 2019) to suggest a scenario in which the mass transfer

rate from the companion is more than three times the Eddington limit (i.e. 1.8×10^{-8} $M_\odot$/yr for a neutron star of 1.4 $M_\odot$), thus proposing a non-conservative mass-transfer scenario, where the mass in excess is expelled from the system. ii) Hellier & Mason (1989) fitting an EXOSAT spectrum of 4U 1822-371, found a ratio of the X-ray luminosity to the optical one of $L_x/L_o \sim 20$, a factor 50 smaller than the typical value usually found for LMXBs, thus possibly indicating that the observed luminosity is reduced by at least a factor 50, compared to the intrinsic one. iii) Jonker & van der Klis (2001) found a pulse period derivative for 4U 1822-371 of (-2.85 ± 0.04) $\times 10^{-12}$ s s^{-1}, concluding that the source is spinning up (see also Mazzola et al. 2019; Iaria et al. 2015; Jain et al. 2010). Using the relation between observed luminosity and spin-up rate given by Ghosh & Lamb (1979b), the authors find that for a luminosity of 10^{36} erg s^{-1} the neutron star magnetic field should be around 8×10^{16}G, extremely odd for a NS in a LMXB, while for a luminosity of 10^{38} erg s^{-1}, around the Eddington limit, the expected value for the magnetic field is a more conceivable value of 8×10^{10}G.

Notwithstanding the high inclination angle of the system, not only X-ray pulsations are observed coming from the neutron star but also a weak blackbody spectrum that seems to be emitted from the neutron star surface, as well as signatures of a reflection component such as a Compton hump at high energy (10-30 keV) in the *NuSTAR* spectrum and a broad Fe emission line with a profile compatible with a smearing produced by Doppler effects in the inner accretion disc. A possible way to justify these evidences is to introduce an extended optically-thin Corona above the whole system that scatters only 5% of the intrinsic luminosity emitted by the central source into the line of sight (as proposed by Iaria et al. 2024). The consequence of this hypothesis is that all the flux that I observe is that part of the total emission produced by the source that is scattered along the line of sight. If the extended Corona is optically thin, so $\tau_c \ll 1$, the scattered flux would be (Iaria et al. 2013a):

$$F_{\rm Obs} = L_0 \frac{(1 - e^{-\tau_c})}{4\pi D^2} \simeq \frac{L_0 \tau_{\rm C}}{4\pi D^2} \ . \tag{5.5}$$

Assuming a distance to the source of D= 6.1 kpc, to obtain an intrinsic luminosity of 10^{38} erg s^{-1} (Eddington limit) with an observed one of about 6×10^{36} erg s^{-1}, τ_c must be ~ 0.05. The presence of a tenuous corona around the system can also explain the values found for the blackbody radius and seed-photon radius; in deriving the value of the two radii I have considered the observed luminosity of 6×10^{36} erg s^{-1}, while I should have used the intrinsic one, that is probably two orders of magnitude larger. Because the luminosity is proportional to R^2, to find the correct radii I must multiply the previous values by a factor 4, getting more reasonable values of R_{bb} = 143 km and $R_{sp} \sim 13$ km, respectively. In this case, I can identify the blackbody emission as due to the inner rim of the accretion disc, which is truncated by the magnetosphere at $\sim$ 140 km from the neutron star center, and the seed-photon emission region as the neutron star surface. This interpretation is in agreement with the fact that the blackbody temperature is lower than the seed-photon temperature, since the temperature in the system is expected to decrease at larger distances from the compact object. In this case, the best-fit value of the inner radius found using the reflection component RFXCONV of 15 ± 3 R_g is hard to reconcile with a blackbody emission

produced at 140 km (i.e. 70 Rg) from the NS.

5.5.2 Inner accretion disc radius

In the following, I will show that a value for the inner disc radius as small as $\sim 15\, R_g$ may be obtained for this source provided that the magnetic field is not stronger than 4×10^{10} G. To understand why, it is necessary to study the variation of the inner accretion disc radius of the system with respect to its mass accretion rate and magnetic field. For this purpose, I assumed a neutron star mass of 1.69 $M_\odot$, as estimated by Iaria et al. (2011) for the 4U 1822-371 system, and a neutron star radius of R = 10^6 cm, and calculated the inner disc radius varying the mass accretion rate in a range 1-10 times the Eddington limit (which is assumed to be 1.53×10^{-8} $M_\odot$/yr for a neutron star with a mass of 1.69 $M_\odot$) and the magnetic field in a range of 1-8 $\times 10^{10}$ G, using the expression reported by Sanna et al. (2017):

$$R_\mathrm{m} = \phi\, R_\Lambda = \phi\, (2GM)^{-1/7} \mu^{4/7} \dot{M}^{-2/7}\ , \tag{5.6}$$

where G is the gravitational constant, M is the neutron star mass assumed to be 1.69 $M_\odot$, μ the star's magnetic dipole moment, and $\dot{M}$ the mass accretion rate. The factor ϕ depends on the structure of the accretion disc, but I can estimate it with the following expression Sanna et al. (2017):

$$\phi = 0.315\, \kappa_{0.615}^{8/27}\, \alpha^{4/15}\, \mu_{26}^{4/189}\, \dot{M}_{-9}^{32/945}\, m^{76/189}\ , \tag{5.7}$$

where μ_{26}, R_6, $\dot{M}_{-9}$ and m are the neutron star magnetic moment in units of 10^{26} G cm^3, the neutron star radius in units of 10^6 cm, the mass accretion rate in unit of 10^{-9} $M_\odot$/yr and the neutron star mass in units of Solar mass, respectively. The mean molecular weight κ can be assumed equal to 0.615 for fully ionised matter, while the parameter α, that expresses the disc viscosity in the standard Shakura–Sunyaev model, is usually set equal to 0.1 (see section 3.1). The results are plotted in the top panel of Fig. 5.5: the region between the dotted lines at 12 and 18 R_g represents the range of our best-fit value, and it is easy to understand that a such value can be found with a different combination of $\dot{M}$ and B, for example assuming an accretion rate few times Eddington and a magnetic field with a strength of few 10^{10} G.

In order to verify whether these values may be plausible for 4U 1822-371, I used the Ghosh & Lamb (1979b) equation that links the spin-period derivative of the neutron star, its magnetic field and its luminosity, in order to understand which pairs of values return the spin period derivative reported in the literature for this source :

$$-\dot{P} = 5.0 \times 10^{-5}\, \mu_{30}^{2/7}\, n\,(\omega_s)\ M_1^{-3/7}\, I_{45}^{-1} \left(P L_{37}^{3/7}\right)^2 \mathrm{s/yr}, \tag{5.8}$$

In this relation, M_1 is the neutron star mass in unit of 1 $M_\odot$, I_{45} is the neutron star moment of inertia in unit of 10^{45} g cm^2 and P is the spin period of the source, that is 0.5915669 s (Mazzola et al. 2019). The parameter n(ω_s) is the dimensionless accretion torque that is a function of the fastness parameter ω_s. When ω_s < 0.95, I can use the following approximate expressions (Ghosh

& Lamb 1979b):

$$
\begin{aligned}
n &\approx 1.39\left\{1-\omega_s\left[4.03\,(1-\omega_s)^{0.173}-0.878\right]\right\}(1-\omega_s)^{-1}\ , \\
\omega_s &\approx 1.35\,\mu_{30}^{6/7} M_1^{-2/7}\left(PL_{37}^{3/7}\right)^{-1}\ .
\end{aligned}
\tag{5.9}
$$

The values of luminosity and magnetic field used in the equations above vary, respectively, in a range from 0.5 to 10 times the Eddington value and from 10^{10} to 8×10^{10} G. The results are shown in the bottom panel of Fig. 5.5, where the dotted line represents the derivative of the spin period measured for the source, (-2.59± 0.03) $\times 10^{-12}$ s/s (e.g. Mazzola et al. 2019). As seen in Fig. 5.5 a luminosity and a magnetic field of the order of the ones found with the Eq. 5.6 are compatible with the $\dot{P}$ relative to the source. In other words, I may obtain a magnetospheric radius as small as $\sim 15\,R_g$ assuming an intrinsic luminosity of a few times the Eddington limit and a magnetic field strength below $4 \times 10^{10}\,G$.

However, our discussion cannot fully justify such a small inner accretion disc radius, which would be incompatible with the inner disc radius I infer from the blackbody component (see above). Furthermore, although the assumed intrinsic luminosity may be plausible, the magnetic field value reported by several authors in literature is of $\sim 8\times10^{10}$G. This value has been reported, for instance, by Iaria et al. (2015) who detected a possible cyclotron absorption feature at ~ 0.7 keV in the low-energy spectrum of the source. On the other hand, the best fit value constrained with Model 2 ($R_{in} = 75^{+19}_{-7}$ R_g), which ensures the best fit to our data with the lowest chi-square, is perfectly in line with the value of luminosity and magnetic field expected for this system.

Alternatively, the small value indicated by the best-fit parameters of the reflection component rfxconv, if confirmed, might be explained by an excess of smearing of the iron line. It is possible that, although the line is actually emitted at $45 - 75\,R_g$, it appears more distorted than it should be, resulting in a smaller inner disc value. The reason for this distortion is unclear (Compton broadening in excess to that expected in the reflection models, blending of lines produced by different ions of iron, disc winds with large turbulent velocities), and may be connected to the accretion rate at the Eddington limit and how it changes the geometry of the disc viewed at such a high inclination angle. Otherwise, considering that the best fit is obtained fitting separately the iron line and the rest of the reflection component, this result may be caused by a not good consistency between the line and the other reflection features, which may be due to the edge-on view and the fact that I do not directly observe the disc inner region, but I just observe its emission scattered into the line of sight by the optically thin corona. Note that the model with rfxconv returns a warning relating to the slope of the power-law, that during the fit goes outside the tabulated range, a suggesting again that more suitable models would be needed to describe the reflection component of sources such as 4U 1822-371.

5.5.3 Emission lines at low energies

As reported in Tab. 5.3, I detected four emission lines at soft X-rays that can be associated to emission from O VII, Ne IX, Mg XI, and Si XIV ions. I identified the Ne and Mg lines with the

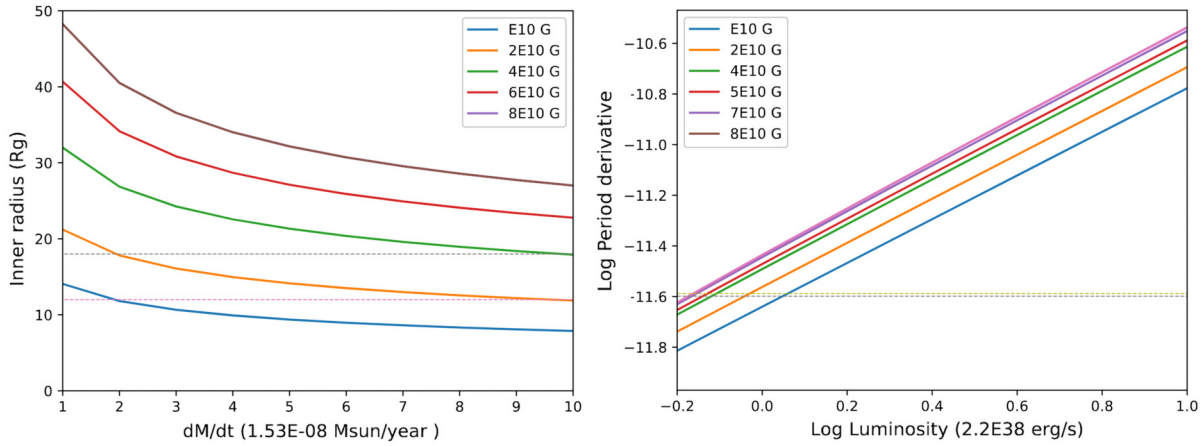

Figure 5.5: Left panel: Inner radius of the accretion disc plotted versus the intrinsic source luminosity for different values of the magnetic field (solid lines), obtained with the Eq. 5.6 described in the text. Right panel: derivative of the spin period as a function of luminosity for different values of the magnetic field in logarithmic scale as indicated in the labels. The dotted lines shown in the plot is the logarithmic of $-2.595(11) \times 10^{-12}$ s/s that is the spin period derivative reported in literature (Mazzola et al. 2019).

inter-combination lines, while the O and Si ones can be easily associated with the Lyman alpha transition. To prove the improvement of the chi-square to the introduction of the four Gaussian lines I use the F-test statistic. This method generally works when comparing nested models and in principle, it should not be used to verify the addition of a Gaussian component in the model, since the boundary of the possible values of the normalization parameter is the null value (Protassov et al. 2002). However, the issue mentioned above can be avoid by expanding the parameter space of the line normalization to include negative values. I compared the best fit obtained with MODEL 2 with one in which I removed individually each of the Gaussian lines. I find that the addition of all the Gaussian lines have a significance higher than 6σ. Thus, because of the presence of expected emission lines at these energies, I can state that these features are most probably real and not related to systematic features. In addition to the F-test, another method to ascertain the significance of the lines is considering their normalization and comparing the latter with the error, at 1 sigma, associated with the parameter. Also in this case the significance of the lines is higher than 6 sigmas for the emission lines associated with O VII, Ne IX, Mg XI, and above 3 sigmas for that associated to Si XIV. Since the lines do not show evidence of Doppler effects I propose they are emitted from an outer region of the disc (in accordance with Iaria et al. 2011). However further investigations are needed to accurately determine the emission region.

5.6.0 Conclusions

I have analyzed *XMM-Newton* and *NuSTAR* observations of 4U 1822-371, with the aim of highlighting the presence of a reflection component in the spectrum, despite the high inclination angle of the system. I first tried to reproduce the result obtained by Iaria et al. (2013a), who fitted the source spectrum without including any reflection component, but, with respect to this model,

I obtained residuals at the iron line region and an excess of emission above $\sim$ 10 keV, reminiscent of a Compton hump caused by a reflection component. I tried to fit the complex residuals at the iron line region with three Gaussian lines achieving unsatisfactory results. Therefore I tested two reflection models, RFXCONV and DISKLINE + PEXRIV, to fit the spectrum obtaining a significant improvement in the fit, suggesting a detection of this component at 7 sigma confidence level. To our knowledge, the presence of the reflection component in a source with such a high inclination has never been observed before, since reflection should be very faint and difficult to detect in a source with an inclination angle higher than 80 degrees. The main continuum emission is well fitted by a thermal blackbody emission, with a temperature of 0.2 keV, and a satured comptonised component with an electron temperature of 3.26 – 4.87 keV, generated by the inverse Compton scattering of seed photons with a temperature of 0.8 keV in an optically thick Corona (τ = 19 – 20), located in the innermost region of the system, possibly around the neutron star. I observe several emission lines that can be associated with O VIII, Ne IX, Mg XI and Si XIV in the RGS spectrum. These lines may be produced in the bulge in the outer region of the accretion disc, as previously proposed (e.g. Iaria et al. 2013b), although a detailed orbital phase-resolved spectral analysis is required to corroborate this hypothesis (Somero et al. 2012a).

I updated the orbital ephemeris of the source by adding two eclipse arrival times derived from *NuSTAR* (2018) and Swift (2007) observations to the ones reported by Mazzola et al. (2019). I fitted the delays of the eclipse arrival times alternatively with a quadratic, a cubic and a sinusoidal model, proving that by adopting the latter two, instead of the quadratic model, the fit significantly improves; in this way I found an orbital period P_{orb} = 5.57063023(34) hr and a $\dot{P}_{orb}$ value of 1.51(5) $\times$ 10^{-10} s s^{-1}. In line with other results present in literature, I assumed the source is emitting at an intrinsic Eddington luminosity of 2×10^{38} erg s^{-1} despite the observed luminosity is just 10^{36} erg s^{-1}. To explain the discrepancy between the intrinsic and the observed luminosity, as well as the presence of a reflection component in the spectrum, the presence of an extended optically-thin corona ($\tau \sim 0.01$) around the whole system has been suggested, which would scatter about 1% of the intrinsic luminosity produced by the central source along the line of sight. Since the whole emission is scattered, this mechanism enables to observe a reflection component, which otherwise would be very difficult to detect at such a high inclination angle.

In my analysis I found a singular feature related to the inner accretion disc radius: the best-fit value of the inner radius achieved with the relativistic component RFXCONV is $15 \pm 3\ R_g$, with a clear improvement of the χ^2 over the fit in which the inner radius was fixed to 75 R_g, that is the theoretically predicted value of the magnetospheric radius in this source. I have discussed the possibility that the iron line is really emitted in a disc region so close to the compact object, concluding that this hypothesis requires, at the Eddington luminosity, a magnetic field of 10^{10} G that deviates from the value reported in literature for this source (of 8.8×10^{10} Iaria et al. 2015). This result would also be at odds with the inferred radius of the blackbody emission region of $\sim$ 140 km that I identify with the inner rim of the accretion disc. Alternatively, the iron line is actually emitted at the predicted magnetospheric radius, but the line profile appears more smeared than it should be, resulting in a smaller value of the inner radius. The mechanism(s) originating this line distortion are unclear, possibly related to the accretion rate at the Eddington limit and to

the scattering the line photons undergo in their travel along the line of sight. However, using a combination of DISKLINE and PEXRIV to fit the reflection component, I obtain an inner disc radius of $\sim 75\ R_g$ and a (slightly) better quality of the fit, showing that this value is still model-dependent. Future, high statistics, broad-band observations may help to solve this ambiguity.

5.7.0 Appendix A: Another reflection component

As discussed in Section 5.4.2, I tried to fit the data using two other reflection models, RELXILLCP and a variant of MODEL 2, where the PEXRIV component is replaced by PEXRAV. I initially fitted the *XMM-Newton* and *NuSTAR* data separately, using the model RELXILLCP that should predict the soft excess in the data that I previously described with the BBODY component. However, it proved unable to model adequately the spectrum of this source and, as seen in Fig. 5.6, *XMM-Newton* data show peculiar residuals in the *Epic-pn* band (the χ^2/dof is 2193.0/1558 and 1636.3/1376 for the *XMM-Netwon* and *NuSTAR* data, respectively). I have to take into account that RELLXILCP includes a Comptonisation spectrum, with a temperature of the soft seed-photons fixed at 0.06 keV, that is in contrast with the seed-photon temperature that I find for this source (0.6-0.8 keV). To solve this problem I added a low-energy exponential roll-off to the model, using the EXPABS component, in order to mimic a cutoff at the seed-photon temperature. I tried also to model our data using RELXILLCP to describe the reflection component only, setting the reflection fraction to -1 but allowing the normalization to vary, and linking the continuum parameters to those of the continuum fitted by the NTHCOMP component. Differently from our best-fit model, RELXILLCP fails to reach stable values of R_{in} and inclination angle, I hence fixed these at the expected values, while the other parameters, like the ionisation parameter, assume different values depending on data-set (see Tab 5.4). I cannot use the F-test statistic to compare this fit with the one that includes RFXCONV, because in this case the lower chi square has the higher number of degrees of freedom. Therefore it is preferable to choose the model with RFXCONV, because the associated fit presents a lower chi square despite the higher number of degrees of freedom. It is clear that using RELXILLCP component does not assure in this case a better fit of the model to the data. Furthermore, using RELXILLCP alone does not fit the soft excess in the data modelled with the black body spectrum, and the data still require a low-energy component to fit soft residuals in the *Epic-pn* band (Fig. 5.6).

Although MODEL 2 ensures the best fit to data with the lowest chi-square, the component PEXRIV may be not appropriate to model the continuum, since it may not be suitable for describing a highly ionised reflection spectrum (Ross et al. 1999). Therefore I tried to replace it with PEXRAV, an exponentially cut off power law spectrum reflected from neutral material (Magdziarz & Zdziarski 1995). I performed the fit keeping the inner disc radius fixed ad 75 R_g, because if this parameter is left free to vary the fit is unstable and the best fit values obtained are physically inconsistent. As shown in Tab.5.4, I obtain reasonable values of the parameters even if the inclination angle results too small with respect to the expected value. Notwithstanding the model that include PEXRAV shows a little improvement of the fit, by using PEXRIV I can constrain the

ionisation parameter, and the whole set of best-fit values obtained with this model is coherent with what I expect from the source. Therefore using PEXRIV does not affect too much the results, also considering that the ionisation parameter obtained using the other models is quite low and PEXRIV should be able to adequately describe the effects of a mild ionisation.

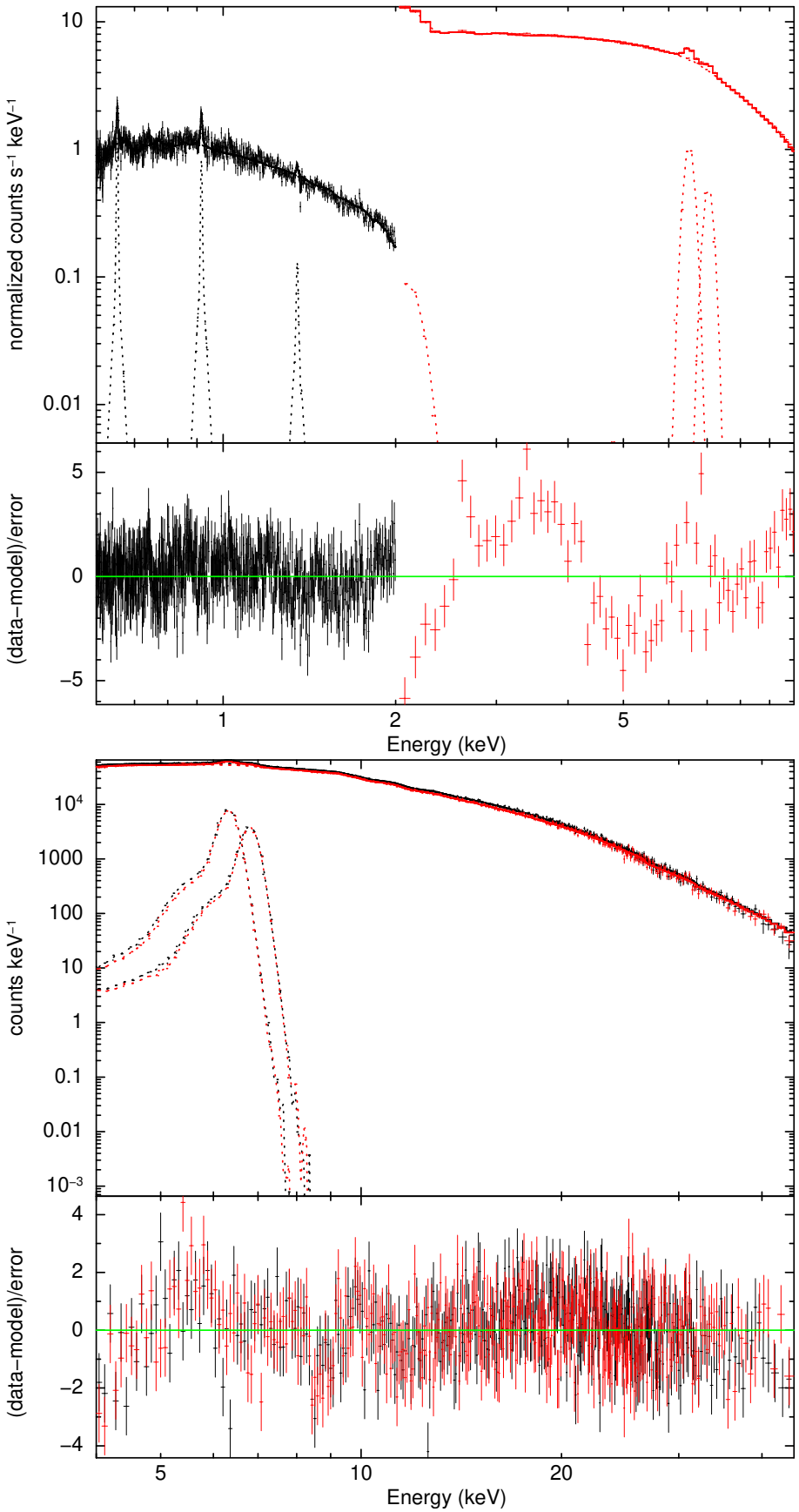

Figure 5.6: Spectra and residuals in units of sigma with respect to MODEL 4, defined as CONSTANT* EDGE* TBABS*(6GAUSSIAN + RELXILLCP), for the *XMM-Newton* spectrum (top panel) and *NuSTAR* spectrum (bottom panel), respectively. Data were rebinned for visual purposes only.

6

Hβ spectroscopy of the high-inclination black hole transient Swift J1357.2-0933 during quiescence

Summary

Swift J1357.2-0933 is a transient low-mass X-ray binary hosting a stellar-mass black hole. The source exhibited optical dips and very broad emission lines during both outburst and quiescence, which are thought to be the result of a high orbital inclination. I present phase-resolved spectroscopy obtained with the 10.4m Gran Telescopio Canarias (GTC). The spectral analysis focus on the Hβ spectral region during X-ray quiescence. The emission line is exceptionally broad (full width at half maximum, FWHM > 4000 Å), in agreement with previous studies focused on Hα. A two-Gaussian fit to the prominent double-peaked profile reveals a periodic variability in the centroid position of the line. I also produced a diagnostic diagram aimed at constraining additional orbital parameters. Together, they allow us to independently confirm the orbital period of the system using a new dataset obtained five years after the previous outburst. However, our estimates for both the systemic velocity and the radial velocity semi-amplitude of the black hole reveal larger values than those found in previous studies. I argue that this could be explained by the precession of the disc and the presence of a hotspot.

I found evidence of a narrow inner core in the double-peaked Hβ emission profile. I studied its evolution across the orbit, finding that it is likely to result from the occultation of inner material by the outer rim bulge, further supporting the high orbital inclination hypothesis.

The work presented in this chapter was published under the title "**Hβ spectroscopy of the high-inclination black hole transient Swift J1357.2-0933 during quiescence**" in Astronomy & Astrophysics, Volume 679, A145, 2023 (https://doi.org/10.1051/0004-6361/202346909).

6.1.0 Introduction

Focusing exclusively on X-rays for the study of an accretion disc provides an incomplete picture of the system. As mentioned in section 3.1.1, the plasma temperatures within the disc depends on the distance to the compact object, resulting in a radiation spectrum that encompasses a broad range of energies. This spectrum includes not only X-rays emanating from the disc inner regions but also extends to optical wavelengths in its outer periphery. Furthermore, the optical spectra of these systems are characterized by a rich array of emission lines, primarily arising from atomic transitions in lighter elements such as Hydrogen and Helium. The distinctive, **double-peaked profiles** observed in these lines, a consequence of the Newtonian Doppler effect, are crucial in deconstructing the system structural and dynamic properties. In this chapter, I shift my focus to the study of these lines that dominate the optical spectra of LMXBs, analyzing optical data from the X-ray transient Low Mass X-ray Binary Swift J1357.2-0933.

6.2.0 Swift J1357.2-0933

Swift J1357.2-0933 (hereafter J1357) is a LMXB X-ray transient discovered during its outburst in 2011, with a lower limit to the distance of d > 2.29 kpc that, combined with the high Galactic latitude, places it above the Galactic thick disc (see Mata Sánchez et al. 2015). Despite the lack of detection of its companion star during quiescence, Casares (2015) utilized the already known correlation between the Full Width at Half Maximum (FWHM) of the Hα line and the velocity semi-amplitude of the donor star ($K2 = 0.233 \pm 0.013 FWHM$), to glean insights about the compact object. Their study suggests that J1357 harbours one of the most massive stellar-mass BHs known in the Galaxy ($M_{BH} > 9.3\,M_{\odot}$, as reported by Mata Sánchez et al. 2015).

The peak X-ray luminosity estimated during the outburst is about $L_x^{peak} \sim 10^{35}(D/1.5\,\mathrm{kpc})^2$ erg s^{-1} (Armas Padilla et al. 2013), placing the source among the very faint X-ray binary transients (VFXTs) (Wijnands et al. 2006). The system's orbital period was measured to be 2.8 ± 0.3 h from the variability on the double-peaked Hα emission line, first during outburst (Corral-Santana et al. 2013) and subsequently during quiescence (Mata Sánchez et al. 2015). A refined value 2.5673 ± 0.0006 h was later obtained by studying the modulation of the Hα line profile trough over 14 months (Casares et al. 2022)

One of the most puzzling properties of J1357 is its dipping activity: the optical light curve shows periodic dips in its evolution during the outburst, while the X-ray light curve does not (Armas Padilla et al. 2014a). The origin of this behaviour is still debated. For instance, Corral-Santana et al. (2013) associated this behaviour with the presence of an obscuring toroidal structure in the inner accretion disc that moves towards the outermost regions during the outburst decay. In their multi-wavelength photometric analysis Paice et al. (2019) found that the source becomes bluer during the dips, and tried to give an updated model that describes the system geometry, proposing that the obscured emission mainly arises from the base of jet. This was

later supported by Jiménez-Ibarra et al. (2019a), who also performed dip-resolved spectroscopy, finding that the optical dips were associated with blue-shifted H and He II absorptions. This behaviour, also observed by Charles et al. (2019), suggests that the dips are related to wind-type outflows.

Even after much debate on the geometry of the system, the dipping activity was found to lead inevitably to a high inclination angle of the system, with most of the literature on the system agreeing on an inclination angle greater than 70 degrees (Corral-Santana et al. 2013). For instance, Torres et al. (2015) presented time-resolved optical spectroscopy, where the authors found evidence of time-variable deep absorption features in the double-peaked profile, supporting the hypothesis that the source is seen at a high inclination. Typically, a high-inclination system exhibits eclipses in its X-ray light curve (e.g. MAXI J1659-152, Kennea et al. 2012b, Kuulkers et al. 2013; 4U 1822-371 Anitra et al. 2021, Iaria et al. 2013b), and the absence of such eclipsing activity in this particular system may appear at odds with the hypothesis of high inclination. However, Corral-Santana et al. (2013) justified the lack of eclipses assuming a high orbital inclination >70 degree and a very low mass ratio, which implies a donor star radius comparable to, or even smaller than, the outer rim of the disc.

Observations collected by the Swift X-ray telescope revealed an equivalent hydrogen column density (N_H) of $(1.2 \pm 0.7) \times 10^{20}$ cm^{-2} (Torres et al. 2015). Such a low N_H implies a low optical extinction, providing us with a unique opportunity to obtain phase-resolved spectra of the system at blue optical bands with sufficiently high S/N, a rare occurrence in BH transients.

In this work I present the first quiescence spectroscopy of J1357 focused on the hydrogen Hβ emission line and covering a full orbit. I analyse its periodic evolution and compare the results with those previously reported using the Hα line during both quiescence and outburst periods (Mata Sánchez et al. 2015; Corral-Santana et al. 2013).

6.3.0 Observations

I analysed eight observations collected by the Optical System for Imaging and low-intermediate-Resolution Integrated Spectroscopy (OSIRIS) at the 10.4 metre Gran Telescopio Canarias (GTC) at the Observatorio del Roque de los Muchachos (ORM) on the island of La Palma (Spain). During the campaign I employed the R2000B grism with a 0.8" slit, which allowed me to analyse the spectral features in the wavelength range 3950 – 5700 Å with a spectral resolution of R=1903 and dispersion of D = 0.86 Å/pix (see Table 4.3). The resolution is estimated by measuring the FWHM of the skylines in the background spectra, while the dispersion value is measured at λ_c = 4755 Å, as reported in the OSIRIS user manual. The eight observations were acquired consecutively, during a quiescent epoch, on the night of 2016 March 05 between 03:32:11.4 and 06:19:51, each with an exposure time of 1235 s, for a total exposure of 2.75 h, thus covering a full orbit of the system.

The data were reduced using IRAF[1] standard routines, applying the bias and flat-field

[1]IRAF is a general purposes software for the reduction and analysis of astronomical data distributed by the

Table 6.1: Best-fit values for the parameters of the two-Gaussian model described in the text. Uncertainties are at the 68% c.l.

Spec	phase	phase†	offset (km s^{-1})	FWHM (km s^{-1})	I_R/I_B	$\chi^2/d.o.f.$	T-value
spec-1	-0.32	-0.11	-133 ± 31	1762 ± 64	1.14 ± 0.08	1.40	0.64 ± 0.02
spec-2	-0.18	0.03	-118 ± 38	2012 ± 79	1.10 ± 0.07	1.30	0.43 ± 0.02
spec-3	-0.05	0.16	-174 ± 38	1946 ± 78	0.96± 0.07	1.76	0.51 ± 0.02
spec-4	0.09	0.30	-235 ± 30	1794 ± 64	1.00 ± 0.07	1.75	0.62 ± 0.02
spec-5	0.23	0.43	-265 ± 32	1835 ± 65	1.27 ± 0.08	1.36	0.59 ± 0.02
spec-6	0.36	0.57	-304 ± 41	1950 ± 83	0.96 ± 0.08	1.34	0.57 ± 0.02
spec-7	0.50	0.71	-296 ± 35	1845 ± 73	0.93 ± 0.07	1.28	0.63 ± 0.02
spec-8	0.64	0.84	-212 ± 28	1724 ± 59	1.11 ± 0.07	1.29	0.67 ± 0.02

† Phases relative to the absolute inferred by Casares et al. (2022).

correction and using the HgAr, Xe, and Ne arcs lamps available for our configuration to calibrate the pixel-to-wavelength solution. The spectra were corrected from cosmic rays using L.A.Cosmic task (van Dokkum et al. 2012), and extracted from the two-dimensional images using the optimal extraction technique (Naylor 1998).

6.4.0 Spectral analysis

The analysis reported in this section was performed by using both MOLLY software[2], and tailored PYTHON routines based on the ASTROPY package (Astropy Collaboration et al. 2022). I first normalised the spectra by dividing them by a third-order polynomial in order to model the continuum component of the spectrum. The wavelength coverage of our spectra allows me to access the Hβ line region with a sufficiently high signal-to-noise ratio (S/N $\sim$ 3, measured in the nearby continuum). The Hγ line was also present, but the lower S/N (barely $\sim$ 1.3), mainly due to the lower response at the edge of the chip, together with a line intensity reaching barely half that of Hβ, prevented me from extracting a reliable line profile from the individual spectra. No other features, like the He II emission line and or the Bowen complex, are present in the spectra. I analysed for the first time the blue part of the spectrum, never studied in quiescence. I focused on the double-peaked Hβ line, a signature profile of the gas orbiting in a Keplerian accretion disc.

6.4.1 Hβ radial velocity

I fit every spectrum with a double-peaked model compound of two Gaussian lines using the Python CURVE FIT routine from the SCIPY package (Virtanen et al. 2020). The free parameters controlling the fit are the intensity of each of the peaks; the FWHM, assumed to be the same for both Gaussians; and the shift of the centroid between the peaks with respect to the rest-frame wavelength, denoted offset. All the best-fit parameters with the associated uncertainties are

National Optical Astronomy Observatories, operated by the Association of Universities for Research in Astronomy, Inc., under contract with the National Science Foundation.

[2]The MOLLY software was developed by T. R. Marsh, and is available at the following link: https://cygnus.astro.warwick.ac.uk/phsaap/software/

reported in Table 6.1, while in Fig. 6.1 I show the fits of each individual spectrum.

I find periodic variability in the individual offsets of each observation, which led me to perform a non-linear fit to the data using the following function:

$$f(T) = \gamma + K_1 \sin\left(2\pi((T - T_0)/P - \phi_0 - 0.5)\right). \tag{6.1}$$

Periodic radial velocity curves were previously observed in the Hα line of other LMXBs, and in particular of J1357 (Corral-Santana et al. 2013; Mata Sánchez et al. 2015). The interpretation is that it reflects the movement of the accretion disc centre of mass, which should therefore trace that of the compact object. Under the assumption of a perfectly symmetric disc, the average offset value across all of our observations (i.e. γ) gives an estimate of the systemic velocity of J1357, the parameter K_1 is an estimate of the radial velocity semi-amplitude, ϕ_0 is an orbital phase shift correction conveniently defined, and the time of the first epoch of observations is $T_0 = 2457452.64776595$ HJD.

I observe a modulation with a P = 0.127 ± 0.008 d, consistent with previous determinations of the orbital period by Corral-Santana et al. (2013) and Mata Sánchez et al. (2015). Casares et al. (2022) provide the most precise determination of the orbital period inferred for the source to date (P = 0.106969 ± 0.000023 d), based on the variability of the emission line over a number of orbits across different epochs. I note that our result is consistent only within 2.5σ of their value. Our study is based on radial velocity measurements, which are most affected by perturbations due to the potential precession of the accretion disc (see Sections 6.4 and 6.5); moreover, it does not take account of the systematic effects due to our having only one orbit (which could lead to an underestimation of the error associated with the period), while the result of Casares et al. (2022) is based on the study of a longer dataset covering several orbits. Together, they led me to adopt their more precise period and readjust the dataset by fixing this parameter.

The sinusoidal function fits the data closely, obtaining a chi-square over degrees of freedom (dof) of 0.75/5, which ensures a level of confidence (c.l.) of 97.5%. Such a low χ^2/dof suggests that the uncertainties on the original spectra are probably overestimated. Rescaling them to a factor of 0.86 produces a χ^2/dof = 1.0. I find the system is moving away from us at a systemic velocity of $\gamma = -220\pm 10$ km s^{-1} and a radial velocity semi-amplitude of $K_1 = 91 \pm 16$ km s^{-1}, as well as $\phi_0 = 0.41 \pm 0.02$.

Under this interpretation, and following the usual definition for zero phase (i.e. corresponding to inferior conjunction), I can calculate the orbital phase for any given epoch using the following equation: $\phi = (T - T_0)/P - \phi_0$. In Table 6.1 I report the relative orbital phase of each observation, under the above convention, and I plot our best fit in Fig. 6.2 (middle panel).

6.4.2 Diagnostic diagram

In our analysis I note a peculiar behaviour of the variation in the ratio of the intensity of the blue to the red peaks of the Hβ profile. The evolution of the intensity variation during the orbital period is shown in Fig. 6.2 (top panel). There is an apparent periodic modulation of this

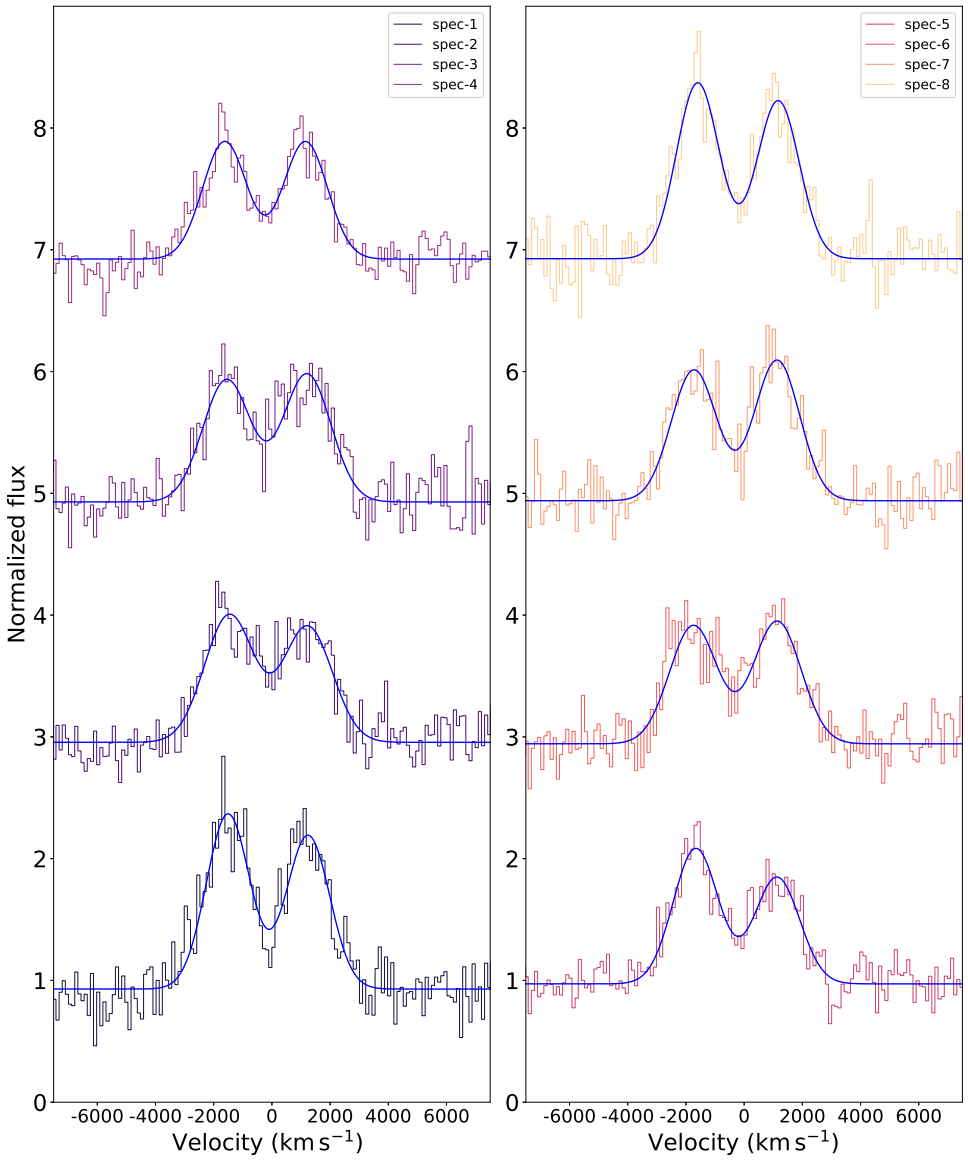

Figure 6.1: Observed spectra and the two-Gaussian model (solid blue line) of all the observations plotted vs the velocity Doppler shift related to the Hβ rest-frame wavelength (4861 Å). The spectra are binned by a factor of 2 and offset by a constant for visualisation purposes.

ratio, similar to that observed previously in the Hα line (see Mata Sánchez et al. 2015), but the ratio associated with spectrum 5 (spec-5) deviates from the expected trend (a visual inspection confirms the blue peak is clearly more intense than the red peak).

This phase-dependent asymmetry of the line profile can be due to different effects; the precession of a disc or the contamination by the presence of a hot spot are the traditionally invoked explanations (Shafter et al. 1986). Consequently, they might complicate the interpretation of the periodic variability described in the previous section: while the presence of a variable hot spot can bias the K_1 determination, a precessing disc might lead to variable γ values when measured in different epochs. In order to get a more reliable measure of the radial velocity variation and to avoid phase-dependent contamination, I decided to focus our analysis on the innermost regions of the disc accessible through optical spectroscopy.

To explore variations in radial velocity and detect any phase-dependent effects, it is effective to

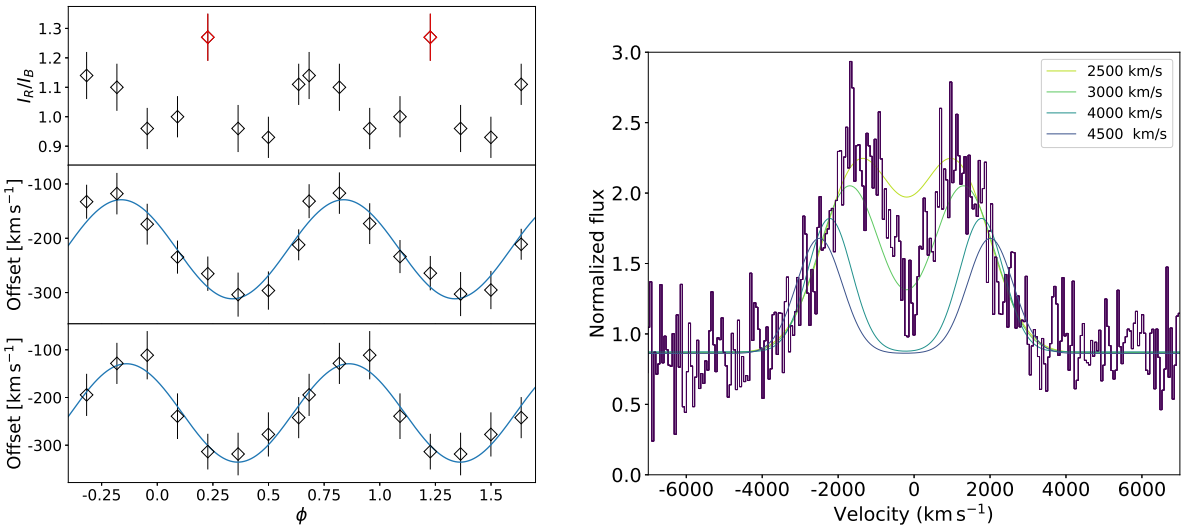

Figure 6.2: **Left panel**: Orbital evolution of Hβ parameters obtained from the two-Gaussian model and a diagnostic diagram. They are all plotted against the orbital phase, and repeated over two orbits for visualisation purposes. *Top panel*: Intensity ratio between the blue and red peak. The value deviating from the trend is in red. *Middle panel*: Offset of the line centroid (black diamonds) and best fit from the double-peaked model (blue solid line). *Bottom panel*: Offset of the line wings centroid (black diamonds) and best fit from the diagnostic diagram (blue solid line), corresponding to a peak-to-peak separation of $a = 3800\,\mathrm{kms}^{-1}$.
Right panel:Visual example of the diagnostic diagram best-fit model to spec-1 for different peak-to-peak separation values.

measure and analyze the data using different peak-to-peak separations for the Gaussian functions. This approach, proposed by Shafter et al. (1986), allows for a thorough "mapping" of the line profile in velocity space, facilitating the identification of any phase-dependent anomalies. To apply it to our dataset, I fitted each spectrum with a model composed of two Gaussians, expressed in terms of the following parameters: the peak-to-peak separation a (for which I explored the range $1600 - 4500\,\mathrm{km\,s}^{-1}$, in steps of $100\,\mathrm{km\,s}^{-1}$), the FWHM and height of both Gaussians (which I kept linked to each other), and the offset of the full structure. I subsequently performed a sinusoidal fit to the resulting radial velocities and determined orbital parameters for each value independently.

Assuming that the contamination is dominant in the external regions, for sufficiently large a values in our modelling I would fit only the wings of the profile, and the measured radial velocities should tend to a stable more reliable measurement that traces the compact object's orbit (Fig. 6.2). Therefore, it is useful to plot the orbital parameters, such as the radial velocity semi-amplitude K_1, the ratio σ_k/K_1 (which estimates the relative error in K_1), the orbital phase (defined under the same convention previously described), and the systemic velocity γ, against the a parameter. The plot produced and shown in Figure 6.3 is commonly referred to as **diagnostic diagram**. To determine the maximum reasonable value of a, I have to look into how σ_k/K_1 varies with the separation: an increase over the average value implies that the continuum noise is dominant. This technique can therefore provide us with estimates of the orbital parameters, although their value is strongly influenced by the choice of separation a, which is somewhat

subjective. As I can see in Fig. 6.3, for $a \lesssim 3800\,\mathrm{km\,s^{-1}}$ K_1 remains stable over a range with a mean value and standard deviation of $91 \pm 18\,\mathrm{km\,s^{-1}}$; above this separation the ratio σ_k/K_1 starts to increase. In particular, K_1 does not considerably deviate from the mean value even though I adopt a peak-to-separation in the range $3400 - 4000\,\mathrm{km\,s^{-1}}$. Additionally, the phase shift, defined as the difference between the value obtained with the method described above and that derived from the double-Gaussian method, which should remain around zero, starts to decrease significantly above $a = 3800\,\mathrm{km\,s^{-1}}$. These considerations led us to think that the most reliable values of the orbital parameters can be obtained for a separation smaller than $3800\,\mathrm{km\,s^{-1}}$, in line with the value obtained by Corral-Santana et al. (2013) based on their analysis of Hα ($a = 3600\,\mathrm{km\,s^{-1}}$). Therefore, the best estimate of the radial semi-amplitude velocity would be provided by its average value below the maximum separation (i.e. $K_1 = 92 \pm 18\,\mathrm{km\,s^{-1}}$), while the systemic velocity of the system remains stable for all the separations with a mean value of $\gamma = -228 \pm 13\,\mathrm{km\,s^{-1}}$.

I subsequently corrected each spectrum from its measured velocity to calculate an average spectrum in the reference frame of the binary. I performed a fit to this averaged profile by making use of a single-Gaussian profile to obtain the FWHM of the line. The model returns FWHM $= 4574 \pm 156\,\mathrm{km\,s^{-1}}$, notably higher than (but still consistent within $\sim 2\,\sigma$ with) the value measured in quiescence for Hα by Torres et al. (2015), Casares (2015), and Mata Sánchez et al. (2015), being $4025 \pm 110\,\mathrm{km\,s^{-1}}$, $4085 \pm 328\,\mathrm{km\,s^{-1}}$, and $4152 \pm 209\,\mathrm{km\,s^{-1}}$, respectively.

6.5.0 Discussion

J1357 is a rather unique BH transient with observational properties that are not yet completely understood, such as recurrent optical dips, presumably as a result of a very high orbital inclination (Corral-Santana et al. 2013), as well as high and variable systemic velocity estimations (Mata Sánchez et al. 2015). A crucial way to better understand this object is to constrain its fundamental parameters, such as the systemic velocity (key to understanding the system evolution; see e.g. Repetto & Nelemans 2015) and its orbital period. Given that the disc (i.e. not the companion) dominates the optical emission even during the quiescent phase, the study of the emission lines during this stage arguably offers the best opportunity to make progress in this area. I present the phase-resolved spectroscopy of the system, focused on the Hβ region. The data were obtained deep into the quiescent phase (~5 yr from the previous outburst) and represent the first study of this line for J1357, and one of the few available for a quiescent LMXB in this spectral region.

I observe a periodic modulation in the radial velocity of the Hβ line profile at $\mathrm{P} = 0.127 \pm 0.008$ d. This result is consistent with that previously found in outburst (Corral-Santana et al. 2013) and quiescence (Mata Sánchez et al. 2015) based on Hα studies. Therefore, I infer that this modulation has remained stable over the five years, further strengthening its association with the orbital period of the system. I also derive a systemic velocity of $-228 \pm 13\,\mathrm{km\,s^{-1}}$ and a $\mathrm{K_1}$ of $91 \pm 18\,\mathrm{km\,s^{-1}}$. Mata Sánchez et al. (2015) derived $\gamma = -79 \pm 12\,\mathrm{km\,s^{-1}}$, a measurement consistent with another quiescence measurement ($\gamma = -130 \pm 50\,\mathrm{km\,s^{-1}}$; Torres et al. 2015).

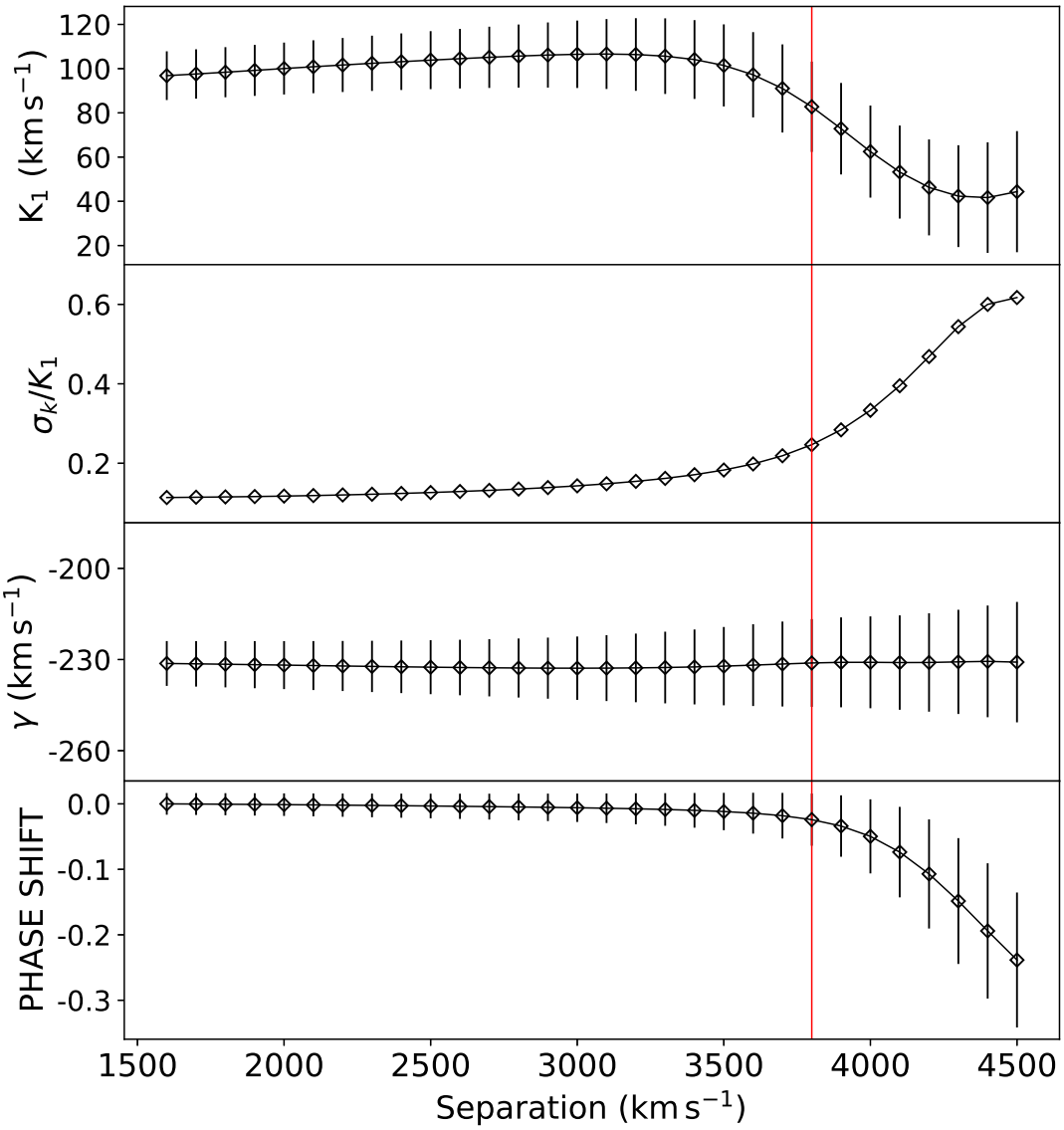

Figure 6.3: Diagnostic diagram for Hβ.
Every parameter was calculated by using two Gaussian lines with the same FWHM. Shown from top to the bottom, plotted vs the peak-to-peak separation, are the semi-amplitude velocity K_1, the ratio of the error associated with K_1 to K_1 itself, the systemic velocity γ, and the corresponding phase shift. The vertical red line represents the peak-to-peak separation ($a = 3800\,\mathrm{km\,s^{-1}}$) above which the measurements begin to be contaminated by noise in the continuum, as inferred from the plot in the second panel.

Although our result, obtained from an analogous analysis but on the Hβ line, is consistent with (Torres et al. 2015) at the 2σ level, it shows a clear deviation from any of the other previously reported results, favouring $\gamma = -228 \pm 13\,\mathrm{km\,s^{-1}}$.

Torres et al. (2015) attributes the variations in the systemic velocity of J1357 as systematic effects, emphasizing that the absence of superhumps in the outburst light curves (Corral-Santana et al. 2013) supports the possibility of a non-precessing disc. Superhumps are indeed photometric modulations triggered by outbursts and marked by a periodicity slightly longer than the actual orbital period, explained by the presence of an elliptical and precessing disc. For example Torres et al. (2004) found a precession period of 52 days for XTE 11118+480, a BH LMXB with an orbital period of 4.08 h. However, given the existence of various data sets in quiescence obtained over approximately 3 years with different instruments and telescopes, and based on the analysis of different spectral lines that show diverse results, it can be concluded that the variation in the systemic velocity of J1357 cannot be solely attributed to systematic issues. The fact that these effects remain after five years of quiescence further reinforces the interpretation that the variable systemic velocity is a persistent and real characteristic of the system.

Although the detection of superhumps would have provided a means to confirm the disc precession and establish constraints on its precession period, their absence is not sufficient to reject this hypothesis. Superhumps may not always develop or remain present during every outburst, therefore, it is highly probable that the observed variations in systemic velocity are related to effects such as disc precession, as reported in several studies (see Mata Sánchez et al. 2015; Jiménez-Ibarra et al. 2019b; Corral-Santana et al. 2013).

Our measurement of the quiescence FHWM of the average Hβ profile is slightly higher than that reported for the Hα line in previous works (though still consistent within 2σ; see Sect. 6.3). However, it is known that higher-order Balmer lines are typically broader than Hα (see Marsh et al. 1987a, 1994). The more energetic Hβ line is expected to be emitted from hotter (i.e. inner) regions of the accretion disc than Hα, where the velocities are higher, and therefore producing a broader profile. Nevertheless, the consistency of the FWHM of Hβ with that reported for Hα two years earlier allows us to infer that the system quiescent properties remained reasonably stable over a period of ~ 2 yr. This demonstrates that J1357 was already in a true quiescent state by then. Together with the orbital period, which I also independently confirm, these are the two key assumptions required for the application of the FWHM–K2 correlation (Casares 2015). Therefore, I provide strong arguments to support the mass function derived by (Mata Sánchez et al. 2015), which implies one of the most massive BHs found in the Galaxy.

6.5.1 Radial velocity of the compact object

Measurement of the compact object's radial velocity through the diagnostic diagram is an indirect method to trace the accretion disc's innermost optically emitting radii. This means that the mismatch of the K_1 semi-amplitude velocity with the previous measurements in quiescence reported in the literature may open up a point of reflection on the state of the source.

Different works in the literature have investigated the spectral evolution of several transient

sources in quiescence after the outburst. One of the most recent examples is provided in Casares (2015), which analysed the evolution of the FWHM of the Hα in the BH LMXB V404 Cygni during the 20 years since the outburst peak. They infer that the FWHM started to increase during the outburst decay, and that it reached a stable plateau phase (called true quiescence), starting $\sim$ 1300 days after the peak of the outburst. On the other hand, Russell et al. (2019) detected a brightening at optical wavelengths prior to an X-ray outburst in four X-ray binaries that were leaving their quiescent state. In their work the authors report that the optical precursor occurred weeks before the first X-ray flare, a delay consistent with the time of refilling of the disc that causes the X-ray brightening.

Our observations during the quiescent state of J1357 lie between two outburst events (2011 and 2017), five years after the previous discovery outburst, and one year before the following event. On the other hand, Mata Sánchez et al. (2015) and Torres et al. (2015) used data from the quiescent epochs between April 2013 and from April to June 2014, respectively (only 2-3 yr after the first outburst). It is true that, as mentioned above, Casares (2015) deduced a period of about 3.5 yr after the outburst for a full quiescent phase to be reached. However, the source analysed by the authors possesses a much larger accretion disc than J1357, so I would expect that our source will take less time to relax in quiescence. Mata Sánchez et al. (2015) found $K_1 = 40 \pm 12\,\mathrm{km\,s^{-1}}$, fully in line with that reported in outburst by Corral-Santana et al. (2013). Similarly, the parameters presented in Torres et al. (2015) are in line with these works. In the present paper, however, the resulting K_1 value is notably larger than those previously derived. The time elapsed between outbursts and quiescent phases studied both in this and previous works does not suggest a different state of the system, and therefore does not explain the different K_1 values.

Another explanation could be related to the fact that our analysis is focused on Hβ and not on Hα. Although both are transitions of the hydrogen Balmer series, the higher energy associated with Hβ might naively suggest that it was formed at an accretion disc ring slightly closer to the compact object than Hα.

The diagnostic diagram technique has been successfully applied to a number of LMXBs (e.g. Cornelisse et al. 2013, Somero et al. 2012b, Muñoz-Darias et al. 2009). Nevertheless, systems where K_1 can be independently measured are scarce, and they have shown that the diagnostic diagram results are better understood as an upper limit to the true compact object radial velocity. In this regard, Unda-Sanzana et al. (2006) showed how the diagnostic diagram method may fail to provide a strong determination of K_1, identifying the root cause of this problem with an asymmetry due to a hot spot that extends to higher velocities, up to the wings of the emission line profile. The fact that applying the same technique in a different line and epoch produces a distinct and larger K_1 value than previous works suggests a similar scenario for J1357.

6.5.2 Inclination angle

Several observational features suggest a high orbital inclination for J1357 (Corral-Santana et al. 2013; Mata Sánchez et al. 2015; Armas Padilla et al. 2014a). Arguably, the most debated

is the presence of optical dips without X-ray counterparts, which sparked the discussion on the geometry of the source (see Sect. 6.2). Recently, Casares et al. (2022) has found a linear correlation between the depth of the inner core of the double-peaked Hα emission profile and the inclination angle in a set of quiescent X-ray transients. The authors applied this correlation to J1357, deducing an inclination of $87.4^{+2.6}_{-5.6}$ degrees, thus supporting the near edge-on geometry of the source.

Visual inspection of the individual spectra reveals that the core of the Hβ line exhibits narrow and variable absorption components, changing in depth during the orbit and even approaching the continuum level (see Fig. 6.1). Deep and narrow absorption cores have been observed in high-inclination cataclysmic variables (with $i \geq 75°$ Schoembs & Hartmann 1983), but never on a LMXB, and they are thought to be caused by occultation of the inner regions of the accretion disc.

Hints of the presence of a narrow core on the HeI 5876 line of J1357 were found by Mata Sánchez et al. (2015), but further confirmation was required due to the low resolution of their spectra, which hampered a clean subtraction of the background. Focusing on the Hβ wavelength range and using the higher-resolution grism, I can now confirm the presence of this feature in a different emission line (Hβ), as well as its narrowness and variable nature along the orbit. This variability can be used to track the motion of the structure responsible for the occultation, as dips are thought to be caused by structures close to the outer rim of the disc (Frank et al. 2002). In particular, the 'bulge' is produced by the impact of the stream of matter from the donor star on the disc. As such, it is expected to impact the disc between orbital phases ~ 0.8 and 0, depending on mass ratio (Smak 1970). In order to test this hypothesis, I adopted the absolute phase 0 derived by Casares et al. (2022) (T0=2456396.6617 HJD, derived from a study of the line through variability in BHs) and redefined the orbital phases for each epoch using the equation mentioned in section 6.4.1. Since the narrow core present in our spectra is particularly prominent in spec-1 ($\phi = 0.89$), I conclude that this scenario is plausible. However, I note that shallower narrow cores are also present at other orbital phases (e.g. spec-7), suggesting a more complex outer rim geometry.

To further inspect the orbital variability of the profiles, I followed the Casares et al. (2022) prescription to calculate the normalised depth of the central trough (T) for all spectra, performing a double symmetric Gaussian fit with equal FWHM and intensity. The variations in T during the orbit appear consistent with the evolution presented in the above-mentioned paper (based on the analysis of Hα), and provide further support to the presence of variable inner cores, reaching maximum depth for spec-1 (see Table 6.1). For this epoch, the best-fit model remains unable to fully fit the observed spectrum core (which almost reaches the continuum level), further supporting the presence of an additional narrow core component. The T value measured in our mean spectrum (0.585 ± 0.008) is consistent with that found by Casares et al. (2022) (0.612 ± 0.125), and therefore with the high inclination they deduced from the T versus inclination diagram. I also considered the possibility of a grazing eclipse by the companion star being at the core of this phenomenon. However, the fact that spec-2, obtained at the epoch of inferior conjunction, does not exhibit a clear deep core led us to disregard this possibility. Corral-Santana et al. (2013) proposed that the extreme mass ratio of the system ($q \sim 0.04$, Mata Sánchez et al. 2015) makes

the donor star radius comparable to or smaller than the disc outer rim. Thus, the companion would not be expected to produce clear eclipsing phenomena, even in a close-to-edge-on configuration.

6.6.0 Conclusions

I have analysed observations performed with the GTC telescope of J1357 during the quiescent phase, $\sim$ 5 yr after the previous outburst. Taking advantage of the low extinction of the source, I have performed, for the first time, a phase-resolved study on the Hβ emission line. I find a periodicity (P = 0.127 $\pm$ 0.008 d), which is fully consistent with previous reports based on different lines and obtained at different epochs and with different facilities. This strongly suggests that this corresponds to the orbital period of the system, confirming J1357 as one of the shortest orbital period BH transients.

Our obtained values for systemic velocity and radial semi-amplitude velocity differ from the previous values derived from the Hα emission line. I interpret this as an effect of a combination of disc precession and the presence of hot spots. Finally, I report, for the first time, the presence of narrow, deep, and variable cores in the Hβ emission line of a LMXB. I propose that these cores are produced by structures in the outer ring of the accretion disc, which may be the outer disc bulge. This provides independent proof to further support the high-inclination nature of the system.

7

An X-ray view of emission lines in optical spectra: spectral analysis of the two LMXB systems Swift J1357.2-0933 and MAXI J1305-704

Summary

I introduce a novel approach for determining the orbital inclination of transient black hole low-mass X-ray binary systems, by modelling the Hα and Hβ line profiles emitted by the accretion disc, with a Newtonian (i.e. non-relativistic) version of DISKLINE. I apply the model to two sample sources, Swift J1357.2-0933 and MAXI J1305-704, analysing two observations collected during a quiescent state and one during an outburst. I add to the model a Gaussian line to describe the deep inner core of the double-peaked profile, which cannot be reproduced by DISKLINE model. I find that the Hβ and Hα emission lines during the quiescent state are consistent with being emitted in a disc ring between $(9.6 - 57) \times 10^3\,R_g$ and $(1.94 - 20) \times 10^4\,R_g$, respectively. I constrain an inclination angle of 83^{+5}_{-3} degrees for Swift J1357.2-0933 and 73 ± 1 degrees for MAXI J1305-704, respectively, entirely consistent with the ones reported in the literature, but with higher precision.

The values of the emission region radii, obtained through analysis of the outburst spectrum exhibit deviations from the expected values, being bigger than the orbital system separation. This outcome implies several potential scenarios, including the presence of line profile contamination, an alternative disc configuration deviating from the Keplerian model, or even the possibility of a circumbinary disc.

I warn the reader that these results are derived from a simplistic model that may not fully describe the complicated physics of accretion discs. Despite these limitations, our results on the inclination angles are remarkably consistent with recent complementary studies and the proposed description of the emitting region remains entirely plausible.

The work presented in this chapter was submitted under the title "**An X-ray view of emission lines in optical spectra: spectral analysis of the two LMXB systems Swift J1357.2-0933 and MAXI J1305-704**" to Astronomy & Astrophysics, 2023.

7.1.0 Introduction

The study of the double-peak emission line profiles which characterized optical spectra of these sources, is a powerful tool which allows us to determine the orbital parameters of the system. Indeed, examining parameters like the orbital period and radial velocity semi-amplitude, allows us to dynamically confirm the nature of compact objects in these systems. It has been acknowledged that the central core within double-peaked lines emitted by an accretion disc becomes deeper as the inclination increases, becoming particularly noticeable for inclinations greater than 67 degrees (Horne & Marsh 1986). Casares et al. (2022) discovered a direct correlation between the depth of the inner core in the double-peaked Hα emission line and the inclination angle in a group of quiescent BH LMXBs. By applying this method, the authors have been able to determine the inclination angle of different sources with a high confidence level. In this work, I investigate a novel method that can provide an estimate of the inclination angle of the system, by applying for the first time the DISKLINE model to fit the double peak emission lines related to the H-series transition that appears in the optical spectra of these transient BH candidates.

7.2.0 X-ray transient systems samples

To ensure the accuracy of the inclination measurements, I have chosen two transient BH X-ray binaries that have been intensely studied in the literature and for which several indications of a high inclination angle have been reported.

The first source chosen is Swift J1357.2-0933, henceforth J1357, already introduced in the preceding chapter. For a detailed description of this source, please refer to Chapter 6.

MAXI J1305-704 (hereafter J1305) has been previously proposed as a high-inclination (BH) X-ray binary because of the detection of dipping behaviour during its outburst (Suwa et al. 2012, Shidatsu et al. 2013, Morihana et al. 2013, Kennea et al. 2012a). The source has an estimated distance of $d = 7.5^{+1.8}_{-1.4}$ kpc, which places it in the Galactic thick disc (Mata Sánchez et al. 2021).

J1305 has been studied in detail in the X-rays, but its follow-up at other wavelengths has been scarce (see Shaw et al. 2017; Miller et al. 2014; Shidatsu et al. 2013). The first optical spectroscopic analysis of this source during its 2012 outburst has been performed by Miceli et al. (2024 (Submitted), and it focused on the analysis of the double-peaked Hα emission line, revealing no conclusive evidence of outflow features within the system.

Shidatsu et al. (2013) revealed the presence of absorption dips in Suzaku X-ray data of the source, with a period of 9.74 ± 0.04 h, which they identified as the orbital period. Thereafter Mata Sánchez et al. (2021) inferred an orbital period of 9.456 ± 0.096 h and a $M_{BH} = 8.9^{+1.6}_{-1.0}\,M_{\odot}$, by analysing the orbital modulation in the quiescence optical light curve. The same authors obtained a constraint on the orbital inclination of $i = 72^{+5}_{-8}$ degrees, which supports the high inclination scenario. The number of observations, both in outburst and quiescence, as well as the well-constrained values of the inclination angle and other orbital parameters (e.g. orbital period, mass of the two objects), make J1305 one of the best candidates for our analysis.

7.3.0 Observations

For my work, I analyse different sets of observations for the two sample sources. The analysed data relating to J1357are the same collected by the GTC on 05-03-2016 between 03:32:11.4 and 06:19:5 and described in the previous chapter. For an in-depth description of their reduction process, please refer to Chapter 6.

J1305 has been observed both during an outburst and in a quiescent state. The initial observation took place during its discovery outburst in 2012, utilizing the 6.5-meter Magellan Clay telescope located at Las Campanas Observatory in Chile. This observation involved the use of the Low Dispersion Survey Spectrograph (LDSS-3) and the VPH-ALL Grism setup, allowing an extended range of wavelength coverage (see Table 4.3). The source was observed during quiescence on 2016 March 31 with the Very Large Telescope Unit Telescope 1 (VLT-UT1; Paranal Observatory, Chile) using the Focal Reducer/low dispersion Spectrograph 2 (FORS2, Appenzeller et al. 1998) in long-slit mode.

The outburst observations covered two consecutive nights, May 2nd (02:18:34 UTC to 02:56:41 UTC) and May 3rd (00:29:36 UTC to 01:09:03 UTC) with a 0.75" slit (see Fig. 7.1). The exposure time for each individual spectrum was set at 300 s, for a total of 6 spectra per night (Miceli et al. 2024 (Submitted). The datasets acquired during the quiescent state have been already presented in Mata Sánchez et al. (2021). They are composed of 16 spectra, with an exposure time of 1800 s each (except for the final one, which was integrated over 1200 s), collected consecutively for a total exposure of $\sim$ 9 h, i.e. covering almost an orbital period (Mata Sánchez et al. 2021). The configuration set up for the outburst observation allows us to focus on a range of wavelengths between 4500 - 6950 Å with a spectral resolution of R = 826, while the quiescence spectra cover a wavelength range between 5800 - 7300 Å with a spectral resolution of R $\sim$ 2140 and a dispersion of 0.76 Å/pix (see Table 4.3). The spectral resolution is obtained by measuring the FWHM of the skylines present in the background spectra.

I reduce the data using standard procedures based on IRAF[1] software, MOLLY tasks and PYTHON packages from ASTROPY and PYASTRONOMY (Astropy Collaboration et al. 2022). These tools allow us to correct the observed spectra from bias and flats, and to calibrate the data set, respectively. The spectra collected during the quiescence were reduced using the EsoReflex data reduction workflow (Freudling et al. 2013). Each spectrum was also corrected to the barycentric reference frame, using ASTROPY tools and the integrated ephemeris.

I note that the presence of cosmic rays contaminated J1357 spectra, so I corrected them using L.A. Cosmic task (van Dokkum et al. 2012), and I adopted the optimal extraction technique (Naylor 1998) to extract the two-dimensional images. J1305 quiescence spectra might be contaminated by the companion emission. However, as claimed by Mata Sánchez et al. (2021) the contamination should be less than 10% of the total flux, and so negligible.

[1] IRAF is distributed by the National Optical Astronomy Observatories, operated by the Association of Universities for Research in Astronomy, Inc., under contract with the National Science Foundation.

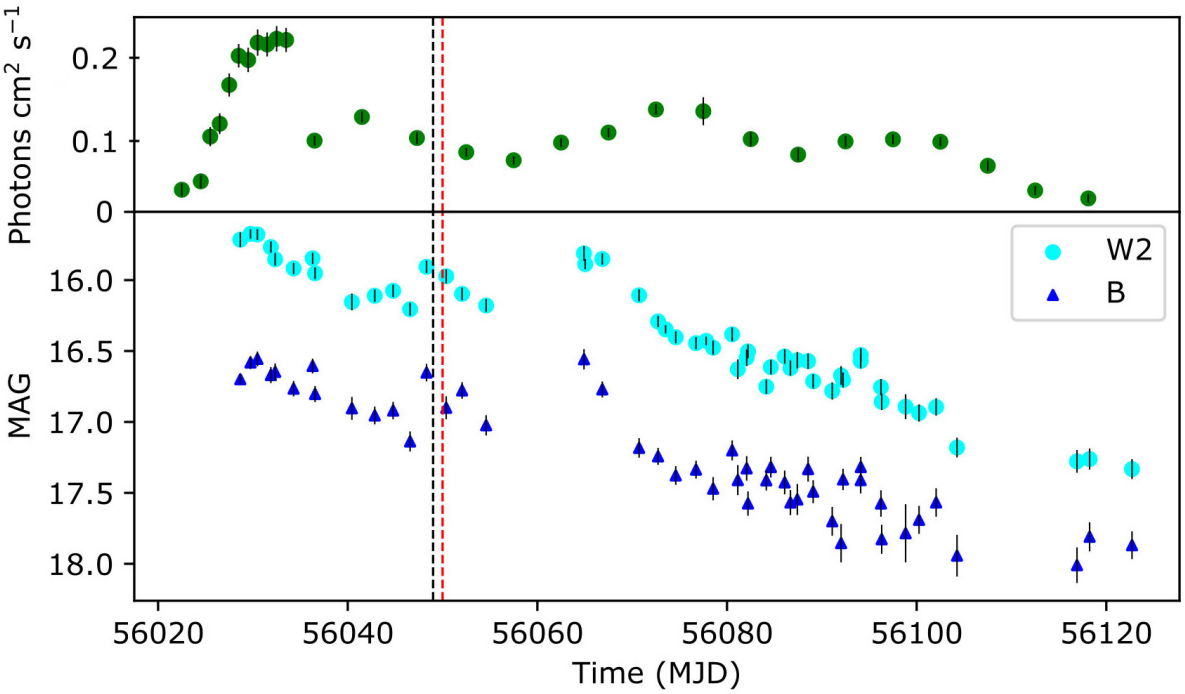

Figure 7.1: X-ray and UV/optical light curves of J1305 during the outburst. **Top panel** : MAXI light curve extracted in the range 2-10 keV. **Bottom panel** : UVOT light curve in the W2 ultraviolet and B optical band. The dotted black and red lines represent the two days of observations. The figure is adapted from Miceli et al. (2024 (Submitted)).

7.4.0 Analysis and results

7.4.1 The Diskline model

Emission lines of the Balmer series, associated with the atomic hydrogen transition, appear as broad symmetrical double-horned lines when observed from accretion discs at high inclination angles. In such systems, the emission is mainly influenced by the Doppler shift caused by the orbital motion of matter in the accretion disc around the compact object.

Considering a disc ring at a certain radius R_D, the matter in it moves at a Keplerian velocity V_{kep}. As explained in Chapter 3, for a distant observer, some of the matter within the disc moves toward the observer, while simultaneously, on the opposite side of the disc, it is moving away. This dual motion causes the observer to perceive the emission line as both blue and red-shifted simultaneously, resulting in the distinctive symmetrical double-horn profile. Additionally, because the emission comes from different regions of the disc surface, the overall line profile is broadened by the velocity distribution across the disc.

As discussed by Horne & Marsh (1986), this effect, and so the final line profile is highly influenced by the inclination angle of the system with respect to the line of sight, since the component of V_{kep} along the line of sight is $V_D = \pm V_{Kep}\,(R_D)\sin i$. Additionally, the resulting profile is influenced by various other effects. For instance, self-absorption by an optically thick disc atmosphere can contribute to deepening the inner core of the line. Simultaneously, disc precession may play a significant role in determining the orbital-averaged velocity shifts observed

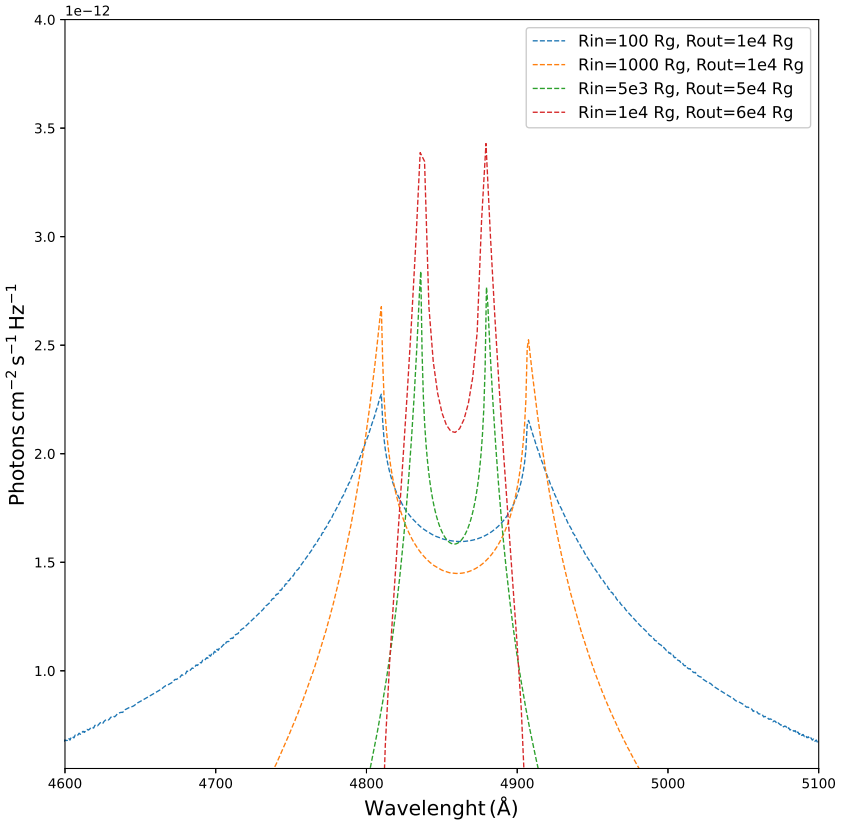

Figure 7.2: A series of examples showcasing the DISKLINE model profiles with fixed inclinations (i = 83 degrees), emissivity index (β = 2.5), and centroid wavelength (λ = 4861.3 Å) across all models. The inner and outer radius values were systematically varied within the ranges of $(100 - 10^4)$ R_g and $(10^4 - 6 \times 10^4)$ R_g, respectively, to highlight the variations in the line profiles. Model normalizations were scaled for visual clarity.

in the emission line centroid (Torres et al. 2002), while the presence of a hot spot can enhance one of the two peaks of the line.

The X-ray spectral-fitting program XSPEC (Arnaud 1996) provides several models to describe an emission line shaped by Doppler effects, from a Keplerian accretion disc. Among them, one of the most commonly adopted to fit double-horned emission lines is the DISKLINE model (Fabian et al. 1989). It is usually adopted to describe the iron Kα emission line that characterises the reflection spectrum observed in LMXBs (see e.g. di Salvo et al. 2009).

The shape of the broad iron fluorescence line observed at X-ray wavelengths, similar to the hydrogen Balmer series lines in optical spectra, is affected by Newtonian Doppler shift; however, its profile appears quite different. We already saw that the Fe Kα line originates in the innermost part of the accretion disc, where the velocity of matter reaches relativistic values. Consequently, the relativistic beaming affects the emission intensifying the blue peak of the line, while weakening the red peak. Furthermore, the line experiences gravitational redshift due to the strong gravitational pull near the compact object, causing it to shift to lower energies in a way that is dependent on the distance from the compact object. As a result, the emission line appears broadened and asymmetric (see Fig. 3.6 in Chapter 3 for a example of how the profile is influenced by these effects).

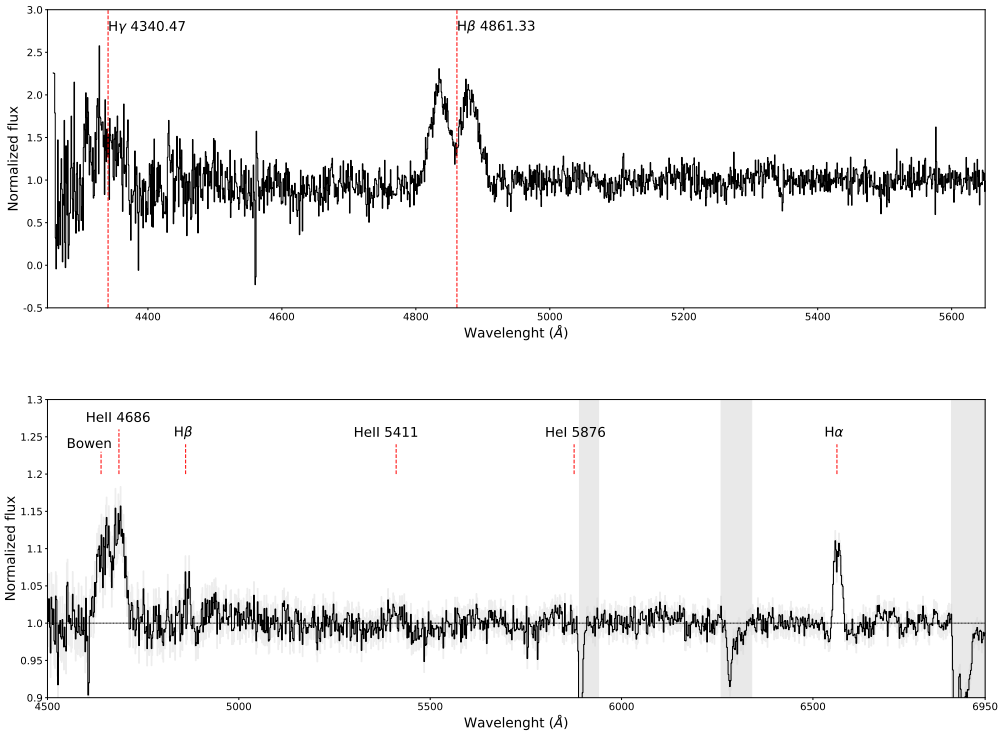

Figure 7.3: Average normalised spectra of the observations presented in the text related to J1357 (top panel) and the first day of J1305 (lower panel).

The DISKLINE model is composed of the following free parameters determining the shape of the emission line profile: the line energy, the inner (R_{in}) and outer radius (R_{out}) of the emission region in the disc (expressed in unit of gravitational radii, $R_g = GM/c^2$), the orbital inclination of the system and the index, β, describing the dependence of the disc emissivity on the distance from the compact object ($E \propto R^{-\beta}$). This model has been previously used several times to obtain constraints on the inclination angle of LMXBs (see e.g. Anitra et al. 2021; Iaria et al. 2009; Cackett et al. 2008), when relativistic effects are not dominant. Although the model mentioned above is usually adopted to describe a (relativistic) emission line, it can be adapted to model the hydrogen lines profile as well. Indeed, if the value of the inner and outer radius is high enough, meaning that the emission region of the line are far from the compact object, the relativistic beaming and the gravitational redshift become negligible and only the Newtonian Doppler shift is predominant (see Fig. 7.2). Under these conditions, the model is equivalent to the optically thin solution presented in Horne & Marsh (1986).

In order to isolate the emission line profile, on which I focus my analysis, I normalised J1357 and J1305 spectra, dividing them by their polynomial best-fit functions. Specifically, I apply a 3rd-order polynomial fit for the first one and a 5th-order polynomial fit for the other. I have therefore adapted our optical data sets to be analysed in the XSPEC environment, by creating a unit diagonal response matrix of the data size. In this paper, I adhere to the following naming convention: spectra linked to J1357 are denoted as src1-Q, whereas those associated with J1305 are labelled as src2-O during outburst, and src2-Q during quiescence.

7.4.2 J1357 spectroscopy

The wavelength coverage of our spectra allows us to focus on the Hβ line region with a sufficiently high signal-to-noise ratio (see Fig. 7.3 for the normalised average spectrum of the source).

I fit the 8 spectra simultaneously using a power-law model to account for the normalised continuum (the associated parameters are not physically relevant), on top of which I added the DISKLINE model to fit the Hβ line profile. Given that the observations are obtained within a time interval of 2.75 h (an orbital period), I expect minimal spectral variations across the different spectra. As a result, I constrain specific parameters, such as the inclination angle, emissivity index, and inner and outer radii, to remain the same for every spectrum, while I let the energy of the line free to vary. The model, hereinafter named MODEL 1, achieves a poor fit to the data, with a χ^2/d.o.f.= 4089.1/2811. Nonetheless, the values for the inner and outer radii of the line emission region within the disc, $9.6 \pm 0.2 \times 10^3$ R$_g$ and $5.4^{+0.1}_{-0.2} \times 10^4$ R$_g$ respectively, align with expectations. Additionally, the emissivity index characterizes a region of the disc located further from the compact object. However, as it is possible to see in Fig. 7.4 (second panel), I noticed the presence of residuals in the region between the two peaks.

To improve the fit without modifying the DISKLINE model, I attempt two different approaches. Firstly, I masked out the core of the line, excluding those data from the fit. The resulting best-fit parameters are consistent with those previously presented, with a χ^2/dof = 4071.72/2805. Secondly, I introduced a Gaussian absorption line with a centroid and FWHM parameters linked for all the spectra but allowing independent variable depth to check whether each spectrum significantly required this feature (see section 7.5). This model, henceforth referred to as MODEL 2, achieves a better fit to the data with a χ^2/dof = 3849.0/2794. I test the improvement of the fit using the statistical test F-TEST, obtaining a probability of chance improvement of $\sim 1.1 \times 10^{-28}$, meaning that the inclusion of the Gaussian line in absorption improves the quality of the fit with a confidence level (c.l.) higher than 7σ. The new model provides a more solid constrain on the inclination angle (i=83^{+5}_{-3} degrees) and the Hβ emission line is consistent with being emitted by a ring in the disc with radii between $9.6^{+0.2}_{-0.1} \times 10^3$ R$_g$ and $5.7^{+0.1}_{-0.2} \times 10^4$ R$_g$, respectively.

7.4.3 J1305 spectroscopy

Outburst

The wavelength coverage and spectral resolution provided by the telescope set-up allow us to perform a high-resolution analysis focused on the Hα emission line. In the spectra collected during the outburst, I identify Hα and Hβ emission lines, corresponding to the Balmer series and He II 4686 Å as the Bowen blend (a mixture of N III and C III emission lines, see e.g. Steeghs & Casares 2002)(see Fig. 7.3). I decided to focus our analysis on the Hα line, which is present which is present in all spectra in the two days. I analyse separately the two days of optical observations. For the first day, I use four of the six spectra (see Fig. 7.5) excluding, in particular, src2-O1 because of its high absorption component and src2-O3 because it does not

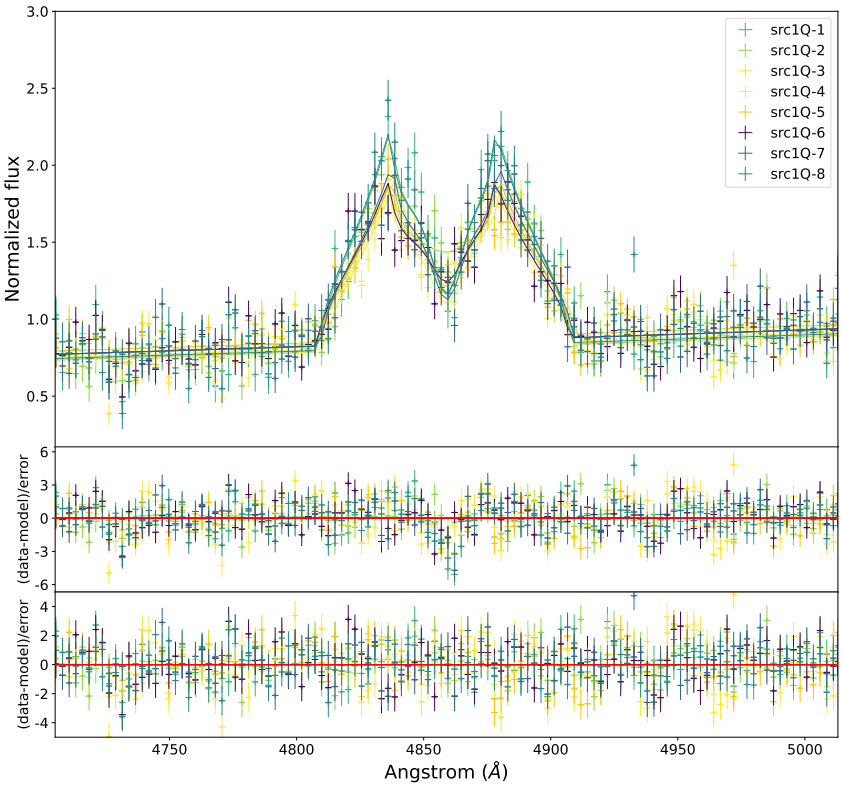

Figure 7.4: J1357 spectra collected during a quiescent phase and residuals in units of sigma with respect to the DISKLINE model described in the test (top panel). The middle and bottom panel shows the residuals obtained by using only the DISKLINE model (MODEL 1) and those obtained with the same model plus a Gaussian absorption line (MODEL 2), respectively.

show a double-peak profile but rather a flat top profile (reminiscences of outflows features, Miceli et al. (2024 (Submitted), see also Cúneo et al. 2020).

I apply MODEL 1 to the data and I link the parameters of each spectrum as described in the previous section. On the second day of observations, a distinct absorption component is evident in all spectra, located at wavelengths longer than those associated with the Hα line (about 6563 Å, as shown in Fig. 7.5). To take account of this feature I add to the previous model, a Gaussian absorption line with centroid and FWHM parameters linked for all the spectra, but allowing independently variable depth. For both days, the adopted models achieve a reasonably good fit to the data, with a χ^2/dof = 139.4/153 (first day) and χ^2/dof = 149.0/222 (second day). The best-fit parameters are reported in Table 7.2, while the spectrum and residuals are shown in Fig. 7.8. On both days I find a value of the inclination angle of 70 ± 4 and 71 ± 4 degrees, consistent with that reported in literature ($i = 72^{+5}_{-8}$ degrees, Mata Sánchez et al. 2021). Additionally, for the first day, I derived inner and outer radii values of $1.20^{+0.09}_{-0.07} \times 10^5$ Rg and $1.96^{+0.32}_{-0.27} \times 10^5$ Rg, respectively. For the second day, these values were $1.66^{+0.10}_{-0.08} \times 10^5$ Rg and $2.73^{+0.9}_{-0.6} \times 10^5$ Rg. Further discussion of these parameters is presented in the following section.

Quiescence

Among the 16 spectra available for the quiescent phase (see Fig. 7.6), I choose those that show a more regular line profile, for a total of 10 spectra. My preference lies with line profiles

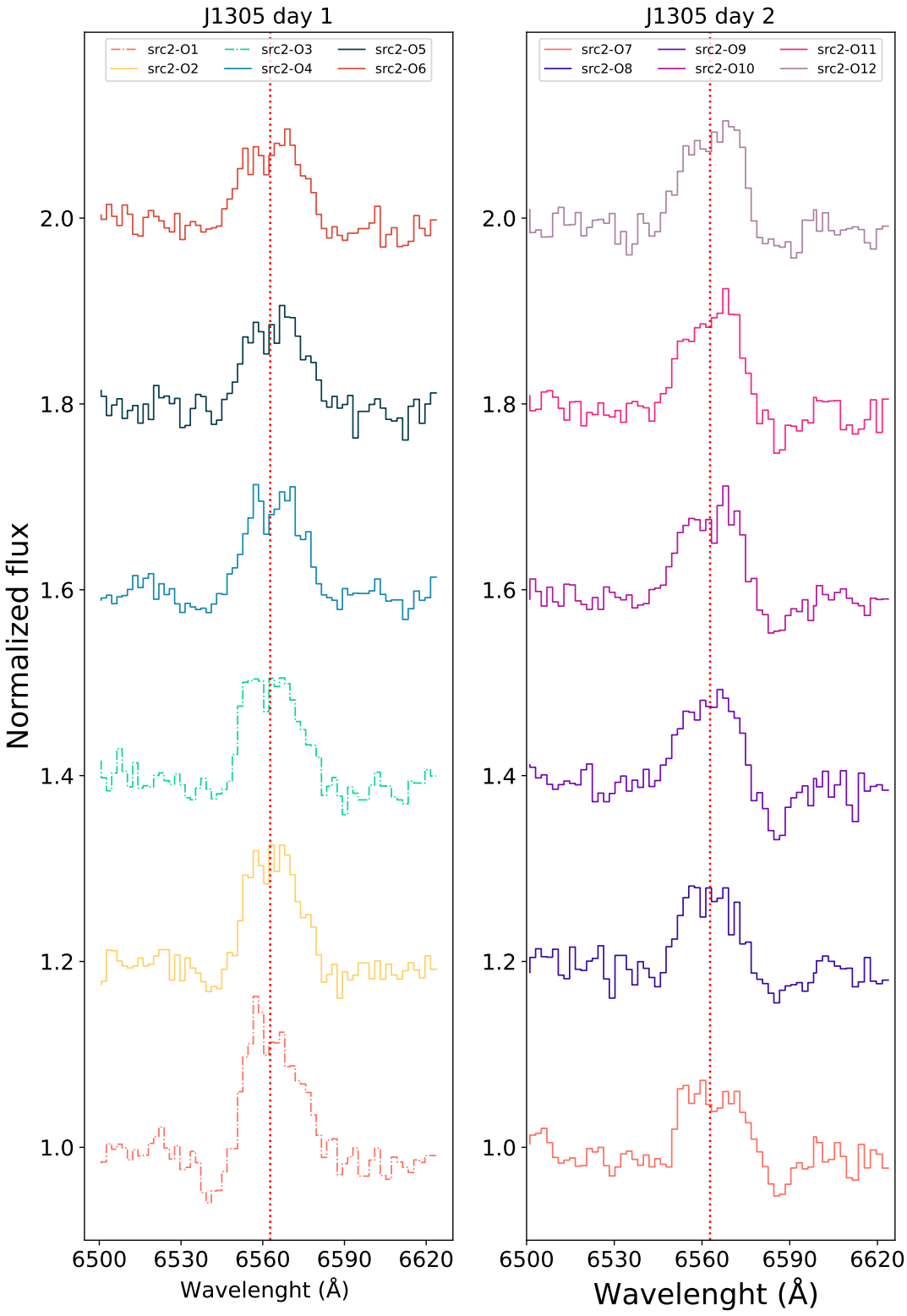

Figure 7.5: Individual Hα emission lines extracted from the outburst spectra obtained during the two days of observation. The solid lines represent the spectra selected for the analysis, whereas the dashed lines correspond to those spectra that have been discarded. For visual clarity, the normalized profiles have been vertically separated by a constant offset.

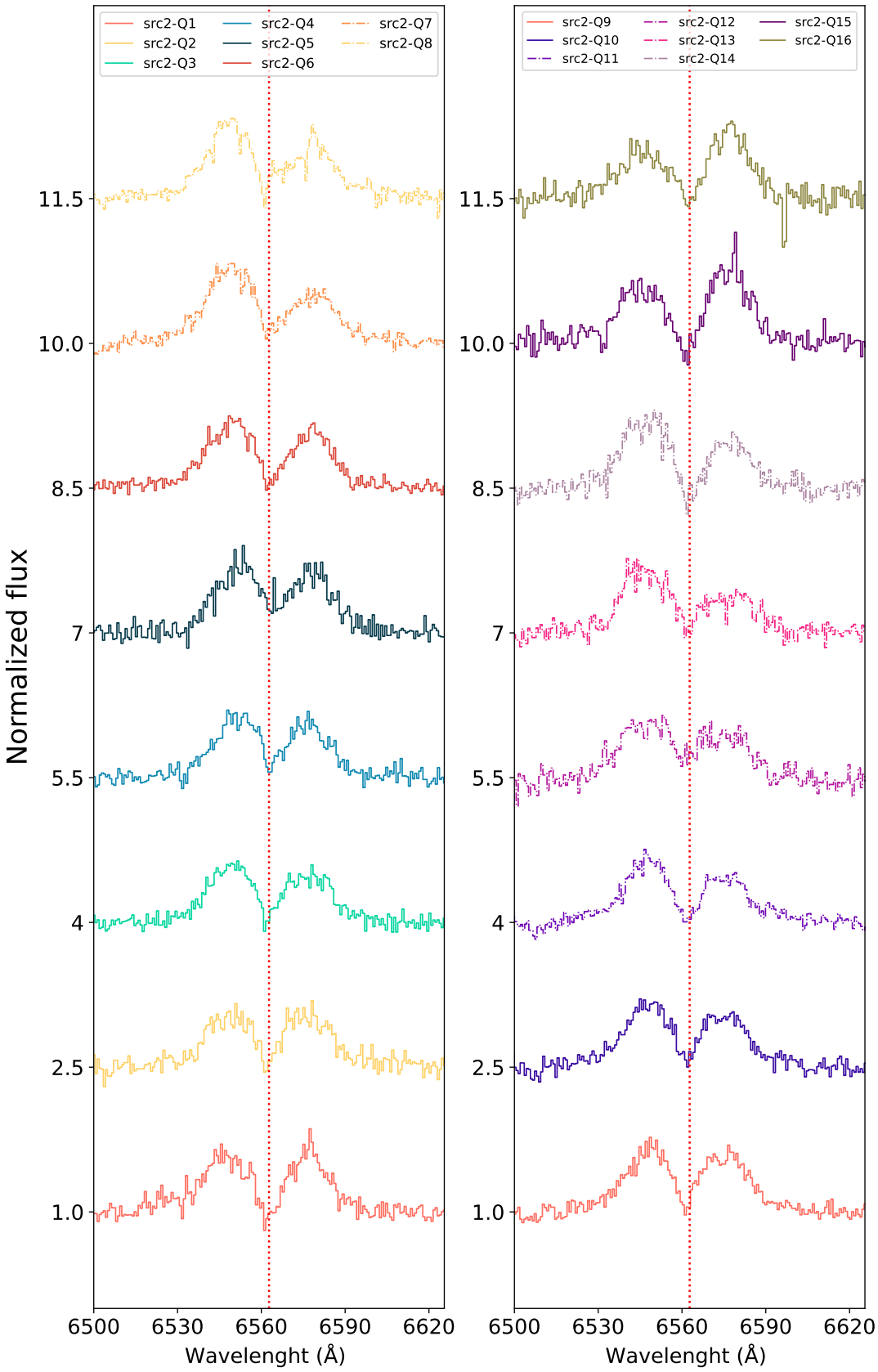

Figure 7.6: Individual Hα emission lines extracted from the spectra collected during the quiescent phase. The solid lines represent the spectra selected for the analysis, whereas the dashed lines correspond to those spectra that have been discarded. For visual clarity, the normalized profiles have been vertically separated by a constant offset.

SPECTRA	I_B/I_R	SPECTRA	I_B/I_R
src2-Q1	1.03 ± 0.09	**src2-Q9**	1.05 ± 0.06
src2-Q2	0.97 ± 0.09	**src2-Q10**	1.20 ± 0.07
src2-Q3	1.18 ± 0.06	src2-Q11	1.34 ± 0.07
src2-Q4	1.17 ± 0.08	src2-Q12	1.28 ± 0.07
src2-Q5	1.13 ± 0.06	src2-Q13	1.64 ± 0.09
src2-Q6	1.22 ± 0.06	src2-Q14	1.51 ± 0.09
src2-Q7	1.55 ± 0.06	**src2-Q15**	0.77 ± 0.08
src2-Q8	1.41 ± 0.07	**src2-Q16**	0.77 ± 0.11

Table 7.1: Values of the ratio between the blue and red peaks of the J1305 spectra collected during quiescence. The bold values represent the spectra chosen for the spectral analysis.

displaying a symmetrical double peak, since the asymmetry in the intensity of the two peaks can be caused by various effects, e.g. the presence of a hot spot (Shafter et al. 1986), and it could bias our measurement. The symmetry of the profile can be estimated by examining the ratios between the two peaks, as reported in Tab. 7.1. Following the same procedure applied to J1357, I first fit the spectra applying MODEL 1. However, the latter does not reach a good fit to the data, with a χ^2/dof of 6432.32/2650, and a clear presence of residuals in the core region. Therefore, I apply MODEL 2, linking the parameters among different spectra as described for J1357 spectra. The model achieved a good fit to the data, ensuring a χ^2/dof of 4161.1/2620 (see Fig. 7.7). I obtain a strong constraint on the inclination angle (73 ± 1 degrees), as well as best-fit values for the inner and outer radius of the emitting region associated with the Hα emission line of $1.94^{+0.06}_{-0.08} \times 10^4$ R_g and $2.01 \pm 0.03 \times 10^5$ R_g, respectively.

7.5.0 Discussion

I analyze GTC observations of J1357 collected during quiescence, along with VLT and Magellan observations of J1305, taken during quiescence and outburst phases, respectively. Our study focuses on the double-peaked profiles of Hβ and Hα emission lines. With the aim of gaining insights into the system's geometry, I employ an innovative approach by incorporating the DISKLINE model. As discussed in the previous section, the model including the DISKLINE component, along with a (Gaussian) absorption line provides a better fit to the data of both systems. This results in a significant improvement in the quality of the fit with respect to the model without the absorption line.

The addition of this feature may be necessary due to the potential limitations in the assumptions made by the aforementioned DISKLINE model. In fact, this model describes a Gaussian emission line profile, modified by the Doppler effect induced by a Keplerian velocity distribution, in an optically thin accretion disc. It is clear that the model does not take into account self-absorption or other features due to the optically thick nature of the disc, an effect already noticed by Orosz et al. (1994). This effect is particularly important for high inclination angles, as it appears to be

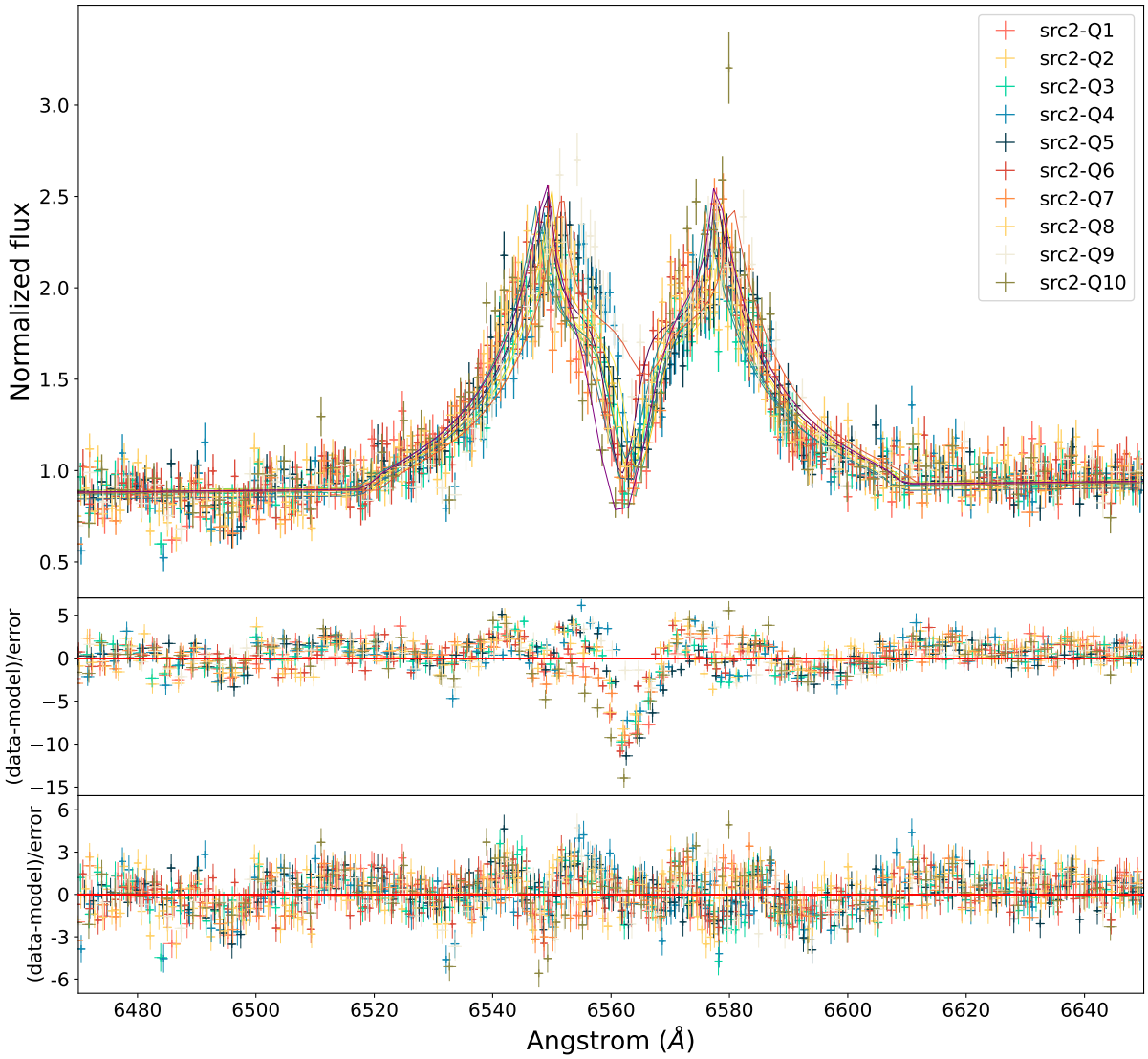

Figure 7.7: J1305 spectra collected during a quiescent phase and residuals in units of sigma with respect to the DISKLINE model described in the test (top panel). The middle and bottom panels show, respectively, the residuals obtained by using only the DISKLINE model (MODEL 1) and those obtained with the same model plus a Gaussian absorption line (MODEL 2).

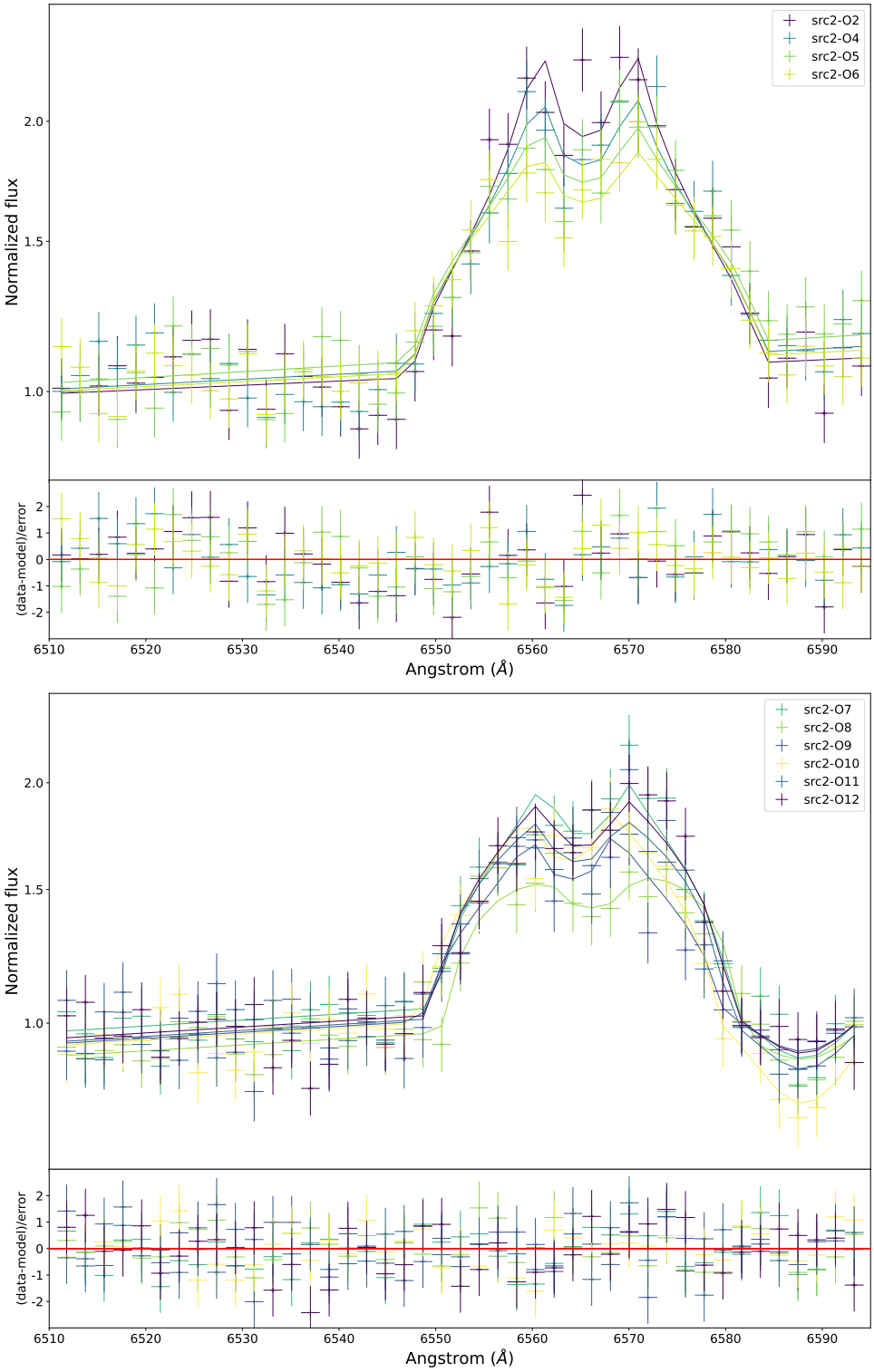

Figure 7.8: **Upper panel**: J1305 spectra collected during an outburst phase and residuals in units of sigma with respect to the DISKLINE (MODEL 1), related to the first day of observation. **Lower panel**: spectra collected during an outburst phase and residuals in units of sigma with respect to the DISKLINE model plus an absorption Gaussian line, related to the second day of observation.

the case of J1357 and J1305. This aligns with our results, where an extra Gaussian absorption enabled a better description of the observed feature.

Investigating the nature of the absorption component between the two peaks of the line can provide further insights into the geometry of the system. Upon visually examining the individual spectra, it becomes clear that the central core of the line displays narrow and variable absorption, changing in depth and even reaching (sometimes going below) the continuum average level. Such features in the emission lines from an accretion disc were mainly detected in cataclysmic variables observed at a high inclination angle (with $i > 75$ degrees, Schoembs & Hartmann 1983), and they are thought to be caused by occultation of the inner regions of the accretion disc.

In this scenario, only the central core of the line, which traces the radiation emitted from the portion of the disc at null velocity, will be concealed. In contrast, the blue and red-shifted peaks associated with high-velocity regions will remain unaffected and unobstructed (Horne & Marsh 1986). Differently from the effects caused by self-absorption, narrow cores are variable with the orbital phase, and they can get much deeper than the optically thick absorption effects, reaching even below the normalised continuum (Rayne & Whelan 1981).

The presence of narrow variable cores in J1357 spectra has been claimed first by Mata Sánchez et al. (2015), who noticed a variation of the normalized flux of the Hα core, and it has been later confirmed by Anitra et al. (2023), analysing high-resolution data focused on the Hβ emission line. Mata Sánchez et al. (2021), performed dynamical studies on the same VLT data of J1305 presented in this paper, reporting narrow cores in the spectra.

As further proof of this, I calculated the significance of the absorption feature in each spectrum in units of sigma, comparing the normalization of the line with its uncertainty at 68% c.l. I found that the intensity of the line in J1357 src1-Q2, src1-Q3 and src1-Q6 is $\leq 3\sigma$, meaning that during these orbital phases, the absorption core of the line is negligible, while it is stronger in src1-Q1, src1-Q7 and src1-Q8. In the quiescent spectra of J1305, all the absorption lines are statistically significant at more than 7σ, except for the line associated with src2-Q15, where such a feature is not necessary. This result is very similar to that observed by Marsh et al. (1987b) in the dwarf nova system Z Cha, which exhibited a core depth variability along the orbit in every line of the Balmer series in the spectrum.

As reported in section 7.4.3, spectra collected during the outburst do not show narrow variable cores. However, the spectra collected on the second day of observation display absorption features at higher wavelengths compared to the Hα line, which may resemble an inverted P-Cygni, associated with the presence of inflows (Cúneo et al. 2020). Miceli et al. (2024 (Submitted) have extensively discussed the nature of this phenomenon and proposed the existence of a broad and variable absorption component observed in all spectra, which can influence the shape of the line. Nonetheless, the origin of this feature remains subject of debate.

7.5.1 Geometry of the emitting region

Inclination angle

The best-fit parameters of both sources provide a description of the system geometry in line with the high inclination hypothesis. I obtain an angle of 73 ± 1 degrees for J1305 during quiescence and angles of 70 ± 4 and 71 ± 4 degrees for the two days of outburst, respectively. These results are consistent with the previous constraint based on optical light curve analysis reported in Mata Sánchez et al. (2021), $i = 72^{+5}_{-8}$ degrees. It is important to note that all the errors calculated in this paper are at 90% c.l., whereas the referenced study presents errors at 68% c.l. Recently Casares et al. (2022) studying the inner core depth in J1357 spectra, derived

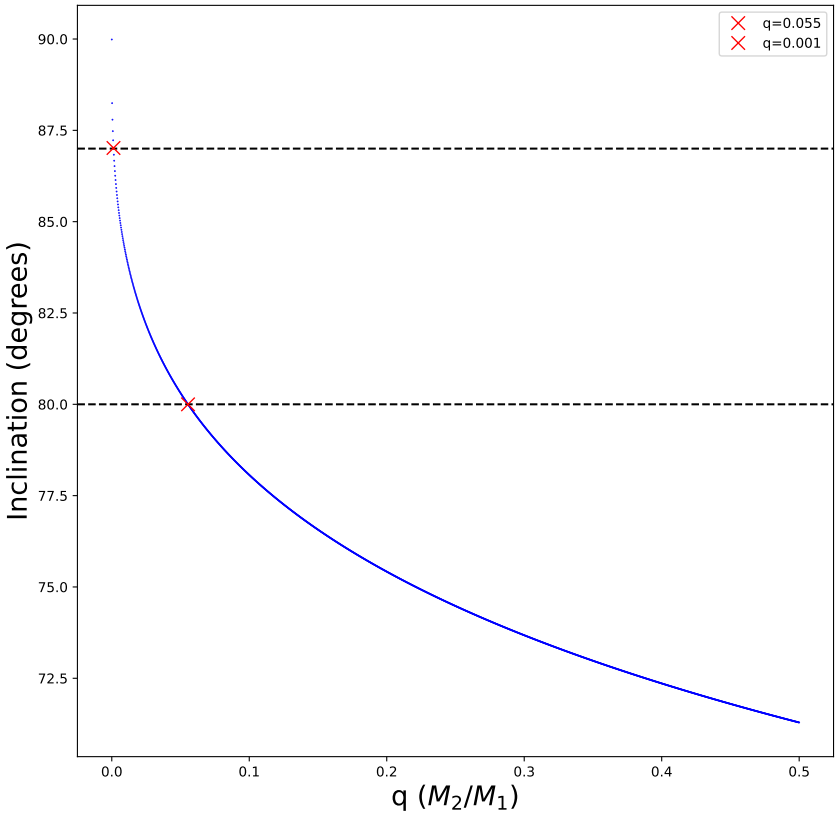

Figure 7.9: Inclination angle obtained with Eq. 7.1 by varying the mass ratio q in a range of 0 to 0.5. The dashed black lines represent the lower and upper bounds of the inclination values determined for J1357 when applying MODEL 2. Consequently, the data points highlighted with a red cross symbolize the lower and upper limits of the mass ratio q allowed for the system in order to preserve the lack of eclipses at that specific inclination.

an inclination angle of $87.4^{+2.6}_{-5.6}$ degrees, which matches the estimation I find by applying the DISKLINE model ($i = 83^{+4}_{-3}$ degrees). However, the lack of eclipses in both the X-ray and optical light curves of this source (Corral-Santana et al. 2013) contradicts the expected behaviour of an edge-on configuration. Corral-Santana et al. (2013) provided an explanation for this phenomenon, which may be due to the low mass ratio of the system, implying that the radius of the donor star is either comparable to or smaller than that of the outer rim of the disc. Consequently, even in an edge-on configuration, the central disc region remains unobstructed from eclipses by the companion star. It is possible to give quantitative credibility to this hypothesis by evaluating whether the mass ratio q given in literature allows the occurrence or absence of eclipses at a

particular inclination angle.

As stated by Iaria et al. (2018), the angle θ between the line of sight and the equatorial plane, defined as $i = (90^{\circ} - \theta)$ where i is the inclination angle, can be also described by the following equation:

$$\tan\theta = \left[\frac{R_2^2 - x^2}{a^2 - \left(R_2^2 - x^2\right)}\right]^{1/2}, \tag{7.1}$$

where R_2 is the Roche lobe radius of the companion star, a the orbital separation of the system and x the obscured region during the eclipse. Given the lack of eclipse, x can be assumed to be zero, while the Roche lobe radius for any value of q is given by the Eggleton (1983b) equation:

$$\frac{R_2}{a} = \frac{0.49q^{2/3}}{0.6q^{2/3} + \ln\left(1 + q^{1/3}\right)}. \tag{7.2}$$

By substituting R_2 into the previous equation, it becomes evident that the angle θ is solely a function of the mass ratio q. In order to investigate which combinations of q and θ preserve the condition of eclipse absence, I varied the q parameter within the range of 0 to 0.5 and determined the corresponding values of θ. The results are shown in Fig. 7.9.

Given the inclination I have derived of 83^{+4}_{-3} degrees, I can establish an upper and lower limit for the q ratio as 0.055 and 0.0013, respectively. This range aligns with the value reported in literature by Mata Sánchez et al. (2015). Moreover, with the mass function for M_1 ($f(M_1) = 11.0 \pm 2.1\,M_\odot$ as per Mata Sánchez et al. 2015) at our disposal, I can derive an analytical estimate for the mass of the companion star M_2. Substituting the obtained limit values for θ and q, I establish a range for M_2, which falls between $0.71 \pm 0.14\,M_\odot$ and $0.014 \pm 0.003\,M_\odot$ (note that Mata Sánchez et al. 2015 report a lower limit of $M_2 > 0.4\,M_\odot$). In other words, the inclination estimated for this system together with the limits on the mass ratio are in line with previous literature, and the mass range for the companion star M_2 characterises it as a low-mass star that fills its Roche lobe.

Inner and outer radius of the emitting regions

I found that the Hβ line in J1357 is emitted from a region bounded between $9.6^{+0.2}_{-0.1} \times 10^3\,R_g$ and $5.7^{+0.1}_{-0.2} \times 10^4\,R_g$, while the H$\alpha$ emission line observed in the J1305 spectrum describes two different emitting regions for outburst and quiescence. During the quiescent phase, the emission line is located between $1.94^{+0.06}_{-0.08} \times 10^4\,R_g$ and $2.01 \pm 0.03 \times 10^5\,R_g$ in the disc, while during the outburst the emitting region extends to radii between $1.20^{+0.09}_{-0.07} \times 10^5\,R_g$ and $(1.96 \pm 0.3) \times 10^6\,R_g$.

To validate our results, I examine whether the best-fit values obtained for the two systems accurately reflect the expected geometrical configuration or if they deviate from expectations. A reasonable way to verify this is by calculating the expected tidal radius of the system, i.e. the outer edge of the disc, truncated by the tidal torque of the companion star (Frank et al. 2002). Tidal radius relies on several binary parameters, but its value can be shown to be close to $R_T = 0.9\,R_1$ (Frank et al. 2002), where R_1 is the Roche lobe radius of the compact object, and this can be computed using Eq. 7.2 by substituting q with q^{-1}. I get an orbital separation value

and tidal radius for J1357 of a = $(1.0259 \pm 0.0002) \times 10^6$ R_g and $R_T = (5.9 \pm 0.004) \times 10^4$ R_g, and a = $(2.524 \pm 0.002) \times 10^5$ R_g, and $R_T = (1.45 \pm 0.06) \times 10^5$ R_g for J1305.

As can be seen in Table 7.2, the J1357 outer radius is smaller than the expected tidal radius, indicating that either the accretion disc does not extend to the tidal radius, or the Hβ emission line does not originate from the outermost region of the accretion disc. As for J1305, the best-fit value for the outer radius obtained during quiescence is consistent with the expected geometry of the system (although slightly higher than the tidal radius), while the radius obtained for the outburst spectra is totally out of scale. Indeed a value of about 2×10^6 R_g is an order of magnitude even larger than the orbital separation. Such deviation is not due to a miscalculation or to a limitation of the application of DISKLINE under certain circumstances. Miceli et al. (2024 (Submitted) reported a Doppler shift velocity of the peaks during the outburst of about 400 km s^{-1}. Considering a Keplerian disc, I can apply the third Keplerian law to calculate the corresponding radius and even in this case, the derived radius exceeded the orbital separation, amounting to approximately 5.49×10^5 R_g. This result could be due to effects present during the outburst that may influence the line profile. It is possible that the velocity distribution of the emitting region is not Keplerian. Under peculiar conditions, the dissipated energy in the disc is advected into the BH, leading to an advection-dominated accretion flow (ADAF) (Narayan et al. 1997). Although it has been reported in Narayan et al. (1997) that ADAF is also theorized at large radii, this behaviour is usually predicted for regions close to the compact object (Abramowicz et al. 1988; Chakrabarti & Titarchuk 1995). I also consider that in standard discs (Shakura & Sunyaev 1973a), the in-flowing material attains a stable equilibrium in which the radial component of the velocity is negligible compared to the azimuthal one. Nonetheless, if there is a surge in viscosity within that region, the radial velocity may cease to be negligible, and the way the matter accretes may deviate from the Keplerian regime.

An alternative explanation might be linked to the existence of a circumbinary disc around the binary system. Due to the high accretion rate, outflows of matter can occur, and the ejected material may subsequently remain around the system, giving rise to the formation of a viscous toroidal disc around the binary system (Chen & Podsiadlowski 2019). Although these discs are typically quite cold, there is a possibility that the enormous emission produced by the central source ($L_x \sim 10^{37}$ erg s^{-1} for J1305 during outburst, see Miller et al. 2014), irradiates these regions, thus providing the energy to trigger the atomic transitions that give rise to the Hα emission line. This would explain an emitting region greater than the orbital separation itself. However, these are only hypothetical answers to a question that needs further analysis to be solved.

7.5.2 Temperatures and Hydrogen ionization

Although our results seem to delineate an emitting region consistent with the disc geometry, at least during quiescence periods, it is crucial to consider the temperatures present at those radii. It is indeed true that the emission lines Hβ and Hα are associated with the energy transitions of neutral hydrogen. This means that if the temperatures are high enough, the amount of neutral

hydrogen will be negligible.

Shakura & Sunyaev (1973a) described the structure of the accretion disc around a BH, under the assumption that the disc is optically thick and geometrically thin. The authors divide the disc into three ideal regions, depending on the predominant type of pressure and cross-section, and derive a system of equations for each of them through which the physics of the accretion disc can be completely described. Since I am analysing the outer part of the disc, the equation that describes how the central temperature of the disc varies with the radius is the following:

$$T = 8.6 \cdot 10^{7} \alpha^{-1/5} \dot{m}^{3/10} m^{-1/5} r^{-3/4} \left(1 - r^{-1/2}\right)^{3/10}, \tag{7.3}$$

where $m, \dot{m}, r$ are non-dimensional parameters which contain the dependence on the mass of BH, the accretion rate and the radius, respectively (see section 3.1 for the explicit dependence). The parameter α denotes the accretion disc viscosity, typically ranging between 0.1 and 0.4 (King et al. 2007). For my analysis, I assumed an α value of 0.1 and used the NS mass values reported in the literature for the two sources (Mata Sánchez et al. 2021, 2015). The accretion rate was deduced using Equation 2.5, based on the quiescent X-ray luminosity values $L_X \sim 1.6 \times 10^{32}$ erg s^{-1} for J1357 (Mata Sánchez et al. 2021) and $L_X \sim 1.3 \times 10^{31}$ erg s^{-1} for J1357 (Armas Padilla et al. 2014a). As density does not significantly vary across the vertical height (z) at these so-large radii, it can be reasonably assumed that the surface temperature of the disc is approximately equal to the central temperature (Shakura & Sunyaev 1973a).

Taking into account the values of R_{in} and R_{out} I obtained through our analysis, I can provide an estimation of the temperature range related to Hβ and Hα emitting region. I have decided to consider only the quiescent phases for J1357 and J1305, as I have already discussed the reliability of the measurements during the outburst. I obtained temperature ranges of 2081 ± 255 K to 353 ± 40 K for J1305 and 2203 ± 317 K to 580 ± 81 K for J1357.

The degree of ionization for the H-atom, i.e. the fraction of ionised hydrogen with respect to neutral hydrogen at the estimated temperatures, can be computed using the Saha equation (Saha 1921):

$$\log \frac{H^+}{H} = \log \frac{u^+}{u} + \log 2 + \frac{5}{2} \log T - 5040 \frac{\chi_{ion}}{T} - \log P_e - 0.48 \tag{7.4}$$

Here $P_e = n_e kT$ is the electron pressure, where n_e is the electron density, typically assumed equal to 10^{18} cm^{-3} (Sincell & Krolik 1998). χ_{ion} is the ionization energy (13.6 eV for the H atom) and u is the partition function of the atom ($u(H) = 2$ and $u(H^+) = 1$, see Böhm-Vitense 1992). Assuming the temperatures I inferred above, I obtain a range of H^+/H between 10^{-25} and 10^{-114} for J1357, and between 10^{-45} and 10^{-186} for J1305. This implies that the amount of ionised hydrogen with respect to neutral hydrogen is negligible, and therefore the radii estimated for the emitting regions of the Hα and Hβ lines, for the two systems, appear physically plausible.

7.6.0 Conclusion

I presented a new approach for analyzing the emission lines found in the optical spectra of binary systems, which involves the use of the DISKLINE model, in order to obtain constraints on the system geometry.

I analysed two observations in quiescence of the X-ray binary BH candidates J1357 and J1305, respectively, and an observation collected during two days of outburst of the latter source. The best-fit parameters allowed us to provide a more detailed description of the geometry of these systems. The Hβ and Hα emission lines in J1357 and J1305 quiescence spectra are emitted by a ring in the disc between $(9.7 - 57) \times 10^3$ R_g and $(1.94 - 20) \times 10^4$ R_g, respectively. The analysis of the outburst spectra yielded an emission region that does not align with the expected system geometry, suggesting an outer radius exceeding even the orbital separation of the binary system. I have put forward several hypotheses to account for this behaviour, including advection-dominated accretion flow, a non-Keplerian disc, or the existence of a circumbinary disc.

Our analysis reveals that the inclination angles of both systems closely match the expected values, confirming their high-inclination nature. The proposed method requires further investigation since the physics of emission lines from accretion discs is far more complex, and the DISKLINE model provides a simplified description of the emission profile modified by Doppler effects in a Keplerian flow, without any consideration of self-absorption effects in the optically thick atmosphere of accretion discs. However, the application of the DISKLINE model to the disc emission lines in the optical band can be a powerful tool to provide a reliable geometrical description of these sources, allowing us to give precise estimations of the inclination angle, and also to gather information on the expected temperature and ionisation level of the emitting region. Further analyses, akin to the one presented in this manuscript, will be useful to provide additional evidence regarding the reliability of this method and to fully explore its capabilities.

Table 7.2: Best-fit values for the parameters of the two models described in the text that include the DISKLINE component. Uncertainties are at the 90% c.l.

	SPECTRA	DISKLINE						GAUSSIAN		
		λ (Å)	Index	$R_{in}(10^3\ R_g)$	$R_{out}(10^4\ R_g)$	Inc (degrees)	N	λ (Å)	σ (Å)	N
J1357	src1-Q1	$4857.522^{+0.001}_{-0.004}$	-2.34 ± 0.05	$9.6^{+0.2}_{-0.1}$	$5.7^{+0.1}_{-0.2}$	83^{+4}_{-3}	104 ± 4	$4861.274^{+0.005}_{-0.002}$	4.975 ± 0.003	-8^{+1}_{-2}
	src1-Q2	$4858.074^{+0.001}_{-0.002}$	*	*	*	*	79 ± 3	$4715.592^{+0.085}_{-0.123}$	*	-2^{+2}_{-1}
	src1-Q3	$4859.902^{+0.002}_{-0.003}$	*	*	*	*	81 ± 3	$4854.175^{+0.005}_{-0.035}$	*	-3.4^{+1}_{-2}
	src1-Q4	$4857.104^{+0.002}_{-0.001}$	*	*	*	*	76^{+2}_{-3}	$4859.217^{+0.005}_{-0.004}$	*	-5 ± 1
	src1-Q5	$4857.351^{+0.001}_{-0.002}$	*	*	*	*	75 ± 3	$4860.284^{+0.012}_{-0.027}$	*	-4 ± 1
	src1-Q6	$4856.780^{+0.003}_{-0.002}$	*	*	*	*	77^{+3}_{-4}	$4857.827^{+0.009}_{-0.006}$	*	-4 ± 2
	src1-Q7	$4858.112^{+0.002}_{-0.002}$	*	*	*	*	85 ± 4	$4857.446^{+0.003}_{-0.006}$	*	-6 ± 2
	src1-Q8	$4857.028^{+0.001}_{-0.002}$	*	*	*	*	103 ± 4	$4858.817^{+0.002}_{-0.008}$	*	-8 ± 2
	χ^2/dof	3849.0/2794								
J1305	src2-Q1	$6561.8715^{+0.0005}_{-0.0015}$	$-1.62^{+0.02}_{-0.03}$	$19.4^{+0.6}_{-0.8}$	20.1 ± 0.4	73 ± 1	$38.4^{+0.9}_{-1.7}$	$6562.9830^{+0.0005}_{-0.0015}$	3.182 ± 0.001	$-5.0^{+0.3}_{-0.7}$
QUIET	src2-Q2	$6562.9483^{+0.0010}_{-0.0008}$	*	*	*	*	34 ± 1	$6561.8715^{+0.0013}_{-0.0005}$	2.426 ± 0.001	$-2.9^{+0.3}_{-0.4}$
	src2-Q3	$6562.9136^{+0.0007}_{-0.0004}$	*	*	*	*	$35.5^{+1.2}_{-0.7}$	$6562.9483^{+0.0007}_{-0.0008}$	2.430 ± 0.001	$-2.8^{+0.3}_{-0.4}$
	src2-Q4	$6563.9907^{+0.0008}_{-0.0028}$	*	*	*	*	$37.5^{+0.8}_{-0.9}$	$6562.9136^{+0.0006}_{-0.0008}$	1.853 ± 0.001	$-1.8^{+0.2}_{-0.3}$
	src2-Q5	$6565.6592^{+0.0006}_{-0.0005}$	*	*	*	*	40 ± 1	6565.66 ± 0.04	2.462 ± 0.005	-3.9 ± 0.3
	src2-Q6	$6564.2687^{+0.0005}_{-0.0006}$	*	*	*	*	$39.6^{+1.1}_{-0.8} \pm 1$	$6563.9907^{+0.0010}_{-0.0006}$	3.013 ± 0.001	$-3.0^{+0.4}_{-0.3}$
	src2-Q9	$6561.5589^{+0.0005}_{-0.0004}$	*	*	*	*	$39.8^{+0.7}_{-1.1} \pm 1$	$6564.2687^{+0.0004}_{-0.0008}$	2.237 ± 0.000	$-4.7^{+0.4}_{-0.7}$
	src2-Q10	6562.5314 ± 0.0007	*	*	*	*	38 ± 1	$6562.5314^{+0.0012}_{-0.0006}$	2.571 ± 0.001	$-2.9^{+0.4}_{-0.3}$
	src2-Q15	$6561.4548^{+0.0009}_{-0.0006}$	*	*	*	*	$43.0^{0.9}_{-1.8}$	$6561.4548^{+0.0007}_{-0.0010}$	3.996 ± 0.001	$-1.0^{+0.2}_{-0.7}$
	src2-Q16	$6562.5314^{+0.0009}_{-0.0007}$	*	*	*	*	38 ± 1	$6561.5589^{+0.0007}_{-0.0017}$	3.507 ± 0.001	$-7.5^{+0.5}_{-0.6}$
	χ^2/dof	4161.1/2620								
J1305	src2-O2	$6565.0682^{+0.0009}_{-0.0009}$	-2.4 ± 0.1	120^{+9}_{-7}	196^{+32}_{-27}	70 ± 4	1.6 ± 0.1	-	-	-
DAY 1	src2-O4	$6565.1377^{+0.0008}_{-0.0019}$	*	*	*	*	1.35 ± 0.09	-	-	-
	src2-O5	$6566.042^{+0.002}_{-0.001}$	*	*	*	*	1.21 ± 0.09	-	-	-
	src2-O6	$6565.173^{+0.002}_{-0.001}$	*	*	*	*	1.20 ± 0.09	-	-	-
	χ^2/dof	139.4/153								
DAY 2	src2-O7	6565.103 ± 0.001	-2.7 ± 0.2	166^{+10}_{-8}	273^{+90}_{-60}	71 ± 4	$1.16^{+0.11}_{-0.08}$	$6587.953^{+0.002}_{-0.002}$	4.901 ± 0.002	$-0.24^{+0.09}_{-0.06}$
	src2-O8	$6566.077^{+0.002}_{-0.001}$	*	*	*	*	$0.9^{+0.11}_{-0.08}$	*	*	$-0.16^{+0.05}_{-0.10}$
	src2-O9	$6563.886^{+0.094}_{-0.002}$	*	*	*	*	$0.9^{+0.11}_{-0.09}$	*	*	$-0.17^{+0.07}_{-0.08}$
	src2-O10	$6563.574^{+0.001}_{-0.002}$	*	*	*	*	$1.11^{+0.07}_{-0.15}$	*	*	$-0.33^{+0.11}_{-0.05}$
	src2-O11	$6564.686^{+0.002}_{-0.001}$	*	*	*	*	$1.11^{+0.11}_{-0.09}$	*	*	$-0.23^{+0.09}_{-0.06}$
	src2-O12	$6564.929^{+0.001}_{-0.001}$	*	*	*	*	1.17 ± 0.09	*	*	$-0.20^{+0.09}_{-0.06}$
	χ^2/dof	149.0/222								

* Kept linked to the first data set during the fit.

8 Ongoing work: The polarized reflection spectrum of 4U 1820-30

Recent advancements in polarimetric capabilities, particularly with the **Imaging X-ray Polarimetry Explorer** (*IXPE*), have opened new opportunities for understanding the geometry of LMXBs. Measuring the degree and angle of polarization in the radiation emitted by these systems is essential for decoding their geometric structure and the fundamental radiative mechanisms at play. This is because distinct spectral components such as Comptonization, blackbody radiation, and reflection each contribute differently to the overall polarization. Before the advent of *IXPE*, X-ray polarimetry was a relatively unexplored field due to technological constraints. *IXPE* high sensitivity in detecting polarized X-rays allows for detailed observations of the polarization properties in these systems.

Among the NS LMXBs, 4U 1820-30 stands out due to its unique characteristics. It has the shortest known orbital period of any X-ray binary at just 11.4 minutes (Stella et al. 1987), classifying it as an Ultra-Compact X-ray Binary (for a review see Armas Padilla et al. 2023). It is also part of a peculiar subclass known for exhibiting super-orbital accretion modulations, which in this system, manifest as a 170-day cycle of varying X-ray flux (Chou & Grindlay 2001). During this cycle, the system predominantly exhibits a soft state, also known as the "banana" state, and does not transit to a full hard state. Spectroscopic analysis I was involved in (Marino et al. 2023), reveals that the X-ray flux modulation is largely driven by changes in the size of the region providing seed photons for the Comptonisation spectrum. This region, believed to be the *boundary layer*, is larger in the high mode and contracts significantly in the low mode. Furthermore, the electron temperature of the corona and the root mean square (RMS) variability in hard X-rays display a slight increase during the low mode. In Di Marco & IXPE Science Team (2023) I conducted a spectral analysis of data from *NuSTAR* and *NICER* of 4U 1820-30, with the aim of providing a robust spectral model for analysing *IXPE* data. This approach enabled us to detect significant polarization in X-rays, particularly above 4 keV, indicating a distinct energy trend. The polarization is interpreted as stemming from the accretion disc, polarized orthogonally to the hard spectral component produced in the boundary/spreading layer.

Currently, my work is focused on analyzing *NICER* and *NuSTAR* data collected concurrently with three *IXPE* observations of this source. *IXPE* observed 4U 1820-303 on October 11, 2022,

from 13:53 to 22:55 UTC for a total exposure of 16 ks and from April 15 to April 16, 2023, from 01:33 to 23:17 UTC for a total exposure of 86 ks per DU. Due to the limited energy range (2-8 keV), *IXPE* is unable to completely characterize the emission components on its own. Therefore, it is necessary to integrate *IXPE* observations with additional methods like spectroscopy and timing analysis from other instruments to provide a more comprehensive picture of the system behavior. During both periods of *IXPE* observations, simultaneous measurements were taken using *NICER* and *NUSTAR*. Specifically, I have been analyzing *NICER* data collected on October 11, 2022, for approximately 1.7 ks, and on April 15 and 16 2023, captured in various snapshots, amounting to roughly 10.3 ks and 13.7 ks in exposure time, respectively. Additionally, *NUSTAR* data from the same days were examined, with a total exposure time of 48.9 ks.

8.0.1 Spectral analysis and results

After a simultaneous initial fit of both *NICER* and *NuSTAR* average spectra, I found the spectral shape from the data collected in October and on April 16 exhibited remarkable similarities. This observation led me to perform a simultaneous fitting of these two datasets while separately analyzing the data from April 15.

The model used to describe the continuum included an emission from the accretion disc consisting of multi-color blackbody component, termed DISKBB in XSPEC (Makishima et al. 1986), alongside a Comptonized component modelled by the COMPTB component (for a complete description of the model see Farinelli et al. 2008). This model deviates from the prior Comptonization models employed in this thesis by introducing a component of inward bulk motion. Nonetheless, this aspect can be neglected by fixing the efficiency of bulk over thermal Comptonization, denoted as δ, to zero. Additionally, a power law comprising the POWERLAW and EXPABS models, introduced to simulate a cutoff at the seed photon temperature to limit the low-energy contribution, was utilized to take into account residuals at high energies. Furthermore, the reflection spectrum, as detailed in Chapter 5, was modeled using a combination of RDBLUR, RFXCONV, and COMPTB, where parameters of the latter were linked to the Comptonization component. To account for the interstellar medium absorption and allow for variations in Iron and Oxygen abundances, the total emission from the system was also multiplied by the TBFEO model. This adjustment was crucial since *NICER* spectra often display residuals potentially linked to the Oxygen K edge (0.56 keV) and Iron L edge (0.71 keV), suggesting an under or overabundance of these elements in the interstellar medium[1]. The model applied for both fits is structured as follows:

$$\begin{aligned}\text{Model 1= constant*TBfeo*(expabs*powerlaw + rdblur*rfxconv*comptb} \\ \text{+ comptb + diskbb).}\end{aligned} \tag{8.1}$$

This model achieved a good fit to the data, indicated by a χ^2/d.o.f. of 816.0/778 for the fit related

[1]See https://heasarc.gsfc.nasa.gov/docs/nicer/data_analysis/workshops/NICER-CalStatus-Markwardt-2021.pdf

to October and 16th April observations and 358.4/411 for the 15th April one. The resulting spectrum and residuals are shown in Figure 8.1. The continuum emission is well fitted by a black body emission at 0.63 ± 0.06 keV and a saturated Comptonisation spectrum produced by an optically thick corona with an electron temperature for 2.9 ± 0.03 keV, for both fits.

Crucially, the derived values align closely with the anticipated system geometry. I found a size of the black body emitting region, calculated through the formula: $K_{\rm disc} = \left(\frac{R_{\rm disc}}{D_{\rm 10kpc}}\right)^2 \cos i$, where i is the inclination of the system obtained from the best fit (see Table 8.1), of 19 ± 2 R_g and 20.4 ± 0.6 R_g, where I corrected of a factor 1.7 to obtain the true size of the region (Kubota et al. 1998). Both the values obtained are in agreement with the inner disc radius determined through the reflection model. Regarding the size of the emission region of the seed photons for Comptonization, I obtained values of 7.6 ± 0.4 R_g and 6.83 ± 0.07 R_g, for both fits, respectively, outlining a region compatible with the surface of the NS.

In my analysis, I have, for the first time, obtained evidence of a strong reflection component in the spectrum of the source. The reflection fraction is about $0.22^{+0.03}_{-0.12}$ for the first fit, and decreases to $0.18^{+0.02}_{-0.05}$ in the second. The best fit parameters indicate an emission originating from a region close to the NS ($R_{in} = 19^{+20}_{-7}$ R_g), even if the value obtained through the second fit is not well contrained ($R_{in} = 48^{+140}_{-25}$ R_g). The obtained inner radii values are furthermore in accordance with the internal system geometry proposed by Marino et al. (2023), obtained using a comparable spectral model, although it did not include any reflection component. Due to the presence of the reflection spectrum, I have obtained, for the first time, a constraint on the system inclination angle: 29^{+7}_{-6} degrees for the first fit and 15^{+16}_{-12} degrees for the second one. This finding is in agreement with the low inclination hypothesis reported in literature (Anderson et al. 1997; Marino et al. 2023). During the fitting process, I allowed for variations in the iron abundance in the disc, as this adjustment improved the fit, especially when the abundance was set lower than solar, finally stabilizing at 0.21. This observed sub-solar iron abundance, both in the disc material and the interstellar medium ($nH_{Fe} < (0.63 - 0.74)$), could be attributable to the source location within a globular cluster. Globular clusters, characterized by their ancient stellar populations, frequently exhibit chemical compositions distinct from the solar ones. They are particularly notable for their varied abundances of heavier elements like iron and likely stemming from their unique evolutionary trajectories and potential formation outside the galactic disk or via distinct nucleosynthetic processes (Kraft et al. 1962). We should also take into account that the companion star is a helium white dwarf (Stella et al. 1987; Rappaport et al. 1987). This observation could provide a plausible explanation for the diminished presence of iron in the disc, potentially shedding light on a shared feature among other ultracompact binary systems (in't Zand et al. 2005).

The detected strong reflection component may play a crucial role in the polarization observed in this case. It offers a plausible explanation for the significant degree of polarization observed above 7 keV in the source, as reported by Di Marco & IXPE Science Team (2023), where the polarimetric spectrum model employed did not include a detailed treatment of reflection component. Moving forward, the next phase of my study involves adapting my model to the

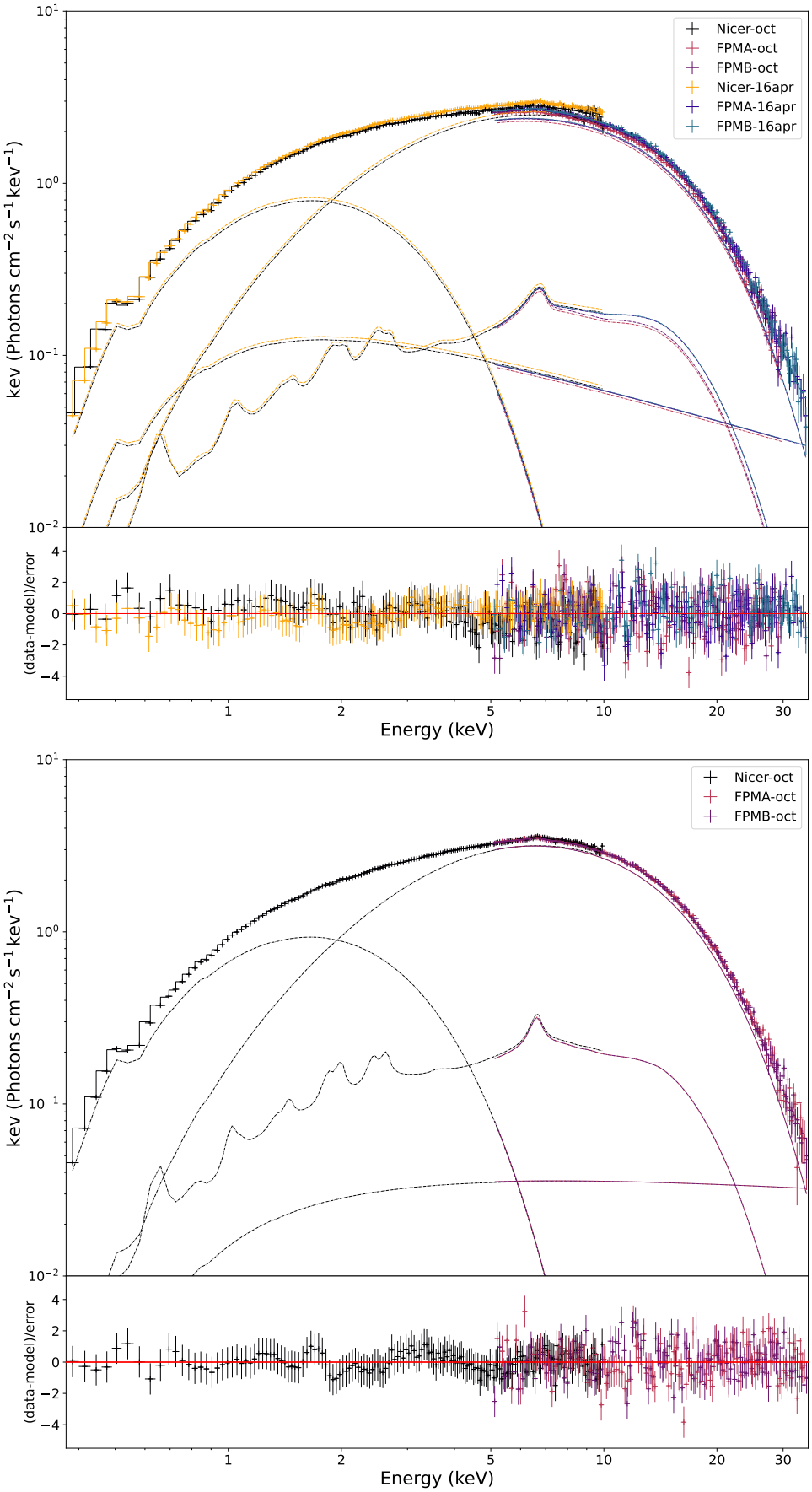

Figure 8.1: Spectra and residuals in units of sigma with respect to the model described in the text. The top panel illustrates the spectral data gathered on October 11 and April 16. In contrast, the bottom panel presents the spectrum obtained on April 15.

Table 8.1: Best-fit values for the two fits described in the text, adopting MODEL 1. Uncertainties are at the 90% c.l.

Model	Component	Oct + 16th April	15th April
TBFEO	nH(10^{22})	0.175 ± 0.005	0.170 ± 0.003
	O	$1.40^{+0.05}_{-0.07}$	1.38 ± 0.09
	Fe	<0.63	<0.74
EXPABS	LowECut(keV)	*	*
POWERLAW	PhoIndex	2.64 ± 0.2	2.13 (frozen)
	norm	0.3 ± 0.2	$0.05 \pm +0.01$
RDBLUR	Betor10	-2.5 (frozen)	-2.5 (frozen)
	Rin_M	19^{+20}_{-7}	48^{+140}_{-25}
	$\mathrm{Rout}_M(10^3)$	1.0 (frozen)	1.0 (frozen)
	Incl(deg)	29^{+7}_{-6}	15^{+16}_{-12}
RFXCONV	rel_{refl}	$-0.22^{+0.03}_{-0.13}$	$-0.18^{+0.02}_{-0.05}$
	Fe_{abund}	0.207103 (frozen)	0.207103 (frozen)
	$\log_{xi}$	$2.69^{+0.06}_{-0.32}$	$2.74^{+0.06}_{-0.21}$
COMPTB	kTs(keV)	$0.83^{+0.1}_{-0.08}$	0.96 ± 0.06
	Γ	3 (frozen)	3 (frozen)
	α Nicer	$0.89^{+0.05}_{-0.02}$	$0.94^{+0.05}_{-0.04}$
	α NuSTAR_{octo}	$0.963^{+0.008}_{-0.007}$	$0.97^{+0.05}_{-0.04}$
	α NuSTAR_{apr}	$0.984^{+0.008}_{-0.007}$	-
	δ	0 (frozen)	0 (frozen)
	kTe(keV)	2.90 ± 0.03	$2.87^{+0.05}_{-0.03}$
	$\log_A$	8 (frozen)	8 (frozen)
	norm	0.051 ± 0.001	0.067 ± 0.002
	$\mathrm{R_{sp}}$ (R_g)	7.6 ± 0.4	6.83 ± 0.07
DISKBB	Tin(keV)	$0.63^{+0.072}_{-0.055}$	$0.626^{+0.041}_{-0.037}$
	norm	820^{+310}_{-180}	990^{+220}_{-170}
	$\mathrm{R_{bb}}$ (R_g)	19 ± 2	20.4 ± 0.6
	χ^2/dof	816.0/778	358.3/411

* Kept linked the seed photon temperature KTs.

IXPE data, which was obtained simultaneously with the *NICER* and *NuSTAR* observations. This fit will enable me to examine whether the degree of the reflection component, in relation to its flux, accounts for the pronounced polarization observed above 7 keV.

9 Conclusions and Future outlook

Low-mass X-ray binary systems stand as some of the most fascinating and extreme entities in our universe. Despite a century of extensive research, comprehending their geometry and the physical processes driving their emission, several characteristics of these sources remain a tangled knot that is difficult to unravel. This thesis illustrates that understanding the geometry of these systems is inseparable from their spectral and temporal analysis. It highlights that a multi-wavelength analysis is one of the most effective diagnostic approach for creating a comprehensive and detailed depiction of these sources.

In my analysis of *XMM-Newton* and *NuSTAR* observations of 4U 1822-371, I have uncovered the presence of a **reflection component** in the spectrum, despite the system's high inclination angle. This discovery challenges existing views, as reflection components are typically faint and challenging to detect in sources with high inclination. Moreover, the unusual findings related to the inner accretion disc radius indicate a scenario more complex than previously thought. In agreement with previous literature (Iaria et al. 2013b) I have proposed the existence of an **extended, optically-thin corona** that scatters the intrinsic luminosity produced by the source along the line of sight, allowing us to observe only about 10% of the total luminosity. This hypothesis adds a significant piece to the complex puzzle of understanding high-inclination systems.

To gain a better understanding of the entire disc, including its outermost regions, it is crucial to turn our attention to lower-energy radiation and enter the domain of optical astronomy. Analyzing data from the GTC telescope during the quiescent phase of Swift J1357.2-0933 revealed distinctive features in its Hβ emission line. The identified periodicity in the varying energy of the line centroid, allowed to estimate systemic and radial velocity and an orbital period, in line with the estimates reported in literature. The study reveals also compelling evidence of a narrow, deep, and fluctuating cores within the emission line, likely associated with occultation by the outer rim bulge, robustly support the **high-inclination nature of this system**.

As observed in the earlier two studies, the presence of eclipses or dips in the X-ray light curve is a significant indicator of a source high inclination angle. This leads to the pertinent question: **How can we accurately determine the system inclination angle?** Our examination of reflection models in X-ray spectral analysis has shown that these can yield insights into several aspects of the system, including the disc size and its inclination. In my most recent work, I have

pioneered a novel approach to analyze emission lines in the optical spectra of binary systems, employing the diskline model to deduce the system geometric structure. This method, applied to Swift J1357.2-0933 and MAXI J1305-704 during both quiescent and outburst phases, has provided a more precise depiction of their geometry. The findings point to emission region consistent with their high-inclination characteristics. This innovative approach, while still open to further investigation, shows great potential for future research in delivering reliable geometric representations and deepening our knowledge of the temperature and ionization conditions within the emitting region.

In conclusion, the research presented in this thesis is a complex task, as each study typically uncovers new ideas needing deeper investigation. A prime example is the application of the DISKLINE model to the emission lines observed in optical spectra. In such analyses, comparing the geometry of disc outer regions obtained via optical spectra and its inner regions via X-ray spectra can reveal if the disc inclination is consistent or varies significantly along the radius, as in presence of a warping. It is resonable that the disc plane is not uniformly flat but exhibits warping or varies in inclination at different radial distances. This warping could arise from multiple physical phenomena, depending on the system in question.

Pringle (1996) investigated the influence of radiation on accretion disc structures, especially around intensely luminous objects like AGNs. The central object radiation pressure can trigger instabilities, leading to warping in the disc that changes over time due to differential radiation forces acting on different disc sections. Ogilvie & Dubus (2001) studied how tidal forces might cause both warping and precession in these discs, a phenomenon of particular interest in X-ray binaries, where the dynamics between a compact object and its companion star govern the accretion process. Uzdensky (2004) highlighted the significance of magnetic fields in the dynamics of accretion discs, particularly in systems with a magnetized central star, such as a pulsar. In these cases, the interaction between the star magnetic field and the ionized material in the disc can lead to warping. If the magnetic field interactions cause warping primarily in the inner region of the disc, then its inclination could differ from what is observed in the outer regions. Di Salvo et al. (2019) study revealed a broad iron line in the spectra of the accreting millisecond pulsar SAX J1808.4-3658, suggesting reflection from the inner accretion disc. This analysis set an upper limit of about 12 R_g for the inner disc radius and indicated a system inclination angle of over 50 degrees. However, when these findings are juxtaposed with the radial velocity measurements of the optical companion (Elebert et al. 2009), a surprisingly low neutron star mass (less than 0.8 solar masses) was suggested. This is noteworthy because theoretical and observational studies generally propose a minimum neutron star mass of about 1.1 to 1.2 solar masses (Lattimer & Prakash 2001), with the Chandrasekhar limit at approximately 1.4 solar masses being a benchmark for neutron star mass. Thus, a mass below 0.8 solar masses would compel us to reconsider our understanding of compact objects. Yet, this anomaly might be explained by a warped inner disc influenced by the pulsar strong magnetic field. Analyzing the emission lines in this source optical spectrum could therefore help determine the inclination angle of the outermost region, in order to verify if it matches the one reported in literature. To reconcile with a plausible neutron star mass, this angle should be around 30 degrees. Based

on a qualitative analysis of a VLT optical spectrum presented by Campana et al. (2004), this method appears applicable to this source, which should exhibit a sufficiently broad Hα line. The next stage would be to secure high-resolution data for this system similar to those examined in Chapter 7.

Moreover, several upcoming X-ray missions like *Advanced Telescope for High-ENergy Astrophysics (Athena)*, *Enhanced X-ray Timing and Polarimetry (eXTP)* and *X-Ray Imaging and Spectroscopy Mission (XRISM)* are set to revolutionize the field in the next few years. *Athena*, an ESA project planned for post-2035 launch, will significantly improve the effective area with two onboard instruments: the X-ray Integral Field Unit (X-IFU) for spatially resolved high-resolution X-ray spectroscopy, and the Wide Field Imager (WFI) for sensitive, wide field imaging and spectroscopy. Launch planned in 2027, the *eXTP* telescope will allow detailed studies due to its large effective area in the X-ray band, aiding in the search for pulsations and polarization in nearby sources. Ultimately, the recently launched *XRISM* will advance high-spectral resolution measurements in the 1-10 keV range, improving the resolution of discrete features compared to previous missions like XMM/RGS and Chandra gratings. These projects will provide data with unparalleled statistical quality, thanks to their increased effective areas and improved spectral resolution and/or polarimetric capabilities. This will deepen our understanding of spectral continuum and assist in analysis both narrow and broad spectral features, such as disc emission lines.

In summary, this thesis offers key insights into the complex geometry of LMXBs, enhancing our understanding of their geometry and emission mechanisms. It underscores the value of a multi-wavelength and multi-faceted approach, integrating polarimetric, spectroscopic, and temporal observations. These findings not only advance our current knowledge, but also open new avenues for future research on this challenging and puzzling celestial objects.

"Questa conclusione, benchè trovata da povera gente, c'è parsa così giusta, che abbiam pensato di metterla qui, come il sugo di tutta la storia. La quale, se non v'è dispiaciuta affatto, vogliatene bene a chi l'ha scritta, e anche un pochino a chi l'ha raccomodata. Ma se in vece fossimo riusciti ad annoiarvi, credete che non s'è fatto apposta."

I promessi sposi, Alessandro Manzoni.

Bibliography

Abbott, R., Abbott, T. D., Abraham, S., et al. 2020, , 125, 101102

Abramowicz, M. A., Czerny, B., Lasota, J. P., & Szuszkiewicz, E. 1988, The Astrophysical Journal, 332, 646

Alonso-Hernández, J., Fürst, F., Kretschmar, P., Caballero, I., & Joyce, A. M. 2022, Astronomy and Astrophysics, 662, A62

Alpar, M. A., Cheng, A. F., Ruderman, M. A., & Shaham, J. 1982, Nature, 300, 728

Anderson, S. F., Margon, B., Deutsch, E. W., Downes, R. A., & Allen, R. G. 1997, The Astrophysical Journal Letters, 482, L69

Anitra, A., Di Salvo, T., Iaria, R., et al. 2021, Astronomy and Astrophysics, 654, A160

Anitra, A., Mata Sanchez, D., Munoz-Darias, T., et al. 2023, arXiv e-prints, arXiv:2310.12636

Appenzeller, I., Fricke, K., Fürtig, W., et al. 1998, The Messenger, 94, 1

Armas Padilla, M., Corral-Santana, J. M., Borghese, A., et al. 2023, Astronomy and Astrophysics, 677, A186

Armas Padilla, M., Degenaar, N., Russell, D. M., & Wijnands, R. 2013, Monthly Notices of the Royal Astronomical Society, 428, 3083

Armas Padilla, M., Wijnands, R., Altamirano, D., et al. 2014a, Monthly Notices of the Royal Astronomical Society, 439, 3908

Armas Padilla, M., Wijnands, R., Degenaar, N., et al. 2014b, Monthly Notices of the Royal Astronomical Society, 444, 902

Arnason, R. M., Papei, H., Barmby, P., Bahramian, A., & Gorski, M. D. 2021, Monthly Notices of the Royal Astronomical Society, 502, 5455

Arnaud, K. A. 1996, in Astronomical Society of the Pacific Conference Series, Vol. 101, Astronomical Data Analysis Software and Systems V, ed. G. H. Jacoby & J. Barnes, 17

Asplund, M., Grevesse, N., Sauval, A. J., & Scott, P. 2009, Annual Review of Astronomy and Astrophysics, 47, 481–522

Astropy Collaboration, Price-Whelan, A. M., Lim, P. L., et al. 2022, The Astrophysical Journal, 935, 167

Baade, W. & Zwicky, F. 1934, Physical Review, 46, 76

Bachetti, M., Rana, V., Walton, D. J., et al. 2013, The Astrophysical Journal, 778, 163

Backer, D. C., Kulkarni, S. R., Heiles, C., Davis, M. M., & Goss, W. M. 1982, Nature, 300, 615

Bambynek, W., Crasemann, B., Fink, R. W., et al. 1972, Reviews of Modern Physics, 44, 716

Barra, F., Pinto, C., Middleton, M., et al. 2023, arXiv e-prints, arXiv:2311.16243

Bayless, A. J., Robinson, E. L., Hynes, R. I., Ashcraft, T. A., & Cornell, M. E. 2010, The Astrophysical Journal, 709, 251

Baym, G., Pethick, C., & Sutherland, P. 1971, The Astrophysical Journal, 170, 299

Belloni, T. 2005, in American Institute of Physics Conference Series, Vol. 797, Interacting Binaries: Accretion, Evolution, and Outcomes, ed. L. Burderi, L. A. Antonelli, F. D'Antona, T. di Salvo, G. L. Israel, L. Piersanti, A. Tornambè, & O. Straniero, 197–204

Belloni, T., Psaltis, D., & van der Klis, M. 2002, The Astrophysical Journal, 572, 392

Böhm-Vitense, E. 1992, Introduction to stellar astrophysics. Volume 3. Stellar structure and evolution., Vol. 3

Bolton, C. T. 1972, Nature, 235, 271

Burderi, L., Di Salvo, T., Riggio, A., et al. 2010, Astronomy and Astrophysics, 515, A44

Burderi, L., Di Salvo, T., Robba, N. R., et al. 1998, The Astrophysical Journal, 498, 831

Burrows, D. N., Hill, J. E., Nousek, J. A., et al. 2000, in Society of Photo-Optical Instrumentation Engineers (SPIE) Conference Series, Vol. 4140, X-Ray and Gamma-Ray Instrumentation for Astronomy XI, ed. K. A. Flanagan & O. H. Siegmund, 64–75

Bussard, R. W., Alexander, S. B., & Meszaros, P. 1986, , 34, 440

Cackett, E. M., Miller, J. M., Bhattacharyya, S., et al. 2008, The Astrophysical Journal, 674, 415

Campana, S., D'Avanzo, P., Casares, J., et al. 2004, The Astrophysical Journal Letters, 614, L49

Casares, J. 2015, The Astrophysical Journal, 808, 80

Casares, J., Muñoz-Darias, T., Torres, M. A. P., et al. 2022, Monthly Notices of the Royal Astronomical Society, 516, 2023

Casella, P., Belloni, T., Homan, J., & Stella, L. 2004, Astronomy and Astrophysics, 426, 587

Chadwick, J. 1932, Proceedings of the Royal Society of London Series A, 136, 692

Chakrabarti, S. & Titarchuk, L. G. 1995, The Astrophysical Journal, 455, 623

Charles, P., Matthews, J. H., Buckley, D. A. H., et al. 2019, Monthly Notices of the Royal Astronomical Society, 489, L47

Chen, W.-C. & Podsiadlowski, P. 2019, The Astrophysical Journal Letters, 876, L11

Chou, Y. & Grindlay, J. E. 2001, The Astrophysical Journal, 563, 934

Corbel, S., Nowak, M. A., Fender, R. P., Tzioumis, A. K., & Markoff, S. 2003, Astronomy and Astrophysics, 400, 1007

Cornelisse, R., Kotze, M. M., Casares, J., Charles, P. A., & Hakala, P. J. 2013, Monthly Notices of the Royal Astronomical Society, 436, 910

Corral-Santana, J. M., Casares, J., Muñoz-Darias, T., et al. 2013, Science, 339, 1048

Cúneo, V. A., Muñoz-Darias, T., Sánchez-Sierras, J., et al. 2020, Monthly Notices of the Royal Astronomical Society, 498, 25

Dauser, T., García, J., Walton, D. J., et al. 2016, Astronomy Astrophysics, 590, A76

Dauser, T., Wilms, J., Reynolds, C. S., & Brenneman, L. W. 2010, Monthly Notices of the Royal Astronomical Society, 409, 1534

Degenaar, N., Miller, J. M., Chakrabarty, D., et al. 2015, Monthly Notices of the Royal Astronomical Society, 451, L85

Degenaar, N. & Suleimanov, V. F. 2018, arXiv e-prints, arXiv:1806.02833

Del Santo, M., Malzac, J., Belmont, R., Bouchet, L., & De Cesare, G. 2013, in European Physical Journal Web of Conferences, Vol. 61, European Physical Journal Web of Conferences, 03006

Di Marco, A. & IXPE Science Team. 2023, in American Astronomical Society Meeting Abstracts, Vol. 55, American Astronomical Society Meeting Abstracts, 329.04

di Salvo, T., Burderi, L., Riggio, A., Papitto, A., & Menna, M. T. 2008, in American Institute of Physics Conference Series, Vol. 1068, A Decade of Accreting MilliSecond X-ray Pulsars, ed. R. Wijnands, D. Altamirano, P. Soleri, N. Degenaar, N. Rea, P. Casella, A. Patruno, & M. Linares, 33–37

di Salvo, T., D'Aí, A., Iaria, R., et al. 2009, Monthly Notices of the Royal Astronomical Society, 398, 2022

Di Salvo, T., Goldoni, P., Stella, L., et al. 2006, The Astrophysical Journal Letters, 649, L91

Di Salvo, T., Iaria, R., Matranga, M., et al. 2015, Monthly Notices of the Royal Astronomical Society, 449, 2794

Di Salvo, T., Robba, N. R., Iaria, R., et al. 2001, The Astrophysical Journal, 554, 49

Di Salvo, T. & Sanna, A. 2020, arXiv e-prints, arXiv:2010.09005

Di Salvo, T. & Sanna, A. 2022, in Astrophysics and Space Science Library, Vol. 465, Astrophysics and Space Science Library, ed. S. Bhattacharyya, A. Papitto, & D. Bhattacharya, 87–124

Di Salvo, T., Sanna, A., Burderi, L., et al. 2019, Monthly Notices of the Royal Astronomical Society, 483, 767

Dieters, S. W. & van der Klis, M. 2000, Monthly Notices of the Royal Astronomical Society, 311, 201

Done, C., Gierliński, M., & Kubota, A. 2007, The Astronomy and Astrophysics Review, 15, 1–66

Eggleton, P. P. 1976, in Structure and Evolution of Close Binary Systems, ed. P. Eggleton, S. Mitton, & J. Whelan, Vol. 73, 209

Eggleton, P. P. 1983a, The Astrophysical Journal, 268, 368

Eggleton, P. P. 1983b, The Astrophysical Journal, 268, 368

Egron, E. 2013, PhD thesis, University of Cagliari

Egron, E., Di Salvo, T., Motta, S., et al. 2013, Astronomy and Astrophysics, 550, A5

Einstein, A. 1915, Sitzungsberichte der Königlich Preussischen Akademie der Wissenschaften, 778

Elebert, P., Reynolds, M. T., Callanan, P. J., et al. 2009, Monthly Notices of the Royal Astronomical Society, 395, 884

Esin, A. A., McClintock, J. E., & Narayan, R. 1997, The Astrophysical Journal, 489, 865

Fabian, A. C., Rees, M. J., Stella, L., & White, N. E. 1989, Monthly Notices of the Royal Astronomical Society, 238, 729

Fabian, , Iwasawa, K., Reynolds, C., & Young, A. 2000, Publications of the Astronomical Society of the Pacific, 112, 1145–1161

Farinelli, R., Titarchuk, L., Paizis, A., & Frontera, F. 2008, The Astrophysical Journal, 680, 602

Fender, R. P., Belloni, T. M., & Gallo, E. 2004, Monthly Notices of the Royal Astronomical Society, 355, 1105

Fiocchi, M., Bazzano, A., Ubertini, P., & Jean, P. 2006, The Astrophysical Journal, 651, 416

Ford, E. C., van der Klis, M., Méndez, M., et al. 2000, The Astrophysical Journal, 537, 368

Fornasini, F. M., Antoniou, V., & Dubus, G. 2023, arXiv e-prints, arXiv:2308.02645

Foster, A. J., Ross, R. R., & Fabian, A. C. 1986, Monthly Notices of the Royal Astronomical Society, 221, 409

Frank, J., King, A., Raine, D., & King, B. 2002, Accretion Power in Astrophysics, Accretion Power in Astrophysics (Cambridge University Press)

Frank, J., King, A., & Raine, D. J. 2002, Accretion Power in Astrophysics: Third Edition

Freudling, W., Romaniello, M., Bramich, D. M., et al. 2013, Astronomy and Astrophysics, 559, A96

Galeev, A. A. 1979, Space Science Reviews, 23, 411

Ghosh, P. & Lamb, F. K. 1979a, The Astrophysical Journal, 234, 296

Ghosh, P. & Lamb, F. K. 1979b, The Astrophysical Journal, 234, 296

Giacconi, R. 1974, in Gravitational Radiation and Gravitational Collapse, ed. C. Dewitt-Morette, Vol. 64, 147

Giacconi, R., Gursky, H., Paolini, F. R., & Rossi, B. B. 1962, Phys. Rev. Lett., 9, 439

Gierliński, M. & Done, C. 2002, Monthly Notices of the Royal Astronomical Society, 331, L47

Gierliński, M. & Done, C. 2003, Monthly Notices of the Royal Astronomical Society, 342, 1083

Gierliński, M., Zdziarski, A. A., Poutanen, J., et al. 1999, Monthly Notices of the Royal Astronomical Society, 309, 496

Gilfanov, M. 2010, in Lecture Notes in Physics, Berlin Springer Verlag, ed. T. Belloni, Vol. 794, 17

Griffiths, R. E., Gursky, H., Schwartz, D. A., et al. 1978, Nature, 276, 247

Gúrpide, A., Parra, M., Godet, O., Contini, T., & Olive, J. F. 2022, Astronomy and Astrophysics, 666, A100

Hanke, M. 2011, PhD thesis, University of Erlangen-Nuremberg, Astronomical Institute

Hartmann, L. 1998, Accretion Processes in Star Formation

Hasinger, G. & van der Klis, M. 1989, Astronomy and Astrophysics, 225, 79

Hawking, S. W. 1975, Communications in Mathematical Physics, 43, 199

Hellier, C. & Mason, K. O. 1989, Monthly Notices of the Royal Astronomical Society, 239, 715

Hewish, A., Bell, S. J., Pilkington, J. D. H., Scott, P. F., & Collins, R. A. 1968, Nature, 217, 709

Horne, K. & Marsh, T. R. 1986, Monthly Notices of the Royal Astronomical Society, 218, 761

Hu, H. D., Esamdin, A., Yuan, J. P., et al. 2011, Astronomy and Astrophysics, 530, A67

Iaria, R., D'Aí, A., di Salvo, T., et al. 2009, Astronomy and Astrophysics, 505, 1143

Iaria, R., Di Salvo, T., Anitra, A., et al. 2024, arXiv e-prints, arXiv:2401.03698

Iaria, R., di Salvo, T., Burderi, L., et al. 2011, Astronomy and Astrophysics, 534, A85

Iaria, R., Di Salvo, T., D'Aì, A., et al. 2013a, Astronomy and Astrophysics, 549, A33

Iaria, R., Di Salvo, T., D'Aì, A., et al. 2013b, Astronomy and Astrophysics, 549, A33

Iaria, R., Di Salvo, T., Matranga, M., et al. 2015, Astronomy and Astrophysics, 577, A63

Iaria, R., Gambino, A. F., Di Salvo, T., et al. 2018, Monthly Notices of the Royal Astronomical Society, 473, 3490

Ichimaru, S. 1977, The Astrophysical Journal, 214, 840

in't Zand, J. J. M., Cumming, A., van der Sluys, M. V., Verbunt, F., & Pols, O. R. 2005, Astronomy and Astrophysics, 441, 675

Israel, G. L., Papitto, A., Esposito, P., et al. 2017, Monthly Notices of the Royal Astronomical Society, 466, L48

Jackson, J. D. 1975, Classical electrodynamics

Jain, C., Paul, B., & Dutta, A. 2010, Monthly Notices of the Royal Astronomical Society, 409, 755

Jayasinghe, T., Stanek, K. Z., Kochanek, C. S., et al. 2020, Monthly Notices of the Royal Astronomical Society, 493, 4045

Jiménez-Ibarra, F., Muñoz-Darias, T., Casares, J., Armas Padilla, M., & Corral-Santana, J. M. 2019a, Monthly Notices of the Royal Astronomical Society, 489, 3420

Jiménez-Ibarra, F., Muñoz-Darias, T., Casares, J., Armas Padilla, M., & Corral-Santana, J. M. 2019b, Monthly Notices of the Royal Astronomical Society, 489, 3420

Jonker, P. G. & van der Klis, M. 2001, The Astrophysical Journal, 553, L43

Jonker, P. G., van der Klis, M., & Groot, P. J. 2003, Monthly Notices of the Royal Astronomical Society, 339, 663

Kaaret, P., Feng, H., & Roberts, T. P. 2017, Annual Review of Astronomy and Astrophysics, 55, 303

Kaastra, J. S. & Mewe, R. 1993, , 97, 443

Kennea, J., Miller, J. M., Beardmore, A., Degenaar, N., & Reynolds, M. T. 2012a, The Astronomer's Telegram, 4071, 1

Kennea, J. A., Yang, Y. J., Altamirano, D., et al. 2012b, The Astronomer's Telegram, 4044, 1

King, A. R., Pringle, J. E., & Livio, M. 2007, Monthly Notices of the Royal Astronomical Society, 376, 1740

Kippenhahn, R. & Weigert, A. 1990, Stellar Structure and Evolution

Kolehmainen, M., Done, C., & Díaz Trigo, M. 2011, Monthly Notices of the Royal Astronomical Society, 416, 311

Kraft, R. P., Mathews, J., & Greenstein, J. L. 1962, The Astrophysical Journal, 136, 312

Kubota, A., Tanaka, Y., Makishima, K., et al. 1998, Publications of the Astronomical Society of Japan, 50, 667

Kuulkers, E., Kouveliotou, C., Belloni, T., et al. 2013, Astronomy and Astrophysics, 552, A32

Landau, L. D. & Lifshitz, E. M. 1975, The classical theory of fields

Lasota, J. P., Alexander, T., Dubus, G., et al. 2011, The Astrophysical Journal, 735, 89

Lattimer, J. M. & Prakash, M. 2001, The Astrophysical Journal, 550, 426

Lattimer, J. M. & Prakash, M. 2016, Physics Reports, 621, 127

Liu, J.-F., Bregman, J. N., Bai, Y., Justham, S., & Crowther, P. 2013, Nature, 503, 500

Longair, M. S. 2011, High Energy Astrophysics

Ludlam, R. M., Miller, J. M., Bachetti, M., et al. 2017, The Astrophysical Journal, 836, 140

Madsen, K. K., Grefenstette, B. W., Pike, S., et al. 2020, arXiv e-prints, arXiv:2005.00569

Magdziarz, P. & Zdziarski, A. A. 1995, Monthly Notices of the Royal Astronomical Society, 273, 837

Makishima, K., Maejima, Y., Mitsuda, K., et al. 1986, The Astrophysical Journal, 308, 635

Malzac, J. 2005, Modélisation de l'émission X et gamma des objets compacts par les méthodes Monte-Carlo

Marino, A., Russell, T. D., Del Santo, M., et al. 2023, Monthly Notices of the Royal Astronomical Society, 525, 2366

Marsh, T. R., Horne, K., & Shipman, H. L. 1987a, Monthly Notices of the Royal Astronomical Society, 225, 551

Marsh, T. R., Horne, K., & Shipman, H. L. 1987b, Monthly Notices of the Royal Astronomical Society, 225, 551

Marsh, T. R., Robinson, E. L., & Wood, J. H. 1994, Monthly Notices of the Royal Astronomical Society, 266, 137

Mason, K. O. & Cordova, F. A. 1982, The Astrophysical Journal, 262, 253

Mata Sánchez, D., Muñoz-Darias, T., Casares, J., Corral-Santana, J. M., & Shahbaz, T. 2015, Monthly Notices of the Royal Astronomical Society, 454, 2199

Mata Sánchez, D., Rau, A., Álvarez Hernández, A., et al. 2021, Monthly Notices of the Royal Astronomical Society, 506, 581

Mazzola, S. M., Iaria, R., Di Salvo, T., et al. 2019, Astronomy and Astrophysics, 625, L12

Méndez, M., van der Klis, M., Ford, E. C., Wijnands, R., & van Paradijs, J. 1999, The Astrophysical Journal Letters, 511, L49

Miceli, C., Mata Sánchez, D., Anitra, A., et al. 2024 (Submitted), Astronomy and Astrophysics

Miller, J. M., Raymond, J., Kallman, T. R., et al. 2014, The Astrophysical Journal, 788, 53

Mitsuda, K., Inoue, H., Nakamura, N., & Tanaka, Y. 1989, Publications of the Astronomical Society of Japan, 41, 97

Miyamoto, S., Kitamoto, S., Hayashida, K., & Egoshi, W. 1995, The Astrophysical Journal Letters, 442, L13

Morihana, K., Sugizaki, M., Nakahira, S., et al. 2013, Publications of the Astronomical Society of Japan, 65, L10

Muñoz-Darias, T., Casares, J., O'Brien, K., et al. 2009, Monthly Notices of the Royal Astronomical Society, 394, L136

Muñoz-Darias, T., Fender, R. P., Motta, S. E., & Belloni, T. M. 2014, Monthly Notices of the Royal Astronomical Society, 443, 3270

Mukhopadhyay, B. & Dutta, P. 2012, New Astronomy, 17, 51

Narayan, R., Kato, S., & Honma, F. 1997, The Astrophysical Journal, 476, 49

Narayan, R. & Yi, I. 1994, The Astrophysical Journal Letters, 428, L13

Narayan, R. & Yi, I. 1995, The Astrophysical Journal, 452, 710

Narayan, R., Yi, I., & Mahadevan, R. 1996, , 120, 287

Naylor, T. 1998, Monthly Notices of the Royal Astronomical Society, 296, 339

Nelson, L. A. & Rappaport, S. 2003, The Astrophysical Journal, 598, 431

Ogilvie, G. I. & Dubus, G. 2001, Monthly Notices of the Royal Astronomical Society, 320, 485

Oppenheimer, J. R. & Volkoff, G. M. 1939, Physical Review, 55, 374

Orosz, J. A., Bailyn, C. D., Remillard, R. A., McClintock, J. E., & Foltz, C. B. 1994, The Astrophysical Journal, 436, 848

Ostriker, J. P. & Gunn, J. E. 1969, in Bulletin of the American Astronomical Society, Vol. 1, 357–358

Paczyński, B. 1971, Annual Review of Astronomy and Astrophysics, 9, 183

Paice, J. A., Gandhi, P., Charles, P. A., et al. 2019, Monthly Notices of the Royal Astronomical Society, 488, 512

Paizis, A., Farinelli, R., Titarchuk, L., et al. 2006, Astronomy and Astrophysics, 459, 187

Parmar, A. N., Oosterbroek, T., Del Sordo, S., et al. 2000, Astronomy and Astrophysics, 356, 175

Patruno, A. & Watts, A. L. 2020, in Timing Neutron Stars: Pulsations, Oscillations and Explosions (Springer Berlin Heidelberg), 143–208

Poutanen, J. & Coppi, P. S. 1998, Physica Scripta Volume T, 77, 57

Pringle, J. E. 1996, Monthly Notices of the Royal Astronomical Society, 281, 357

Protassov, R., van Dyk, D. A., Connors, A., Kashyap, V. L., & Siemiginowska, A. 2002, The Astrophysical Journal, 571, 545

Psaltis, D., Belloni, T., & van der Klis, M. 1999, The Astrophysical Journal, 520, 262

Radhakrishnan, V. & Cooke, D. J. 1969, , 3, 225

Rappaport, S., Nelson, L. A., Ma, C. P., & Joss, P. C. 1987, The Astrophysical Journal, 322, 842

Rayne, M. W. & Whelan, J. A. J. 1981, Monthly Notices of the Royal Astronomical Society, 196, 73

Rea, N. 2013, in Neutron Stars and Pulsars: Challenges and Opportunities after 80 years, ed. J. van Leeuwen, Vol. 291, 11–18

Remillard, R. A. & McClintock, J. E. 2006, Annual Review of Astronomy and Astrophysics, 44, 49

Repetto, S. & Nelemans, G. 2015, Monthly Notices of the Royal Astronomical Society, 453, 3341

Reynolds, C. 2003, Physics Reports, 377, 389–466

Reynolds, C. S. 1996, PhD thesis, University of Cambridge, UK

Ross, R. R., Fabian, A. C., & Young, A. J. 1999, Monthly Notices of the Royal Astronomical Society, 306, 461

Russell, D. M., Bramich, D. M., Lewis, F., et al. 2019, Astronomische Nachrichten, 340, 278

Saha, M. N. 1921, Proceedings of the Royal Society of London Series A, 99, 135

Salpeter, E. E. 1964, The Astrophysical Journal, 140, 796

Sanna, A., Riggio, A., Burderi, L., et al. 2017, Monthly Notices of the Royal Astronomical Society, 469, 2–12

Sathyaprakash, R., Roberts, T. P., Walton, D. J., et al. 2019, Monthly Notices of the Royal Astronomical Society, 488, L35

Schoembs, R. & Hartmann, K. 1983, Astronomy and Astrophysics, 128, 37

Schwarzschild, K. 1916, in Sitzungsberichte der Königlich Preussischen Akademie der Wissenschaften zu Berlin, 424–434

Shafter, A. W., Szkody, P., & Thorstensen, J. R. 1986, The Astrophysical Journal, 308, 765

Shakura, N. I. & Sunyaev, R. A. 1973a, Astronomy and Astrophysics, 24, 337

Shakura, N. I. & Sunyaev, R. A. 1973b, Astronomy and Astrophysics, 500, 33

Shaw, A. W., Charles, P. A., Casares, J., & Steeghs, D. 2017, in 7 years of MAXI: monitoring X-ray Transients, ed. M. Serino, M. Shidatsu, W. Iwakiri, & T. Mihara, 45

Shidatsu, M., Ueda, Y., Nakahira, S., et al. 2013, The Astrophysical Journal, 779, 26

Sincell, M. W. & Krolik, J. H. 1998, Advances in Space Research, 21, 113

Smak, J. 1970, , 20, 311

Somero, A., Hakala, P., Muhli, P., Charles, P., & Vilhu, O. 2012a, Astronomy and Astrophysics, 539, A111

Somero, A., Hakala, P., Muhli, P., Charles, P., & Vilhu, O. 2012b, Astronomy and Astrophysics, 539, A111

Steeghs, D. & Casares, J. 2002, The Astrophysical Journal, 568, 273

Stella, L., Priedhorsky, W., & White, N. E. 1987, The Astrophysical Journal Letters, 312, L17

Strüder, L., Briel, U., Dennerl, K., et al. 2001, Astronomy and Astrophysics, 365, L18

Sturner, S. J. & Dermer, C. D. 1994, Astronomy and Astrophysics, 281, L101

Suwa, F., Negoro, H., Nakahira, S., et al. 2012, The Astronomer's Telegram, 4035, 1

Torres, M. A. P., Callanan, P. J., Garcia, M. R., et al. 2002, The Astrophysical Journal, 569, 423

Torres, M. A. P., Callanan, P. J., Garcia, M. R., et al. 2004, The Astrophysical Journal, 612, 1026

Torres, M. A. P., Jonker, P. G., Miller-Jones, J. C. A., et al. 2015, Monthly Notices of the Royal Astronomical Society, 450, 4292

Turner, M. J. L., Abbey, A., Arnaud, M., et al. 2001, Astronomy and Astrophysics, 365, L27

Unda-Sanzana, E., Marsh, T. R., & Morales-Rueda, L. 2006, Monthly Notices of the Royal Astronomical Society, 369, 805

Uzdensky, D. A. 2004, Astronomy and Astrophysics, Supplement, 292, 573

van der Klis, M. 1989, Annual Review of Astronomy and Astrophysics, 27, 517

van Dokkum, P. G., Bloom, J., & Tewes, M. 2012, L.A.Cosmic: Laplacian Cosmic Ray Identification, Astrophysics Source Code Library, record ascl:1207.005

Verbunt, F. 1993, Annual Review of Astronomy and Astrophysics, 31, 93

Verbunt, F. & Zwaan, C. 1981, Astronomy and Astrophysics, 100, L7

Verner, D. A., Ferland, G. J., Korista, K. T., & Yakovlev, D. G. 1996, The Astrophysical Journal, 465, 487

Virtanen, P., Gommers, R., Oliphant, T. E., et al. 2020, Nature Methods, 17, 261

Vrtilek, S. D., Penninx, W., Raymond, J. C., et al. 1991, The Astrophysical Journal, 376, 278

Warner, B. 1995, Cataclysmic variable stars, Vol. 28

Webster, B. L., Martin, W. L., Feast, M. W., & Andrews, P. J. 1972, Nature Physical Science, 240, 183

White, N. E. & Mason, K. O. 1985, Space Science Reviews, 40, 167

White, N. E., Stella, L., & Parmar, A. N. 1988, The Astrophysical Journal, 324, 363

Wijnands, R., in't Zand, J. J. M., Rupen, M., et al. 2006, Astronomy and Astrophysics, 449, 1117

Wijnands, R. & van der Klis, M. 1998, Nature, 394, 344

Wilms, J., Allen, A., & McCray, R. 2000, The Astrophysical Journal, 542, 914

Zdziarski, A. A., Gierliński, M., Mikołajewska, J., et al. 2004, Monthly Notices of the Royal Astronomical Society, 351, 791

Zdziarski, A. A., Johnson, W. N., & Magdziarz, P. 1996, Monthly Notices of the Royal Astronomical Society, 283, 193